

## INFORMATION TO USERS

This material was produced from a microfilm copy of the original document. While the most advanced technological means to photograph and reproduce this document have been used, the quality is heavily dependent upon the quality of the original submitted.

The following explanation of techniques is provided to help you understand markings or patterns which may appear on this reproduction.

1. The sign or "target" for pages apparently lacking from the document photographed is "Missing Page(s)". If it was possible to obtain the missing page(s) or section, they are spliced into the film along with adjacent pages. This may have necessitated cutting thru an image and duplicating adjacent pages to insure you complete continuity.
2. When an image on the film is obliterated with a large round black mark, it is an indication that the photographer suspected that the copy may have moved during exposure and thus cause a blurred image. You will find a good image of the page in the adjacent frame.
3. When a map, drawing or chart, etc., was part of the material being photographed the photographer followed a definite method in "sectioning" the material. It is customary to begin photoing at the upper left hand corner of a large sheet and to continue photoing from left to right in equal sections with a small overlap. If necessary, sectioning is continued again — beginning below the first row and continuing on until complete.
4. The majority of users indicate that the textual content is of greatest value, however, a somewhat higher quality reproduction could be made from "photographs" if essential to the understanding of the dissertation. Silver prints of "photographs" may be ordered at additional charge by writing the Order Department, giving the catalog number, title, author and specific pages you wish reproduced.
5. PLEASE NOTE: Some pages may have indistinct print. Filmed as received.

**Xerox University Microfilms**

300 North Zeeb Road  
Ann Arbor, Michigan 48106

76-1859

MARTIN, Richard Alan, 1944-  
STUDIES OF SCALAR TURBULENCE IN AIR  
DOWNSTREAM OF A HEATED GRID.

Iowa State University, Ph.D., 1975  
Engineering, aeronautical

**Xerox University Microfilms,** Ann Arbor, Michigan 48106

Studies of scalar turbulence in air  
downstream of a heated grid

by

Richard Alan Martin

A Dissertation Submitted to the  
Graduate Faculty in Partial Fulfillment of  
The Requirements for the Degree of  
DOCTOR OF PHILOSOPHY

Major: Aerospace Engineering

Approved:

Signature was redacted for privacy.

In Charge of Major Work

Signature was redacted for privacy.

For the Major Department

Signature was redacted for privacy.

For the Graduate College

Iowa State University  
Ames, Iowa

1975

## TABLE OF CONTENTS

	Page
LIST OF SYMBOLS AND ABBREVIATIONS	iv
I. INTRODUCTION	1
A. General Background	1
B. Hot-Wire Anemometer	2
C. Crossed-Beam Schlieren	3
D. Objectives and Scope	7
II. LITERATURE REVIEW	9
A. Scalar Turbulence	9
B. Experimental Techniques	16
1. Hot-wire anemometry	16
2. Studies in geophysical or high Reynolds number flows	23
3. Optical remote sensing	25
III. THEORY	29
A. Grid-Generated Turbulence	29
B. Crossed-Beam Schlieren	44
C. Hot-Wire Anemometer	54
IV. EXPERIMENTAL APPARATUS	62
A. Flow System	62
B. Crossed-Beam Schlieren	77
C. Hot-Wire Anemometer	81
D. Analog Signal Processing Electronics	84
E. Miscellaneous	92

	Page
V. EXPERIMENTAL PROCEDURE	94
A. Vibration Reduction Measures	94
B. Crossed-Beam Schlieren	96
1. Calibration	96
2. Signal processing	99
3. Measurement reliability	107
C. Hot-Wire Anemometer	118
1. Velocity mode	118
2. Resistance thermometer mode	124
3. Mixed mode	129
VI. RESULTS AND DISCUSSION	143
A. Basic Flow Model	144
B. Longitudinal Turbulence Decay and Spectra	153
C. Scalar Turbulence	161
1. CBS noise identification with probability density and correlation function samples	161
2. Temperature fluctuation decay	181
3. Scalar spectra	192
4. Convection speed	223
5. Isotropy test	230
D. Estimates of Dissipation Rates and Scales	232
E. Hot-Wire Mixed Mode	239
VII. SUMMARY OF RESULTS AND CONCLUSIONS	241
VIII. REFERENCES	247
XI. ACKNOWLEDGEMENTS	252

LIST OF SYMBOLS AND ABBREVIATIONS<sup>1</sup>

A	area
B	signal bandwidth
BPF	band pass filtered
c	constant
C	crossed-beam schlieren sensitivity
C <sub>D</sub>	drag coefficient
C <sub>p</sub>	specific heat at constant pressure
CBS	crossed-beam schlieren
d	diameter
e	fluctuating component of voltage
E	instantaneous voltage
E <sub>1</sub>	one-dimensional energy spectrum of longitudinal velocity fluctuations
E <sub>θ</sub>	three-dimensional spectrum function of temperature fluctuations
E <sub>θ1</sub>	one-dimensional spectrum of temperature fluctuations
f	frequency
f <sub>e</sub>	frequency marking the range of maximum energy containing eddies
f <sub>N</sub>	highest frequency of interest in signal or Nyquist frequency
$\vec{\text{grad}}( )$	gradient operator $[ = \frac{\partial}{\partial x} ( ) \vec{i} + \frac{\partial}{\partial y} ( ) \vec{j} + \frac{\partial}{\partial z} ( ) \vec{k} ]$
H	enthalpy or heat per unit mass

---

<sup>1</sup>Symbols and abbreviations not found in this list are defined and used locally within.

HWA	hot-wire anemometer
$i$	$(-1)^{1/2}$
$i, j, k$	unit vectors along the axes of a Cartesian coordinate system
$I$	instantaneous current
$k$	wavenumber
$k_e$	wavenumber marking the range of maximum energy containing eddies ( $= 1/\ell_e$ )
$k_d$	wavenumber marking the range of dissipation eddies
$k_{\theta, d}$	wavenumber marking the range where molecular diffusion is dominant
$k_1, k_2, k_3$	wavenumber components along the axes of a Cartesian coordinate system
$\ell$	distance from point disturbance to a knife edge for one arm of crossed-beam schlieren
$\ell_e$	average size of energy containing eddies
$L$	length
$\dot{m}$	mass flow rate ( $= \bar{T} \bar{U} A$ )
$M$	periodic (or center-to-center) spacing of grid rods
$n$	fluctuating component of index of refraction
$n_o$	mean change of index of refraction relative to ambient
$N$	instantaneous index of refraction
$Nu$	Nusselt number ( $= hd/k$ )
$p$	fluctuating component of pressure
pdf	probability density function
$P$	instantaneous pressure

$Pe$	Peclet number ( $= u' \lambda_0 / \alpha$ )
$Pr$	Prandtl number ( $= C_p \mu / k = \nu / \alpha = Sm$ )
$\overline{q^2}$	twice the kinetic energy of turbulence ( $\overline{q^2} = \overline{u^2} + \overline{v^2} + \overline{w^2}$ )
$Q$	two-point density covariance ( $= \overline{\rho_1 \rho_2}$ )
$\dot{Q}$	heat transfer rate
$\overline{Q}$	mean dynamic pressure
$Q_{AB}(\tau)$	cross-correlation between signals A and B
$Q_{CBS}$	crossed-beam schlieren density covariance
rms	root-mean-square value
$r_E(\tau)$	Eulerian time autocorrelation coefficient of longitudinal velocity fluctuations
$r_{AB}(\tau)$	correlation coefficient between signals A and B
$r_{u\theta}$	correlation coefficient between longitudinal velocity and temperature fluctuations
$R$	resistance
$R_b$	resistance at 212°F
$Re_M$	Reynolds number based on M ( $= \overline{U} M / \nu$ )
$Re_\lambda$	turbulence Reynolds number ( $= \overline{U} \lambda g / \nu$ )
$R_i$	resistance at 32°F
R.T.	resistance thermometer
$\hat{s}$	unit vector along light path
$Sm$	Schmidt number ( $= Pr$ )
S.R.	sampling rate
St	Strouhal number ( $= fM / \overline{U}$ )
$S_u$	velocity sensitivity of hot-wire sensor
$S_\theta$	temperature sensitivity of hot-wire sensor



$t$	time
$T$	record length
$T_E$	Taylor integral time scale
$u,v,w$	fluctuating components of velocity along the axes of a Cartesian coordinate system
$U,V,W$	instantaneous velocity components along the axes of a Cartesian coordinate system
$\bar{U}_c$	mean convection speed of thermal eddies
$x$	longitudinal distance downstream of grid
$x_o$	apparent or virtual origin
$x,y,z$	Eulerian Cartesian coordinate axes
$x_1,x_2,x_3$	distances from origin along the axes of a Cartesian coordinate system
$X,Y,Z$	same as $x,y,z$
$\alpha$	thermal diffusivity ( $= k/\bar{T} C_p$ )
$\beta$	angle
$\gamma$	mean local rate of strain
$\Gamma$	instantaneous mass density
$\delta$	deflection of a beam relative to a knife edge
$\Delta$	grid overhear ( $= \bar{\theta}_a - \bar{\theta}_{amb}$ )
$\Delta\tau$	time increment between samples
$\varepsilon$	dissipation by turbulence per unit of mass
$\eta$	Kolmogoroff length scale ( $= 1/k_d$ )
$\theta$	fluctuating component of temperature
$\Theta$	instantaneous temperature
$\lambda_f$	Taylor longitudinal spatial micro scale

$\lambda_g$	Taylor lateral spatial micro scale
$\lambda_\theta$	micro scale for temperature fluctuations
$\Lambda_f$	longitudinal spatial integral scale
$\Lambda_g$	lateral spatial integral scale
$\Lambda_\theta$	integral scale for temperature fluctuations
$\mu$	viscosity
$\nu$	kinematic viscosity ( $= \mu/\bar{\Gamma}$ )
$\xi, \eta, \zeta$	distances from beam intersection point along the axes of a Cartesian coordinate system
$\rho$	fluctuating component of mass density
$\rho_o$	mean change of mass density relative to ambient
$\tau$	time delay between two signals
$\tau_E$	Taylor micro time scale
$\phi$	fluctuating component of beam deflection angle at a point
$\Phi$	instantaneous beam deflection angle at a point
$\chi$	rate of decay of scalar variance
$\Omega$	ohm

Subscripts:<sup>1</sup>

$( )_a$	refers to conditions of air inside the wind tunnel test section
$( )_A$	refers to beam A
$( )_{amb}$	refers to ambient conditions at the wind tunnel inlet

---

<sup>1</sup>Unless already presented or used locally below.

$( )_{\text{atm}}$	refers to atmospheric conditions
$( )_B$	refers to beam B
$i,j,k$	denotes tensor notation
$( )_{\text{max}}$	maximum value
$( )_{\text{min}}$	minimum value
$( )_0$	initial value
$( )_{\text{peak}}$	value at peak
$( )_w$	refers to conditions of hot-wire sensor
1,2,3	successive values in time or space
$( )$	vector quantity
$( \overline{ } )$	time average value obtained over a sufficiently long integration time
$( )'$	root-mean-square value or standard deviation of a fluctuating quantity
$( \dot{ } )$	time rate of change of quantity

## I. INTRODUCTION

### A. General Background

"Scalar turbulence" implies random, three-dimensional fluctuations in a dynamically passive scalar quantity--like density, temperature, or concentration. One of the important defining characteristics of any turbulent flow field is a rapid spreading of scalar and velocity fluctuations with the result that mixing may occur several orders of magnitude faster than in non-turbulent flows. This characteristic is exploited by engineers in a wide range of practical applications such as mixers and chemical reactors.

While turbulent flows are perhaps the most difficult in fluid dynamics to model mathematically, it is well-known that most natural as well as engineering flows are turbulent. Indeed, special conditions of small sizes and high viscosities are a prerequisite for the existence of laminar flows. Examples of turbulent scalar fields in natural flows are the dispersion of chemical pollutants and temperature fluctuations in the oceans and atmosphere.

Existing theoretical predictions can be compared with "point" measurements in a scalar field. These measurements also provide empirical data from which to calculate the scattering of acoustic and electromagnetic waves by a random scalar field. It is evident, therefore, that measurements of the statistical parameters which describe the mixing of scalar fluid properties by a turbulent flow field are important from a practical standpoint as well as from the more

fundamental standpoint of better understanding turbulent mixing processes.

Because of the prevalence of turbulent flows and their importance in engineering, considerable theoretical and experimental work in this area has been conducted over the past 40 years. The famous closure problem has hindered theoretical progress on both velocity and scalar problems; in fact, direct mathematical attacks using advanced statistics and Fourier analysis have been mostly unsuccessful.

As will be discussed more fully below, the theoretical progress to date has been mainly in two areas of prediction: (1) decay of fluctuations in time or space, and (2) shape of the energy or power spectra for specific frequency or wavenumber regions.

The necessity of relatively high frequency response and sensitivity limits the number of suitable devices available to the experimentalist for making reliable measurements in turbulent flows. The modern measurement techniques divide into two general categories, those in which a detecting element is introduced into the flow field and those which utilize optical remote sensing.

#### B. Hot-Wire Anemometer

Of course, the salient example from the first category is the hot-wire or hot-film anemometer (HWA) whose extensive, almost universal use has molded both the theoretical and experimental approaches to turbulence until quite recently.

Calibration for, and interpretation of measurements of velocity

statistics using a hot-wire system are relatively straightforward in isothermal flows and consequently velocity statistics have received by far the most attention. When temperature fluctuations of low level are present, a HWA system may be readily applied in the resistance thermometer mode which corresponds to the limiting case of vanishingly small wire overheat. An alternative procedure is to operate the wire at a number of overheats with mixed sensitivity and then separate the combined effects of velocity and temperature. This last technique produces a considerable increase in complexity of calibration and interpretation but is a necessity when attempting measurements in compressible flows where a third variable, density, enters to further complicate the analysis. A number of experimenters have applied resistance thermometers in geophysical flows which provide high Reynolds numbers and therefore wide spectral subranges for comparison with theoretical predictions. But apart from these studies very few direct measurements of scalar statistics are available. Particularly, in the case of supersonic flows, a distinct disadvantage to the use of hot-wires is probe interference. In combusting flows the HWA is all but ruled-out from a practical standpoint leaving the experimenter with little recourse but to turn to optical methods for high-frequency capability.

### C. Crossed-Beam Schlieren

Parks (42) has included a concise summary of the available modifications of optical crossed-beam devices in his literature survey;

he also noted several advantages, namely, they work well for liquids, provide reliable results at low mean speeds, have good spatial resolution, and in some cases, calibrate easily. A relatively new turbulence measuring instrument (52) which falls in this category has been developed by Wilson. It is called the crossed-beam schlieren (CBS) and has, in addition to the advantages inherent in remote sensing, the capability of direct measurement of scalar property statistics. The CBS consists of a pair of identical, orthogonal laser schlieren systems as shown schematically in Figure 1. Each system is comprised of a thin collimated beam of optical radiation which is passed through a flow region of interest in which there exist turbulent density fluctuations due, perhaps, to temperature or compressibility effects. After leaving the flow region, each beam is partially cut-off by a knife edge oriented normal to the mean flow direction and then focused onto a light sensitive detector whose electrical output is proportional to the amount of light passing the knife edge. For local measurements of density or temperature statistics the two beams are made to intersect at a point in the flow and cross-correlation of the two detector outputs with a small, special purpose, all-digital computer is used to extract the information common to the two signals.

Basically, the CBS works in the following way: Each beam is continuously refracted by density gradients along its path through the flow which causes minute oscillations of the beam on the knife edge.

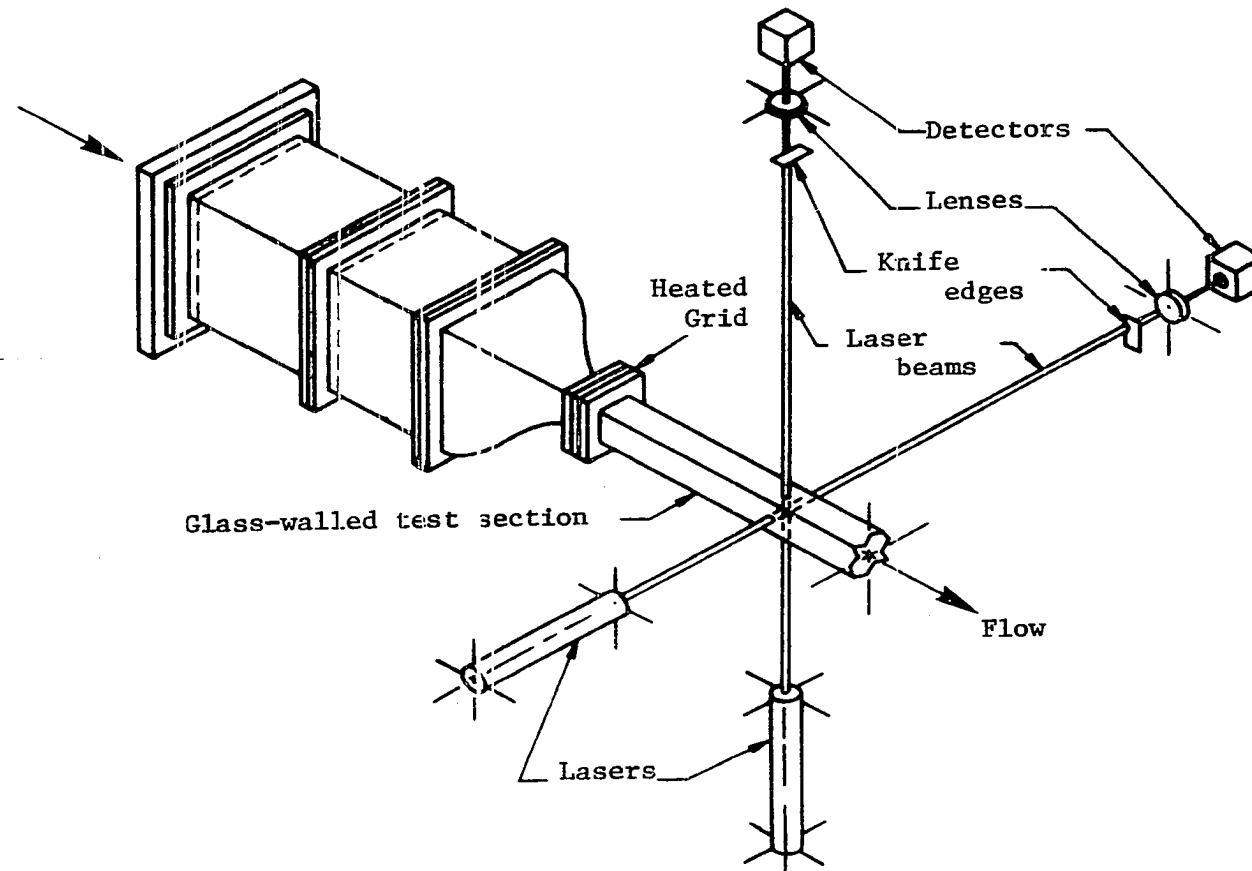


Figure 1. Orientation of crossed-beam schlieren



The detector therefore "sees," in the corresponding oscillations of light intensity, an integrated effect of the first derivative of density limited to the mean flow direction. When two such outputs are multiplied together and averaged in the cross-correlation procedure (for certain conditions), the double integration cancels the two first derivatives yielding a result proportional to mean square density. This will be shown analytically below. Thus, the CBS can be used to measure the distribution and decay of density variance or temperature variance when these variables are proportional.

Another important capability of the CBS is its ability to measure directly one component of the true three-dimensional scalar power spectrum. This capability is presently unique to systems using the crossed-beam correlation technique developed by Fisher and Krause (21). The 3-D spectrum is to be contrasted with the aliased one-dimensional scalar or velocity spectrum measured by HWA apparatus as will also be shown analytically below. In addition, the CBS will measure several other important kinematic flow properties, such as eddy convection speed, eddy lifetime, and turbulence scales. Unlike the HWA which is used almost exclusively in flows with substantial mean flow, so that the sensitivity coefficients will depend only on mean operating conditions, the CBS may be readily applied to make scalar turbulence measurements when  $\bar{U} = 0$  or of "turbulence decay in a box."

While the CBS is unfamiliar to many investigators, it has already been used in several studies with a large measure of success. So far,

there has been minimal effort to "prove" the instruments theoretical capabilities under nearly ideal, controlled conditions.

#### D. Objectives and Scope

Thus, the present study has two objectives. The first objective is to prove the CBS instrument as fully as possible in the easiest and best understood flow model available, namely, grid-generated, incompressible, isotropic turbulence. The first objective is to be accomplished by comparing results obtained with the CBS to results obtained with another (presumably) more familiar instrument (HWA) applied in the same flow, comparing with previous experimental results, and with theoretical predictions. If this objective can be fully realized, then the CBS will be available for use with confidence in more complex flows which take full advantage of its remote sensing feature, such as supersonic flows and turbulent combustion. For example, Parks (42) has shown the CBS satisfies most of the stringent requirements of instruments to be used in turbulent flame studies and used the CBS in a successful experimental program which is on-going at the present time at Iowa State University.

The second objective is to provide and interpret experimental data on scalar turbulence decay and spectra obtained with the CBS for the classical grid-generated model to add to a minimal supply.

A small-scale, open circuit, low turbulence wind tunnel was specially designed as the flow model facility. Overall, the tunnel was about five feet in length and featured a relatively long settling

chamber with flow straightening and turbulence damping devices, a 16 to 1 contraction ratio, and a two square inch by two foot long test section. The walls of the test section were transparent to accommodate the laser beams of the CBS.

A unique specially designed biplane grid was installed at the entrance to the test section. The 1/8 inch diameter round rods of the grid were made of a porous ceramic material and strung internally with high resistance heating wire so that they could be heated electrically to produce simultaneously a turbulent velocity field and superimposed turbulent temperature field.

The primary test variables were position downstream of the grid  $x/M$ , grid overhear  $\Delta$ , and mean speed  $\bar{U}$ . Except for lateral traverses of  $\bar{P}_t$ ,  $\bar{U}$ ,  $u'$ ,  $\bar{\theta}$ , and  $\theta'$  to verify homogeneity of the flow field, all measurements were taken on the longitudinal centerline of the test section. The test variables were controlled within the following ranges:  $6.78 \leq x/M \leq 45.6$ ,  $0 \leq \Delta \leq 60^\circ\text{F}$ , and  $8 \leq \bar{U} \leq 21 \text{ ft/sec}$ . While the full ranges of  $x/M$  and  $\Delta$  were explored, most of the tests were conducted at about  $\bar{U} = 8.5 \text{ ft/sec}$ .

Temperature and velocity turbulence spectral and decay data were obtained using both CBS and HWA systems. The constant temperature hot-wire apparatus was operated in its three modes, high overhear for isothermal velocity measurements, very low overhear (resistance thermometer) for temperature fluctuations, and mixed-sensitivity (multiple overheats) for estimates of combined  $\theta$  and  $u$  effects.

## II. LITERATURE REVIEW

Considerable theoretical work on scalar turbulence has been set forth over the past quarter century. Also, a number of experimental studies have been conducted in grid-generated isotropic turbulence, boundary-free turbulent shear flows, and wall-bounded turbulent shear flows. This review will concentrate on the origin of, and developments in scalar turbulence theories (but not on mathematical details) and on two of the primary experimental techniques, namely, those associated with hot-wire or hot-film anemometry and a particular optical remote-sensing device, the CBS. It will consider a number of applications of these techniques in the lab and in geophysical flows. While supersonic flows and nonisotropic shear flows may be outside the scope of this paper, several papers reporting measurements in these flows will be reviewed because of our interest in the experimental techniques used.

It will be noted that the only study cited in this review in which measurements of scalar turbulence were made in a grid-generated flow of low-speed air was done at Johns Hopkins University, first reported by Kistler et al. (33) and later by Mills et al. (39).

### A. Scalar Turbulence

One of the first investigators to treat the problem of scalar, in addition to velocity turbulence was Corrsin in two important papers (13 and 16). It is interesting to review his assessment of the situation regarding the state of theoretical progress in isotropic turbulence as of 1951, for essentially the same comments apply to the

state of theoretical progress in isotropic scalar turbulence today. The attack has been waged on two partially independent fronts which yield predictions of (a) the mean random kinetic energy and turbulence scales during decay and (b) the shape of the power spectrum for certain ranges of wavenumber. Corrsin (13) wrote,

"The synthetic independence of the work on (a) and on (b), as well as the necessity for restrictions in (a) and piecemeal treatment in (b), is a result of the extreme difficulty of the problem, including the unfortunate fact that in its statistical formulation the problem has more unknowns than equations. In spite of these hardships, attention to single cases and the use of judicious postulates in the more complicated cases have been combined to yield a considerable body of theory on the statistical behavior of an isotropic, homogeneous, random velocity fluctuation field in an incompressible continuum. Furthermore, much of this theory has been verified by experiment."

"Scalar" could be safely substituted for "velocity" in the above quote; the comment seems to be as valid today as in 1951.

Reference 13 is a theoretical introduction to the scalar problem corresponding to (a) above. The theory was developed in terms of temperature simply because this was considered the easiest field in which to attempt experimental verification. Corrsin's procedure followed the classical approach of Taylor, von Karman and Howarth, and Loitsiansky for the velocity field (namely, deriving and interpreting the dynamic equation for the temperature covariance or correlation function). Temperature fluctuations were assumed to be small enough not to influence the velocity field. Estimates of decay and scale growth in the limits of small and large Peclet number were obtained and it was predicted that the temperature field would decay more slowly than the velocity field.

In Reference 16 Corrsin derived the one- and three-dimensional spectral equations for an isotropic temperature field by Fourier transforming all the terms of the correlation equation. Using dimensional arguments that the fine structure of scalar fields mixed by turbulence should depend only on  $\varepsilon$ ,  $\nu$ , and  $\chi$ , the rate of dissipation of scalar variance and a few postulates including stationarity, he obtained the form of the temperature energy spectrum for certain wavenumber ranges. (These will be elaborated in Chapter III.) An effective "conductive" cutoff wavenumber was suggested after which the scalar spectrum might be expected to drop off sharply below a length scale of  $(\alpha^3/\varepsilon)^{1/4}$  in analogy with the viscous cutoff in the velocity spectrum at about the Kolmogoroff length scale of  $(\nu^3/\varepsilon)^{1/4}$ .

Equations relating one- and three-dimensional spectra in an isotropic scalar field were given in a short letter by Kovaszny et al. (36).

Chandrasekhar (10) found the equations governing density fluctuations in an isotropic, compressible turbulent flow.

The problem of heat transfer in stationary isotropic turbulence was examined by Corrsin (15) from the Lagrangian and Eulerian viewpoints. In this paper Corrsin's objective was to predict the turbulent heat transport rate using known statistical information and mean thermal boundary conditions.

The next major theoretical work to emerge was by Batchelor (3). It was an investigation of the form of the scalar spectrum at high

wavenumbers which accounted for the effects of convection and molecular diffusion with diffusivity  $\alpha$ . Batchelor considered the case of weakly diffusive scalars ( $Pr = \nu/\alpha \gg 1$ ; for example,  $Pr \approx 7$  for water) and argued that in this case the scalar fluctuations would probably survive to a much smaller scale than the velocity fluctuations which were being cut off by viscous effects. As a result, he maintained that the mechanism by which these eddies would be mixed is pure strain and deduced the shape of the high wavenumber spectrum in terms of a new parameter  $\gamma$ , the mean local rate of strain. Batchelor's procedure was to integrate the linear scalar diffusion equation for a typical small (compared to  $(\nu^3/\epsilon)^{1/4}$ ) fluid element in pure strain with the instantaneous distribution of  $\theta$  resolved into its Fourier components. The  $Pr \gg 1$  spectrum is shown schematically in Figure 2.

Reference 5 is an extension of the above paper to the case of strongly diffusive scalars ( $Pr \ll 1$ ; for example,  $Pr \approx 0.02$  for mercury). The assumed physical model restricted interaction of Fourier elements of the scalar and velocity fields to wavenumbers between  $(\epsilon/\alpha^3)^{1/4}$  and  $(\epsilon/\nu^3)^{1/4}$  to direct interaction of small eddies in regions of constant scalar gradient. This led to a spectral subrange with slope  $-17/3$  for scales greater than the Obukhov-Corrsin scale  $(\alpha^3/\epsilon)^{1/4}$  as summarized in Figure 3. The  $-17/3$  power law and underlying physical ideas have been contested by Gibson (25).

The first of two theoretical papers by Gibson (24) examines the physical mechanisms by which the smallest scale features of scalar

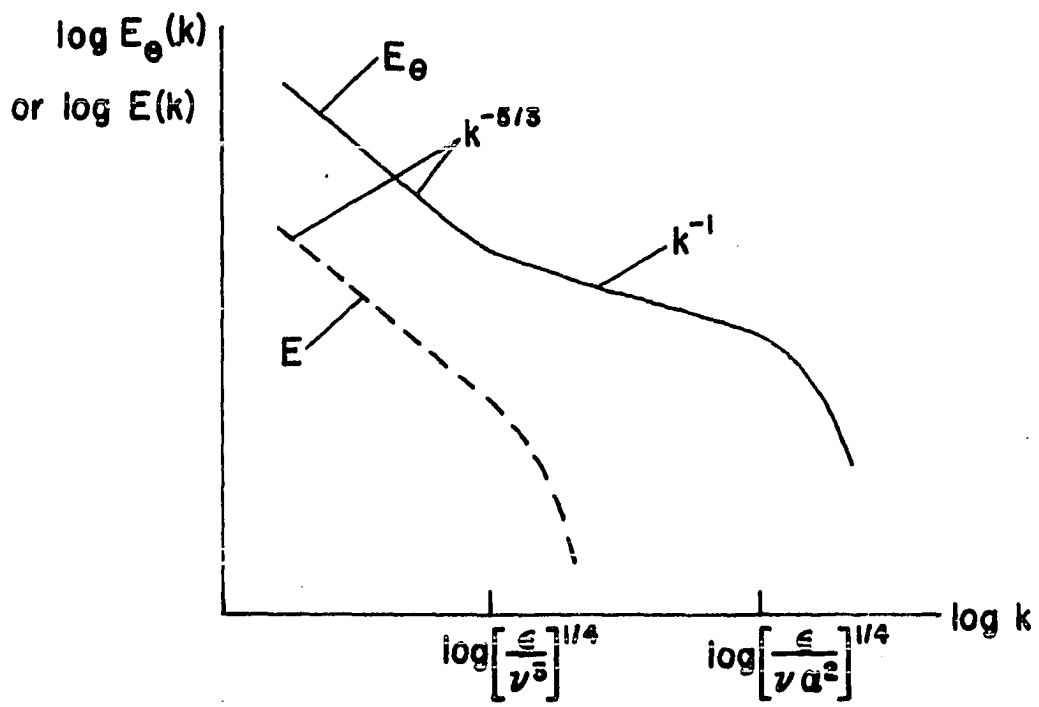


Figure 2. Predicted spectrum for weakly diffusive scalar,  $Pr \gg 1$  (Reference 3)



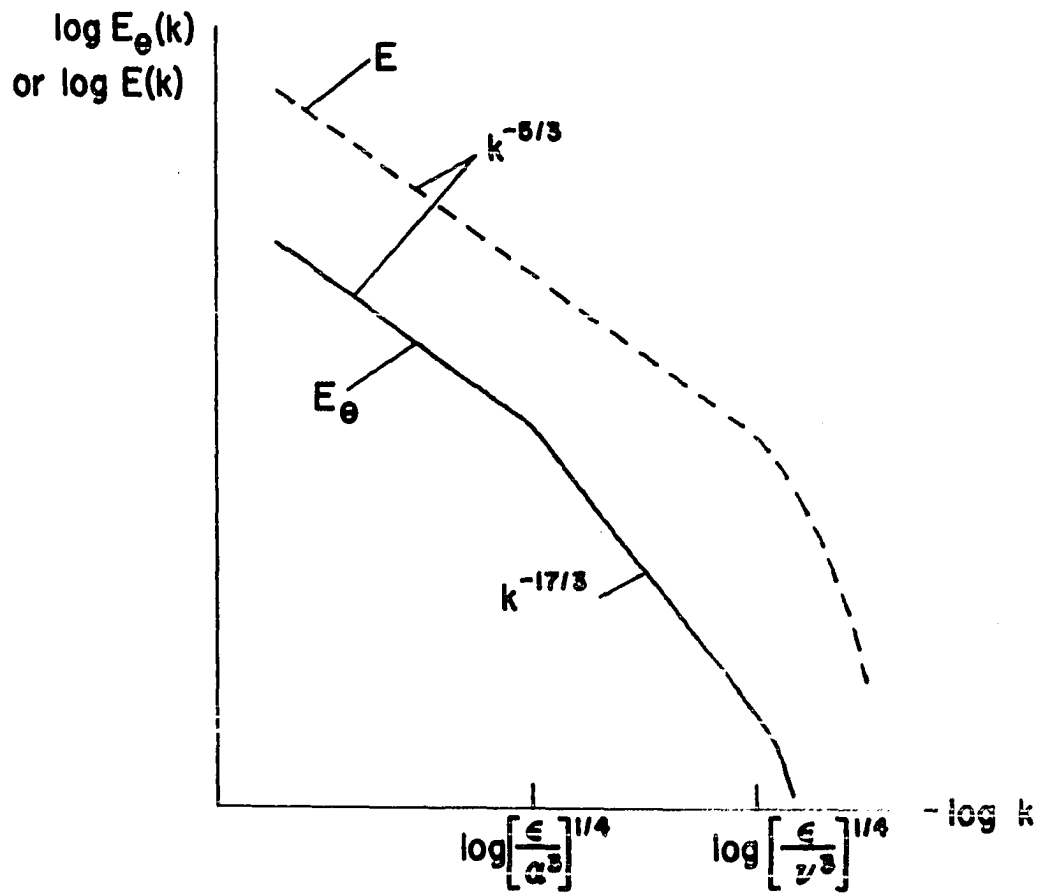


Figure 3. Predicted spectrum for strongly diffusive scalar,  $Pr \ll 1$   
(Reference 5)

fields are produced by turbulent convection. He claims that even for strongly diffusive scalars, the magnitude of the local rate of strain is a key factor in formation of the smallest eddies in contrast to the ideas of Reference 5 where it was assumed the local strain rate has no effect on scalar structure for fields of low Pr. More specifically, Gibson identifies the dominant mechanism of production of smallest eddies as local stretching of the scalar distribution, where the scalar gradient is small, or, "minimal gradient straining."

Gibson's companion paper (25) uses the results of (24) to formulate new universal similarity hypotheses which emphasize the importance of Pr and are formulated in terms of three sets of scales, Kolmogoroff, Batchelor, and Obukhov-Corrsin. These hypotheses permit conclusions about the high wavenumber spectral shape. The inertial subrange of Corrsin  $E_\theta(k) \sim k^{-5/3}$  and the large Pr viscous-convective subrange of Batchelor  $E_\theta(k) \sim k^{-1}$  are reproduced. For small Pr, however, a new inertial-diffusive subrange is predicted with  $E_\theta(k) \sim k^{-3}$  and cutoff at  $k = (\gamma/\alpha)^{1/2}$  in contrast to the Batchelor-Howells-Townsend model which predicted the much faster cutoff  $k^{-17/3}$ . Gibson identifies failure to consider those portions of the scalar field where convective transport dominates as leading to this faulty result. Tentative support for the  $k^{-3}$  subrange was claimed based on limited spectral measurements in mercury. As will be seen below, however, several independent investigations have provided results which lend qualitative support of the  $k^{-5/3}$  and  $k^{-1}$  subranges, so they stand reasonably firm.

We note that for the present study, Prandtl numbers of order 1.0 were obtained and, therefore, the above theories are not directly applicable.

## B. Experimental Techniques

At this stage we turn to literature describing instruments available for measuring scalar turbulence, primarily the hot-wire or hot-film anemometer and crossed-beam schlieren. First, a number of both theoretical and experimental papers tracing the development of hot-wire techniques will be considered. The works of interest here have analyzed the interpreted hot-wire response in flows with temperature and density as well as velocity variations. Selected studies will be cited in which hot-wire apparatus was applied to measure scalar turbulence in laboratory flows and, additionally, geophysical or high Reynolds number flows.

### 1. Hot-wire anemometry

Some exposure to hot-wire anemometry is inevitable for anyone interested in fluid flow measurements. For a few applications to incompressible, isothermal flows the hot-wire can be operated successfully using essentially routine procedures. However, for flows with significant variations in both temperature and velocity, the hot-wire must be used carefully because it then presents significant problems in calibration and interpretation. In high-speed applications probe interference must be considered and a third variable, density, enters

adding more difficulty. Also, the use of multiple sensors to obtain spatial correlations may add considerable complexity to the data analysis. In spite of the difficulties, hot-wires or films have been used successfully in non-isothermal flows of both air and water, shear flows, and compressible flows.

After Corrsin's report (14) the procedures by which the HWA could be applied to measure scalar fluctuations in incompressible flows were apparent. He presented an analysis of the hot-wire response equations needed to apply the instrument to turbulent flows with  $\theta$ -fluctuations or in which two different gases are mixed isothermally. The analysis was based on a Reynolds decomposition of variables and linearization of the governing heat transfer equation (King's law).

Corrsin stated that his response equations were limited by the accuracy of the assumed form of King's law and called for a complete re-examination of the fundamental heat-transfer law. A major study answering this request emerged with Collis and Williams' (12) measurements of heat transfer from the fine circular wires at low Reynolds numbers. A semi-empirical law relating the Nusselt and Reynolds numbers was obtained of form

$$\text{Nu} \left( \frac{\bar{\theta}_w + \bar{\theta}_a}{\bar{\theta}_a} \right)^{-0.17} = A + B \text{Re}^n$$

where the factor in parentheses is used to take into account the temperature loading of the heated wire, that is, to account for variation

of fluid properties with temperature. As noted by Chevray and Tutu (11), the effects of changes in this term are usually small (less than 2%). The values of  $n$ ,  $A$ , and  $B$  were found to depend on whether the Reynolds number was above or below about 44. Free convection effects were found to be negligible except at very low velocities.

Once the HWA response equations have been linearized, analytical expressions become available for the HWA velocity and temperature sensitivities as, for example, in Corrsin (14) or Sandborn (44). But the most accurate method of determining these sensitivities is via direct experimental calibration. Arya and Plate (1) have described one such procedure in which it is assumed that the individual effects of wire and air temperature are negligible, except in the factor  $\bar{\theta}_w - \bar{\theta}_a$  in the Nusselt number. Then, wire calibration curves may be obtained by operating at different wire temperatures  $\bar{\theta}_w$  in a constant temperature air stream  $\bar{\theta}_a$ . The sensitivities to  $u$  and  $\theta$  are then determined graphically or analytically from plots of  $\bar{E}$  vs  $\bar{U}$  and  $\bar{\theta}_w - \bar{\theta}_a$ , respectively. They showed that use of an independent measurement of  $\bar{\theta}^2$  can provide better accuracy when solving the multiple overheat equations and that neglecting  $\bar{\theta}^2$  may lead to appreciable errors even at high overheats. Freymuth (23) has listed several approximate methods for obtaining HWA  $u$  and  $\theta$  sensitivities and ranked them in order of accuracy and simplicity of use.

Recently, Burchill and Jones (8) have developed and demonstrated a technique for interpreting the linearized response of two or more

hot-wire or film sensors in a non-isothermal field with a temperature gradient. The effect of mean temperature gradient was effectively calibrated-out by special adjustments of the sensors overheat during a traverse. Simultaneous measurement of  $\bar{U}$ ,  $\bar{\theta}$ , velocity fluctuation components, and  $\theta$ -fluctuations were obtained without multiple overheats or traverses. An in-depth analysis of errors in the response interpretation was included along with supportive data.

A method of using two closely spaced hot-wires, one operating upstream as a compensated resistance thermometer and the other in the mixed-sensitivity mode was described by Chevray and Tutu (11). A special circuit was used to electrically compensate the downstream wire (ahead of its linearizer) for the effects of local temperature using the signal from the first. In this way linear and separate signals of  $u$  and  $\theta$  were expected separately and simultaneously.

For hot-wire measurements in compressible flows one has no choice but to separate the scalar effects of temperature from density and velocity. Historically, the first major effort in supersonic flows was by Kovaszny (34) who reported experiments to determine the heat transfer law in flows up to Mach 2.0. A law was found for the case of small  $\bar{\theta}_w - \bar{\theta}_a$ .

Kovaszny (35) later gave the first-order perturbation theory which reveals the vorticity (velocity fluctuations), entropy (temperature fluctuations), and sound-wave disturbance "modes" of a compressible, viscous, heat-conducting gas. For small fluctuations

these modes are independent but interact when linearization is not permissible. By operating a hot-wire sensor at different overheats, the parameter sensitivities vary and the modes can be separated via "fluctuation-" or "mode-diagrams." This procedure allows a graphical determination of three unknowns after making a large number of measurements and replaces the least squares technique which is usually used when only  $u$  and  $\theta$  are present (see Chapter III). Measurements were made in several supersonic flows including a turbulent supersonic boundary layer.

The fluctuation-mode diagram technique was formalized by Morkovin (40) and generalized to include low speeds. He derived general expressions for the three mode sensitivities and specialized these for various speed ranges. Morkovin discusses practical aspects of calibration, operation, and interpretation of the signals.

The most commonly measured correlations and spectra are those accessible from a single sensor fixed in the lab reference frame. These measurements depend on the validity of Taylor's hypothesis which, practically speaking, says that the instantaneous time and space variables can be interchanged when  $\bar{U} = \text{constant}$  and  $u'/\bar{U} \ll 1$ . To remove the dependence on Taylor's hypothesis and to obtain correlations as functions of spatial separation between two points in the field such as the lateral correlations (see Hinze 29, Chapter 1) it is necessary to use more than one sensor.

The two-sensor correlation technique has been applied in

compressible flow by Demetriades (18). This state-of-the-art paper documents the tedious procedure required to separate velocity and temperature correlations (when pressure fluctuations are negligible). Kovasznay's work was extended in that correlations (between two sensors) were decomposed into vorticity and entropy modes without requiring equal wire sensitivities; sensitivity coefficients were computed using formulas given by Morkovin. Experimental measurements were made in the Mach 3, axisymmetric wake of a rod using constant current hot-wire apparatus and .00002 inch diameter wires. For each correlation, 15 traverses were made for 15 different combinations of wire overheat to increase accuracy.

A number of examples of applications of hot-wire equipment to measurement of scalar turbulence will now be reviewed. Corrsin and Uberoi (17) compared 1-D  $\overline{u^2}$  and  $\overline{\theta^2}$  power spectra measured in the shear flow of a heated, round turbulent jet using HWA and resistance thermometer apparatus. They also measured  $u'$  and  $\theta'$  downstream of a local (line) heat source inserted into the jet wake.

An early attempt to study turbulent diffusion in the flow behind a grid was by Townsend (49) who used a heated fine wire filament to mark eddies with thermal spots. A resistance thermometer was used to detect the distribution of heat spots. Uberoi and Corrsin (50) conducted a similar but more extensive experimental and analytical study of turbulent heat diffusion behind a heated fine wire with variations in speed, grid size, and downstream wire location. The problem was



treated from both the Eulerian and Lagrangian viewpoints.

By heating metal grid rods, Mills et al. (39) produced a flow field in which an isotropic  $\theta$ -field was superimposed on an isotropic  $u$ -field. The rods were 1/4" in diameter and spaced 1" center to center in a biplane grid installed at the entrance to a 2' square test section. With a "hot grid" it was expected that approximately equal integral scales of velocity and scalar turbulence would be obtained. All measurements were made at about  $\bar{U} = 14$  ft/sec and a grid overheat of about  $\Delta = 9^\circ\text{F}$ . HWA and resistance thermometer measurements of  $u$ - and  $\theta$ -fluctuation decay, higher-order correlations, and 1-D  $\overline{u^2}$  and  $\overline{\theta^2}$  spectra were reported. The measurement of third and fourth order correlations presented in this report are rare, despite the central importance of the closure problem in solving the dynamic equation (see Reference 51). A  $\overline{\theta^2}$  spectrum was determined by subtracting their  $\Delta=0$   $\overline{u^2}$  spectrum from a  $\overline{u^2} + \overline{\theta^2}$  spectrum obtained by operating the wire with equal sensitivity to velocity and temperature. This seems reasonable since the two spectra should be uncorrelated in isotropic flow ( $\overline{u\theta} = 0$ ). The shapes of the  $\overline{u^2}$  and  $\overline{\theta^2}$  spectra were the same showing a continually increasing negative slope; that is, an appreciable  $-5/3$  power law region was not discernable in the 1-D spectra. Hinze (29) suggests that this might have been suspected due to the low  $R_M$  of about 7420.

Carr, Connor, and Buhr (9) have investigated the influence of free convection effects on a forced convection flow of air in a vertical pipe with uniform heat flux. Constant current hot wire apparatus

was used to measure profiles of  $\bar{U}$ ,  $\bar{\theta}$ ,  $u'$ ,  $\theta'$ ,  $\overline{u\theta}$ , and  $\overline{uv}$  for Reynolds numbers of 5,000 to 14,000. The turbulent shear stress and heat flux distributions were calculated. They used  $u$  and  $\theta$  sensitivity relations given by Hinze (29) and the procedure of Arya and Plate (1) to obtain  $\overline{u^2}$  and  $\overline{u\theta}$  from the best least squares fit to data obtained at five overheats. In this calculation  $\overline{\theta^2}$  was obtained from resistance thermometer measurements. The authors note that the calculation of  $\overline{u\theta}$  is particularly sensitive to experimental inaccuracies.

## 2. Studies in geophysical or high Reynolds number flows

Because of the large Reynolds numbers characterizing most oceanic or atmospheric experiments, large inertial subranges are observed in the spectral data. This makes these and other high Re flows of special importance in verifying theoretical predictions for the inertial subrange.

Gibson and Schwartz (26) have used a specially designed single electrode conductivity probe in a bridge circuit to measure the spectra and decay of a homogeneous field of concentration and temperature behind a grid. They used a constant temperature hot-film anemometer to measure decay of the velocity field. Measurements of velocity, temperature, and concentration spectra in dilute salt water were compared with the general predictions of local-isotropy and universal similarity theory, and with Batchelor's (3) predicted spectrum for a weakly diffusive ( $v/\alpha \gg 1$ ) scalar field. The authors obtained the scalar variance decay law for grid turbulence (in the initial period) with

$10,000 \leq Re_M \leq 70,000$  with both concentration and temperature mixing for two grid mesh sizes.

The data presented by Gibson and Schwartz support the  $-5/3$  power law for the inertial subrange, and the  $-1$  power law for the viscous-convective subrange. After coordinate transformation in accord with local isotropy theory and Kolmogoroff-like similarity hypotheses, both the  $\overline{u^2}$  and  $\overline{\theta^2}$  spectra presented appeared to be universal equilibrium spectra.

Measurements of 1-D  $\overline{\theta^2}$  spectra made using a hot-film resistance thermometer in the open sea and in a tidal channel with flow Reynolds numbers around  $10^8$  were reported by Grant et al. (27). For these conditions the scales of the energy containing eddies were so large that the measurement platform, a ship, was carried about by them. The scalar spectra were found to have a  $-5/3$  inertial subrange over more than 3.5 decades in wavenumber and to rise above the  $-5/3$  line and go approximately as  $-1$  in agreement with Batchelor's theory.

$\overline{u^2}$  and  $\overline{\theta^2}$  spectra and cospectra have been recently computed by Kaimal et al. (31) from data they obtained in the atmospheric "surface" layer during the 1968 Air Force Cambridge Research Laboratories Kansas experiments. Spectra were reduced to a single universal curve in the inertial subrange using appropriate normalization which showed consistency with similarity theory and local isotropy. The power law observed for this range was  $-5/3$  in agreement with Kolmogoroff's and Corrsin's theoretical predictions. The data were obtained on a flat

site in Kansas using hot-wire anemometers and resistance thermometers mounted at three levels on a 32 meter tower. A computer-controlled data acquisition system was used to sample, digitize, and store the data on magnetic tape. Spectra were computed using the fast-Fourier transform method.

### 3. Optical remote sensing

In 1967 Fisher and Krause (21) reported their ideas forming the basis of a new experimental technique called crossed-beam correlation. This technique allows remote measurement of local flow properties in a turbulent fluid. It entails passing two mutually perpendicular beams of radiation through the flow region of interest to obtain integrated effects of either scattering or absorption at appropriate detectors with cross-correlation of the two signals to obtain local estimates of turbulence parameters. To substantiate the technique Fisher and Krause present results from a round low-speed jet with water mist injected as a tracer to facilitate use of the scattering mode.

While use of both scattering from tracer particles and absorption of light by a particular flow constituent are feasible and in fact have been used, Wilson points out that neither is entirely satisfactory (52). In the case of scattering, artificial seeding may be necessary to obtain adequate signal levels; consequently, the results would not be directly relatable to a scalar property. The practical usefulness of absorption is limited by complexity and the fact that most interesting

fluids have no strong absorbers in the visible spectrum. A further limitation of scattering-absorption is the requirement that the integral length scales in the directions of the beams be estimated in order to obtain absolute levels of the flow property fluctuations.

Reference 53 presents the analysis to measure sound source intensities in turbulent jets. The turbulence properties required were difficult to measure and inaccessible to conventional instrumentation at high speeds. Wilson et al. here used an infrared absorption crossed-beam system to obtain direct measurements of density fluctuations in a round subsonic jet. This system used selectively band-passed radiation in the near infrared portion of the spectrum to excite the corresponding fundamental vibration band of carbon dioxide. Only naturally occurring  $\text{CO}_2$  was used so that the fluctuations in beam intensity could be related directly to density fluctuations. To calibrate this system an elaborate study using an absorption calibration cell is necessary because absorption is also dependent on temperature and pressure. Since absorption measurements are always influenced to some extent by scattering of contaminant particulates, the authors include a method of decoupling the two effects by correcting for scattering.

Becker et al. (6) have described a light-scatter measurement technique which uses a single beam, slitted diaphragm, and multiplier phototube to detect concentration fluctuations during the turbulent mixing of colloidal dispersions. The system response was analyzed,

problems of noise and spatial resolution examined, and experimental data presented for a round jet of oil condensation smoke-marked air. The technique appeared to work well for measuring the convective range of the concentration spectrum, but fails where molecular diffusion is important because the colloidal particles do not portray the gas behavior for these smaller scales. System noise was the ultimate limiting factor in detecting concentration fluctuations.

Theoretical and experimental work done on a turbulence measuring technique based on beam modulation by refractive index fluctuations has been reported by Roe (43). Here each beam was passed through the turbulent region and analyzed after exit on gratings of periodic transmissivity (Fourier optical analysis). The theory yielded the spatial power spectrum of refractive index fluctuations and the velocity distribution in the beam aperture, single- and dual-beam theory were presented along with results of applying a single beam to measure convective turbulence in a heated water tank.

The idea of using the schlieren sensing mode together with the crossed-beam correlation technique of Fisher and Krause was formalized by Wilson and Damkevala (52). Under conditions of homogeneity in the flow field a CBS system was theoretically shown to have the capability of measuring the 3-D spectrum function. It was shown to obtain directly the local fluctuating density variance at the beam intersection "point" for locally isotropic conditions. Results from a preliminary study in a subsonic air jet tended to verify the proposed theory.

The crossed-beam correlation technique was conceived with interference-free measurements in high-speed turbulent shear flows in mind as its design environment. Fisher et al. (22) recently reported initial results of a program which applied the CBS and two other remote-sensing techniques, a laser Doppler velocimeter (to measure mean and fluctuating velocities), and a pulsed laser interferometer (to measure mean density profiles) in an investigation of supersonic jet noise generation and reduction.

A series of tests were conducted to determine the feasibility of using a CBS to measure the kinematic properties of supersonic jets. Successful measurements of radial covariance profiles, single beam spectra, and space-time correlation plots were made and evaluated in heated and cold, subsonic and supersonic jet flows.

### III. THEORY

#### A. Grid-Generated Turbulence

The simplest type of turbulence to describe theoretically and a relatively easy type to produce in a laboratory is grid-generated turbulence. Grid turbulence is at present the closest laboratory approach to the flow conditions of homogeneity and isotropy. Turbulence is said to be "homogeneous" if the statistics describing its structure are quantitatively the same in all regions of the flow field, which is the same as saying the statistics may be expressed as functions of distance (or time) differences irrespective of absolute values. Turbulence is said to be "isotropic" if its statistical parameters for a given point in the field are independent of the coordinate system rotation and of reflection into the coordinate planes. This is to say, isotropic turbulence has no directional preference at a point and is, therefore, perfectly random.

A consequence of isotropy is that there can be no mean velocity gradient since no average shear stress can occur. By ruling out gradients in mean speed, we are evidently excluding wall-bounded and boundary-free shear flows which are nonisotropic in their large scale structure. Actually, isotropic turbulence is an idealized model, as no real turbulent flow shows true isotropy; however, theory and experiment have shown that most actual nonisotropic turbulent flows are locally isotropic in their fine structure.

A further assumption made at the outset to simplify analysis is



that the fluid is incompressible with constant viscosity. Other important assumptions often made about the flow model are that its structure remains "similar" and "self-preserving" during decay. The structure is said to be similar if it is uniquely determined by a length scale and a velocity scale alone. It is said to be self-preserving if the similarity is maintained during decay.

The flow model selected for this study was grid-generated isotropic scalar turbulence superimposed on an isotropic turbulent velocity field. While the velocity field itself is of secondary interest, its validation is essential and, therefore, some useful expressions describing its characteristics will be presented as needed for later use. These relations are derived and discussed in Hinze's book (29).

A hot-wire anemometer operating a single sensor is capable of measuring Taylor's one-dimensional velocity energy spectrum  $E_1(f)$  defined such that

$$u^2 = \int_0^{\infty} E_1(f) df \quad (3-1)$$

For turbulence homogeneous in time, Taylor has shown the relationship between  $E_1(f)$  and the Eulerian time autocorrelation coefficient  $r_E(\tau)$  where

$$r_E(\tau) = \frac{\overline{u(t)u(t-\tau)}}{u'^2} \quad \begin{array}{l} \text{(averaging with} \\ \text{respect to } t) \end{array} \quad (3-2)$$

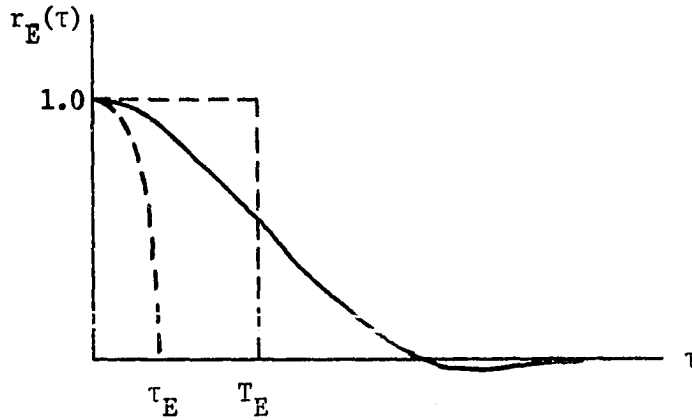
is that the two functions are Fourier cosine transform pairs. If  $r_E(\tau)$  is approximated as a parabola for small  $\tau$ ,

$$r_E(\tau) \approx 1 - \frac{\tau^2}{2\tau_E^2} \quad (3-3)$$

where  $\tau_E$  is called the micro Eulerian time scale and gives a measure of the duration of the most rapid u-fluctuations. The integral Eulerian time scale

$$T_E = \int_0^{\infty} r_E(\tau) d\tau \quad (3-4)$$

is a measure of an average time over which an eddy can be considered to be perfectly correlated with itself. The following sketch illustrates the relationship between  $r_E(\tau)$ ,  $\tau_E$ , and  $T_E$ .



If the velocity field is homogeneous in its average statistical structure and has a constant mean velocity  $\bar{U}$ , then approximately

$$\frac{\partial}{\partial t} = -\bar{U} \frac{\partial}{\partial x} \quad (\text{Taylor's hypothesis})$$

is conventionally assumed. This relation between the local time derivative and the convection derivative allows interchange of time and space dependence with

$$|x - x_0| = \bar{U} |t - t_0|$$

or

$$x = \bar{U}t \quad (3-5)$$

when  $\bar{U}$  is large relative to  $u$  and  $u'/\bar{U} \ll 1$ . This is shown analytically in Hinze (29). In other words, when the mean flow velocity is large compared to the fluctuations, the flow pattern will be swept in the  $x$ -direction parallel to the mean flow past a point as though it were "frozen-in," that is, before it has a chance to change appreciably. One can then assume as a first approximation that the time history detected by the sensor is equal to a record of the moving turbulence pattern along  $x$ ; and, events associated with long times are associated with conditions far downstream in  $x$ .

Kistler and Vrebalovich (32) have observed that the applicability of Taylor's hypothesis is one of two important useful features of grid turbulence (besides nearness to homogeneity and isotropy). The other feature is that since the change in average properties of the field with distance is controlled by dissipation, the dissipation rate can be obtained readily by measuring the change in turbulence intensity with distance downstream.

If Taylor's hypothesis holds, the space integral scale  $\Lambda_f$  may be obtained from

$$\Lambda_f = \bar{U} T_E \quad (3-6)$$

Also, from known relations between  $r_E(\tau)$  and  $E_1(f)$ , the following useful results are obtainable.

$$\begin{aligned}
 \lim_{f \rightarrow 0} \frac{1}{u^2} E_1(f) &= 4 \int_0^{\infty} r_E(\tau) d\tau \\
 &= 4T_E = \frac{4\Lambda_f}{U}
 \end{aligned} \tag{3-7}$$

This shows that  $T_E$  and  $\Lambda_f$  can be estimated from the intersection of the  $E_1(f)$  vs  $f$  curve and the  $E_1(f)$  axis. Furthermore,

$$\frac{1}{\tau_E^2} = \frac{2\pi^2}{u^2} \int_0^{\infty} f^2 E_1(f) df \tag{3-8}$$

and

$$\frac{1}{\lambda_f^2} = \frac{2\pi^2}{U u^2} \int_0^{\infty} f^2 E_1(f) df \tag{3-9}$$

which show that the Taylor microscales  $\tau_E$  and  $\lambda_f$  can be determined from the dissipation spectrum  $f^2 E_1(f)$  vs  $f$ . Of course, relations such as these may be transformed into wavenumber  $k$  (or spatial frequency) using the definition

$$k = \frac{2\pi}{\lambda} = \frac{2\pi f}{U} \tag{3-10}$$

with units  $(\text{length})^{-1}$ .

Corrsin (13) was one of the first investigators to treat the problem of isotropic scalar turbulence superimposed on isotropic velocity turbulence. His classical theoretical approach parallels that for the velocity field as outlined below; for a complete derivation see Hinze (29). The dynamic equation (analogous to the Karman-Howarth equation) describing the behavior of the covariance of  $\theta$  at two points A and B

$$[Q_{\theta,\theta}(r,t)]_{A,B} = \overline{\theta_A \theta_B} \quad (3-11)$$

or its correlation coefficient

$$[r_{\theta,\theta}(r,t)]_{A,B} = \frac{\overline{\theta_A \theta_B}}{\theta'^2} \quad (3-12)$$

where  $\theta' = \left( \overline{\theta_A^2} \right)^{1/2} = \left( \overline{\theta_B^2} \right)^{1/2}$  is derived from the equation for the diffusion and convection of a dynamically passive scalar fluid property  $H$  (such as temperature or concentration),

$$\frac{\partial H}{\partial t} + U_i \frac{\partial H}{\partial x_i} = \alpha \frac{\partial^2 H}{\partial x_i \partial x_i} \quad (3-13)$$

It is assumed that  $\alpha$ , the molecular transport coefficient is constant. For a temperature contaminant  $H = C_p \Theta$  = enthalpy or heat per unit mass, and  $\alpha = k/\bar{T}C_p$ . For heterogeneous mixing,  $H$  is a concentration and  $\alpha$  is the coefficient of molecular diffusivity. The dynamic equation derived from (3-13) presents one of the fundamental difficulties of the statistical approach to solving the turbulence problem, namely, as a consequence of non-linear terms in the diffusion equation, the unknowns outnumber the available equations. Attempts to circumvent this "closure problem" usually involve assumptions about the correlations based on similarity, statistical, or physical considerations. The dynamic equation reduces to an expression for the decay of  $\theta$ -fluctuations in time at a point ( $r \rightarrow 0$ ) in the field,

$$\frac{d\theta'^2}{dt} = -12 \frac{\alpha}{\lambda_\theta^2} \theta'^2 \quad (3-14)$$

which is comparable to the similarly derived velocity decay

$$\frac{du'^2}{dt} = -10 \frac{\nu}{\lambda_g^2} u'^2 \quad (3-15)$$

The correlation equation referred to above describes  $\theta$ -fluctuations in the time or space domain. A spectral analysis of these fluctuations is required to reveal details of the behavior of turbulence in the frequency or wavenumber domain. As described in Batchelor's (2) book, one of the basic physical ideas about turbulent flows proposed by Taylor (1935) and formulated mathematically by Kolmogoroff (1941) is that the kinetic energy represented by the velocity fluctuations of large-scale (or low-frequency) anisotropic eddies continuously transfers or cascades through ranges of smaller and smaller scales until at a certain size the energy is dissipated directly into heat. While the largest, but not necessarily the most energetic eddies, are fully dependent on the conditions of their formation, the theory hypothesizes an inertial interaction producing successively smaller eddies with a tendency toward statistical independence of the directional details of the larger ones. This tendency eventually leads to "locally isotropic" conditions.

These notions led Kolmogoroff to make the following two hypotheses:

(1) "At sufficiently high Reynolds numbers there is a range of high wavenumbers where the turbulence is statistically in equilibrium and uniquely determined by the parameters  $\epsilon$  and  $\nu$ . This state of equilibrium is universal," and

(2) "If the Reynolds number is infinitely large, the energy spectrum in the subrange satisfying  $k_e \ll k \ll k_d$  is independent of  $\nu$

and solely determined by one parameter  $\varepsilon$ ." This region is called, of course, the inertial subrange. In the first hypothesis a high enough Reynolds number is assumed to significantly separate the integral scale from the microscale  $\eta$ . However, the basic idea of the small scale structure being independent of the details of the large scale structure should be valid even at low Reynolds numbers.

The consequences of Kolmogoroff's theory of local isotropy and universal similarity have been extended to scalar spectra by Corrsin (16) and Gibson (25, 26). Gibson discusses the proper coordinates in which velocity and scalar spectra should be plotted in order to test the similarity hypotheses.

The 1-D scalar spectrum measured by a hot-wire sensor  $E_{\theta 1}(k_1, t)$  is defined so that

$$\theta'^2 = \int_0^\infty E_{\theta 1}(k_1, t) dk_1 \quad (3-16)$$

$E_{\theta 1}(k_1, t)$  can be shown to be the Fourier transform of  $Q_{\theta, \theta}(x_1, t)$ . For three dimensions this is also true and can be expressed

$$E_{\theta, \theta}(k_1, k_2, k_3, t) = \frac{1}{8\pi^3} \iiint_{-\infty}^{\infty} Q_{\theta, \theta}(x_1, x_2, x_3, t) \exp(-ik_j x_j) dx_1 dx_2 dx_3 \quad (3-17)$$

where the scalar  $Q_{\theta, \theta}$  depends only on  $r$  and  $t$ .

The 3-D scalar spectrum function  $E_\theta(k, t)$  is defined as the average of Equation 3-17 over wavenumber space and given by

$$E_\theta(k, t) = 4\pi k^2 E_{\theta, \theta}(k, t) \quad (3-18)$$

Then

$$\overline{\theta'^2}(t) = \int_0^\infty E_\theta(k, t) dk \quad (3-19)$$

(The  $t$  dependence of  $E$ 's and  $Q$ 's will hereafter be implicit; in practice, the  $\theta$  signals analyzed were assumed to be stationary or homogeneous in time.) While  $E_{\theta 1}(k_1)$  and  $E_\theta(k)$  are often referred to as energy spectra, power spectra, or power spectral densities, clearly  $\overline{\theta'^2}$  is not really energy in the same sense as  $\overline{u^2}$ .

Theoretical relations relating  $E_{\theta 1}$  and  $E_\theta$  have been found for isotropic conditions by Kovasznay et al. (36) to be

$$\begin{aligned} E_\theta(k_1) &= -k_1 \frac{E_{\theta 1}(k_1)}{\partial k_1} \\ &= -\frac{\partial}{\partial k_1} [k_1 E_{\theta 1}(k_1)] + E_{\theta 1}(k_1) \end{aligned} \quad (3-20)$$

and

$$E_{\theta 1}(k_1) = \int_{k_1}^\infty \frac{E_\theta(k)}{k} dk \quad (3-21)$$

Notice Equation 3-20 shows that the 1-D and 3-D spectra must obey the same negative power law in a given wavenumber range. The same equation reveals that  $E_\theta(k_1) = E_{\theta 1}(k_1)$  when  $E_{\theta 1}(k_1) \sim k_1^{-1}$  thus locating the crossover intersection point of the two spectra. From Equation 3-21 it is evident that the 1-D scalar spectrum is an aliased spectrum containing at a given wavenumber  $k_1$ , contributions from the 3-D spectrum for all wavenumbers greater than  $k_1$  (or scales smaller than  $1/k_1$ ). A



good discussion of this effect is in Tennekes and Lumley (48, pp. 248-9).

The integral scale  $\Lambda_\theta$  and the microscale  $\lambda_\theta$  are obtainable from the spectrum functions using

$$\begin{aligned}\Lambda_\theta &= \frac{\pi}{2} \frac{1}{\theta^{1/2}} E_{\theta 1}(0) \\ &= \frac{\pi}{2} \frac{1}{\theta^{1/2}} \int_0^\infty \frac{E_\theta(k)}{k} dk\end{aligned}\quad (3-22)$$

and

$$\begin{aligned}\frac{2}{\lambda_\theta^2} &= \frac{1}{\theta^{1/2}} \int_0^\infty k^2 E_{\theta 1}(k) dk \\ &= \frac{1}{3} \frac{1}{\theta^{1/2}} \int_0^\infty k^2 E_\theta(k) dk\end{aligned}\quad (3-23)$$

The dynamic equation for  $E_\theta(k)$  or spectral equation follows from taking the Fourier transform of each term of the correlation equation and can be solved only if some relation between  $E_\theta(k)$  and the energy transfer function (representing the inertial interaction of eddies) is assumed.

In the case of velocity turbulence the relative importance of the inertial transfer term in the dynamic equations is determined by the Reynolds number of the turbulence,  $Re_\lambda = u'\lambda_g/\nu$ ; similarly, for temperature turbulence the importance of the corresponding term is determined by the Peclet number of the velocity and temperature fields,  $Pe = u'\lambda_\theta/\alpha$  which may be interpreted as the ratio of forced convection

effects to conduction effects, or as the ratio of the diffusivity by the small eddies  $u'\lambda_\theta$  and the molecular diffusivity  $\alpha$ .

Some of the classical assumptions and resulting solutions of the scalar spectral equation and their limitations are reviewed elsewhere, for example, Hinze (29) or Gibson (25). Only the results will be summarized here for later comparison with experimental data. Corrsin (16) showed that for the lowest end of the wavenumber range the scalar variance spectrum  $E_\theta(k) \sim k^2$ . For conditions when the Peclet number is sufficiently high Corrsin theoretically predicted a scalar inertial subrange (equivalent to the velocity inertial subrange) for which  $E_\theta(k) \sim k^{-5/3}$ . And, he proposed a cutoff in the temperature spectrum above a wavenumber  $k_{\theta,d} = (\epsilon/\alpha^3)^{1/4}$  when the local spectral phenomena are no longer dominated by forced convection effects but where conductive or molecular diffusion effects become important (small Peclet number). This wavenumber is analogous to the viscous cutoff of the velocity spectrum above the Kolmogoroff wavenumber  $k_d = 1/\eta = (\epsilon/\nu^3)^{1/4}$ . For the highest wavenumber range where viscous and molecular diffusion effects dominate, Corrsin used the same dimensional approach as Heisenberg to predict  $E_\theta(k) \sim k^{-7}$ ; however, Hinze explains why this result is unacceptable. When  $Re_\lambda$  and  $Pe$  are sufficiently small and the inertial interaction transfer term can be neglected altogether then Corrsin obtained  $E_\theta(k) \sim k^2 \exp(-2\alpha k^2 t)$ . For locally isotropic and weakly diffusive scalars, that is, scalars for which the Prandtl (or Schmidt) number  $Pr = Sm = \nu/\alpha \gg 1$ . Batchelor (3) theoretically deduced a region

in which  $E_\theta \sim k^{-1}$  until the eddy scales become short enough for diffusion to dominate and result in exponential decay. In a companion paper Batchelor, Howells, and Townsend (5) predicted an  $E_\theta \sim k^{-17/3}$  spectral cutoff at about the Corrsin scale  $(\epsilon/\alpha^3)^{1/4}$  for strongly diffusive scalars ( $Pr \rightarrow 0$ ). However, Gibson (25) rejects the physical arguments behind the  $k^{-17/3}$  cutoff and has proposed a much slower decay of  $k^{-3}$  using his theory of minimal gradient straining. In this work Gibson has extended and consolidated the hypotheses of local isotropy and universal similarity as applied to turbulent scalar fields.

While no theoretical solution has been obtained for the range in which the 3-D energy spectrum peak occurs (energy-containing eddies), Hinze (29) suggests the following algebraic interpolation equation which fits a curve to the range including  $k \rightarrow 0$  through the inertial subrange:

$$E_\theta(k) = \text{constant} \frac{(k/k_0)^2}{[1 + (k/k_0)^2]^{11/6}} \quad (3-24)$$

When an isotropic scalar field is superimposed on an isotropic velocity field as in the present study, both fields will decay simultaneously if there are no sustaining sources. Hinze (29) cites numerous studies of the decay of velocity turbulence behind grids and mentions that different periods of decay have been distinguished: initial, final, and transition. The initial period is associated with  $x/M \leq 100$  to 150 which includes the present study, and the final period is associated with  $x/M \geq 500$ , low  $Re_\lambda$ , and negligible inertia

effects. It can be shown theoretically by several different approaches (see Hinze 29, pp. 208-14) that turbulence should decay with  $u'^2 \sim x^{-n}$  where  $n = 1$  in the initial period (and  $5/2$  in the final period).

Batchelor and Townsend (4) have proposed the following expression for  $10 \leq x/M \leq 100$  based on this "linear" decay law:

$$\left( \frac{\bar{U}}{u'} \right)^2 = A \left( \frac{x}{M} - \frac{x_0}{M} \right) \quad (3-25)$$

Here  $x_0$  is an effective or virtual origin which seems to be at about  $x/M = 10$  for grids with  $M/d = 4$  to  $5$  and decreases with decreasing  $M/d$ . Equation 3-25 relates the turbulence intensity to the grid characteristics these being its geometry and specific drag since the power (work rate done against this drag) used in forcing the air through the grid appears as turbulence (and internal energy). Thus

$$A = \frac{c}{C_D}$$

where  $c$  is a constant depending on grid geometry.  $C_D$  is the drag per unit area and has been found to be a function only of  $M/d$ . For typical grids ( $M/d = 4$  to  $6$ ),  $A \approx 135$ .

Many measurements have shown grid turbulence approaches isotropy at  $x/M = 10$  to  $20$  depending particularly on the  $M/d$  ratio and decreasing with decreasing  $M/d$ . For larger values of  $M/d$  the length parameter becomes  $d$  instead of  $M$  (which characterizes the size of the initial mixing layers or "jets"). These measurements have supported a linear increase in  $(\bar{U}/u')^2$  with  $x/M$ , provided  $Re_M$  and  $Re_\lambda$  are sufficiently

large (see Hinze 29, Chapter 3).

Once the decay law (3-25) has been obtained by measuring the change in turbulence intensity  $u'/\bar{U}$  as a function of distance from the grid, the dissipation rate  $\epsilon$  can be estimated. In general

$$\epsilon = -\frac{1}{2} \frac{d\overline{q^2}}{dt} \quad (3-26)$$

where  $\overline{q^2} = \overline{u^2} + \overline{v^2} + \overline{w^2}$ . If the turbulence is isotropic so that  $\overline{u^2} = \overline{v^2} = \overline{w^2}$  then

$$\epsilon = -\frac{3}{2} \frac{d\overline{u^2}}{dt} \quad (3-27)$$

$\epsilon$  can be calculated when Taylor's hypothesis is assumed by using  $x = \bar{U}t$  in Equation 3-25 and differentiating in Equation 3-27. Knowing  $\epsilon$  the Taylor microscales  $\lambda_g$  and  $\lambda_f$  and the Kolmogoroff scale  $\eta$  can be estimated.

A second independent method of estimating  $\epsilon$  is to calculate the dissipation spectrum  $k_1^2 E_1(k)$  vs  $k_1$  from  $E_1(k_1)$  measured at a particular location downstream of the grid and apply the relations

$$\epsilon = 30\nu \frac{\overline{u'^2}}{\lambda_f^2} = 15\nu \frac{\overline{u'^2}}{\lambda_g^2} \quad (3-28)$$

and

$$\frac{1}{\lambda_f^2} = \frac{1}{2\overline{u'^2}} \int_0^\infty k_1^2 E_1(k_1) dk_1 \quad (3-29)$$

where (3-29) follows directly from (3-9) using  $k_1 = 2\pi f/\bar{U}$  and

$$E_1(k_1) = \frac{\bar{U}}{2\pi} E_1(f) \quad (3-30)$$

which holds so that  $E_1(k_1)dk_1 = E_1(f)df$ . Dissipation spectra describe the wavenumber distribution of the rate of decay of turbulent kinetic energy per unit mass.

The other important turbulence-characterizing scale is the Taylor integral scale  $\Lambda_f$ , which is of the same order as  $\ell_e$ , the average size of energy-containing eddies.  $\Lambda_f$  can be estimated from the graph of  $r_E(\tau)$  vs  $\tau$  as shown above or from the  $k_1 = 0$  intercept of the  $E_1(k_1)$  vs  $k_1$  graph since

$$\Lambda_f = 2\Lambda_g = \frac{\pi}{2u'^2} E_1(0) \quad (3-31)$$

Hinze discusses the assumptions and theory which lead to a power law for the decay of scalar fluctuations of the form

$$\theta'^2 \sim x^{-m} \quad (3-32)$$

where  $m = 3/2$  in the high Re, high Pe initial stage (as well as in the final stage). A decay law for the temperature fluctuations analogous to (3-25) may be measured and differentiated to estimate the rate of decay of scalar variance  $\chi$  where

$$\chi = - \frac{d}{dt} \overline{\theta'^2} \quad (3-33)$$

Knowing  $\chi$  the scalar microscale  $\lambda_\theta$  can be estimated from

$$\chi = 12 \alpha \theta'^2 \left( \frac{1}{\lambda_\theta^2} \right) \quad (3-34)$$

$\chi$  can be independently estimated from the scalar dissipation spectrum  $k_1^2 E_\theta(k_1)$  vs  $k_1$  using (3-34) and (3-23) above. The scalar integral

scale  $\Lambda_0$  can be estimated at the  $k_1 = 0$  intercept of the  $E_{01}(k_1)$  vs  $k_1$  graph was indicated in (3-22).

Most of the equations appearing above may be found in Chapters 1 or 3 of Hinze's book (29) with more discussion; they were repeated here for convenience and reference from below. We will now turn to the theory underlying the crossed-beam schlieren instrument (CBS).

### B. Crossed-Beam Schlieren

The next few pages will review Wilson's application of the crossed-beam correlation technique to the schlieren mode of operation. The analysis appears in reference (52) and has been presented here for completeness and for the reader's convenience.

The basic principles of the crossed-beam correlation technique were first presented by Fisher and Krause (21). In essence, two beams of radiation are intersected at a point in the flow region of interest and each beam is modulated by turbulence-induced fluctuations in an optical property of the gas under study. The resulting intensity modulations of each beam as they exit the flow region are monitored by a suitable detector. The practical usefulness of a system mode emerges when the optical property can be simply related to a thermodynamic scalar property as in the present study. Here the optical property is the local refractive index which is related to mass-density through the Gladstone-Dale equation; and, fluctuations in index of refraction are recorded by operating each beam in the schlieren mode as discussed below.

The crossed-beam schlieren instrument consists of two orthogonal laser-schlieren systems as has been indicated in Figure 1. The coordinate axes orientation used in the following description and analysis is shown in Figure 4. Two collimated beams of light (A and B shown parallel to the x and y axes, respectively) are passed through the flow region such that originally when  $\xi = 0$ , the two intersecting beams form a plane normal to the X axis. On exit from the flow region, each beam is partially intercepted by a knife edge oriented perpendicular to the mean flow direction and then focused by a lens into a detector. With the knife edge so oriented, each detector emits an electrical signal proportional to the refractive index gradient in the X direction. To see this, consider that when the beam encounters a gradient in refractive index in the X direction at a particular point on its path it is slightly deflected in the X direction by angle  $\phi$ . If  $l$  is the distance from the point to the knife edge, the result is a deflection  $\delta = l\phi$  normal to the knife edge and, therefore, a change in light intensity on the detector. The corresponding change in detector output  $e$  (the mean detector output  $\bar{E}$  is eliminated by ac-coupling) may be related to a deflection  $\delta = l\phi$  at the knife edge by

$$e = Cl\phi = C\delta \quad (3-35)$$

where  $C$  is the schlieren sensitivity as shown in Liepmann and Roshko (38).

For circular beams the detector output will be a linear function of beam deflection  $\delta$  and hence of refractive index gradients only when



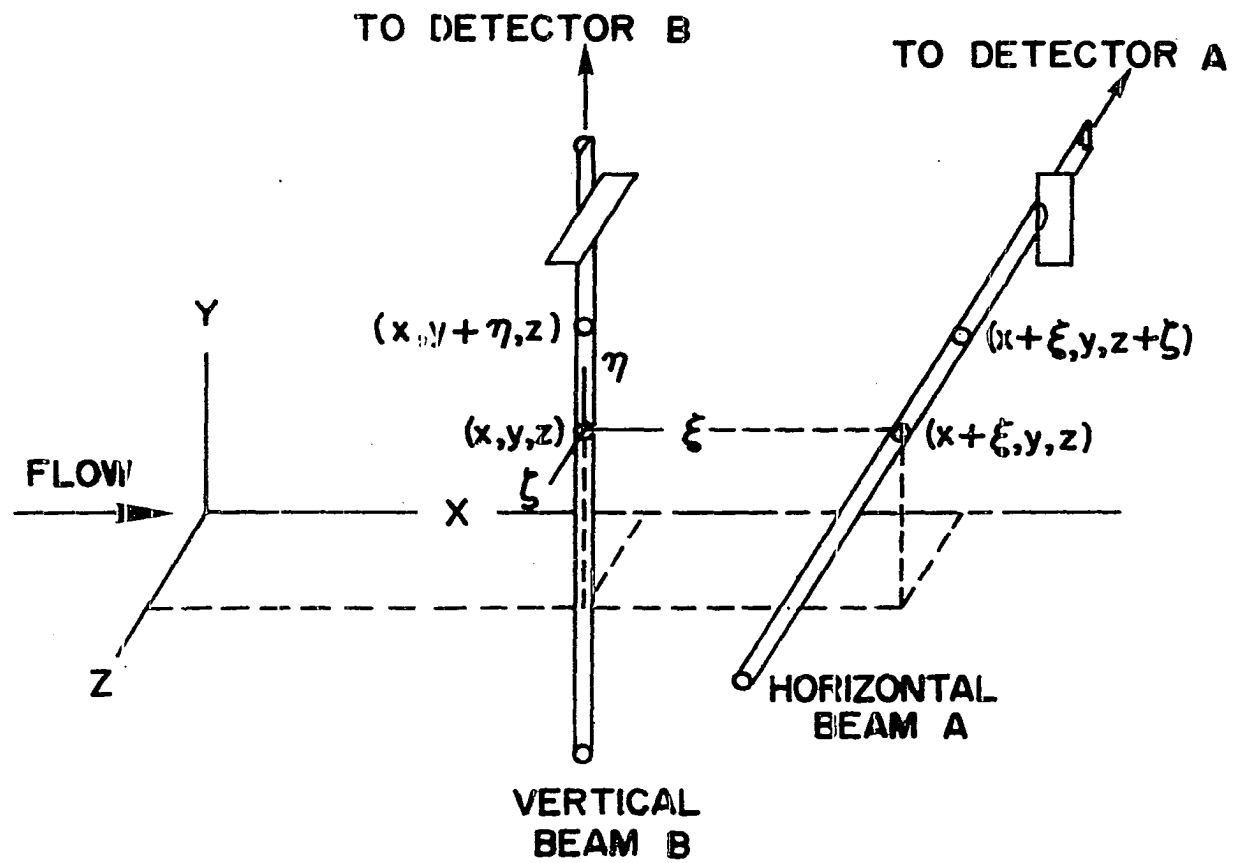


Figure 4. Coordinate axes for crossed-beam schlieren analysis

$\delta \ll$  beam diameter. The anticipated signal weighing due to  $\ell$  changing across the flow region is small if  $\ell \gg$  correlated scales. In addition to these considerations it is clear that the spatial resolution of the CBS is dependent on the beam diameter.

The law governing the net angular deflection  $\Phi$  of a ray of light traversing a region of varying index of refraction is

$$\Phi(t) = \int_{L_0}^L (\vec{n} \cdot \frac{1}{N} \vec{\text{grad}} N) d\vec{s} \quad (3-36)$$

where  $L_0$  is the beam origin ( $a_0$  or  $b_0$ ),  $L$  is the location of the knife edge ( $a$  or  $b$ ), and  $\vec{n}$  is the unit vector normal to the light path  $\vec{s}$ .

$N = N(t)$  is the refractive index decomposed such that  $N = N_0 + n_0 + n$  where the terms on the right-hand side are respectively ambient value, mean change relative to ambient, and fluctuating value. Equation (3-36) may be written for beam A assuming the configuration depicted in Figure 4 as

$$\Phi_A(t) = \int_{a_0}^a \frac{1}{N_0 [1 + (n_0 + n)/N_0]} \frac{\partial (N_0 + n_0 + n)}{\partial x} dz \quad (3-37)$$

since  $\vec{i} \cdot \vec{\text{grad}} N = \frac{\partial N}{\partial x}$ . Since  $n_0$  and  $n$  are expected and assumed to be several orders of magnitude smaller than  $N_0$ , (3-37) becomes for all points  $(x, y, z)$  along beam A

$$\begin{aligned}\phi_A(t) &\approx \frac{1}{N_o} \int_{a_o}^a \frac{\partial n_o}{\partial x} dz + \frac{1}{N_o} \int_{a_o}^a \frac{\partial n}{\partial x} dz \\ &= \bar{\phi}_A + \phi_A\end{aligned}\quad (3-38)$$

and similarly for all points  $(x + \xi, y, z)$  along beam B

$$\begin{aligned}\phi_B(t) &\approx \frac{1}{N_o} \int_{b_o}^b \frac{\partial n_o}{\partial x} dy + \frac{1}{N_o} \int_{b_o}^b \frac{\partial n}{\partial x} dy \\ &= \bar{\phi}_B + \phi_B\end{aligned}\quad (3-39)$$

The mean beam deflections  $\bar{\phi}_A$  and  $\bar{\phi}_B$  were found to be too small to be measurable in the present study. At any rate, for stationary conditions and a long averaging time interval the mean product of  $\phi_A$  and  $\phi_B$  is

$$\begin{aligned}\overline{\phi_A \phi_B} &= \frac{1}{N_o^2} \int_{a_o}^a \int_{b_o}^b \left( \frac{\partial n}{\partial x} \right)_{(x,y,z)} \left( \frac{\partial n}{\partial x} \right)_{(x+\xi,y,z)} dy dz \\ &= \frac{e_A e_B}{C_A C_B \bar{C}_A \bar{C}_B}\end{aligned}\quad (3-40)$$

where we have used Equation 3-35. The Gladstone-Dale equation

$$N - 1 = \alpha \Gamma \quad (3-41)$$

may be used to relate  $N$  to the gas density  $\Gamma$ . The specific refractivity  $\alpha$  is a constant property of the gas and a function of the source radiation wavelength. If we decompose  $\Gamma = \Gamma_o + \rho_o + \rho$  (as for  $N$ ), then differentiation of (3-41) gives

$$\frac{\partial n}{\partial x} = \alpha \frac{\partial \rho}{\partial x} \quad (3-42)$$

substitution of (3-42) in (3-40) and transformation to the  $(\xi, \eta, \zeta)$

coordinates yields the experimentally accessible CBS density covariance

$$Q_{\text{CBS}}(\xi, x, y, z) = \frac{\overline{e_A e_B N_o^2}}{C_A C_B \ell_A \ell_B \alpha^2} \quad (3-43)$$

$$= \int_{-a/2}^{a/2} \int_{-b/2}^{b/2} \frac{\partial \rho(x, y+\eta, z)}{\partial x} \frac{\partial \rho(x+\xi, y, z+\zeta)}{\partial x} d\eta d\zeta$$

It is expected and assumed that only eddies passing through a small area near the beam intersection point will appreciably contribute to the integral in (3-43) and, therefore, the integration limits may be extended to infinity without consequence; this is the first important assumption. The second important assumption is that the turbulence is homogeneous in the correlated area. Since only distances between points are then important, the result is that all points contributing to the double integration along, say, beam B at  $(x, y+\eta, z)$  can be returned by a translation of coordinates to the single point  $(x, y, z)$  provided all contributing points along A at  $(x+\xi, y, z+\zeta)$  are shifted by  $\eta$  to preserve  $r$  in the plane  $x + \xi = \text{constant}$ . Then the integrand of (3-43) can be written

$$\frac{\partial \rho}{\partial x}(x, y+\eta, z) \frac{\partial \rho}{\partial x}(x+\xi, y, z+\zeta)$$

$$= \frac{\partial \rho}{\partial x}(x, y, z) \frac{\partial \rho}{\partial x}(x+\xi, y+\eta, z+\zeta) \quad (3-44)$$

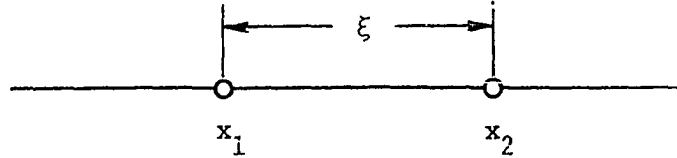
$$= \frac{\partial \rho}{\partial x_1} \frac{\partial \rho'}{\partial x_2} = \frac{\partial}{\partial x_1} \frac{\partial}{\partial x_2} (\overline{\rho \rho'})$$

As a consequence (3-43) can be written

$$Q_{\text{CBS}}(\xi) = \frac{\partial \rho(x, y, z)}{\partial x} \iint_{-\infty}^{\infty} \frac{\partial \rho(x+\xi, y+\eta, z+\zeta)}{\partial x} d\eta d\zeta \quad (3-45)$$

where dependence of  $Q_{\text{CBS}}$  on the location of the beam intersection point  $(x, y, z)$  is now implicit. Equation (3-45) shows that the covariance  $Q_{\text{CBS}}$  obtained by measuring  $\overline{e_A e_B}$  with the CBS as indicated by (3-43) is a so-called "point-area" covariance between fluctuations in  $\rho$  at the beam intersection point  $(x, y, z)$  and in the plane  $x + \xi = \text{constant}$ . Physically, this means that only waves whose wavenumber vectors are normal to the plane contribute Fourier components to  $Q_{\text{CBS}}$ . For this reason when we take Fourier transform of  $Q_{\text{CBS}}$ , one component of the true 3-D spectrum is obtained as shown analytically below.

The notation in the last equality of (3-44) was used for convenience to show the following effect of homogeneity in the x-direction.



Homogeneity implies  $\rho = \rho(\xi)$ , but  $\xi = \xi(x_1, x_2) = x_2 - x_1$ , therefore

$$\frac{\partial}{\partial x_1} = \frac{\partial}{\partial \xi} \frac{\partial \xi}{\partial x_1} = - \frac{\partial}{\partial \xi}$$

$$\frac{\partial}{\partial x_2} = \frac{\partial}{\partial \xi} \frac{\partial \xi}{\partial x_2} = \frac{\partial}{\partial \xi}$$

Thus, (3-44) becomes

$$\begin{aligned} & \overline{\frac{\partial \rho}{\partial x}(x, y+\eta, z) \frac{\partial \rho}{\partial x}(x+\xi, y, z+\zeta)} \\ &= -\frac{\partial^2}{\partial \xi^2} \overline{\rho(x, y, z) \rho(x+\xi, y+\eta, z+\zeta)} \end{aligned}$$

This allows (3-43) to be written in another interesting way

$$\begin{aligned} Q_{\text{CBS}}(\xi) &= - \iint_{-\infty}^{\infty} \frac{\partial^2}{\partial \xi^2} \overline{\rho(x, y, z) \rho(x+\xi, y+\eta, z+\zeta)} d\eta d\zeta \\ &= - \iint_{-\infty}^{\infty} \frac{\partial^2 Q(\xi, \eta, \zeta)}{\partial \xi^2} d\eta d\zeta \end{aligned} \quad (3-46)$$

where (3-46) relates  $Q_{\text{CBS}}(\xi)$  to the familiar two-point density covariance  $Q(\xi, \eta, \zeta)$ .

Performing a 1-D Fourier transform of (3-46) we obtain the CBS energy spectrum  $E_{\text{CBS}}(k_1)$ ,

$$\begin{aligned} E_{\text{CBS}}(k_1) &= \frac{1}{8\pi^3} \int_{-\infty}^{\infty} Q_{\text{CBS}}(\xi) \exp(-ik_1 \xi) d\xi \\ &= \frac{-1}{8\pi^3} \iiint_{-\infty}^{\infty} \frac{\partial^2 Q(\xi, \eta, \zeta)}{\partial \xi^2} \exp(-ik_1 \xi) d\xi d\eta d\zeta \end{aligned} \quad (3-47)$$

where  $k_1$  = x-component of wavenumber. Integrating (3-47) by parts twice with respect to  $\xi$  gives

$$E_{\text{CBS}}(k_1) = \frac{k_1^2}{8\pi^3} \iiint_{-\infty}^{\infty} Q(\xi, \eta, \zeta) \exp(-ik_1 \xi) d\xi d\eta d\zeta \quad (3-48)$$

For comparison consider Equation 3-17 written for  $\rho$  in the  $(\xi, \eta, \zeta)$  coordinates

$$E_{\rho, \rho}(k_1, k_2, k_3) = \frac{1}{8\pi^3} \iiint_{-\infty}^{\infty} Q(\xi, \eta, \zeta) \exp[-i(k_1 \xi + k_2 \eta + k_3 \zeta)] d\xi d\eta d\zeta$$

which can be reduced to

$$E_{\rho, \rho}(k_1, 0, 0) = \frac{1}{8\pi^3} \iiint_{-\infty}^{\infty} Q(\xi, \eta, \zeta) \exp(-ik_1 \xi) d\xi d\eta d\zeta$$

Using this and (3-48) we see

$$E_{\text{CBS}}(k_1) = k_1^2 E_{\rho, \rho}(k_1, 0, 0) \quad (3-49)$$

showing the CBS may be used to measure the  $k_1$  or streamwise component of the true 3-D spectrum. Equation (3-49) shows that the CBS spectrum is proportional to the 3-D scalar spectrum function defined by Hinze (see Equation 3-18). We expect the CBS spectrum to peak in the region of energy containing eddies as does the 3-D velocity spectrum.

Up to here the assumptions have been small  $n$ , constant  $\alpha$ , beam paths long relative to, and homogeneity in the correlated area and in the  $x$ -direction. By making an additional assumption of local isotropy within the correlated volume, an expression for the mean square density is obtainable. Equation 3-46 may then be written after a little geometry

$$Q_{\text{CBS}}(\xi) = -2\pi \int_{\xi}^{\infty} \frac{\partial^2 Q(r)}{\partial \xi^2} r dr \quad (3-50)$$

where  $r^2 = \xi^2 + \eta^2 + \zeta^2$  ( $r$  is the distance between the beam intersection

point and any point in the plane  $x + \xi = \text{constant}$ ). For isotropic conditions  $Q = Q(r)$  and  $r = r(\xi, \eta, \zeta)$ ; therefore, using the chain rule

$$\frac{\partial^2 Q}{\partial \xi^2} = \frac{\xi^2}{r^2} \frac{d^2 Q}{dr^2} + \frac{1}{r} \left( 1 - \frac{\xi^2}{r^2} \right) \frac{dQ}{dr}$$

Substituting this in (3-50) gives

$$Q_{\text{CBS}}(\xi) = 2\pi \frac{d[\xi Q(\xi)]}{d\xi} \quad (3-51)$$

which reduces to

$$Q_{\text{CBS}}(0) = 2\pi Q(0) = 2\pi \overline{\rho^2} \quad (3-52)$$

and

$$Q(\xi) = \frac{1}{2\pi\xi} \int_0^\xi Q_{\text{CBS}}(\xi') d\xi' \quad (3-53)$$

Equation (3-52) says that the mean square density may be estimated from the CBS covariance when the beams are intersecting and (3-53) prescribes the calculation of  $Q(\xi)$  the two-point density covariance. It is interesting to note Wilson's comment that (3-52) follows intuitively from (3-46) when conditions are right (isotropic) to allow the double integration to nullify the double differentiation for  $\xi = 0$ .

For measurements in low-speed flows as in the present study, density fluctuations due to compressibility effects are negligible. Then  $\rho$ -fluctuations due to grid heating are relatable to  $\theta$ -fluctuations through the perfect gas law as

$$\frac{\overline{\rho^2}}{\overline{\Gamma^2}} = \frac{\overline{\theta^2}}{\overline{\theta^2}} \quad (3-54)$$



### C. Hot-Wire Anemometer

The HWA transducer is a very small resistance element which is heated and controlled at an elevated temperature by an electric current. The sensor is usually either a fine short wire filament or a thin conducting film on a ceramic substrate. It is included as one leg of a Wheatstone bridge circuit (of varying sophistication) for detection of minute, rapid resistance changes. Electrical operation of the sensor in the bridge is accomplished in one of two ways: constant current or constant resistance (temperature). Sandborn (44) discussed the details of theory, design, operation, and relative merits of these two types of anemometers. For most present-day applications (including this study) the constant temperature set is used.

If a sensor is immersed in a supersonic turbulent flow, its resistance will fluctuate in response to velocity, temperature, and density fluctuations. These fluctuations will be detected by the bridge and amplified for analysis. While combined effects of the variables are difficult to separate, an analytic procedure has been developed and used successfully by Kovaszny (34 and 35). This so-called mode- or fluctuation-diagram technique has been summarized by Morkovin (40), and recently extended to a two-sensor correlation technique by Demetriades (18).

In low speed flows the density fluctuations due to compressibility are negligible and only the influences of velocity and temperature need be considered. For these applications a HWA may be operated

in essentially three different modes. First, the sensor may be operated hot or at a high overheat ratio  $R_w/R_a$  (equivalently high  $\bar{\theta}_w - \bar{\theta}_a$ ) in which case it will be relatively insensitive to temperature fluctuations. This mode is most common and usually used in measurements of  $\bar{U}$  and u-fluctuations in isothermal flow, or in the presence of low-level uninteresting  $\theta$ -fluctuations. Secondly, the sensor may be operated at very low overheat in the resistance thermometer mode. Here the sensor is in equilibrium with the fluid temperature, and sensitive only to  $\theta$ -fluctuations. Finally, it may be operated in the mixed sensitivity mode at some intermediate overheat so that the sensor responds to both u- and  $\theta$ -fluctuations.

The earliest reported technique for separating u- and  $\theta$ -fluctuations in low-speed flows was developed by Corrsin (14) who derived analytic expressions for the respective sensitivities and considered limiting cases. Corrsin began by assuming a particular form of the semi-empirical heat transfer equation governing the dissipation of heat from sensor to fluid. The total heat exchanged is dependent on the mean velocity, the difference in temperature between the wire and fluid, the fluid properties, and the physical properties of the wire. One modification of this equation called King's law is

$$\frac{\bar{E}_w^2}{\bar{R}_w} = [A + B(\rho \bar{U})^n] (\bar{\theta}_w - \bar{\theta}_a) \quad (3-55)$$

where A and B depend on the fluid properties and physical properties

of the sensor, but are essentially constant in a given application if temperature changes are small. A precise or most accurate form of King's law is not universally accepted (see References 14 and 11). This is particularly true of the Reynolds number exponent  $n$  (or power-law exponent governing the effect of velocity). A particular value (usually about 0.5) may be assumed for  $n$  based on past experience, or it may be determined experimentally.

Collis and Williams (12) have suggested one refinement of King's law

$$\frac{\bar{E}_w^2}{\bar{R}_w} = k \left[ A_1 + B_1 \left( \frac{\rho \bar{U}}{\mu} \right)^{0.45} \right] \left[ \frac{\bar{\theta}_w + \bar{\theta}_a}{\bar{\theta}_a} \right]^{0.17} (\bar{\theta}_w - \bar{\theta}_a) \quad (3-56)$$

in which Freymuth (23) used the following expressions as estimates of the temperature dependence of thermal conductivity, density, and viscosity

$$\begin{aligned} k &= (\bar{\theta}_w + \bar{\theta}_a)^{0.8} \\ \rho &= \frac{1}{(\bar{\theta}_w + \bar{\theta}_a)} \\ \mu &= (\bar{\theta}_w + \bar{\theta}_a)^{0.76} \end{aligned} \quad (3-57)$$

Substituting (3-57) in (3-56) gives

$$\frac{\bar{E}_w^2}{\bar{R}_w} = [A_2 (\bar{\theta}_w + \bar{\theta}_a)^{0.8} + B_2 \bar{U}^{0.45}] \left[ \frac{\bar{\theta}_w + \bar{\theta}_a}{\bar{\theta}_a} \right]^{0.17} (\bar{\theta}_w - \bar{\theta}_a) \quad (3-58)$$

The procedure for calibration of a HWA sensor for velocity, that is, for determining the velocity sensitivity in isothermal flow

is straightforward and will be discussed later in Chapter V. Likewise, the procedure for calibration of a HWA resistance thermometer for  $\theta$ -fluctuations is relatively simple, so it also will be deferred. However, calibration for mixed sensitivity applications in the presence of both  $u$ - and  $\theta$ -fluctuations deserves more attention. Prior to this discussion we point out that if interest is only in  $\bar{U}$  and  $u$  then HWA measurements can be approximately corrected for not too large  $\bar{\theta}$ -changes or  $\theta$ -fluctuations using relations derivable from (3-55) as shown in Reference 47. Correction for temperature effects is also possible by reference to predetermined calibration curves, by independent temperature measurement, or by directly and automatically compensating in the bridge circuit.

The generalized equation governing the linearized response sensitivity of a constant temperature HWA is given by Sandborn (44). This equation is valid for every type of aerodynamic flow except those associated with very high temperatures. For incompressible flow and a sensor oriented normal to the flow direction, it reduces to the simple form

$$\begin{aligned} e &= \frac{\partial \bar{E}}{\partial \bar{U}} u + \frac{\partial \bar{E}}{\partial \bar{\theta}} \theta \\ &= S_u u - S_\theta \theta \end{aligned} \quad (3-59)$$

that is,  $S_u = \frac{\partial \bar{E}}{\partial \bar{U}}$  and  $S_\theta = -\frac{\partial \bar{E}}{\partial \bar{\theta}}$ .

Squaring and averaging (3-59) gives

$$\overline{e^2} = S_u^2 \overline{u^2} - 2S_u S_\theta \overline{u\theta} + S_\theta^2 \overline{\theta^2} \quad (3-60)$$

Dividing through by  $S_\theta^2$  produces the form suggested by Kovasznay (35)

$$\frac{\overline{e^2}}{S_\theta^2} = \left(\frac{S_u}{S_\theta}\right)^2 \overline{u^2} - 2\left(\frac{S_u}{S_\theta}\right)\overline{u\theta} + \overline{\theta^2} \quad (3-61)$$

or

$$Y = X^2 \overline{u^2} - 2X\overline{u\theta} + \overline{\theta^2} \quad (3-62)$$

which is parabolic relating the mean square HWA voltage fluctuation to the wire sensitivity parameter  $X$ .

Let us first consider several different ways of using Equation 3-62 and then a number of ways of determining  $S_u$  and  $S_\theta$  which fix  $X$  for a particular overheat and mean speed. Operating the sensor at three different overheats is theoretically sufficient to obtain the three unknowns  $\overline{u^2}$ ,  $\overline{u\theta}$ , and  $\overline{\theta^2}$ . However, this procedure is inadvisable; experience shows that small errors in the measured  $\overline{e^2}$  give highly inaccurate results. As suggested by Arya and Plate (1) a better procedure is to least squares fit the parabola (3-62) using six to eight pairs of measured  $X$  and  $Y$ . Even then the results may be considerably scattered for  $\overline{u\theta}$  and  $\overline{\theta^2}$ . This is especially true if the overheats selected are too high producing large values of  $X$ ; this leaves the shape of (3-62) poorly defined for the low values of  $X$  which tend to determine  $\overline{u\theta}$  and  $\overline{\theta^2}$ . Arya and Plate propose a more consistent method which allows the crucial  $X = 0$  point of the parabola to be specified by an independent but simultaneous measurement of  $\overline{\theta^2}$  with a resistance thermometer

(with the same frequency response). Using this procedure they propose four to six overheats as sufficient to determine  $\overline{u^2}$  and  $\overline{u\theta}$  accurately by least squares fitting

$$Z = X^2 \overline{u^2} - 2X \overline{u\theta} \quad (3-63)$$

where  $Z = Y - \overline{\theta^2}$ . Arya and Plate also point out that neglect of  $\overline{\theta^2}$  in (3-62) may be unjustifiable even at high overheats.

Now, there are a number of ways of evaluating  $S_u$  and  $S_\theta$ . We first consider purely empirical techniques and then partly analytical techniques. The most accurate (but also the most difficult) method is direct experimental calibration by varying the flow mean temperature  $\overline{\theta}_a$  and producing a graph of  $\overline{E}$  vs  $\overline{U}$  for different values of  $\overline{\theta}_w - \overline{\theta}_a$ .  $S_u$  can then be obtained graphically by differentiating a polynomial curve fit to the data points.  $S_\theta$  can be determined in similar fashion by cross-plotting the original data as  $\overline{E}$  vs  $\overline{\theta}_w - \overline{\theta}_a$  for constant  $\overline{U}$ . Of course, the calibration may change during operation and applies only to a particular sensor. The problem with this method is that temperature control of a laminar stream is difficult to accomplish.

Arya and Plate (1) have proposed a variation of this method which assumes the individual effects of  $\overline{\theta}_w$  and  $\overline{\theta}_a$  to be negligible compared to  $\overline{\theta}_w - \overline{\theta}_a$ . Their technique is identical to the above except that the wire temperature  $\overline{\theta}_w$  is varied in a constant temperature laminar stream ( $\overline{\theta}_a$ ) to produce the  $\overline{E}$  vs  $\overline{U}$  graphs.

Another procedure, which assumes the experimental determination of the  $\overline{E}$  vs  $\overline{U}$  curves either by  $\overline{\theta}_a$  or  $\overline{\theta}_w$  variation, is to derive a

generalized similarity law for the HWA response of the form

$$\bar{E} = C \bar{U}^n (\bar{\theta}_w - \bar{\theta}_a)^m \quad (3-64)$$

This empirical equation approximately collapses the calibration data to a single point. Once obtained it can be easily differentiated to obtain  $S_u$  and  $S_\theta$ . Kovasznay's mode diagrams could also be used; however, this scheme has been applied nearly exclusively to the evaluation of HWA data obtained in supersonic flows where it is necessary to separate three effects.

All of the above methods of obtaining  $S_u$  and  $S_\theta$  are completely experimental. An alternative method is to compute them by differentiating an analytical expression such as (3-55) or (3-58). To do this, values of the constants A and B must be determined either by calculation using expressions such as are available in Hinze (29) or, preferably, by experimental calibration. As noted by Arya and Plate (1) the complexity and uncertainty in determining certain constants in the available analytic HWA sensitivity and response relations render them limited in usefulness.

Other techniques of separating u- and  $\theta$ -fluctuations have been developed. Chevray and Tutu (11) describe a two-sensor temperature compensation technique using a special analog circuit. Burchill and Jones (8) propose a multi-sensor procedure which permits  $\bar{U}$ ,  $\bar{\theta}$ , u and  $\theta$  measurements in the presence of mean temperature gradients by manual adjustment of the sensors operating resistance.

We conclude this section with the following observation by

Sandborn (44):

"The present discussion assumes that it is possible to obtain a turbulent flow in which only velocity and temperature fluctuate. If temperature fluctuations are kept small (of the order of 5°F or less) and the velocity is also low, then a turbulent flow field might exist in which fluctuations in density can be neglected. Whether such a case actually exists has not been completely established, however, measurements have been reported based on the assumption that density fluctuation can be neglected."



#### IV. EXPERIMENTAL APPARATUS

The apparatus used in this study will be described in the following order: flow system, crossed-beam schlieren, hot-wire anemometer, analog signal processing electronics, and miscellaneous items.

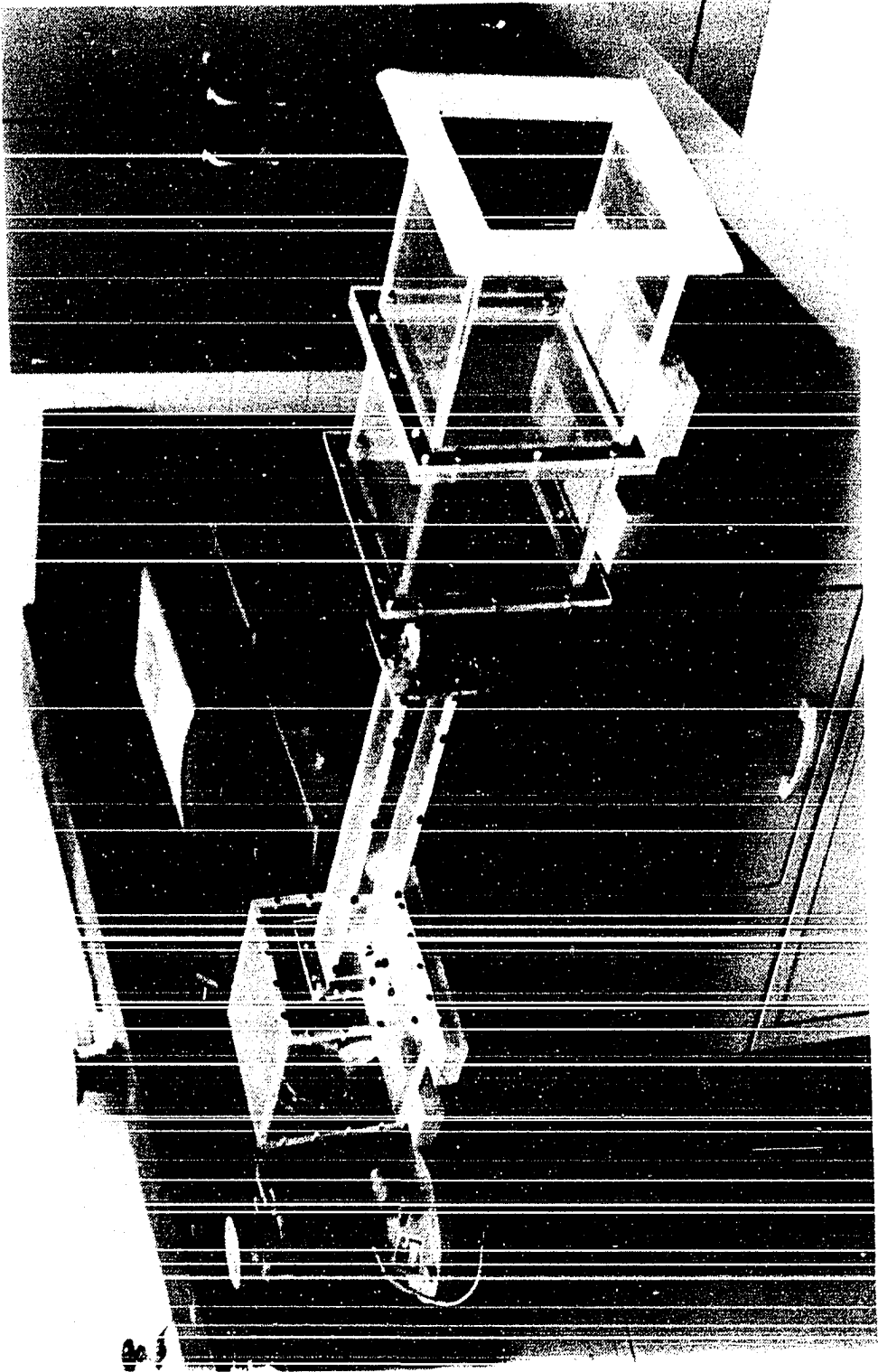
##### A. Flow System

A flow system was desired which would produce an isotropic temperature field simultaneously with an isotropic velocity field. The fields had to be accessible to the CBS and HWA measuring systems. There was little doubt that such fields could best be realized as previously by Mills et al. (39) in the flow downstream of a grid mounted in a wind tunnel, provided the test section was built with transparent walls. In addition, a number of other important detailed design considerations dictated construction of a special-purpose facility. These constraints relate to wind tunnel size and grid geometry and will be discussed in order below. References 19, 28, and 46 were useful in designing the tunnel.

Figure 5 presents a photograph of the wind tunnel which emerged as a result of the design requirements. The wind tunnel configurations and its nominal dimensions are shown schematically in Figure 6. This small-scale open-circuit tunnel consisted of a relatively large settling chamber, contraction cone, grid, test section, and exhaust diffusion chamber. Downstream of the exhaust chamber was exhaust tubing, a second large exhaust stilling chamber, an airflow control device, and

Figure 5. Wind tunnel

.



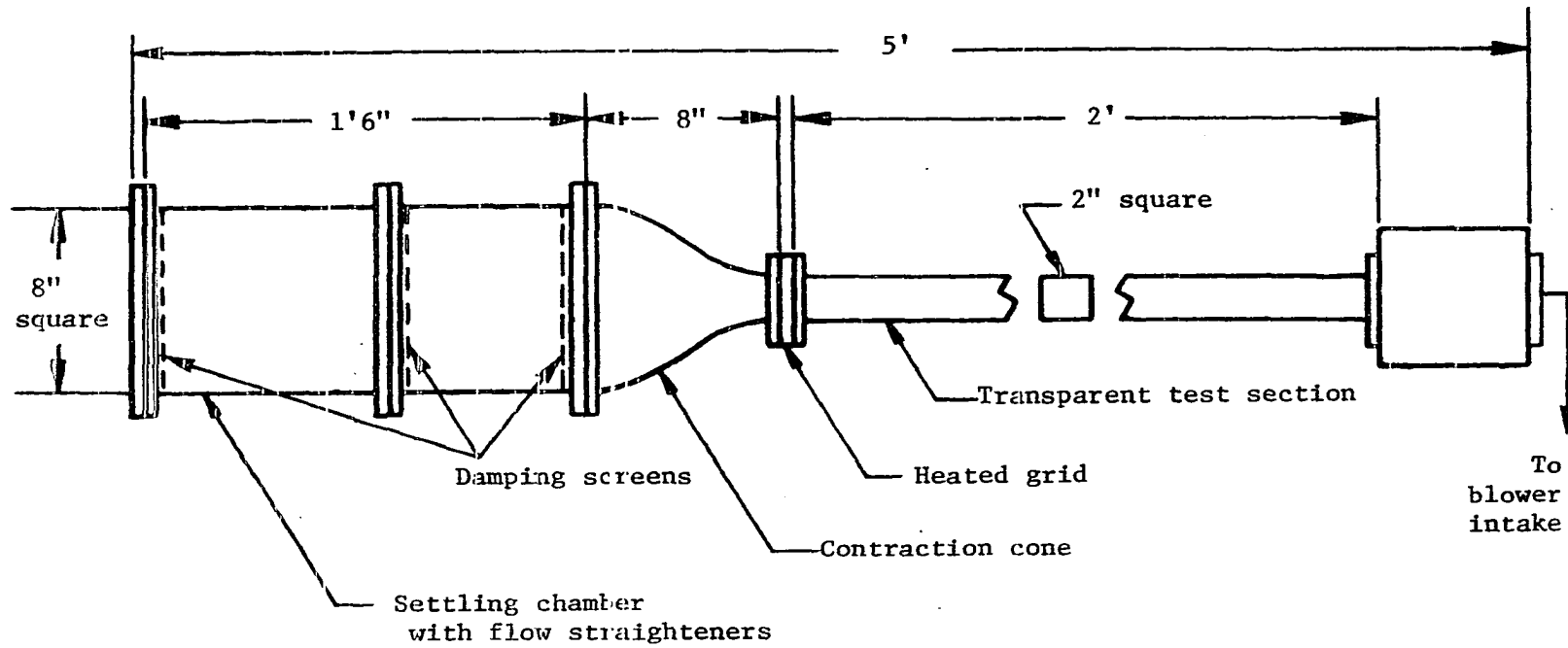


Figure 6. Wind tunnel layout

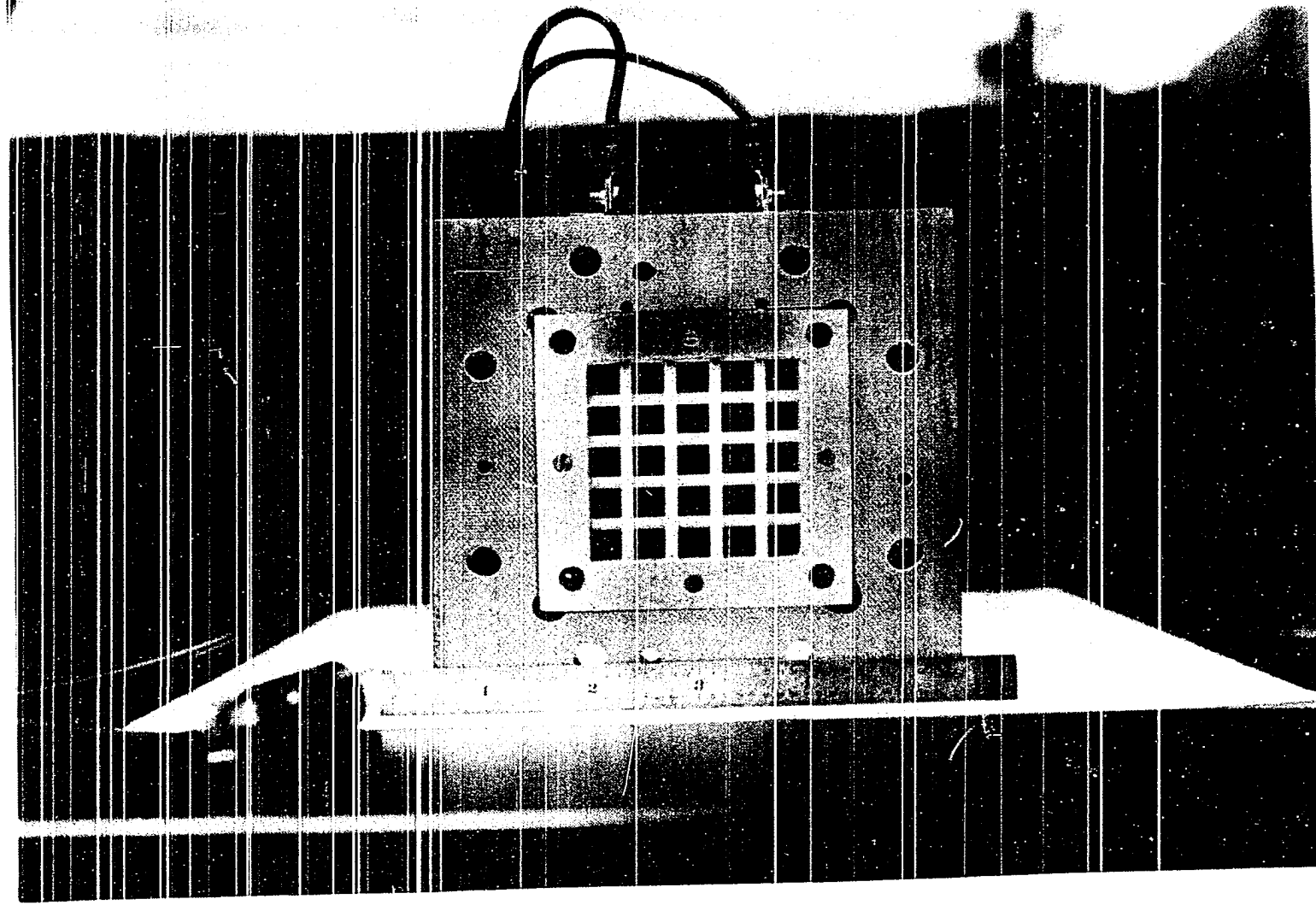
a blower, The tunnel exhaust was connected-up to the blower inlet which provided a vacuum to induce the desired airflow. With exception of the contraction cone, the entire tunnel was constructed from 0.5" thick plexiglass sheet.

Included in the settling chamber were 2.0" diameter semi-circular inlet lip fairings, flow straighteners, and turbulence damping screens. Eleven hundred plastic soda straws, 1/4" in diameter, and 8 7/8" long were tightly packed into the forward section between two screens and served as a flow straightening honeycomb. Three screens were used: two 30 mesh per inch stainless steel screens 10" apart were followed 8" back by a 38 mesh per inch brass screen.

A contraction cone fabricated from 0.032" thick stainless steel (for rigidity) reduced the flow area by a factor of 16 to 1 in two tangent arcs, a 4" radius (center inside) followed by an 8" radius (center outside), between the settling chamber and the grid. The objective of the part of the tunnel described thus far was to provide a low-turbulence intensity ( $u'/\bar{U}$ ) flow with uniform velocity profile into the grid.

The grid heater shown close-up in Figure 7 was constructed of round  $d = 1/8"$ , ceramic (alumina), Omega Engineering Inc. thermocouple insulators mounted in a special frame. The rods each contained four 0.020" diameter holes and were arranged in a biplane grid of four rods in each direction spaced  $M = 0.425"$  center to center with 0.30" between the first rod and the wall. A heat resistant asbestos/cement

Figure 7. Heated grid



composite material insert was used to support the grid rods which were internally strung in series with one continuous strand of 30 gage, Kanthal, high-resistance (8.51 ohm/ft) heating wire which fuses at 4 1/2 amps. This unit was inserted into a fiberglass/exoxy composite material outer frame for insulation and additional heat resistance. The ends of the heating wire passed through the holes drilled in the outer frame and were secured at terminals glued to the frame top. Between these terminals, the grid resistance measured about 87 ohms at ambient conditions.

Figure 8 is a circuit diagram of the power supply which was built to provide a variable controlled voltage across the grid terminals. It contained a 240 volt variac which was wired across two legs of the lab 208 volt 3-phase outlet. The power supply was followed by a full-wave bridge (rectifier) circuit shown in Figure 9. The purpose of the rectifier was to convert the 60 Hz ac voltage supplied by the power supply to dc (plus some 120 Hz ripple). Eliminating the ac current fluctuations in the grid precluded the appearance of a 60 or 120 Hz temperature fluctuation at the rod surfaces and any chance of vibration of the rods due to magnetic effects. In addition this unit provided outputs for monitoring both the grid current and voltage and, hence, the power dissipated. As an example, when the voltage across the grid was set at 152 volts the current drawn was 2.1 amps for a power of 319 watts. At a mean flow of  $\bar{U} = 9.5$  ft/sec this setting consistently produced a change in the mean air temperature of  $\Delta \cong 47^\circ\text{F}$ . Using this



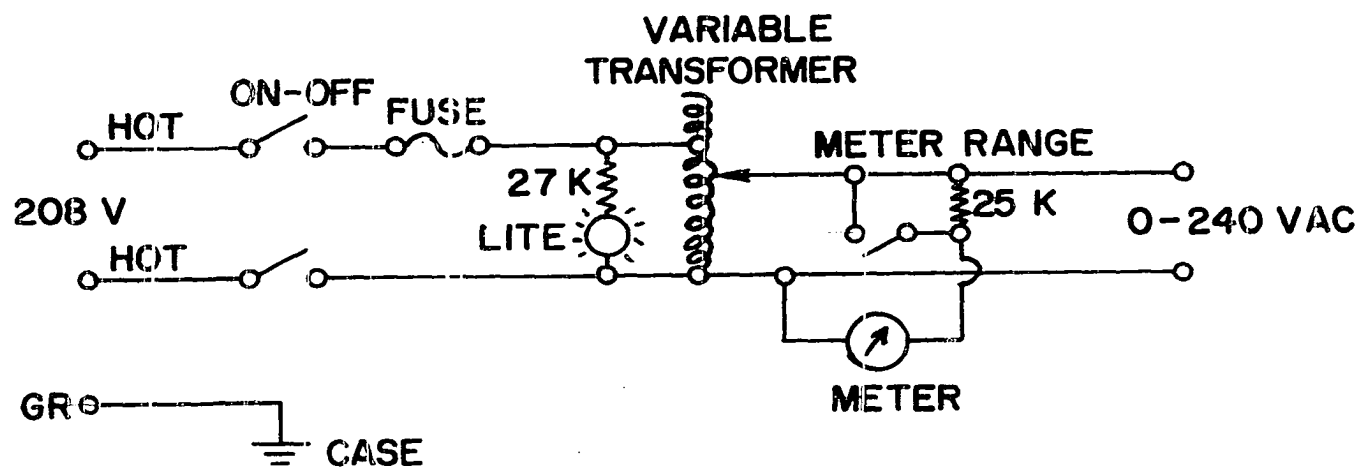


Figure 8. Circuit diagram of power supply for heated grid

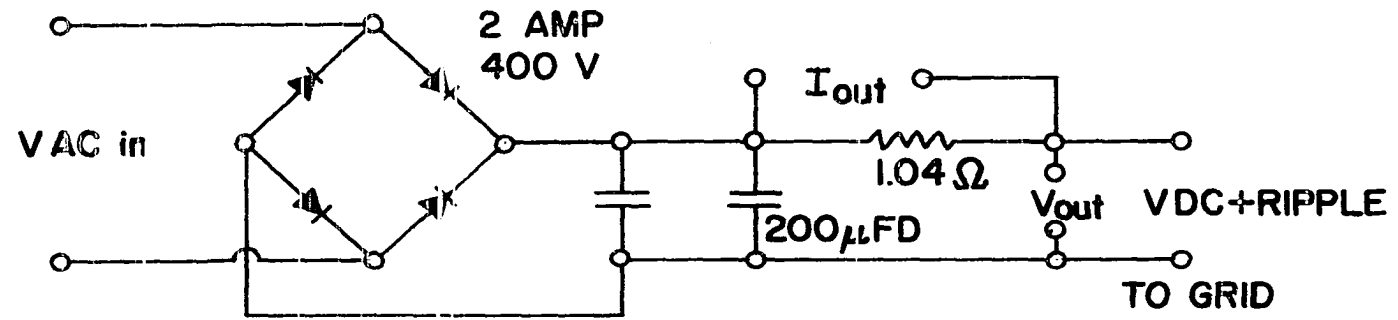


Figure 9. Full-wave bridge (rectifier) circuit

information and

$$P = \dot{Q} = \dot{m} C_p \Delta T = \bar{T} \bar{U} A C_p \Delta \quad (4-1)$$

a rough calculation gives  $P \approx 250$  watts as an estimate of the power actually dissipated to the flow.

In this way for a mean flow velocity of, say,  $\bar{U} = 9.5$  ft/sec the driving temperature or grid overheat  $\Delta$  could be preset and controlled from  $\Delta = 0^\circ\text{F}$  to about  $\Delta = 60^\circ\text{F}$  over periods of up to 1/2 hour without damage to the grid or tunnel. An approximate calibration curve of grid voltage vs grid overheat was obtained to facilitate setting a desired overheat.

Following the grid was a transparent test section 2" square by 2' long. One side of the test section was fully removable; this side had special access ports for support of instrumentation. The diffusion chamber into which the test section emptied was connected to a large stilling chamber by about 9' of 5" I.D. Flexhaust wire reinforced general service hose. Inside the 3'x1'x1' stilling chamber was foam for acoustic damping and a honeycomb of 2" diameter, 2' long tubes for flow straightening. The object of this chamber was to decouple the blower both acoustically and aerodynamically from the test section. At the chamber exit and connected to the blower inlet was a perforated plexiglass tube section which was used for flow control. Airflow through the tunnel was regulated by selectively covering holes drilled in the surface of the plexiglass tube with flexible covers. The covers were "calibrated" by cutting them to the size required to provide a

given mean speed.

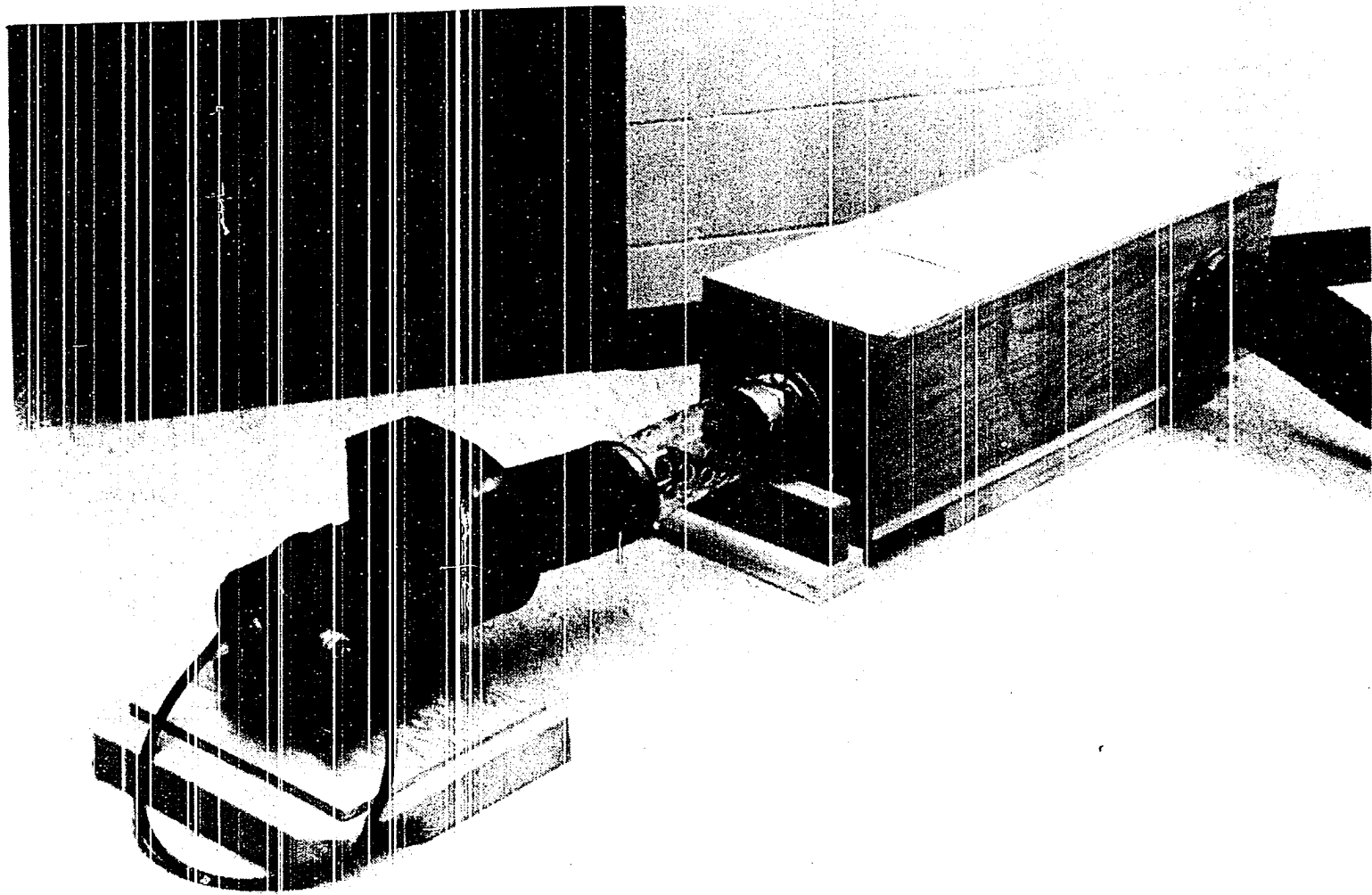
The blower was an I.L.G. Electric Ventilating Co. centrifugal type with a 3 3/4" circular inlet and a 3 1/2" by 4" rectangular exhaust. Driven by a 3/4 horsepower G. E. electric motor at 3450 RPM, it moved in excess of 500 ft<sup>3</sup>/min. Since the wind tunnel tests were conducted for flow rates under 50 ft<sup>3</sup>/min. the preponderance of air demanded by the blower was supplied through holes in the control tube. The stilling chamber, flow control tube, and blower are shown connected in Figure 10.

Several factors influencing the design of the grid and test section, in particular their small size, will now be discussed. The theoretical considerations involved a trade-off between flow homogeneity across the test section and CBS signal-to-noise ratio. In Reference 20 it has been shown that the correlation coefficient  $r$ , which is a measure of a crossed-beam system s/n ratio is inversely proportional to the number of integral scale lengths along either beam. Under the idealized conditions of  $N$  identical "cells" along both beams

$$r_{\text{CBS}}(0) = \left[ \frac{e_A e_B}{e'_A e'_B} \right]_{\xi=0} = \frac{1}{N} \quad (4-2)$$

In Reference 52 which introduced the CBS technique, values of 0.25 for  $r_{\text{CBS}}(0)$  were typically obtained; however, in Fisher and Krause's original paper (21) successful measurements were obtained in the scattering mode with  $r(0) \cong 0.05$ . From Equation 4-2 it is evident that

Figure 10. Stilling chamber, flow control tube, and blower



if we desire  $r_{\text{CBS}}(0) = 0.2$  then the width of the test section should be no more than five dominant scales or approximately  $5M$ . Hinze (29) notes that grids usually applied have  $M/d = 4$  to  $6$  which includes  $M/d = 4$  used in Reference 39.

On the other hand, homogeneity of the flow field was assumed in deriving the CBS response equations in Chapter III. Homogeneity could be jeopardized with too few grid rods. With these factors in mind, four rods (with five spaces) and the dimensions listed above were selected. The dimensions give  $M/d = (0.425/0.125) = 3.4$ . As will be seen below, values of  $r_{\text{CBS}}(0) = 0.10$  to  $0.19$ , depending on grid over-heat and location, were obtained in this study.

Another important theoretical factor which entered into the choice of a small scale test section is that the detector signal  $e$  of each arm of the CBS system increases with increasing  $\ell$ , the distance between the flow disturbance and the knife edge, as seen from Equation 3-35. Furthermore, it is necessary to keep  $\ell$  much larger than the flow region to avoid more heavily weighting disturbances furthest from the knife edge. From a practical standpoint, the small size was therefore convenient not only in terms of expense of materials and labor, blower and heater power requirements, but also in terms of CBS system size.

Once the grid mesh size was selected, determination of the test section length became a trade-off between obtaining an adequate region of isotropic flow (expected by  $x/M = 10$  to  $15$ ) and avoiding undesirable effects of too much turbulent boundary layer growth (namely, significant acceleration of the flow or modification of the grid-generated

turbulence). For these reasons the 2' length was employed allowing up to about 60 mesh lengths to be investigated.

### B. Crossed-Beam Schlieren

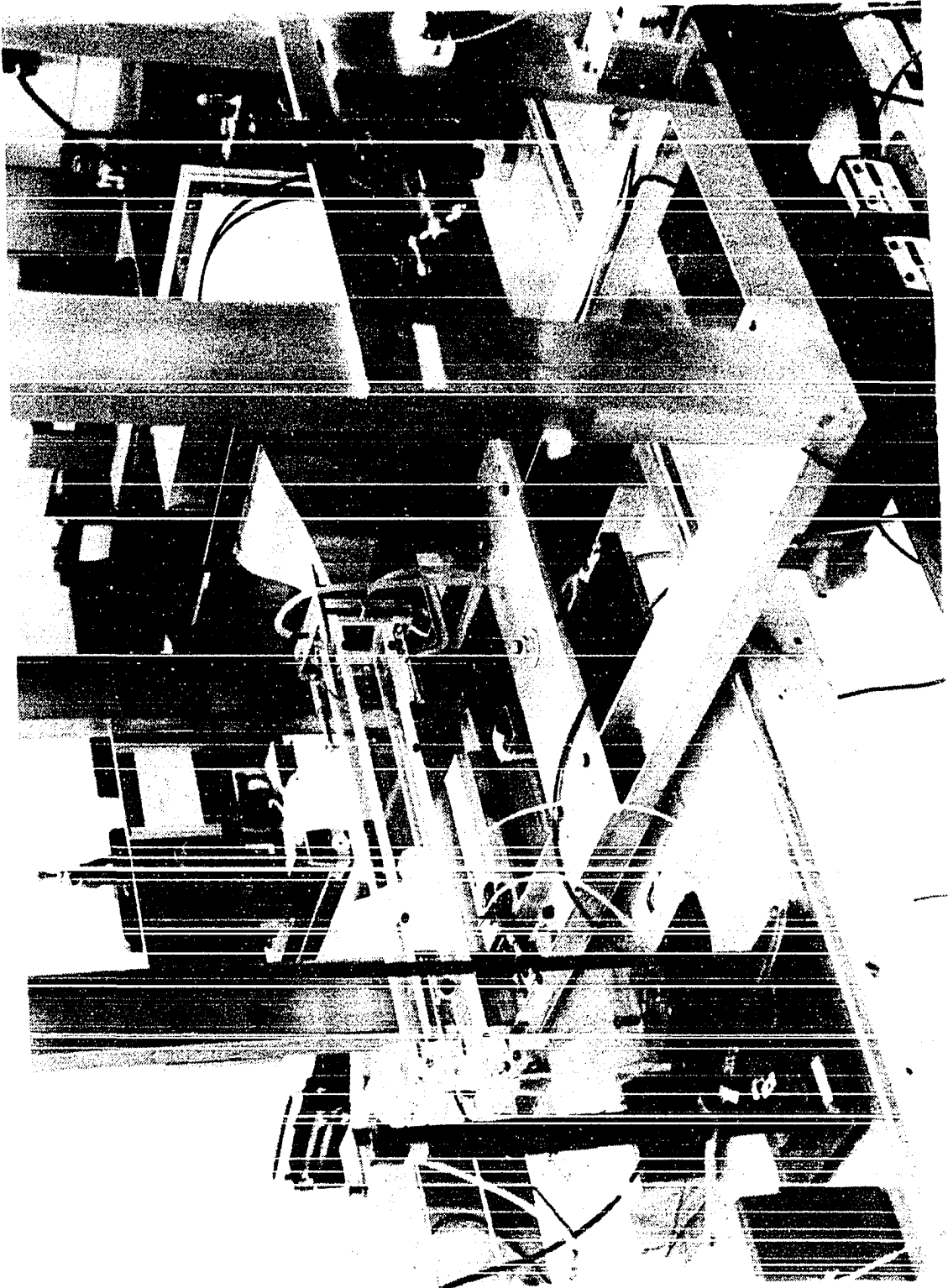
The crossed-beam schlieren instrument used in this study was shown schematically in Figure 1; it was modelled after the one used in Reference 52. Figure 11 is a photograph of the instrument in place around the wind tunnel test section. It consisted of an aluminum frame, lasers and mounts, knife edges and lens supports, detectors and detector housings, and laser and detector positioning tables.

Both arms of the CBS were supported on a frame constructed of 4" aluminum channel with welded joints. The frame was 42" square by 22" wide and was rigidly attached to a heavily constructed wooden bench. As can be seen in Figure 11, a rectangular hole was cut in the bench top to clear the vertical system laser head and its positioning support. Notice also that the test section has been deliberately located in one corner of the CBS frame to obtain a large  $\ell$  and, hence, maximal sensitivity. It was positioned so that  $\ell_A = \ell_B = 36"$  in Equation 3-43. With the arrangement shown, coarse movements of the beam intersection point along the longitudinal axis of the test section could be obtained by moving the entire tunnel along the bench while fine adjustments and single beam displacements could be accomplished using the positioning tables.

Two Spectra-Physics Model 133 helium-neon gas lasers provided circular, collimated light beams. Characteristics of the beam were



Figure 11. Crossed-beam schlieren



as follows:

Output power.....	2.0 milliwatts
Beam diameter.....	0.9 mm @ $1/e^2$ points
Wavelength.....	6328 angstroms (visible red)
Beam divergence.....	1.0 milliradians
Spatial mode.....	TEM <sub>00</sub>
Amplitude ripple.....	0.5% at 120 Hz

Warmup time recommended was about 15 minutes. Overall dimensions of the laser heads were 2.28" by 2.63" by 13.6". In this application coherency or phase matching of the laser radiation was unimportant; however, collimated or parallel rays were required. The TEM<sub>00</sub> mode of the plasma tubes provided a Gaussian-shaped intensity distribution across the beams as opposed to the more divergent but uniform distribution of "multimode" beams. L-shaped aluminum brackets were used to mount the laser heads to their positioning tables.

After traversing the test section, the laser beams were partially cut off by the straight sides of semi-circular knife edges cut from 0.006" brass shim stock. These knife edges were attached to small hollow aluminum cylinders in which 25 mm diameter, 85 mm focal length, double convex lenses were cemented to inner ledges. These units were inserted into larger receiving cylinders wherein they could be moved axially, rotated, and fastened to orient the knife edges at any cutting angle. (In practice the inner cylinders were positioned longitudinally so that the beam spot was somewhat out of focus to prevent local over-exposure to the photodiode detectors.) The cylinders were mounted over

an orifice in the mounting plate in which the detectors were centered but mobile up to 1/8" in any direction. Both detector assemblies were bolted to positioning tables.

The two detectors were E.G. and G. Electro-Optics Division Model SGD-160 silicon diffused pin photodiodes. These photodiodes offer an extremely rapid linear response up to on the order of 30 M Hz over an active area of 13 mm<sup>2</sup>. Figure 12 shows a circuit diagram of the photodiode hookup. Eveready No. 420, 22 1/2 volt, long-life batteries were used to provide a reverse bias across the photodiodes. Potentiometers were included simply to match the detector dc outputs at full beam illumination (no knife edge) during calibration and set-up. The entire photodiode circuits were isolated from their enclosures and their support plates.

Four miniature Model 500 milling tables manufactured by Mastercraft Engineering Co. supported and positioned the two laser heads and two detector assemblies on the CBS frame. These tables were relatively lightweight (15 lbs each) and provided calibrated indication of fine adjustments in increments of 0.001" over a travel of about 4" along two orthogonal axes. The 7" by 7" table tops were rotatable; however, this feature was not used.

Both laser heads and knife edges were masked to exclude multiple reflections of the beam image from surfaces of the test section walls.

### C. Hot-Wire Anemometer

The hot-wire anemometer system used in this study included a

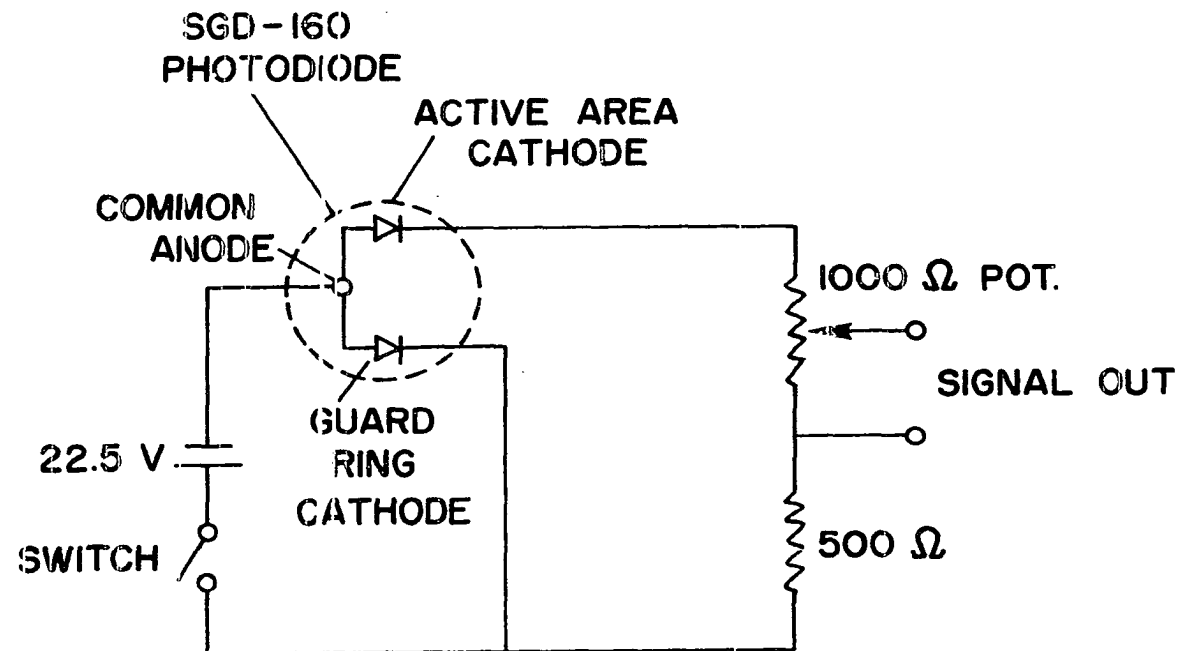


Figure 12. Photodiode circuit

Thermo-Systems Inc. Model 1050 constant temperature anemometer, Model 1051-2 monitor and power supply, and Model 1052 polynomial signal linearizer. The modular units were contained and interconnected in a single package which also contained a Model 1054A self-linearized anemometer as a second channel which was not used.

Frequency response of the 1050 was dc to 200 K Hz, far above the range of interest in this study. In fact, a built-in 100 K Hz low pass filter was applied for all measurements to reduce high frequency noise. In the constant temperature mode, wire resistance could be measured or set for control in 0.01 ohm steps. The 1050 had a constant current mode option in which a sensor could be operated at low overheat as a resistance thermometer. In this mode current could be adjusted between 0 and 10 ma.

For isothermal measurements the anemometer velocity signal was fed to the 1052 and linearized. An analog fourth order curve was applied by adjusting variable coefficients of each of four terms. Polynomial coefficients supplied by the manufacturer (for the particular sensor used and velocity range 0 to 30 ft/sec) were found to accurately linearize the calibration data as desired. The 1052 had zero setting and range span controls and was set up with a convenient 0 to 10 volt output.

A single hot-wire sensor supplied by T.S.I. and calibrated in the tunnel was used for all HWA measurements reported here. The sensing element consisted of a single platinum-plated tungsten wire 0.00015"

in diameter and 0.05" in length soldered to gold plated supports of a plug-in type probe tip. This sensor was denoted by the manufacturer as a Model 1210-T1.5 standard straight probe. It was used with a Model 1151-1 plug-in adapter to BNC support and 15' of coaxial cable.

#### D. Analog Signal Processing Electronics

Figure 13 is a block diagram of the data processing and analysis chain used in this study while Figure 14 is a photograph of the electronic apparatus test set-up. The set-up shown allowed reduction of all desired forms of CBS data when two channels were used and all forms of HWA data using one channel. Most of the electronic devices referred to in the block diagram are standard inventory in most laboratories, for example, a dc voltmeter, band-pass filters, ac amplifiers, an X-Y plotter, oscilloscope, and true RMS voltmeter. A more specialized instrument was the correlator and probability analyzer which will be described more fully along with the other items below. Amplification and correlation were essential ingredients for CBS data analysis. The variable filters were ac coupled (that is, they rejected any dc components to produce a zero mean value,  $\bar{E} = 0$ ), so only fluctuating signals were admitted beyond here. Of course, the scope was used where necessary to monitor signal characteristics at points other than those shown. Unfortunately, a research quality, two-channel F.M. tape recorder did not become available until after all of the data reported here had been obtained and reduced in real time.

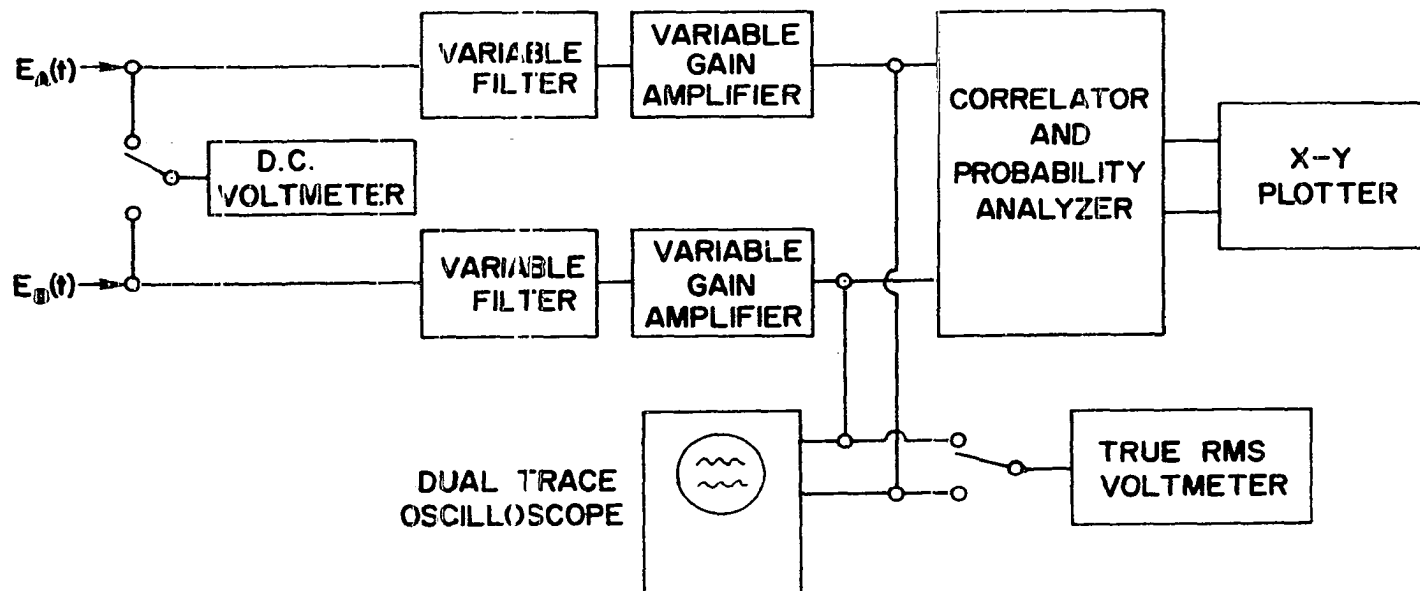
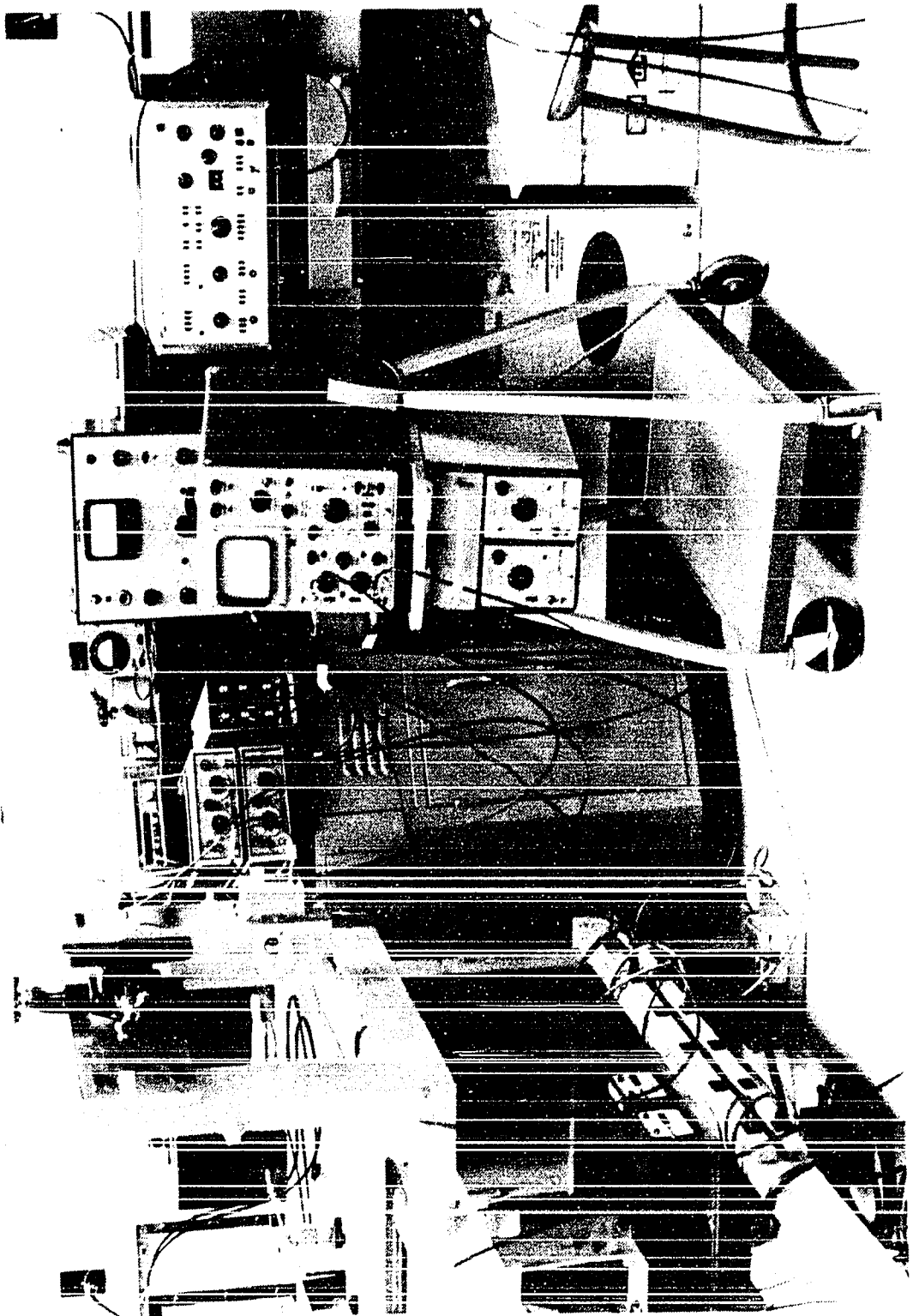


Figure 13. Analog signal measurement and analysis chain



Figure 14. Analog signal processing electronics



A DigiTec Model 2110 solid state digital multimeter was employed to measure dc volts on a "3 1/2 digit" display. On the  $\pm 1.999$  volt range its resolution was 0.001 volt with an accuracy of  $\pm (0.25\% \text{ reading} + 0.1\% \text{ full scale})$ .

Signals could be filtered with two matching Krohn-Hite Model 3550 solid state multifunction filters. These filters were operable in band-pass, band-reject, low-pass, or high-pass modes with cutoff frequencies independently and continuously adjustable between 2 and 200 K Hz (where all settings are referred to the -3dB points). A 4 pole Butterworth (maximally flat) response was used for all measurements. Other electrical specifications included a nominal 24 dB/octave attenuation slope, and  $0 \pm 1$  dB insertion loss (except for minimum band-pass with coinciding cut-off frequencies where it was -6 dB).

Two identical Ithaco 430 series solid state data acquisition amplifiers followed the filters. Amplification was controllable over -10 to 90 dB in steps of 1 dB. Six dB/octave high-pass filtering was available from 1 to 10 K Hz in decade intervals but the 1 setting was used for all measurements. These amplifiers featured a 100 K Hz bandwidth, low distortion, and 1% gain accuracy.

The heart of the analysis chain for CBS data analysis was a Model SAI-42A correlation and probability analyzer manufactured by Signal Analysis Operation, Test Instruments Division, of Honeywell, Inc. This all-digital, high-speed instrument provided on-line, real time computation in three operating modes, correlation (auto and cross),

probability (density and distribution functions), and signal enhancement (or recovery). The correlation and probability modes were used extensively while the signal enhancement mode was not used at all. In all modes 100 analysis points were computed, 100 time delay increments for correlation and 100 discrete amplitude levels for probability, and could be displayed as dc voltage levels either on the scope or X-Y plotter.

Other features provided by the correlator were sampling intervals from  $0.5 \mu \text{ sec}$  to 1 sec ( $0.1 \text{ sec}$  was used almost exclusively, occasionally  $50 \mu \text{ sec}$  or  $.2 \text{ ms}$ ) precomputation delay of 1500 sample increments  $\Delta\tau$  (for viewing the correlation on both sides of  $\tau = 0$  or far removed from  $\tau = 0$ ), a clipped correlation mode for rapid calculation of noisy signals, start-stop-resume control over averaging, a bin marker and selector switch (for precise location on the scope and readout on the dc voltmeter of any of the 100 coefficients in all modes), and exponential averaging (continuous averaging with memory updating from fresh data).

Operating controls on the correlator were divided into three categories, input, analysis, and computation and display. The input controls were ac-dc coupling switches and coarse and fine attenuators for both channels. The coupling used was invariably ac; however, the attenuators had to be adjusted prior to each computation to size the input signals to suit the correlator as described below.

Pertinent analysis controls were mode, channel, sample increment, and precomputation delay selector switches. The mode switches determined the type of computation (auto- or cross-correlation or probability density functions) while the channel selector determined which signal would be so analyzed or delayed in cross-correlation. A setting on the sample increment control determined the time interval between samples or sampling rate; this setting was therefore chosen according to the signal bandwidth to adhere to sampling theorem constraints (as covered below). Precomputation delay allowed selection of different ranges in  $\tau$  to be calculated and displayed.

The computation and display controls were summations and storage bin selectors, and read-out and start-stop-resume controls. In the correlation mode the summations selector determined the number of sums per coefficient linearly averaged (integrated) for each of the 100  $\Delta\tau$  values. This selection was analogous to choosing a particular R-C time constant on an analog integrator. In the probability mode the summations selector set the total number of level determinations to be entered in the 100 divisions of the histogram. For all data reported here the correlator was set to process 32,768 summations. While the sample increment control was set at 0.1 m sec, the record length was

$$T = 32,768 (0.1 \times 10^{-3} \text{ sec}) = 3.28 \text{ sec}$$

One extremely useful feature of this correlator was its resume control which would add an additional 32,768 summations to the previous result

stored in memory each time it was depressed. This capability was used extensively to retrieve low level correlations, particularly when obtaining points on the CBS  $\overline{\theta^2}$  spectra at high frequency.

The read-out control simply selected an appropriate memory readout rate for matching the oscilloscope or X-Y plotter.

A Hewlett-Packard Model 7044A X-Y plotter was used to plot functions calculated (and output as dc voltage levels) by the correlator. Pertinent performance specifications were:

Slewing speed to full scale.....	20 in/sec minimum
Acceleration (peak)	
Y-axis.....	1000 in/sec
X-axis.....	500 in/sec
Accuracy.....	$\pm 0.2\%$ full scale
Linearity.....	$\pm 0.1\%$ full scale
Overshoot.....	2% full scale

The author appreciates the fact that all of the above electronic instruments, as well as the CBS system components and hot-wire system were purchased new and first used in this study. Each instrument was carefully checked and found to meet the manufacturer's specifications.

The dual beam oscilloscope consisted of a Tektronix Type 561A cathode ray tube with modular Type 3A72 dual trace amplifier and Type 2B67 time base. A Bruel and Kjaer Type 2603 microphone amplifier served as a true rms voltmeter. On the voltmeter the meter switch was set to "rms slow" and the frequency response switch to "linear 2 to 40 K Hz" for all measurements. The crest factor was

$F_c = e_{\text{peak}}/e_{\text{rms}} = 5$  for the rms circuit.

All of the instruments described above except for the scope were isolated from ground; care was taken to disconnect the scope during data processing. Thus, the entire data processing chain was operated with a floating ground to avoid the creation of "ground loops." In addition, all connections between instruments were made with minimal lengths of newly constructed RG58 shielded coaxial cables.

#### E. Miscellaneous

A bare iron-constantan thermocouple was inserted into the tunnel from the diffusion chamber and positioned in the test section. Thermocouple voltages were converted to temperature readings by a Leeds and Northrup Co. Model 8692 temperature potentiometer which had automatic reference-junction compensation and a standard range scale Model 009 for -100 to 500°F. Experience showed that mean temperature measurements were repeatable to within about  $\pm 0.2^\circ\text{F}$ . Ambient temperature at the tunnel inlet was monitored on a Fisher Scientific mercury in-glass thermometer graduated in  $0.1^\circ\text{C}$  increments over 0 to  $50^\circ\text{C}$ . This thermometer was also used to check the thermocouple by water immersion.

The reference against which the HWA sensor was calibrated for velocity was a Dwyer Model No. 167-6, 1/8" diameter, pitot-static tube used together with a micromanometer graduated in increments of 0.001" of water. Manometer measurements were found to be repeatable to within  $\pm 0.004$ " of water.

For total pressure traverses a tube was bent from 1/16" O.D. hypodermic, stainless steel tubing and used with the manometer.

An aluminum rod passing through a special holder machined from brass round stock and secured with a set screw supported the HWA sensor in the test section. The holder was supported and positioned laterally by a steel rod which passed through special access ports in the test section removable sidewall. Lateral access was available at  $x/M = 12.7, 26.8, 36.2, 50.3,$  and  $64.4$ . These lateral parts were plugged when not in use.

A Konica 35mm single lens reflex camera with focal plane shutter exposed the photographs.

All of the data were reduced by hand on a Texas Instruments SR-50 10-digit miniature calculator except for the HWA mixed-mode data which were reduced on an IBM 360 computer. The Fortran program called a library subroutine to solve the three simultaneous "normal equations" for a quadratic least-squares curve fit.



## V. EXPERIMENTAL PROCEDURE

This section of the dissertation has been divided into three parts: Vibration Reduction Measures, Crossed-Beam Schlieren, and Hot-Wire Anemometer. Individually, the second and third parts encompass Instrument Calibration, Signal Processing, and Measurement Reliability. For the CBS system a basic signal study including a detailed breakdown and identification of signal and noise are presented in Chapter VI; however, since noise was less of a factor in the HWA system, it will be discussed here under Measurement Reliability. Equations necessary to convert voltage readings to physical quantities like velocity and temperature using experimental calibrations are included under Signal Processing. In general, all electronic devices described in the previous chapter were allowed to warm up for at least 1/2 hour prior to data procurement. The laboratory in which the test apparatus were set up was air conditioned and the ambient room temperature rarely varied more than  $\pm 1^{\circ}\text{F}$  from  $75^{\circ}\text{F}$ .

### A. Vibration Reduction Measures

It was expected and found out in practice that both arms of the CBS system were highly sensitive to vibration. There were three vibration paths into the supporting wooden bench: the floor, the flexible hose (because of steel spiral wire reinforcement), and directly by human contact. Vibrations of the bench were readily

transmitted to the CBS support frame and could cause relative oscillating displacements between the beams and knife edges. In addition, relative motions between the test section walls and CBS frame could refract the beams with the same effect, namely, spurious noise due to system vibration. Vibration of the test section could also be hazardous because the hot-wire sensor was supported by rods attached to the removable sidewall as described above. A number of special vibration reduction measures were therefore incorporated and are enumerated below.

1. The blower, exhaust stilling chamber, and connecting hose were isolated from the floor by 2" thick foam pads.
2. Rubber pads were inserted between the bench legs and floor.
3. The blower was "uncoupled" from the exhaust stilling chamber by a flexible duct tape connection. This same precaution was applied between the connecting hose and tunnel.
4. Rubber pads were installed between the bench and the frame with restraining bolts isolated from the bench by oversized holes, washers, and rubber pads to reduce high frequency transmission.
5. About 75 pounds of dead weight was added to the frame, nearly doubling the CBS system weight, to reduce low frequency oscillations (especially for the vertical system).
6. Care was taken not to bump the supporting structure during data acquisition.

These measures were effective in eliminating CBS and HWA noise pickup due to system vibrations as will be shown below by measurement.

## B. Crossed-Beam Schlieren

### 1. Calibration

Here we wish to determine the CBS sensitivities  $C_A$  and  $C_B$  in Equation 3-35 relating the photodiode voltage outputs  $e$  to the beam deflection  $\delta = \ell\phi$ . These sensitivities are required for use in Equation 3-43. Calibration is accomplished rather easily by moving the knife edges relative to their beams using the detector positioning tables. A traverse of the beam then yields a plot of  $\bar{E}$  vs  $\delta$  where the photodiode output  $\bar{E}$  is monitored on a dc digital voltmeter and  $\delta$  is recorded from the table setting.

Figure 15 shows the CBS calibration data for both horizontal and vertical systems. Several points are noteworthy. First, the lateral position of the curves along the  $\delta$ -axis is arbitrary depending on where  $\delta = 0$  (allowing full exposure of the beams on the photo-cells) happened to be set. Next, the  $\bar{E}$  corresponding to  $\delta = 0$  was about -0.660 volt for both beams after passing through the test section plexiglass side-walls which attenuated the full output available because of reflections. Actually, the full dc signal available from the diodes was about -0.700 volts including test section attenuation; however, this value was trimmed-down to -0.660 using potentiometer adjustments to allow a safety margin of reset adjustment to account for variations in dc output as the test section was traversed longitudinally. It can be seen

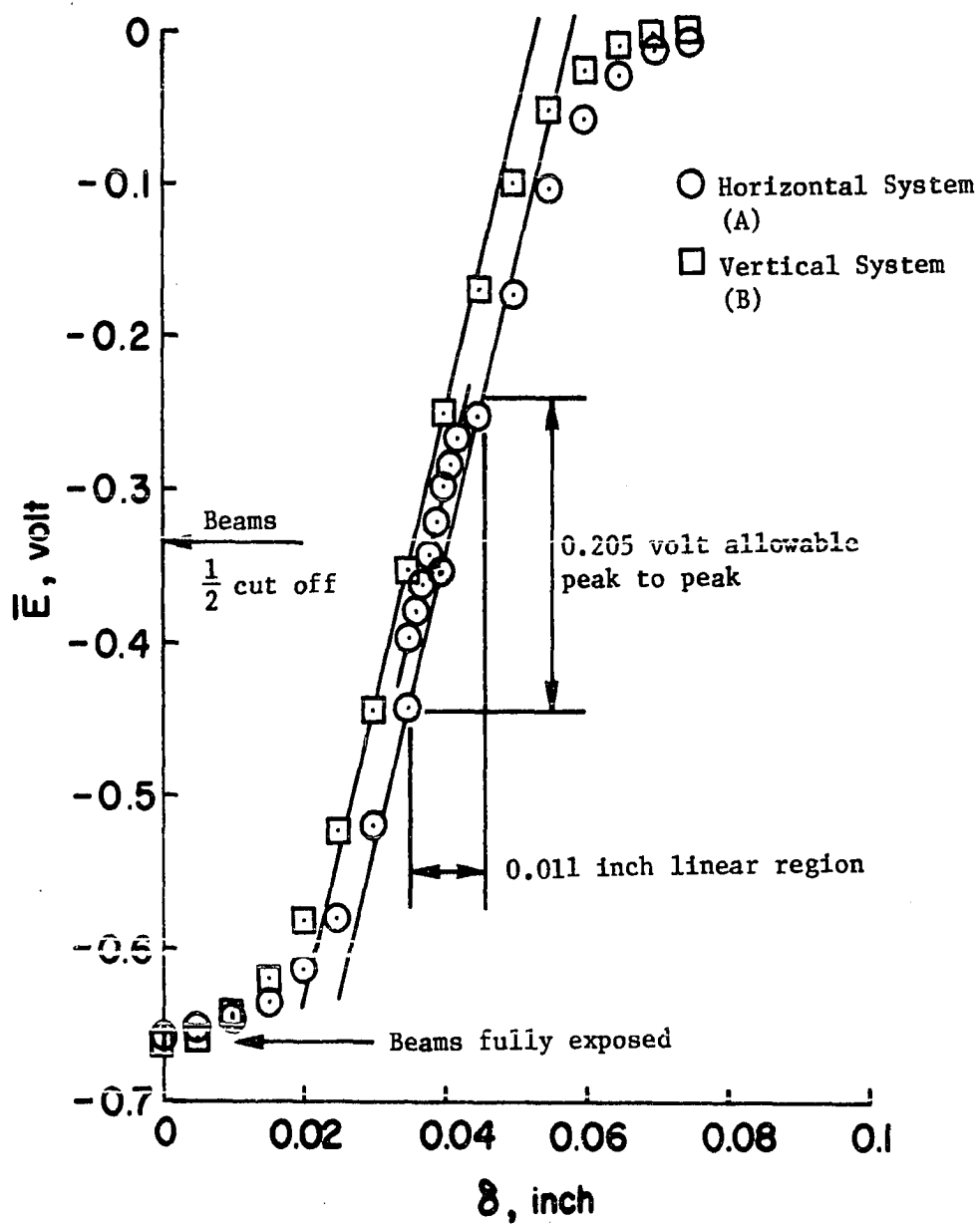


Figure 15. Crossed-beam schlieren calibration;  
 $d\bar{E}/d\delta = 18.9$  volt/inch

that by setting the same overall dc output for both systems, approximately equal sensitivities were obtained.

Notice that the calibration curves of Figure 15 are actually S-shaped with an approximately 0.010" linear region in  $\delta$  corresponding to an allowable peak-to-peak excursion of the photodiode output of about 0.200 volt. The ranges in  $\bar{E}$  and  $\delta$  for which the system response is linear are approximately centered about the position where the beam is half cut off. The nonlinear tails occur only because we are cutting a circular area of the beam with a straight knife edge. As a check on the maximum signal to be encountered under operating conditions, a measurement at the nearest grid position used,  $x/M = 6.78$ , and nearly the highest grid overheat,  $\Delta = 47^\circ\text{F}$ , gave

$$\overline{e_A^2} \approx \overline{e_B^2} = \overline{e^2} = 3.42 \times 10^{-4} \text{ (volt)}^2$$

Therefore,

$$e' = 1.85 \times 10^{-2} \text{ volt}$$

and

$$e_{\text{peak to peak}} \approx 6e' = 0.111 \text{ volt}$$

which is well within the dynamic range limit of 0.200 volt.

To assure accurate determination of the CBS sensitivity in the  $\bar{E}$  operating region, closely spaced data points were obtained as shown. This calibration was checked periodically throughout the testing interval of about six months and found not to change appreciably. Thus, the value

$$C = C_A = C_B = 18.9 \text{ volt/inch}$$

was used for both beams for all data reduction. '

## 2. Signal processing

a. Mean square or rms levels      The objective of this section is to describe the test procedures used to obtain CBS measurements of  $\overline{\theta^2}$  or  $\theta'$  for given  $x/M$ ,  $\overline{U}$ , and  $\Delta$  conditions in heated flow. Once data were recorded, the pertinent equations were (3-43), (3-52), and (3-54) as will be seen.

During the warm-up period, one beam was positioned at the desired  $x/M$  location by external measurement. The test section sidewall was then removed and the beams were crossed by merging the two red laser spots on an opaque surface. After the warm-up period the dc outputs of the diodes with full illumination were read and adjusted if necessary to -0.660 volt using the photodiode potentiometers. Then the beams were cut with the knife edges until the dc outputs were -0.330 volt (so that the beams were 1/2 cut off). With the tunnel running, a desired speed was set on the flow control tube. Ambient temperature was then recorded from the thermocouple potentiometer after standardization and from the thermometer. Next, a desired power was set on the variac and the temperature rise was monitored on the potentiometer until it stabilized at a desired grid overheat  $\Delta$ .

To prepare the signal processing electronics for data acquisition, the band-pass filters were set. Then, the amplifiers and input

attenuators of the correlator were mutually adjusted to provide little or no clipping of the signal peaks as observed from repeated calculation and display of the probability density function of both channels. These adjustments were necessary prior to each calculation to obtain accurate results with the correlator. Final positions of the correlator analysis and computation and display controls were set and a cross-correlogram was calculated by depressing the start control. If necessary, the resume control was depressed N times and the number N + 1 was recorded for data reduction. For calculation of  $\overline{\theta^2}$  the value of the cross-correlogram at  $\tau = 0$ , say v volts, was observed on the scope and read out on the dc voltmeter. This correlogram computation was then twice repeated for a total of three v determinations recorded and averaged for each data point. Next, single beam autocorrelations were computed and three  $\tau = 0$  voltage levels recorded and averaged for determination of  $r_{\text{CBS}}(0)$ .

A single calculation was required to obtain the actual cross-correlation level of the input signals knowing v for any  $\tau$ ,

$$\begin{aligned} Q_{AB}(\tau) &= \overline{e_A e_B}(\tau) \\ &= \frac{v}{125(N+1)} \frac{[10^{(dB_A + dB_B)/20}]_{\text{atten.}}}{[10^{(dB_A + dB_B)/20}]_{\text{ampl.}}}, (\text{volt})^2 \end{aligned} \quad (5-1)$$

where 125 is the correlator gain. For autocorrelation, Equation 5-1 also applied provided  $dB_A = dB_B$ .

Returning to our  $\overline{\theta^2}$  calculation, if we combine Equations 3-43 and 3-52 assuming  $C_A = C_B = C$ ,  $\ell_A = \ell_B = \ell$ ,  $\alpha = \text{constant}$ ,  $N_o = 1$  and  $\xi = 0$  then

$$\rho' = \left( \overline{\rho^2} \right)^{1/2} = \frac{[\overline{e_A e_B} (\tau = 0)]^{1/2}}{(2\pi)^{1/2} C \ell \alpha}, \quad \frac{\text{lbm}}{\text{ft}^3} \quad (5-2)$$

Using this together with Equation 3-54 we can obtain  $\theta'$  since

$$\theta' = \left( \overline{\theta^2} \right)^{1/2} = \frac{\overline{\theta}}{\overline{\Gamma}} \rho', \quad ^\circ\text{F or } ^\circ\text{R} \quad (5-3)$$

where the term  $\overline{\theta}/\overline{\Gamma}$  essentially converts units. Equations 5-2 and 5-3 were combined with  $C = 18.9 \text{ volt/in} = 226.8 \text{ volt/ft}$  from Figure 15,  $\ell = 3 \text{ ft}$  as measured, and the assumptions of  $\alpha = 0.243 \frac{\text{cc}}{\text{g}} = 3.894 \times 10^{-3} \text{ ft}^3/\text{lbm}$ ,  $\overline{\Gamma} = 0.0765 \text{ lbm/ft}^3$ , and  $\overline{\theta} = 58.8^\circ\text{F} = 518.8^\circ\text{R}$  to get

$$\theta' = 1021 [\overline{e_A e_B} (\tau = 0)]^{1/2}, \quad ^\circ\text{F} \quad (5-4)$$

This completes the procedure and equations used to obtain CBS temperature fluctuation decay data or  $\theta'$  as a function of  $\Delta$  and  $x/M$ .

b.  $\overline{\theta^2}$  spectra We wish to obtain plots of CBS three-dimensional temperature spectra

$$E_\theta(f) = \frac{\overline{\theta^2}(f, B)}{B}, \quad \frac{(^{\circ}\text{F})^2}{\text{Hz}} \text{ vs } f, \text{ Hz} \quad (5-5)$$

The notation  $\overline{\theta^2}(f, B)/B$  implies  $\theta$  has been band-pass filtered, squared, averaged, and normalized per Hz by the filter bandwidth  $B$  over the frequency range of interest to produce a power spectrum as discussed by Bendat and Piersol (7). Now, to get (5-5) consider (5-2) rewritten



with the same assumptions and  $\tau = 0$  implicit as

$$\frac{\overline{\rho^2(f, B)}}{B} = \frac{\overline{e_A e_B}(f, B)/B}{2\pi(C\ell\alpha)^2} \quad (5-6)$$

Using this and (3-54) again, we obtain

$$E_\theta(f) = \frac{\overline{\theta^2(f, B)}}{B} = \left[ \frac{\overline{\theta}}{\overline{\Gamma}} \right]^2 \frac{\overline{e_A e_B}(f, B)/B}{2\pi(C\ell\alpha)^2} \quad (5-7)$$

This says that the desired spectrum is proportional to the real part or co-spectral density function of the CBS cross-spectral density function, namely,  $\overline{e_A e_B}(f, B)/B$  (see Reference 7).

The procedure necessary to obtain the CBS co-spectrum is, therefore, to (1) filter individually each of the CBS detector outputs with narrow band-pass filters using the same center frequency and bandwidth, (2) multiply the instantaneous filtered outputs (with no phase shift), (3) average this product over the record length, and (4) divide the result by B. As the center frequency of the band-pass filters was swept across the frequency range of interest, a graph of  $E_\theta(f)$  vs  $f$  could therefore be obtained. While the technique of obtaining a co-spectrum from two related signals is hardly novel, its application to acquisition of CBS 3-D scalar spectra is believed to have been initiated in this study. Previous investigators (52 and 22) have suggested direct Fourier transformation of the CBS covariance given by Equation 3-46 to obtain the CBS spectrum; however, such procedure requires a high time delay resolution of the covariance and the shape of the resulting spectrum is known to be highly sensitive to the

precise covariance shape. It may be noted in passing that a rough estimate of the dominant or peak frequency of a co-spectrum may be estimated from its covariance plot as

$$f_p = \frac{1}{4\tau_c} \quad (5-8)$$

where  $\tau_c$  is the time delay of first zero crossover. Equation 5-8 is exact for two periodic, in-phase signals in which case the covariance plot is periodic (and symmetric about  $\tau = 0$ ) with the same frequency  $f_p$ , while the co-spectrum is an impulse at  $f_p$ .

In practice to obtain the CBS  $\overline{\theta^2}$  spectra for given  $x/M$ ,  $\overline{U^2}$ , and  $\Delta$  conditions, the same procedure described in a. above was followed except that the filters were manually tuned to pass-bands centered on the 1/10 decade points. That is, the center frequencies  $f_n$  were

$$f_n = f_o (10)^{n/10} \quad n = 0, 1, \dots, 10 \quad (5-9)$$

where  $f_o$  is 10 to any power, and were therefore equally spaced on a base 10 logarithmic scale. The actual upper and lower filter settings chosen were

$$\begin{aligned} (f_n)_u &= f_o (10)^{(2n+1)/20} \\ (f_n)_l &= f_o (10)^{(2n-1)/20} \end{aligned} \quad (5-10)$$

so that

$$\frac{(f_n)_u}{(f_n)_l} = (10)^{1/10} = 1.26 \quad (5-11)$$

and

$$B = (f_n)_u - (f_n)_l \quad (5-12)$$

This selection yields progressively larger bandwidths  $B$  with increasing frequency as summarized in Table 1 for the case  $f_o = 1$ .

Table 1. Band-pass filter settings for spectral analyses

$f_n$	$(f_n)_l$	$(f_n)_u$	$B$
1.00	0.891	1.12	0.229
1.25	1.12	1.41	0.29
1.60	1.41	1.78	0.37
2.00	1.78	2.24	0.46
2.50	2.24	2.82	0.58
3.15	2.82	3.55	0.73
4.00	3.55	4.47	0.92
5.00	4.47	5.62	1.15
6.30	5.62	7.08	1.46
8.00	7.08	8.91	1.83
10.00	8.91	11.2	2.29

Our results will show that the frequency range of interest in this study was from dc up to about 2000 Hz.

Figure 16 is presented to demonstrate the equivalence of the filter roll-off rate of 24 dB/octave and the roll-off of the spectrum of a pure tone. This area normalized power spectrum was obtained by sweeping the filters through a 120 Hz pure tone with  $\overline{e^2} = 0.090 \text{ volt}^2$  (provided by an audio generator) in the same manner as for all spectra measured and as described above the the CBS  $\overline{\theta^2}$  spectra. It shows that

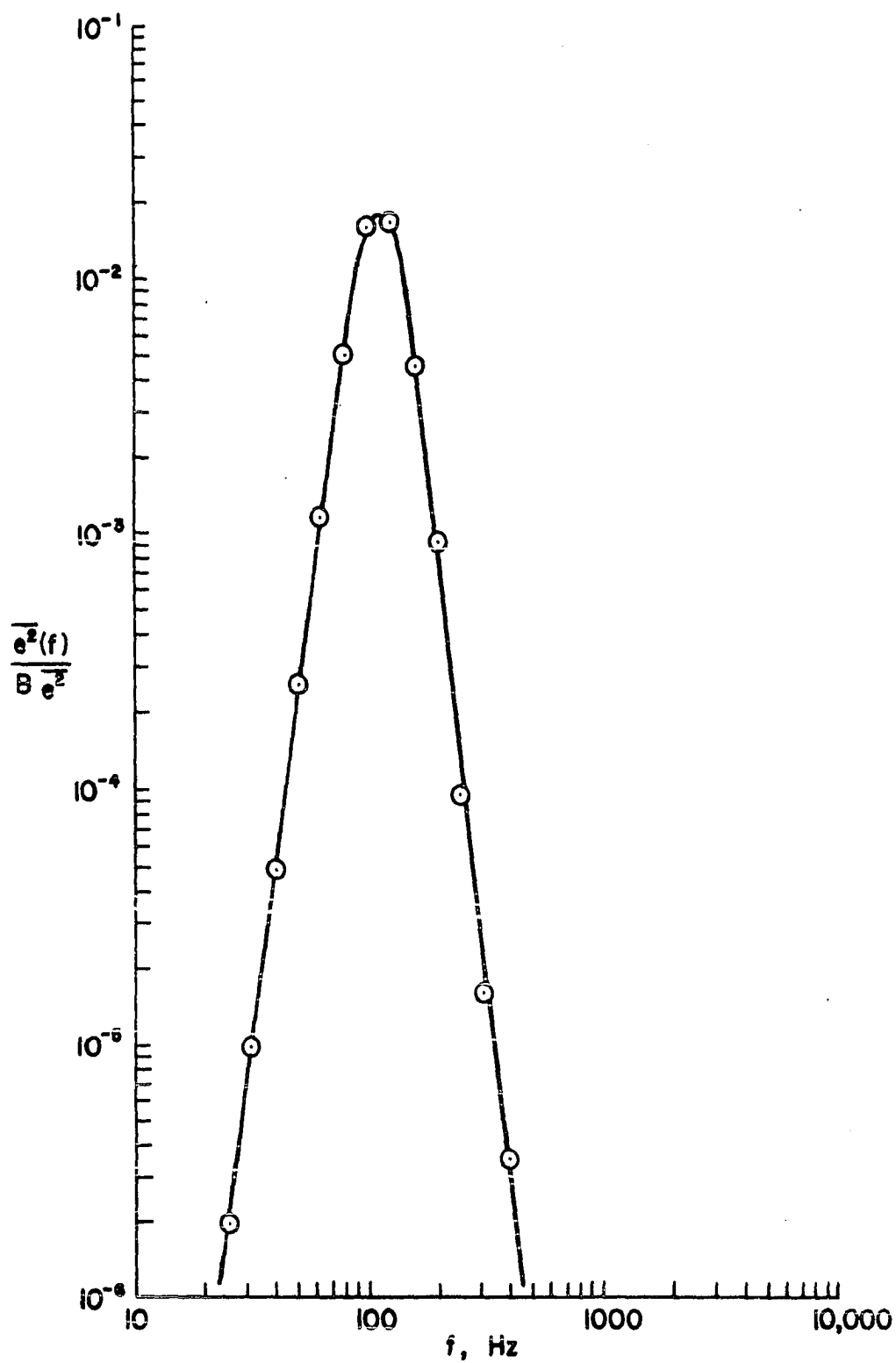


Figure 16. Pure tone (120 Hz) spectrum produced by method of Chapter 5  
 $(\overline{e^2} = 0.090 \text{ volt}^2)$

when sweeping the filters through the 1/10 decade settings a spectral "spike" appears as a "tent" with sides rolling-off at 24 dB/octave. This is the steepest slope obtainable with these filters.

It was unfortunate that a spectrum analyzer was not available which could more rapidly compute the desired spectra and co-spectra because the above procedure was relatively time consuming. Each spectrum estimated required approximately 1/2 hour. As a result some drift in grid overheat, up to 5°F at a high overheat such as  $\Delta = 45^\circ\text{F}$ , was tolerated. Another solution would have been to tape record several minutes of data or form a tape loop using an even shorter record for processing in either way.

Part of the reason for the long analysis time was that the "resume" control on the correlator was used to advantage to bring out the correlations. For frequencies below about 800 Hz,  $N = 4$ ; above,  $N = 9$ .

c. Convection speed      The same set-up was used to obtain CBS space-time correlations, from which eddy convection velocities may be obtained as discussed in References 52 and 22. At given  $x/M$ ,  $\bar{U}$ , and  $\Delta$  conditions, a cross-correlogram was plotted for crossed beams  $\xi = 0$  which peaked at  $\tau = 0$ . The horizontal beam system was then displaced a small increment, for example,  $\xi = 0.05''$  and another correlogram (with the upstream beam signal delayed in  $\tau$ ) plotted. Now the peak had shifted in  $\tau$  reflecting beam separation and convection. This peak was accurately located in  $\tau$  and read out through use of the bin marker switch. Repetitions of this process at progressively larger separations until

no cross-correlation signal was discernible (indicating the convected thermal eddy had vanished) produced a sequence of space-time correlograms as desired.

### 3. Measurement reliability

This subdivision consists of three parts, sources of error, signal statistics, and repeatability. However, the errors discussed fall into either of two general categories, systematic or random, where systematic errors are those which can be theoretically eliminated by calibration or some form of compensation, and random errors or noise can be reduced by such factors as good design and averaging processes, but generally not eliminated. The first part enumerates possible errors of both types, while the remaining two parts deal exclusively with random errors by definition.

a. Sources of errors      When the CBS system is in operation measuring scalar fluctuations in terms of mean square values or spectra, it is measuring eddy fluctuations at a point. However, as has been seen, the signal at each detector contains contributions due to eddies over the entire path of its respective beam. Thus, for point measurements, most of the signal at each detector is noise. It is the cross-correlation technique which recovers the common information buried in noise on both signals. This technique has been known and used for some time, particularly in the Radar field (see References 7 and 37).

While the (uncorrelated) noise composed of electronic noise and

flow noise will effectively cancel out in the cross-correlation operation, there are some types of noise which are well-correlated between detector signals and these must be eliminated or dealt with by the experimenter. It is conceivable that a common signal could be induced via an electrical (ground) coupling between the detectors; however, we have precluded this by purposely isolating them. In this study, one (and we believe the only appreciable) source of correlated noise was the beam power intensity ripple at 120 Hz due to incomplete smoothing or filtering of the lab 60 Hz ac during rectification in the laser power supplies. A check showed that this ripple was approximately 0.5% of the detector dc output in agreement with the manufacturer's specifications; but, this relatively small power ripple constituted a non-negligible part of the CBS cross-correlation within the 20 to 2000 Hz frequency range of interest here and is fully discussed, separated, and successfully corrected for in results presented below. In another study (22) this problem was successfully circumvented by high-pass filtering since the interesting part of the spectrum was much higher than 120 Hz.

Another possible source of systematic errors may have been violation of any of the necessary assumptions such as homogeneity and isotropy of the velocity field, small fluctuations in both velocity and temperature, and a perfect gas relationship between  $\rho$  and  $\theta$  at constant pressure. While grid-generated turbulence may approach isotropy as close as any other flow, the assumption is non-exact, the

usual result being  $u' > v'$  (see Reference 32). An evaluation was not made of nearness to isotropy of the velocity field using, for example, an "X-probe" and two channels of the HWA to verify that the off-diagonal terms of the Reynolds stress tensor were indeed zero or that  $u' = v' = w'$ . However, a test using the CBS was performed and roughly confirmed isotropy of the scalar field. It is believed that the velocity fluctuations were generally small enough ( $u'/\bar{U} < 0.03$ ) sufficiently far downstream of the grid to warrant the linearized approximation used in deriving HWA response equations. But, for the temperature field it is possible that this assumption may have been stretched at the higher overheats which, while providing the desired maximum signal for the CBS, may have taxed the resistance thermometer capability. In taking logs and differentiating both sides of the perfect gas law to obtain Equation 3-54, we assumed

$$\frac{p}{\bar{p}} \ll \frac{\rho}{\bar{\rho}} + \frac{\theta}{\bar{\theta}} \quad (5-13)$$

where  $p \approx dP$ ,  $\rho \approx d\bar{\rho}$ , and  $\theta \approx d\bar{\theta}$ . Hinze gives

$$p' = 0.7 \bar{\rho} u'^2 \quad (5-14)$$

If we assume  $\bar{\rho} = 0.0765 \text{ lbm/ft}^3$ , and  $u' = 0.03\bar{U} = 0.03(9 \text{ ft/sec}) = 0.27 \text{ ft/sec}$  then (5-14) gives

$$\begin{aligned} p' &\approx \frac{0.7(0.0765 \text{ lbm/ft}^3)(0.27 \text{ ft/sec})^2}{32.2(\text{lbm ft/lbf sec}^2)} \\ &\approx 1.21 \times 10^{-4} \text{ lbf/ft}^2 \end{aligned}$$



We might expect for a Gaussian distribution of pressure fluctuations,  $p_{\text{peak to peak}} \approx 6p' = 7.27 \times 10^{-4}$  psf, so the term on the left-hand-side of (5-13) is of the order  $10^{-3}/2000 = 0.5 \times 10^{-6}$  which is certainly several orders of magnitude less than our results for  $\rho/\bar{T}$  ( $\approx 2 \times 10^{-3}$ ) and surely  $\theta/\bar{\theta}$  as well. Thus, (5-13) is probably a reasonable assumption.

Due to the long processing times involved in measuring  $\overline{\theta^2}$  spectra, a slow increase in grid overheat usually occurred. This effect was worst at the higher overheats, say,  $\Delta = 50^\circ\text{F}$  where  $\Delta$  might drift upward about  $5^\circ\text{F}$  over a period of one-half hour. Such an increase would tend to produce spectral levels higher than actual with increasing frequency. However, measurements of overall signal level generally showed insignificant changes and, therefore, this possible source of systematic error was deemed small. It was not a problem in obtaining overall  $\theta'$  levels due to the far shorter data acquisition times.

Other examples of potential sources of systematic errors might have been fluctuation levels greater than the linear limits of the CBS calibration or not having the beams precisely crossed which would cause a reduction and shift of the cross-correlogram peak in  $\tau$ . However, we have shown that even the highest CBS fluctuations were well-within the linear range; and, experience showed that the beams could be crossed at least to within the equivalent of  $\Delta\tau = 0.1$  m sec, that is, within one sample increment with a little care.

Potential sources of random errors in the CBS signals were vibration of the supporting structure, electronic noise, and effects due to absorption and/or scattering of light from particulate matter in the flow. We will see that the effects of vibration and/or electronic noise were measurable but very small, and no effects of absorption/scattering were discernible.

b. Signal statistics      The four main types of functions used in the analysis of random data are mean square or rms values, probability density functions (pdf), auto- or cross-correlation functions, and power or cross-power spectral density functions, all of which have been estimated at some time in this study. Bendat and Piersol (7) provide a comprehensive discussion of the assumptions requisite in data records for valid estimates of these parameters, namely, randomness, stationarity, and normality. They offer formal, yet practical, tests for these basic characteristics. As a minimum, all of the data analyzed in this study has been visually inspected to confirm presence of the three basic characteristics as will be shown in brief here for the CBS data and later for the HWA data. Furthermore, it was assumed that the statistical parameters evaluated by time averaging a single record of the process were equivalent to those which would have resulted from ensemble averaging of many records (ergodic hypothesis).

Since the data processing electronics were ac coupled, the signals were automatically detrended to zero mean value. Evidence for at least weak stationarity was provided by the observation that rms values and

autocorrelations of the signals were found not to change significantly during continuous or repeated calculation for fixed flow conditions. It appeared that changes in these parameters were within the expected uncertainty limits and, therefore, due only to sampling variations. Also, the minimum sample duration of 3.28 sec was very long compared to the random fluctuations.

To test for randomness the data were searched for the presence of sinusoids due to periodic components. While the 120 Hz laser ripple was observable in the CBS spectra, especially for low overheats, its effect in the composite signal was not enough to produce the characteristic dished-out shape of single beam pdf's, nor to produce the characteristic ringing (periodic oscillation at the dominant frequency) of either the auto- or cross-correlations at reasonable grid overheats.

Numerous computations of single beam pdf's (required to set-up the correlator) showed them to be approximately Gaussian in shape; this lends strong support to the assumption of normality.

Reference 7 also includes a theoretical treatment of the statistical errors associated with estimates of the four statistical functions listed above. Record length, of direct importance to statistical accuracy, as well as sampling rate requirements, are given. Statistical errors were developed in terms of a parameter  $\epsilon$  called the "normalized standard error" of the estimate. For each function,  $\epsilon^2$  is the variance of the estimated values divided by the square of the true value.

Since cross-correlation was the key parameter in analysis of CBS data, we will compute  $\epsilon$  for this case as an example. If  $\hat{Q}_{AB}(\tau)$  is the sample cross-correlation estimate and  $Q_{AB}(\tau)$  is the true value, then for the ideal case of band-limited white noise (a perfectly flat spectrum) within the signal bandwidth  $B$

$$\epsilon^2 = \frac{\text{Var}[\hat{Q}_{AB}(\tau)]}{Q_{AB}^2(\tau)} \approx \frac{1}{2BT} \left[ 1 + \frac{Q_A(0)Q_B(0)}{Q_{AB}^2(\tau)} \right] \quad (5-15)$$

or

$$\epsilon^2 \approx \frac{1}{2BT} \left[ 1 + \frac{1}{r_{AB}^2(\tau)} \right] \quad (5-16)$$

where  $T$  = record length and  $r_{AB}(\tau)$  is the correlation coefficient. Note that for a given  $r_{AB}$ ,  $\epsilon$  is proportional to  $(2BT)^{-1/2}$ .

For the case of  $N + 1 = 1$  on the correlator in the cross-correlation mode we found  $T = 3.28$  sec. Then, using typical values stated above of  $r_{AB}(0) \approx 0.15$  and  $B \approx 2000$  Hz for the CBS  $\theta'$  data, we obtain from (5-16)  $\epsilon \approx 0.06$ . This number is ambiguous in that for low level correlations, longer record lengths were analyzed using the "resume" control.

Cross-correlation was also required to reduce CBS  $\theta^2$  spectral data as shown above. However, in this case data were filtered to as narrow a bandwidth as about  $B = 5$  Hz for the lowest center frequency  $f = 20$  Hz (see Table 1). Since Equation 5-16 still applies, evidently  $\epsilon$  is higher for points estimated near the low end of the spectrum where  $B$  is smallest; so there is more statistical uncertainty for data points

with decreasing frequency.

Another measure of statistical accuracy is the number of statistical degrees of freedom  $n$  where

$$n = 2BT \quad (5-17)$$

It can be shown that the number of statistically independent discrete samples required to describe a data record of bandwidth-limited Gaussian white noise is  $2BT$ . For the CBS  $\theta'$  data

$$n = 2(2000)(3.28) = 13,120 \text{ samples}$$

which is well below the 32,768 summations performed by the correlator (at each  $\tau$ ).

Combining (5-16) and (5-17) we see that

$$\epsilon \sim \frac{1}{(2BT)^{1/2}} \sim \frac{1}{(n)^{1/2}} \quad (5-18)$$

The important general conclusion to be observed is that to improve the accuracy of an estimate (or reduce  $\epsilon$ ) one may increase the number of samples or the record length consistent with the available data and stationarity.

The correlator was essentially a special purpose digital computer which included analog to digital conversion on input, and digital to analog on output. Since it digitized the data records by sampling, the Nyquist sampling theorem had to be obeyed to avoid aliasing, that is, ambiguity as to whether the sampled values represent higher or lower frequencies than those actually present. Aliasing in this sense is only a problem if the time interval between samples  $\Delta t$  is too large.

The Nyquist theorem states that the sampling rate S.R. should be at least twice the highest frequency of interest (in other words, two samples per cycle are necessary for proper interpretation) or

$$\text{S.R.} \geq 2f_N \quad \text{where} \quad \text{S.R.} = \frac{1}{\Delta t} \quad (5-19)$$

Thus, we desire a sample increment

$$\Delta t \leq \frac{1}{2f_N} \quad (5-20)$$

to prevent aliasing. (The correlator manual suggested starting with  $\Delta t = 1/10f_N$  for a first look.) Bendat and Piersol (7) suggest low-pass filtering the data at  $f_N$  as an added precaution. In this study for the  $\theta'$  data  $f_N = 2000$  Hz, thus,  $\Delta t = 0.25$  m sec. As stated above, we used  $t = 0.10$  m sec or 10,000 samples per second almost exclusively, and the data were filtered above 2000 Hz so that  $\Delta t = 1/5f_N$ .

The measured frequency range of dc to 2000 Hz is well-within the CBS convective or spatial resolution. Small eddy sizes of the order of a beam diameter ( $d = 1$  mm) can be properly resolved. Therefore, the CBS frequency resolution for a given mean speed is

$$\begin{aligned} f_{\max} &\approx \frac{1}{T_{\min}} = \frac{\bar{U}}{d} \\ &= \frac{\bar{U}}{(1 \text{ mm})(3.28 \times 10^{-3} \text{ ft/mm})} \end{aligned}$$

c. Repeatability      Repeatability of the CBS data obtained in this study has been confirmed and used to reduce random errors. For

the  $\theta'$  data, at each test point, results from three repeated calculations were averaged to produce a point on the graph. Uncertainty limits will be shown on the CBS  $\theta'$  data when presented. Also, several reruns were performed to check and assure repeatability of this data. For the  $\overline{\theta^2}$  spectra, each spectrum presented has been measured at least twice in real time. Single beam spectra were measured using both the true rms voltmeter and correlator to compute  $\overline{e^2}$  as a cross-check on the accuracy of results. In one case, a CBS  $\overline{\theta^2}$  spectrum was measured three times with a day and then with over two months separating the respective measurements; the results showed excellent repeatability and stability of the CBS calibration and data processing procedure.

A natural and important check on any spectrum is provided by its definition. In the case of our CBS 3-D  $\overline{\theta^2}$  spectra, Equation 3-19 defines  $E_\theta(k)$ ; an equivalent expression for  $E_\theta(f)$  is

$$\overline{\theta^2} = \int_0^\infty E_\theta(f) df = \int_0^\infty \frac{\overline{\theta^2}(f,B)}{B} df \quad (5-21)$$

Now  $\overline{\theta^2}$  can be separately measured by band-pass filtering both detector signals 20 to 2000 Hz as described above for a total or overall mean square temperature; then the filtered data  $\overline{\theta^2}(f,B)$  can be summed for comparison. As an example for the conditions  $x/M = 17.4$ ,  $\bar{U} = 8.5$  fps, and  $\Delta = 34^\circ\text{F}$ , this check is presented on voltage for convenience (volts and  $^\circ\text{F}$  were related by Equation 5-4). The overall signal (filtered 20 to 2000 Hz) gave  $(\overline{e_A e_B})_0 = 1.90 \times 10^{-6} \text{ volt}^2$ ; summing the spectrum (over 20 to 2000 Hz) gave  $(\overline{e_A e_B})_s = \Sigma(\overline{e_A e_B})_n = 2.12 \times 10^{-6} \text{ volt}^2$ . Thus, the

deviation was

$$\frac{(\overline{e_A e_B})_s - (\overline{e_A e_B})_o}{(\overline{e_A e_B})_o} = 0.12$$

The pure tone spectrum of Figure 16 may be checked in the same way. Its overall signal was  $(\overline{e^2})_o = 0.090 \text{ volts}^2$  (for a band-pass of 20 to 2000 Hz); summing the spectral data (from 20 to 2000 Hz) gave  $(\overline{e^2})_s = 0.108$ . So,

$$\frac{(\overline{e^2})_s - (\overline{e^2})_o}{(\overline{e^2})_o} = 0.20$$

This deviation is discussed by Sandborn (44) and occurs not so much because of poor repeatability but rather because we have not used corrected filter bandwidth settings to account for the non-rectangular filter shape. The settings used were those of Table 1 and determine the -3 dB points of the actual filter shape as specified by the manufacturer. A method of correcting for this effect is to determine an "effective filter bandwidth" in the manner described by Sandborn and done by Corrsin and Uberoi (17) which would have resulted in narrower settings about each center frequency. An error of higher overall level results from this effect but not in spectral shape. Sandborn (44) takes up another effect which tends to decrease the effective bandwidth at high frequencies. The latter problem arises when the turbulence spectrum rolls-off faster than the filter and, therefore, acts as its high frequency cutoff.



### C. Hot-Wire Anemometer

This section will include calibration, signal processing, and measurement reliability information for the three HWA modes, velocity, resistance thermometer, and mixed sensitivity. The sensitivity coefficients for turbulent fluctuations derived below are assumed to depend only on the mean operating conditions.

#### 1. Velocity mode

a. Calibration For velocity measurements in isothermal flow, the sensor was controlled at a relatively high overheat by the hot-wire set, and the bridge voltage signal  $E$  was fed to the analog linearizer. The calibration procedure used was standard and will therefore be described only in brief. A "zero-ohm control" on the HWA allowed compensation for the probe tip and adaptor resistance (the 15' cable resistance had been factory compensated); thus, the control resistance selected was the true wire resistance maintained in the flow. During calibration the hot-wire sensor was mounted next to the pitot-static probe in the test section at about  $x/M = 45.6$  with the grid removed. Figure 17 shows the results of two calibration runs. On this graph  $\bar{E}$  is not the wire voltage  $\bar{E}_w$  given in Equations 3-55 or 3-58 nor is it the bridge voltage; it is the linearizer output after zero suppression and span controls were set up and was read on the dc voltmeter.

The slope of Figure 17 is the velocity sensitivity

$$S = \frac{\Delta \bar{E}}{\Delta U}, \frac{\text{volt}}{\text{ft/sec}} \quad (5-22)$$

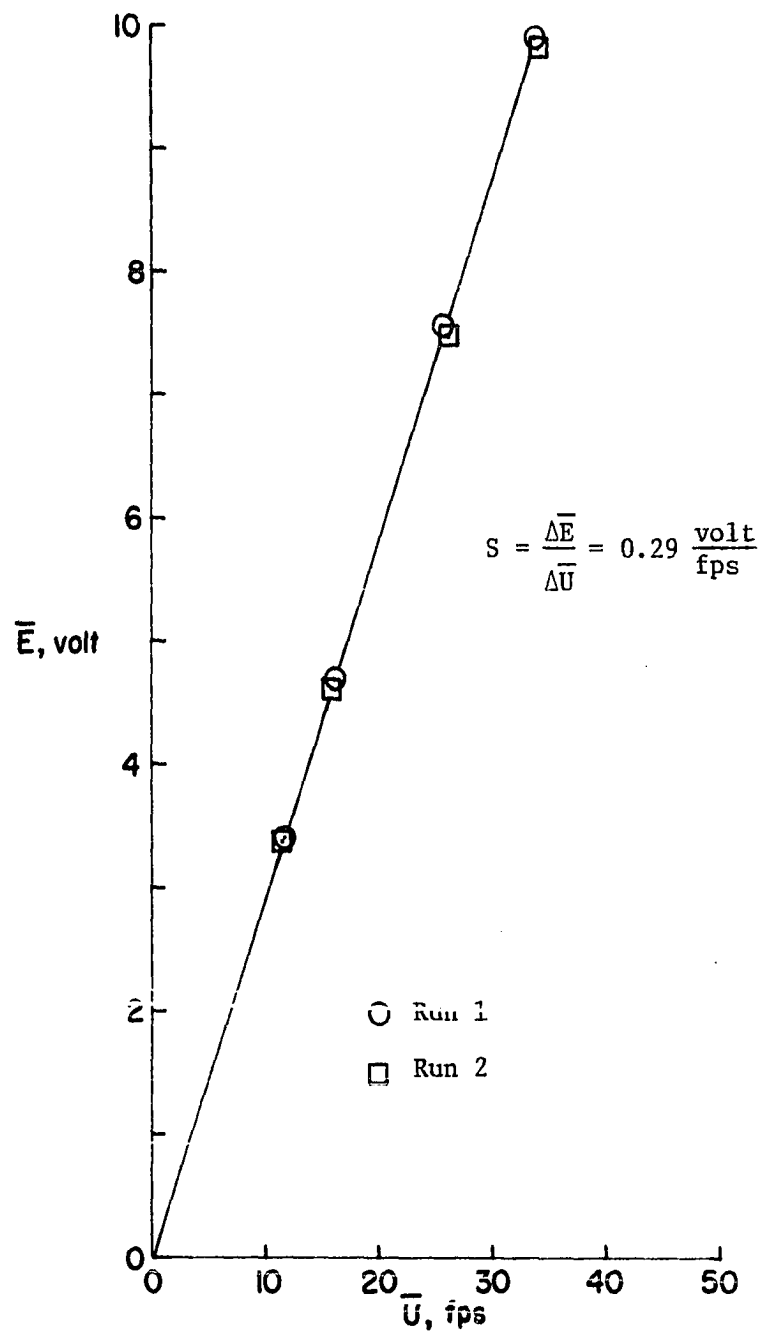


Figure 17. Hot-wire anemometer velocity calibration with  $R_w = 10.54$  ohm

For mean speed measurements  $\bar{U}_0 = \bar{E}_0 = 0$ , so  $\bar{U} - \bar{U}_0 = (\bar{E} - \bar{E}_0)/S$  becomes

$$\bar{U} = \frac{\bar{E}}{S} \quad (5-23)$$

For turbulence measurements let  $u = \Delta\bar{U}$  and  $e = \Delta\bar{E}$  be small, so  $u = e/S$ ; taking rms values of this gives

$$u' = \left( \overline{u^2} \right)^{1/2} = \frac{e'}{S} \quad (5-24)$$

Turbulence intensity is then easily obtained from dividing (5-24) by (5-23) or

$$\frac{u'}{\bar{U}} = \frac{e'}{\bar{E}} \quad (5-25)$$

$\bar{U}$  in Figure 17 was obtained by measuring dynamic pressure  $\bar{Q}$  with the pitot-static probe; assuming steady, incompressible, inviscid flow

$$\bar{Q} = \bar{P}_t - \bar{P}_s = \frac{\bar{\Gamma}_a \bar{U}^2}{2g_c} \quad (5-26)$$

Solving for  $\bar{U}$

$$\bar{U} = \left[ \frac{2g_c \bar{Q}}{\bar{\Gamma}_a} \right]^{1/2} = \left[ \frac{2(32.2)\bar{Q}}{\bar{\Gamma}_a} \right]^{1/2}, \frac{\text{ft}}{\text{sec}} \quad (5-27)$$

where

$$[\bar{U}] = \left[ \frac{2(32.2 \text{ lbm ft/lbf sec}^2)(\text{lbf/ft}^2)}{(\text{lbm/ft}^3)} \right]^{1/2} = \frac{\text{ft}}{\text{sec}}$$

and  $\bar{Q}$  and  $\bar{\Gamma}_a$  were obtained from the micromanometer and ideal gas law respectively, as follows. The hydrostatic equation is

$$\bar{P} - \bar{P}_0 = \frac{\bar{\Gamma}_f g \Delta h}{g_c}$$

where  $\bar{P}_0$  is the pressure at a free surface and  $\bar{P}$  is the higher pressure at depth  $\Delta h$ . Thus, the manometer gave

$$\bar{Q} = \bar{P}_t - \bar{P}_s = \frac{\bar{\Gamma}_f g \Delta h}{g_c} \quad (5-28)$$

where

$$[\bar{Q}] = \frac{(62.4 \text{ lbm/ft}^3)(32.2 \text{ ft/sec}^2)(\Delta h \text{ in})}{(32.2 \text{ lbm ft/lbf sec}^2)(12 \text{ in/ft})} = \frac{\text{lbf}}{\text{ft}^2}$$

or

$$\bar{Q} = \frac{62.4}{12} \Delta h, \frac{\text{lbf}}{\text{ft}^2} \text{ with } \Delta h \text{ in inches of water} \quad (5-29)$$

The perfect gas law is

$$\bar{\Gamma}_a = \frac{\bar{P}_a}{R\bar{\Theta}_a}$$

Assuming  $\bar{P}_a = 14.7 \text{ lbf/in}^2 = 2117 \text{ lbf/ft}^2$  and  $R = 53.3 \text{ ft lbf/lbm } ^\circ\text{R}$ , this becomes

$$\bar{\Gamma}_a = \frac{2117}{53.3(460 + \bar{\Theta}_a)}, \frac{\text{lbm}}{\text{ft}^3} \quad (5-30)$$

where  $\bar{\Theta}_a$  is the ambient temperature in  $^\circ\text{F}$ . Thus,  $\bar{Q}$  and  $\bar{\Gamma}_a$  were calculated from (5-29) and (5-30) respectively for use in (5-27) to obtain  $\bar{U}$ .

b. Signal processing Having calibrated the HWA sensor for velocity in the tunnel with a laminar stream, it was then available for measuring longitudinal and lateral traverses of  $\bar{U}$ ,  $u'/\bar{U}$ , and  $1-D u'^2$  spectra with the grid installed for particular  $x/M$  and  $\bar{U}$  conditions.

The  $\bar{U}$  measurements in turbulent flow were obtained using (5-22) and a readout of  $\bar{E}$  on the dc voltmeter. Measurements of  $u'/\bar{U}$  were obtained at the same time by monitoring  $e'$  on the true rms voltmeter after band-pass filtering 2 to 2000 Hz (for reasons seen below) and using (5-24). No amplification of  $e'$  was necessary using the linearizer.

The  $\overline{u'^2}$  spectra were obtained by filtering in the same manner as described above for one channel of CBS signal; here, amplification was used and  $e'(f,B)$  was read out on the true rms voltmeter. Then (5-24) gave

$$u'(f,B) = \frac{e'(f,B)}{S \cdot 10^{\text{dB}/20}} \cdot \frac{ft}{\text{sec}} \quad (5-30)$$

where  $e'$  was in volts and dB was the amplification setting. Squaring (5-30) and normalizing by B gave  $\overline{u'^2}(f,B)/B$  for plotting vs  $f$  as desired.

c. Measurement reliability Resolution limits of HWA's are reviewed and discussed elsewhere (see, for example, References 44 and 29). The velocity resolution and frequency response of the HWA system in isothermal flow were assumed to be more than adequate for our purposes. No corrections have been applied to the data for noise or any other effects.

Prior to each data run the wire ambient resistance was checked for drift; however, it was found to be stable over the test period. In addition, the electronic noise level was checked by measuring  $e'(\bar{U} = 0)$  and found typically to be 0.22 mv out of 40 mv (or more) with the tunnel on. Noise which may have been present due to vibration was not

separated but was believed negligible.  $\overline{E}(\overline{U} = 0)$  was checked to be 0 as set up.

The velocity  $u'$  data were band-pass filtered 2 to 2000 Hz. A study of the basic  $u$  signal revealed that as much as about 8% of the total rms signal was contained between 2 and 20 Hz since the 1-D  $\overline{u^2}$  spectrum was nearly flat as  $f \rightarrow 0$ , but that negligible energy lay above 2000 Hz.

One probable source of random error in  $e'$  was too little meter damping on the true rms voltmeter, especially at the higher  $e'$  levels and narrower band-passes. Final values of  $e'$  read from the meter were carefully averaged by eye. Maximum excursions in  $e'$  were less than  $\pm 10\%$  when measuring the lower frequency pass bands of the spectra and less than  $\pm 5\%$  when measuring composite  $e'$  signals. Averaging by eye probably gave results within a few percent. Fluctuations in  $E$  on the dc voltmeter were less than  $\pm 2\%$ .

Absolute measurements of velocity at low speeds are notoriously difficult. While changes in  $\overline{U}$  measured with the HWA could be monitored to within  $\pm 2\%$ , the calibration standard on which absolute levels were based was less certain. As an example for  $\overline{U} = 10$  ft/sec ( $\overline{Q} = 0.115$  lbf/ft<sup>2</sup>),  $h = 0.022$  inches of water. Since repeatability of the  $\Delta h$  measurement was about  $\pm 0.004$  inches, the uncertainty in the absolute level of  $\overline{U}$  was about  $\pm 18\%$ .

An example is provided to check

$$\overline{u^2} = \int_0^\infty E_1(f) df = \int_0^\infty \frac{\overline{u^2}(f, B)}{B} df \quad (5-31)$$

for conditions  $x/M = 17.4$  and  $\overline{U} = 8.5$  ft/sec. Summing the spectrum (20 to 2000 Hz) gave  $(\overline{e^2})_s = 5.69 \times 10^{-3}$  volt<sup>2</sup>, whereas the overall signal (filtered 2 to 2000 Hz) gave  $(\overline{e^2})_o = 5.33 \times 10^{-3}$  volt<sup>2</sup> for

$$\frac{(\overline{e^2})_s - (\overline{e^2})_o}{(\overline{e^2})_o} = 0.07$$

## 2. Resistance thermometer mode

a. Calibration Resistance thermometers are generally thought of as being the primary instruments available for measuring temperature fluctuations near or above 1000 Hz (see Reference 44). The resistance thermometer or constant current mode was selected on our HWA by setting the current  $\overline{I}$  and depressing a switch. Resistance-temperature data supplied by the manufacturer enabled calculation of temperature sensitivity as follows. The resistance-temperature equation is

$$\overline{R} = \overline{R}_o [1 + \alpha(\overline{\Theta} - \overline{\Theta}_o)] \quad (5-32)$$

where  $\alpha$  is the temperature coefficient of resistance associated with the reference temperature  $\overline{\Theta}_o$ , and where second order and higher effects in  $\overline{\Theta}$  are being neglected. Sensor data supplied were

$$\overline{R}_b - \overline{R}_i = 2.02 \quad \Omega$$

$$\overline{R}_i = 5.47 \quad \Omega$$

$$\overline{R}_w = 10.54 \quad \Omega \text{ (suggested operating)}$$

where  $\bar{R}_b$  and  $\bar{R}_i$  are associated with the boiling point ( $\bar{\Theta}_b = 212^\circ\text{F}$ ) and ice point ( $\bar{\Theta}_i = 32^\circ\text{F}$ ) respectively. Note that two accurate pairs of  $(\bar{R}, \bar{\Theta})$  data must be known for a sensor to perform any of the following calculations. If these were not supplied, they would have to be measured in the user's temperature calibration facility (oven or bath) using a high impedance ohmeter. An ordinary multimeter can burn-out a sensor on a low resistance scale. Rewriting (5-32) gives with  $\bar{R} = \bar{R}_b$  and  $\bar{R}_o = \bar{R}_i$

$$\alpha \bar{R}_i = \frac{\bar{R}_b - \bar{R}_i}{\bar{\Theta}_b - \bar{\Theta}_i} \quad (5-33)$$

or with the given data

$$\alpha = \frac{2.02 \, \Omega}{5.47 \, \Omega(180^\circ\text{F})} = 0.00205 \, \Omega/\Omega^\circ\text{F}$$

or

$$\alpha \bar{R}_i = 0.0112 \, \Omega/^\circ\text{F}$$

Now the RWA response to a change in resistance is simply

$$\Delta \bar{E} = \bar{I} \, \Delta \bar{R} \, G \quad (5-34)$$

or

$$\bar{E}_2 - \bar{E}_1 = \bar{I}(\bar{R}_2 - \bar{R}_1)G$$

where  $\bar{E}$  is the bridge voltage and  $G = 1000$  is the given amplifier gain.

Writing Equation 5-32 twice gives

$$\bar{R}_2 - \bar{R}_i = \alpha \bar{R}_i (\bar{\Theta}_2 - \bar{\Theta}_i)$$

$$\bar{R}_1 - \bar{R}_i = \alpha \bar{R}_i (\bar{\Theta}_1 - \bar{\Theta}_i)$$



Subtracting these we get

$$\bar{R}_2 - \bar{R}_1 = \alpha \bar{R}_1 (\bar{\theta}_2 - \bar{\theta}_1)$$

which in (5-34) becomes

$$\bar{E}_2 - \bar{E}_1 = \alpha \bar{R}_1 G \bar{I} (\bar{\theta}_2 - \bar{\theta}_1) \quad (5-35)$$

Assuming  $e = \bar{E}_2 - \bar{E}_1$  and  $\theta = \bar{\theta}_2 - \bar{\theta}_1$  for small changes

$$e = \alpha \bar{R}_1 G \bar{I} \theta$$

so that the resistance thermometer sensitivity is seen to be  $\alpha \bar{R}_1 G \bar{I}$ .

Taking the rms of both sides gives

$$\theta' = \frac{e'}{\alpha \bar{R}_1 G \bar{I}} \quad (5-36)$$

Substituting given values for the constants and assuming additional amplification yields

$$\theta' = \frac{e'}{11.2 \bar{I} 10^{11.2/20}}, \text{ } ^\circ\text{F} \quad (5-37)$$

where  $e'$  is in volts and  $\bar{I}$  was set to  $1.5 \times 10^{-3}$  amp as recommended by the manufacturer for all resistance thermometer measurements reported here.

As an example using given data, we check the calculated value of sensor ambient resistance against the lab measured value of  $\bar{R}_{\text{amb}} = 5.93 \Omega$ . From (5-32)

$$\begin{aligned} \bar{R}_{\text{amb}} &= \bar{R}_1 + \alpha \bar{R}_1 (\bar{\theta}_{\text{amb}} - \bar{\theta}_1) \\ &= 5.47 + 0.0112 (74.1 - 32.0) = 5.94 \Omega \end{aligned} \quad (5-38)$$

The value of  $\bar{R}_{amb} = 5.39 \Omega$  was measured before zero-ohm compensation was applied as discussed above. It may be noted that this compensation reduces  $\bar{R}_i$  and  $\bar{R}_b$  (or any  $\bar{R}$  reading) by the set amount but does not change the  $\alpha\bar{R}_i$  product. To continue this example, we calculate the sensor operating temperature at  $\bar{R}_w = 10.54 \Omega$ . From (5-32)

$$\bar{R}_w = \bar{R}_i - \alpha\bar{R}_i(\bar{\theta}_w - \bar{\theta}_i) \quad (5-39)$$

But, using the given data

$$\alpha\bar{R}_i = \frac{\bar{R}_b - \bar{R}_i}{\bar{\theta}_b - \bar{\theta}_i} = \frac{\bar{R}_b - \bar{R}_i}{180}$$

Substituting in (5-39) and solving for  $\bar{\theta}_w$

$$\bar{\theta}_w = 180 \left[ \frac{\bar{R}_w - \bar{R}_i}{\bar{R}_b - \bar{R}_i} \right] + 32, ^\circ\text{F} \quad (5-40)$$

For this case  $\bar{\theta}_w = 484^\circ\text{F} = 251^\circ\text{C}$ . The sensor overheat ratio defined as  $\bar{R}_w/\bar{R}_{amb}$  was  $10.54/5.94 = 1.77$ . Notice that the zero-ohm compensation does affect the values of  $\bar{\theta}_w$  and  $\bar{R}_{amb}$  calculated using (5-40) and (5-38).

b. Signal processing The resistance thermometer was used to measure longitudinal and lateral traverses of  $\theta'$  and 1-D  $\bar{\theta}^2$  spectra. To obtain  $\theta'$ , the true rms voltmeter gave  $e'$  for (5-37) after filtering 20 to 2000 Hz and amplification. Spectra of  $\bar{\theta}^2$  were produced by measuring the amplified  $e'(f,B)$  on the true rms meter and applying (5-37).

c. Measurement reliability When it was decided to try the T.S.I. model 1210-T1.5 sensor in our flow model there were two questions: Would such a "massive" wire have (1) adequate frequency response, and

(2) adequate sensitivity? For transient measurements at high frequencies, much smaller diameter (and higher resistance) wires are generally used to obtain as small a time constant as possible and delay the response roll-off due to thermal inertia of the filament. For example, Sandborn (44) discusses use of a  $d = 2.5 \times 10^{-5}$  inch wire of more than  $900 \Omega$  which could respond to up to 3000 Hz at  $\bar{U} = 0$ . In Reference 39,  $d = 5.0 \times 10^{-5}$  inch and  $\ell = 0.1$ " wires of  $R = 75$  to  $150 \Omega$  were applied. T.S.I. markets a  $d = 5.0 \times 10^{-5}$  inch,  $\ell = 0.02$ ", and  $R \approx 40 \Omega$  sensor which is quoted good to 1800 Hz at  $\bar{U} = 10$  ft/sec. As might be expected, these wires are extremely fragile.

The frequency response of our sensor in constant current operation was identical to the uncompensated wire because the constant temperature feedback amplifier was disconnected. The amplifier stage was used only to provide 60 dB gain. (A well-known procedure for improving a wires natural response is that used in constant current hot-wire sets; here an analog differentiating amplifier can provide a first-order increase in gain to counteract the roll-off of the wire as  $1/f$  as shown in Reference 30.) Using data published T.S.I., the response of our sensor was estimated good to about 400 Hz. Since most of the energy in our signal was known to be below this limit from low-pass filtering the basic signal, we decided to try it.

Prior to each run  $R_{amb}$  was checked as well as the electronic noise; at  $\bar{U} = 0$  typically  $e' = 4$  mV out of 90 mV or more (both amplified 20 dB) during heating. Vibration and velocity effects were

isolated by measuring  $e'$  with the tunnel on but with a cold grid, and were found to increase  $e'$  less than 1 mV.

One certain and one probable source of systematic errors were, respectively, data mistakenly filtered 20 to 2000 Hz (to match the CBS settings) for  $\theta'$  measurements instead of 2 to 2000 Hz, and an assumption of small fluctuations (which may have been exceeded at the high overheats). Because of the filtering problem, the  $\theta'$  levels were low by 5% or more. The possible gain in sensitivity available from increasing  $\bar{I}$  (at the expense of more velocity sensitivity) was not explored. A typical check on

$$\overline{\theta^2} = \int_0^\infty E_{\theta 1}(f) df = \int_0^\infty \frac{\overline{\theta^2}(f, B)}{B} df$$

for  $x/M = 17.4$ ,  $\bar{U} = 8.5$  ft/sec, and  $\Delta = 36^\circ\text{F}$  gave  $(\overline{e_s^2} - \overline{e_o^2})/\overline{e_o^2} = 0.20$ .

### 3. Mixed mode

One way to get around the problem of reduced frequency response for an uncompensated wire is to analytically separate the combined effects of velocity and temperature from the composite signal obtained while operating in the constant temperature mode. Since a feedback amplifier circuit is controlling wire resistance in this mode,  $u$  and  $\theta$  frequency response will be identical. However, this technique certainly has drawbacks as will be seen.

Several procedures for obtaining the necessary sensitivities  $S_u$  and  $S_\theta$  and for analyzing data were discussed in Chapter III. In the present

study mixed mode data were obtained at given conditions by operating the sensor at five different overheats and recording  $\bar{E}$ ,  $e'$ , and  $\bar{\theta}_a$  on the dc voltmeter, true rms voltmeter, and thermocouple potentiometer, respectively, at each overheat. Here  $\bar{E}$  was the non-linearized HWA bridge output;  $e'$  was filtered 2 to 2000 Hz. The calibration procedure used was that of operating the wire in a constant temperature laminar stream and varying the wire temperature  $\bar{\theta}_w$  (or  $\bar{R}_w$ ) as suggested in Reference 1. This procedure yielded curves of  $\bar{E}$  vs  $\bar{U}$  from which an empirical similarity law of the form of (3-64) was derived and differentiated to give  $S_u$  and  $S_\theta$ . Knowing  $S_u$  and  $S_\theta$  and having the five sets of  $\bar{E}$ ,  $e'$ , and  $\bar{\theta}_a$  data for each overheat, the quantities  $\bar{u}^2$ ,  $\bar{u}\bar{\theta}$ , and  $\bar{\theta}^2$  were calculated by least-squares fitting the parabola (3-62).

Figure 18 presents the set of calibration curves from which a similarity law was derived.  $\bar{U}$  was obtained from pitot-static tube data. Conditions for Figure 18 are summarized in Table 2.

Table 2. Mixed-mode calibration curve conditions with  $\bar{\theta}_a = 73^\circ\text{F}$

$\bar{R}_w, \Omega$	$\bar{\theta}_w, ^\circ\text{F}$	$\bar{\theta}_w - \bar{\theta}_a, ^\circ\text{F}$
10.50	493	420
9.50	403	330
8.50	314	241
7.50	225	152
6.50	136	63

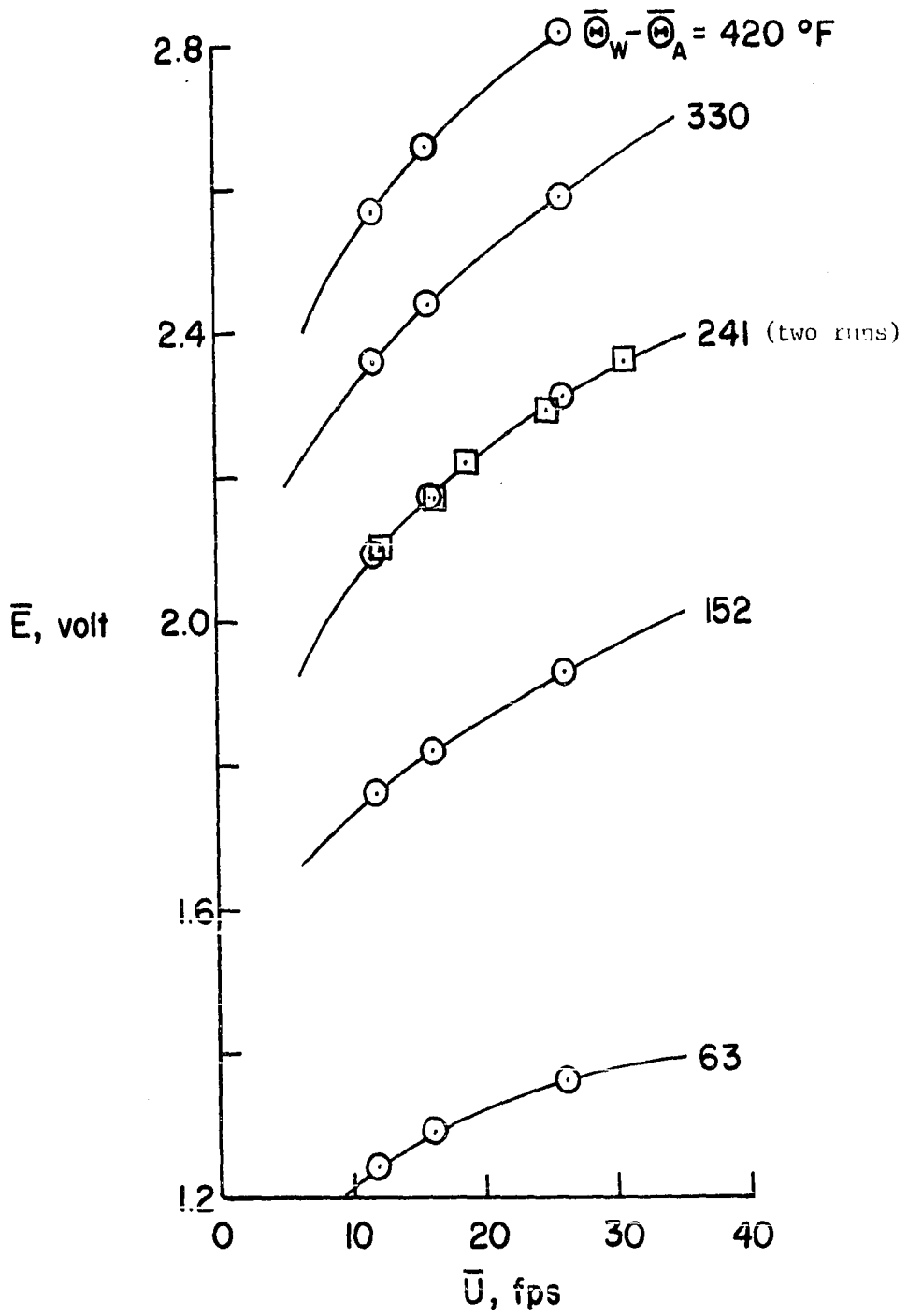


Figure 18. Hot-wire anemometer mixed mode calibration (non-linear bridge output)

In Table 2,  $\bar{\Theta}_w$  was calculated using (5-40) with  $\bar{R}_1 = 5.33 \Omega$  which reflects the manufacturers value (5.47  $\Omega$ ) less 0.14  $\Omega$  which was taken up by the zero-ohm adjustment ( $\bar{R}_{amb}$  became about 5.79  $\Omega$ ). The lowest  $\bar{R}_w$  was chosen so that  $\bar{\Theta}_w - \bar{\Theta}_a > 0$  for all anticipated test conditions.

Equations 3-55 or 3-58 are essentially similarity laws relating  $\bar{E}_w$  to power laws in  $\bar{U}$  and  $\bar{\Theta}_w - \bar{\Theta}_a$ . However, the voltage output of our HWA set was not  $\bar{E}_w$  but the bridge voltage  $\bar{E}$ . These two were simply related as follows. Figure 19 is a schematic of the bridge circuit. Clearly,

$$\bar{E} = \bar{I}_w (\bar{R}_3 + \bar{R}_w)$$

but

$$\bar{E}_w = \bar{I}_w \bar{R}_w = \frac{\bar{R}_w}{\bar{R}_3 + \bar{R}_w} \bar{E} \quad (5-41)$$

Using this in (3-58) for the heat dissipated

$$\frac{\bar{E}_w^2}{\bar{R}_w} = \frac{\bar{E}^2 \bar{R}_w}{(\bar{R}_3 + \bar{R}_w)^2} \quad (5-42)$$

which will be used later. But this extra calculation is unnecessary if we assume

$$\bar{E} = C \bar{U}^n (\bar{\Theta}_w - \bar{\Theta}_a)^m \quad (3-64)$$

The exponents  $n$  and  $m$  were obtained as follows. Data points for  $\bar{\Theta}_w$  in  $\bar{\Theta}_a = 241^\circ\text{F}$  in Figure 18 were replotted on log-log paper as Figure 20.

Since the line was straight, we may assume

$$\bar{E} = C_1 \bar{U}^n$$

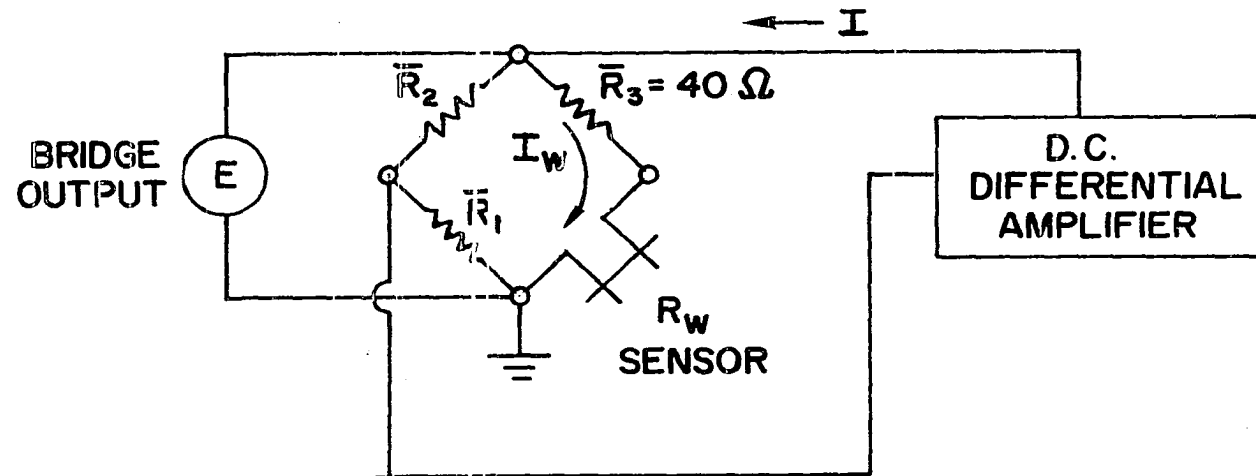


Figure 19. Hot-wire anemometer bridge circuit



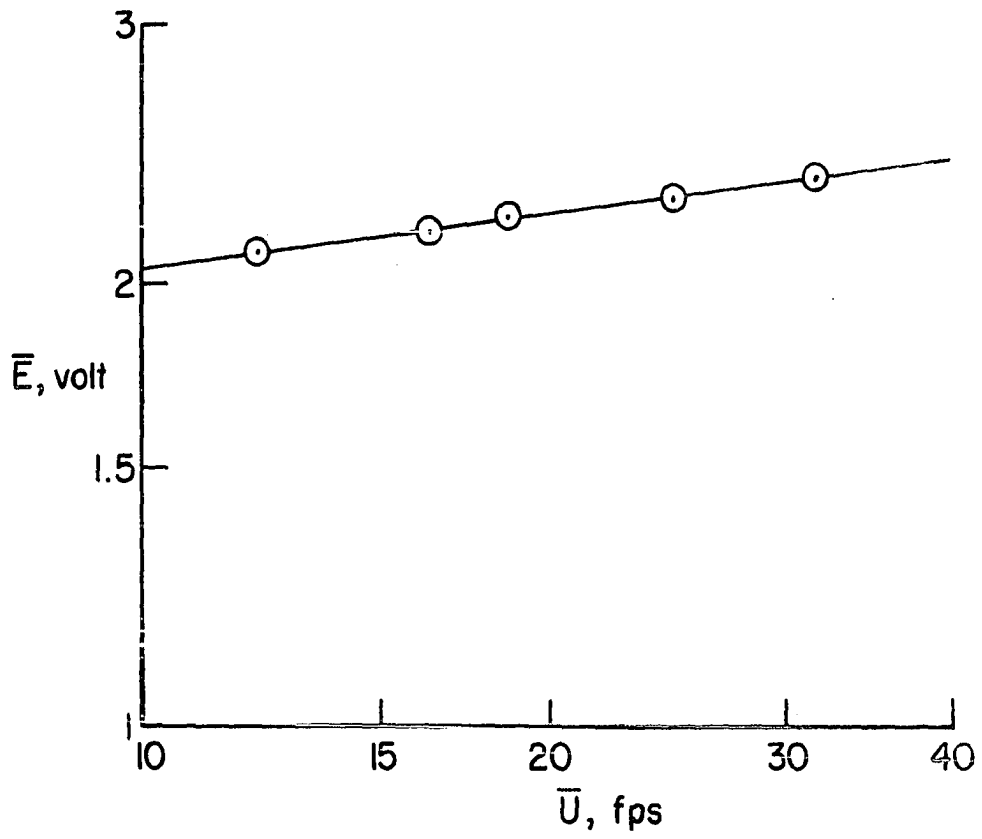


Figure 20. Hot-wire anemometer velocity power law determination;  
 $\bar{\theta}_w - \bar{\theta}_a = 241^\circ\text{F}$

Therefore,  $\log \frac{\bar{E}_2}{\bar{E}_1} = n \log \frac{\bar{U}_2}{\bar{U}_1}$  and two points gave  $n = 0.126$ . Next, data

points for  $\bar{U} = 26$  ft/sec in Figure 18 were replotted as Figure 21.

Again the line was straight so

$$\bar{E} = C_2 (\bar{\theta}_w - \bar{\theta}_a)^m$$

Therefore,

$$\log \frac{\bar{E}_2}{\bar{E}_1} = m \log \frac{(\bar{\theta}_w - \bar{\theta}_a)_2}{(\bar{\theta}_w - \bar{\theta}_a)_1}$$

and two points gave  $m = 0.384$ . Thus, (3-64) becomes

$$\bar{E} = C(\bar{U})^{0.126} (\bar{\theta}_w - \bar{\theta}_a)^{0.384}$$

Then with  $\bar{U} = 26$  ft/sec,  $\bar{\theta}_w - \bar{\theta}_a = 420^\circ\text{F}$ , and  $\bar{E} = 2.82$  volts from

Figure 18, we calculate  $C = 0.184$ . Consequently, we may approximate Figure 18 with the expression

$$\bar{E} = 0.184(\bar{U})^{0.126} (\bar{\theta}_w - \bar{\theta}_a)^{0.384} \quad (5-43)$$

For each point in Figure 18, its value of  $\bar{E}$  was compared with  $\bar{E}_c$  calculated from (5-43) with the result  $(\bar{E} - \bar{E}_c)/\bar{E} \leq 0.02$  for all points.

Differentiating (5-43) gives easily

$$s_u = \frac{\partial \bar{E}}{\partial \bar{U}} = 0.0232(\bar{U})^{-0.874} (\bar{\theta}_w - \bar{\theta}_a)^{0.384} \quad (5-44)$$

$$s_\theta = -\frac{\partial \bar{E}}{\partial \bar{\theta}_a} = 0.0710(\bar{U})^{0.126} (\bar{\theta}_w - \bar{\theta}_a)^{-0.616}$$

which hold for all values of  $\bar{U}$  and  $(\bar{\theta}_w - \bar{\theta}_a)$ . Now (5-44) are to be

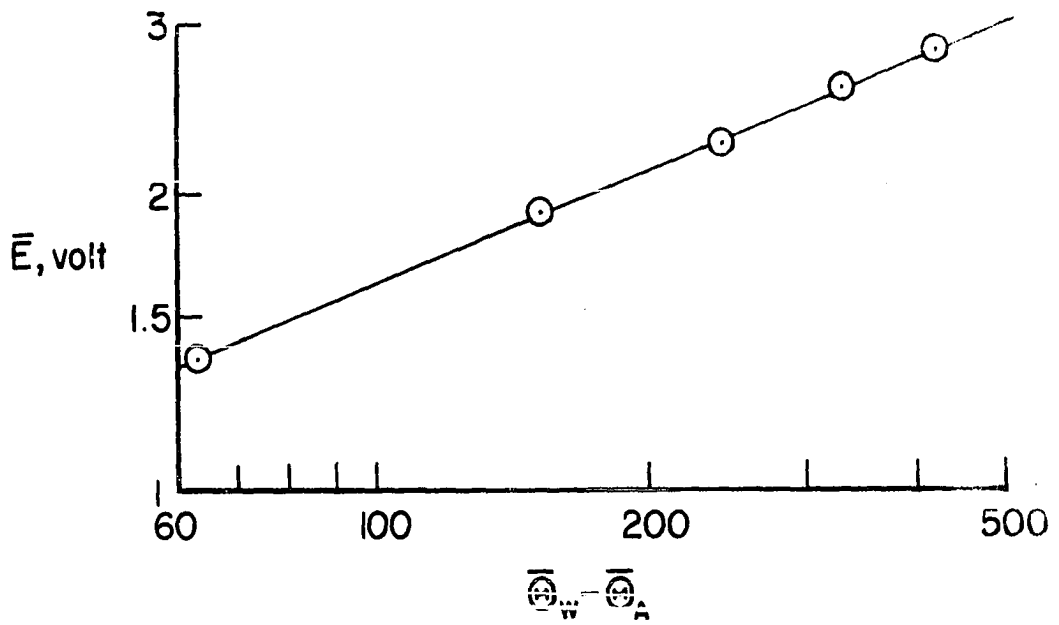


Figure 21. Hot-wire anemometer temperature power law determination;  
 $U = 26 \text{ fps}$

used with

$$Y_k = a + b X_k + c X_k^2 \quad (5-45)$$

where from (3-61) and (3-62)

$$Y_k = \left[ \begin{array}{c} \overline{2} \\ e \\ s \\ \theta \end{array} \right]_k \quad (5-46)$$

$$X_k = \left[ \begin{array}{c} s \\ u \\ s \\ \theta \end{array} \right]_k$$

and  $a = \overline{\theta^2}$ ,  $b = -2\overline{u\theta}$ , and  $c = \overline{u^2}$ . It was necessary to compute

$(X_k, Y_k)$  for  $N = 5$  sets of data and to solve the normal equations

$$\begin{aligned} \sum_{k=1}^N Y_k &= aN + b \sum_{k=1}^N X_k + c \sum_{k=1}^N X_k^2 \\ \sum_{k=1}^N X_k Y_k &= a \sum_{k=1}^N X_k + b \sum_{k=1}^N X_k^2 + c \sum_{k=1}^N X_k^3 \\ \sum_{k=1}^N X_k^2 Y_k &= a \sum_{k=1}^N X_k^2 + b \sum_{k=1}^N X_k^3 + c \sum_{k=1}^N X_k^4 \end{aligned} \quad (5-47)$$

for  $(a,b,c)$ . This set of equations is known to be extremely sensitive to small changes in  $Y_k$  as may be seen in the following example calculation of repeated runs at  $x/M = 45.6$ , and  $\Delta = 18^\circ\text{F}$ . Data read into the computer were  $\overline{U} = 9.48 \text{ ft/sec}$ ,  $\overline{\theta}_a = 74^\circ\text{F}$  and the values of  $\overline{\theta}_w - \overline{\theta}_a$  and  $e'$  tabulated in Table 3. Table 3 also summarizes the computed values of  $S_u$  and  $S_\theta$  rounded to three significant figures. Results of solving Equations 5-45 through 5-47 for these two cases denoted by  $(R_1)$  and  $(R_2)$ , as well as others, are tabulated in Table 4.

Table 3. Mixed-mode data at  $x/M = 45.6$ ,  $\Delta = 18^\circ\text{F}$ ,  $\bar{U} = 9.48$  ft/sec,  $\bar{\Theta}_a = 74^\circ\text{F}$

	$\bar{R}_w, \Omega$	$\bar{\Theta}_a, ^\circ\text{R}$	$\bar{\Theta}_w - \bar{\Theta}_a, ^\circ\text{F}$	E, volts	e', volts	$S_u, \text{v/fps}$	$S_\theta, \text{v}/^\circ\text{F}$	X, $^\circ\text{F/fps}$
Run 1	10.50	551	402	2.45	0.0047	0.0324	0.00234	13.8
	9.50	551	312	2.23	0.0045	0.0295	0.00274	10.8
	8.50	552	222	1.96	0.0044	0.0259	0.00338	7.66
	7.50	552	133	1.60	0.0043	0.0212	0.00463	4.58
	6.50	553	43	1.02	0.0050	0.0138	0.00929	1.49
Run 2	10.50	551	402	2.44	0.0046	0.0325	0.00234	13.9
	9.50	552	311	2.22	0.0045	0.0294	0.00275	10.7
	8.50	552	222	1.96	0.0044	0.0259	0.00338	7.66
	7.50	553	132	1.59	0.0043	0.0212	0.00466	4.55
	6.50	553	43	1.02	0.0049	0.0138	0.00929	1.49

Table 4. Computer solution of mixed-mode data

$x/M$	$\bar{U}$ , ft/sec	$\Delta$ , °F	$u'/\bar{U}$	$\overline{u\theta}$ , ft° F/sec	$\theta'$ , °F
6.78	8.00	34	0.0577	-2.67	2.22
10.3	8.10	34	0.0315	-0.657	1.23
12.7	8.30	34	0.0326	-0.393	1.20
15.0	8.30	33	0.0280	-0.293	0.987
17.4	8.50	34	0.0191	-0.336	0.725
45.6	9.48	31	0.0107	-0.131	0.555
45.6(R <sub>1</sub> )	9.48	18	0.0117	-0.0553	0.315
45.6(R <sub>2</sub> )	9.48	18	0.0104	-0.0710	0.184

Reference to the last entries in Table 4 shows that 2% differences in  $e'$  (Table 3) produced 13%, 22%, and 71% differences in  $u'/\bar{U}$ ,  $\overline{u\theta}$ , and  $\theta'$ , respectively. The reason for the poor repeatability especially in  $\overline{u\theta}$  and  $\theta'$  has been illustrated by Arya and Plate (1). Apparently, it results from the parabola (3-62) being poorly defined for low values of  $X$ . They show that using more overheats can improve consistency of these calculations, but that a better method is to measure  $\theta'$  independently as described in Chapter III. Perhaps another way to improve consistency would have been to select five or more lower overheats for better definition at low  $X$ . For the case of Run 1 in Table 3, our overheats corresponding to  $\bar{R}_w = 10.5, 9.5, 8.5, 7.5$ , and  $6.5$  were using

$$\bar{R}_a = 5.33 + 0.0112 (\bar{\theta}_a - 32^\circ\text{F})$$

$\bar{R}_w/\bar{R}_a = 1.75, 1.59, 1.42, 1.25, \text{ and } 1.08$ , respectively.

Sufficient data are included in Table 4 to calculate the correlation coefficient

$$r_{u\theta} = \frac{\overline{u\theta}}{\overline{u'\theta'}}$$

at each  $x/M$ . Of course, for physical meaningfulness it is necessary that  $|r_{u\theta}| \leq 1$  (see Reference 7); however, in all cases presented  $|r_{u\theta}| > 1$ . This is simply another indication of large experimental errors as have been observed by other investigators (for example, Corrsin and Uberoi 17). It should be clear that our mixed mode data are of limited usefulness, perhaps as indications of trends only. Limited comparisons of  $\theta'$  and  $u'/\bar{U}$  from Table 4 will later be made with results from the other two modes. This data, as well as the discussion immediately above, has been included in the spirit of illustrating the technique and focusing on some of its inherent problems. Clearly, a number of alternative, perhaps more complex, procedures are available.

For comparison with the sensitivities given for Run 1 in Table 3,  $S_u$  and  $S_\theta$  were calculated from Equation 3-58 as follows. First  $A_2$  and  $B_2$  were determined using Equations 3-58 and 5-42 and two values of  $(\bar{E}_w, \bar{U})$  from each curve in Figure 18. While it was hoped to find  $A_2$  and  $B_2$  constant for all curves, they were found to vary 48% for  $A_2$  and 19% for  $B_2$ . Thus, a temperature effect was present in  $A_2$  and

$B_2$ ; and, therefore, for best accuracy a calibration curve at the particular  $\bar{\theta}_w - \bar{\theta}_a$  of interest should have been used. This tends to defeat the usefulness of the similarity law (3-58), a problem not suffered by (5-43) representing the actual calibration of Figure 18 as well as all other points in that figure. Because of the variations in  $A_2$  and  $B_2$ , average values were used. This illustrates the uncertainty referred to in Chapter III.

Differentiating (3-58) gives

$$S_u = \frac{\partial \bar{E}}{\partial \bar{U}} = \frac{\bar{E}}{2} \frac{0.45 B_2 (\bar{U})^{-0.55}}{[A_2 (\bar{\theta}_w + \bar{\theta}_a)^{0.8} + B_2 (\bar{U})^{0.45}]} \quad (5-48)$$

and

$$-S_\theta = \frac{\partial \bar{E}}{\partial \bar{\theta}_a} = \frac{\bar{E}}{2} \left\{ \frac{1}{\bar{\theta}_w + \bar{\theta}_a} \left[ \frac{0.8}{1+\alpha} + 0.17 \right] - \frac{0.17}{\bar{\theta}_a} - \frac{1}{\bar{\theta}_w - \bar{\theta}_a} \right\} \quad (5-49)$$

where

$$\alpha = \frac{B_2 (\bar{U})^{0.45}}{A_2 (\bar{\theta}_w + \bar{\theta}_a)^{0.8}}$$

and we have used Equation 5-41. Using the data for Run 1 in Table 3, these equations gave the results in Table 5. The differences in calibration data in Tables 3 and 5 are probably due mostly to the temperature dependence of  $A_2$  and  $B_2$ . The reader is reminded that validity of the data in either table is predicated on the assumption that an HWA sensor may be calibrated for thermal effects by varying wire temperature in isothermal flow. Accordingly, the results in Table 4 are subject to this approximation.



Table 5. Summary of  $S_u$  and  $S_\theta$  calculated for Run 1 of  
 Table 3 from (3-58) with  $(A_2)_{\text{avg}} = 9.66 \times 10^{-8}$   
 and  $(B_2)_{\text{avg}} = 9.32 \times 10^{-6}$

$R_w, \Omega$	$S_u, v/\text{fps}$	$S_\theta, v/^\circ\text{F}$
10.50	0.0251	0.00292
9.50	0.0235	0.00344
8.50	0.0213	0.00427
7.50	0.0179	0.00588
6.50	0.0118	0.0118

## VI. RESULTS AND DISCUSSION

The validity and viability of the crossed-beam technique in several radiation intensity modification configurations and its usefulness, particularly in determining kinematic flow properties, has been demonstrated in a number of studies as discussed above. Here, we would like to verify the ability of a particular configuration, the CBS, to measure absolute density or temperature fluctuation levels and their three-dimensional spectra as well as the kinematic properties. This attempt to provide a more complete assessment of the CBS (52) is in direct response to the request made by Wilson. The logical approach seems to be to compare measurements made with the CBS to those made with an independent instrument in the simplest and best understood flow model, grid-generated turbulence.

The desired flow model providing both isotropic and nonisotropic regions is readily available, and an independent instrument is available as well, namely, the HWA. However, temperature varying flows are notoriously difficult to treat experimentally using all hot-wire methods except resistance thermometry. Furthermore, since the HWA is the only device capable of the high frequency response desired, there has been no other instrument to date with which to compare its measured absolute temperature fluctuation levels. If the hot-wire is to be used for comparison, one must keep in mind that the theory describing HWA response is a linearized theory applying only to small fluctuations.

In this study both instruments have been used to measure temperature fluctuations and their spectra at various positions downstream of a heated grid. Unfortunately, the HWA measures an aliased 1-D spectrum while the CBS measures a 3-D spectrum; but, the two spectra are theoretically relatable in isotropic turbulence as has been shown in Chapter III. Data obtained using both instruments will be compared; at the same time, comparisons will be made with theoretical predictions hoping to verify, for example, the scalar decay rate and spectral shape predictions from Chapter III. Since the  $-5/3$  power law for the inertial subrange has been substantiated by several investigators as stated in Chapter II, this might also serve as a check on the validity of the "point-area correlation" concept for the CBS, as well as its measured spectral content.

The material in this chapter has been organized into the following divisions: Basic Flow Model, Longitudinal Turbulence Decay and Spectra, Scalar Turbulence, Estimates of Dissipation Rates and Scales, and Hot-Wire Mixed Mode. The most important part is Scalar Turbulence, which goes into a CBS basic signal breakdown and presents samples of probability density and correlation functions as well as data on temperature fluctuation decay, one- and three-dimensional scalar spectra, convection speed, and an isotropy test.

#### A. Basic Flow Model

The object of this section is to substantiate for the miniature wind tunnel a well-behaved, uniform flow field consisting of

homogeneous scalar and velocity turbulence. Lateral traverses of total pressure, mean velocity and temperature, as well as velocity and temperature fluctuation levels will be presented for several downstream locations. And, the longitudinal variation in mean velocity will be discussed.

Total pressure profiles across the test section were measured at four locations downstream of the grid station. Figure 22 shows these profiles in absence of the grid, and Figure 23 shows them with the grid installed. In both figures the parameter plotted as the abscissa was atmospheric pressure minus pitot tube total (or stagnation) pressure  $\bar{P}_{atm} - \bar{P}_t$  for convenience since the manometer was easily connected to read this difference. For no viscous losses  $\bar{P}_{atm} - \bar{P}_t = 0$ . A noticeable increase in viscous losses in the core flow differentiates the two figures, as expected, as well as about a 13% decrease in  $\bar{U}$  due to the presence of the grid. The main point we wish to make here is that while in both figures a significant boundary layer growth may be observed, it is well behaved and has left a uniform core flow in both the laminar and turbulent cases. Some acceleration of the flow between the outer grid rods and the wall is noticeable in Figure 23 at  $x/M = 12.7$ ; however, this effect appears to diminish rapidly further aft. Table 6 summarizes data obtained with the HWA at  $x/M = 45.6$  and for several mean velocities with and without the grid. The "no grid" data include the characteristic base-line turbulence intensity of the tunnel, about  $u'/\bar{U} = 0.007$

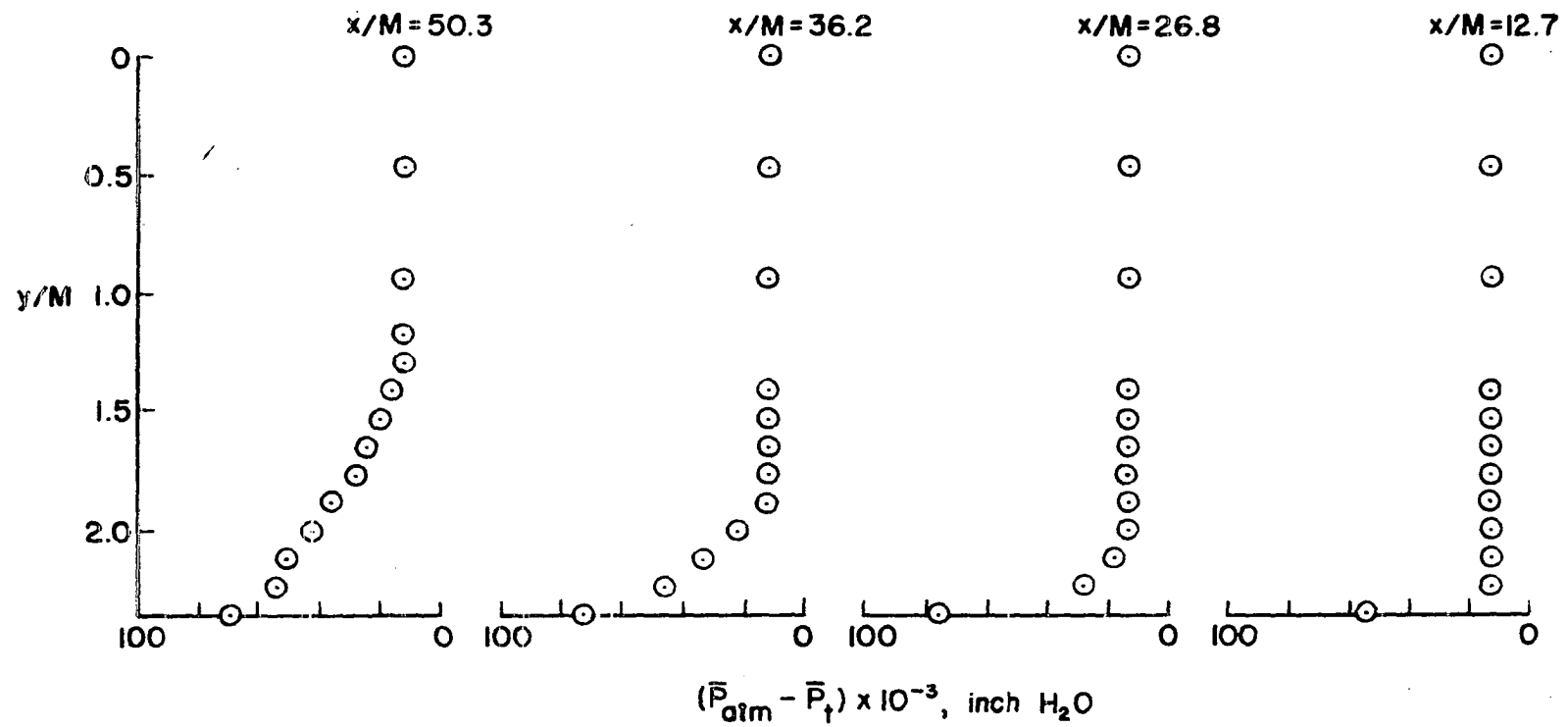


Figure 22. Total pressure profiles with grid removed;  
 $\bar{U}(x/M = 45.6) \approx 16$  fps

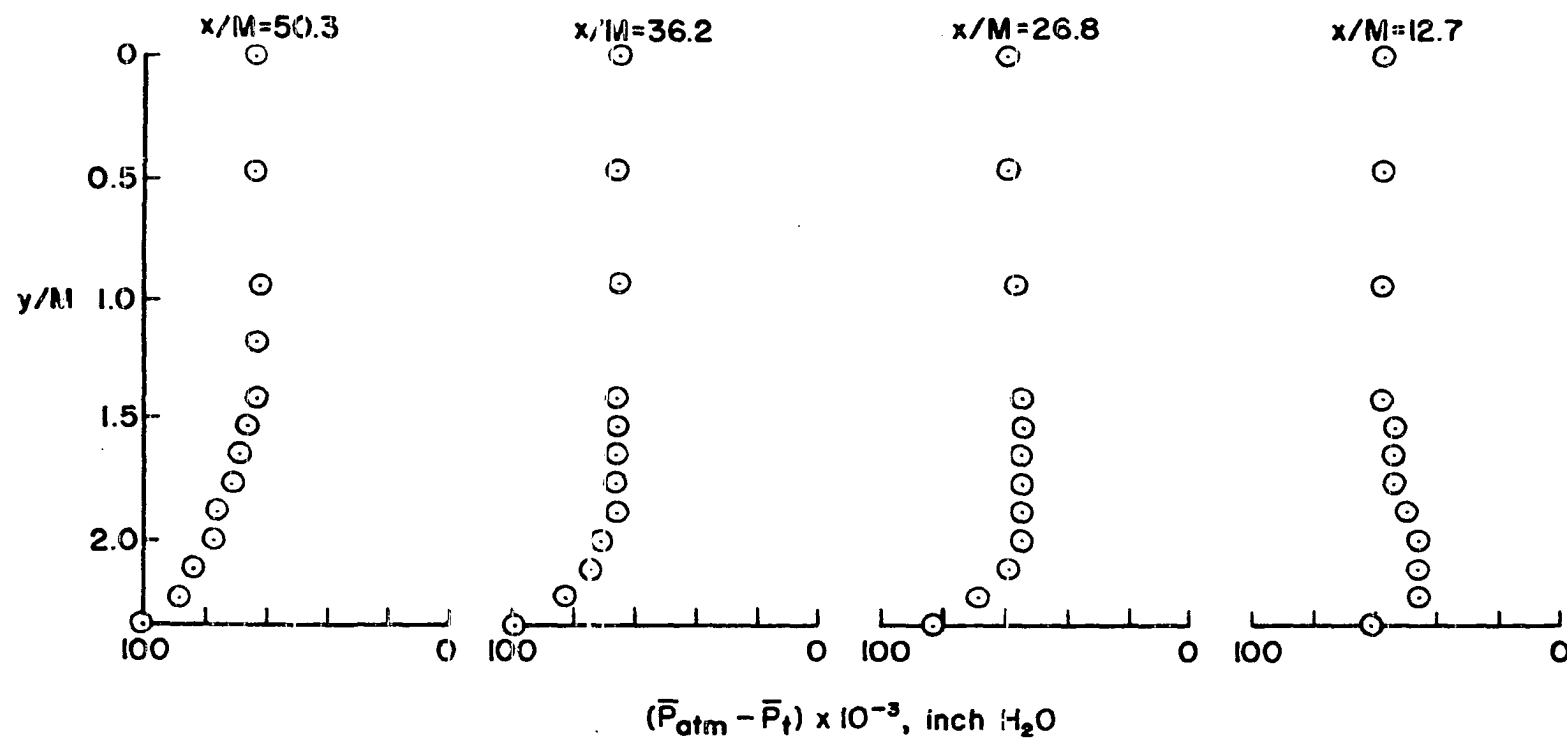


Figure 23. Total pressure profiles with grid installed;  
 $\bar{U}(x/M = 45.6) \approx 14$  fps

Table 6. Effect of presence of grid on  $\bar{U}$  and  $u'/\bar{U}$  at  $x/M = 45.6$  for fixed settings on the flow control tube

Setting	No grid		Grid in	
	$\bar{U}$ ,fps	$u'/\bar{U}$	$\bar{U}$ ,fps	$u'/\bar{U}$
1	11.5	0.00726	9.83	0.0161
2	15.9	0.00753	13.8	0.0175
3	25.7	0.00640	21.7	0.0175
4	33.7	0.00594	28.4	0.0176

at  $\bar{U} = 11.5$  ft/sec, a low level for such a low mean velocity. A value of  $u'/\bar{U} = 0.002$  was obtained at  $\bar{U} = 52.5$  ft/sec in a far more complex acoustic wind tunnel designed by Hanson (28). Our value is also consistent with data obtained by Schubauer and Spangenberg (46) downstream of a single 24 mesh per inch screen installed in a low-turbulence flow.

Figures 24 and 25 present lateral traverses of  $\bar{U}$ ,  $u'$ , and  $u'/\bar{U}$  for two downstream positions with the grid in. In these figures it is evident that our core flow is uniform in  $\bar{U}$  within several percent, and that homogeneity of  $u'$  in the core flow has been achieved. In addition, lateral traverses of  $\bar{\theta}$  and  $\theta'$  (Figure 26) show the core flow to be approximately uniform in  $\bar{\theta}$  and homogeneous in  $\theta'$ . Note that in Figures 24 and 26,  $x/M \leq 12.7$  is only 5.38" behind the grid rods in the expected nonisotropic region ( $x/M \leq 20$ ).

For simplicity and ease of use with the CBS, the test section was built with parallel sidewalls or constant area. Unfortunately, this

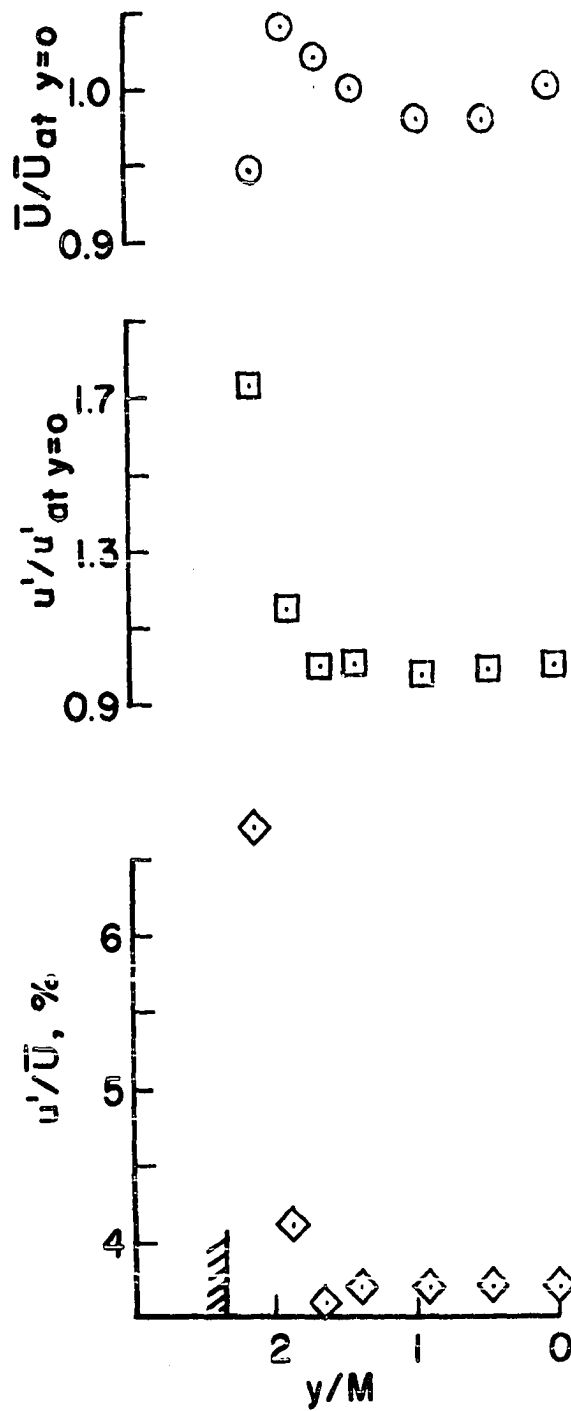


Figure 24. Lateral traverses of  $\bar{U}$  and  $u'$ ;  $x/M = 12.7$  and  $\bar{U} = 8.3$  fps



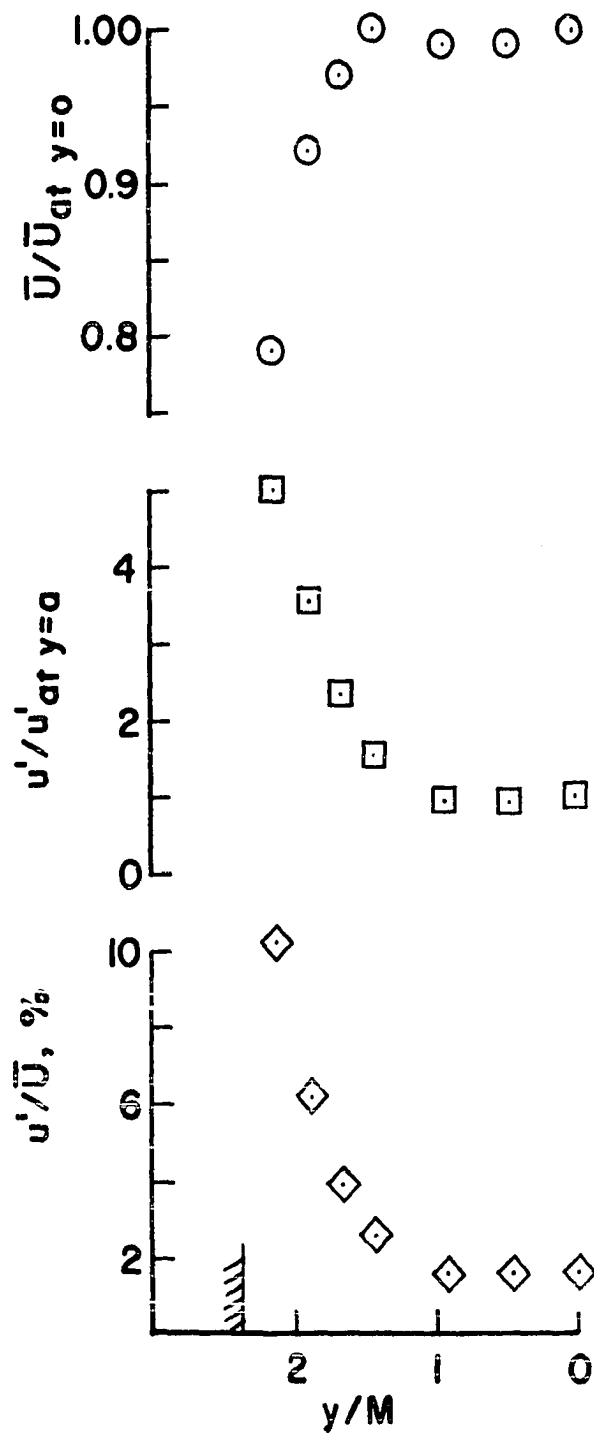


Figure 25. Lateral traverses of  $\bar{U}$  and  $u'$ ;  $x/M = 36.2$  and  $\bar{U} = 9.3$  fps

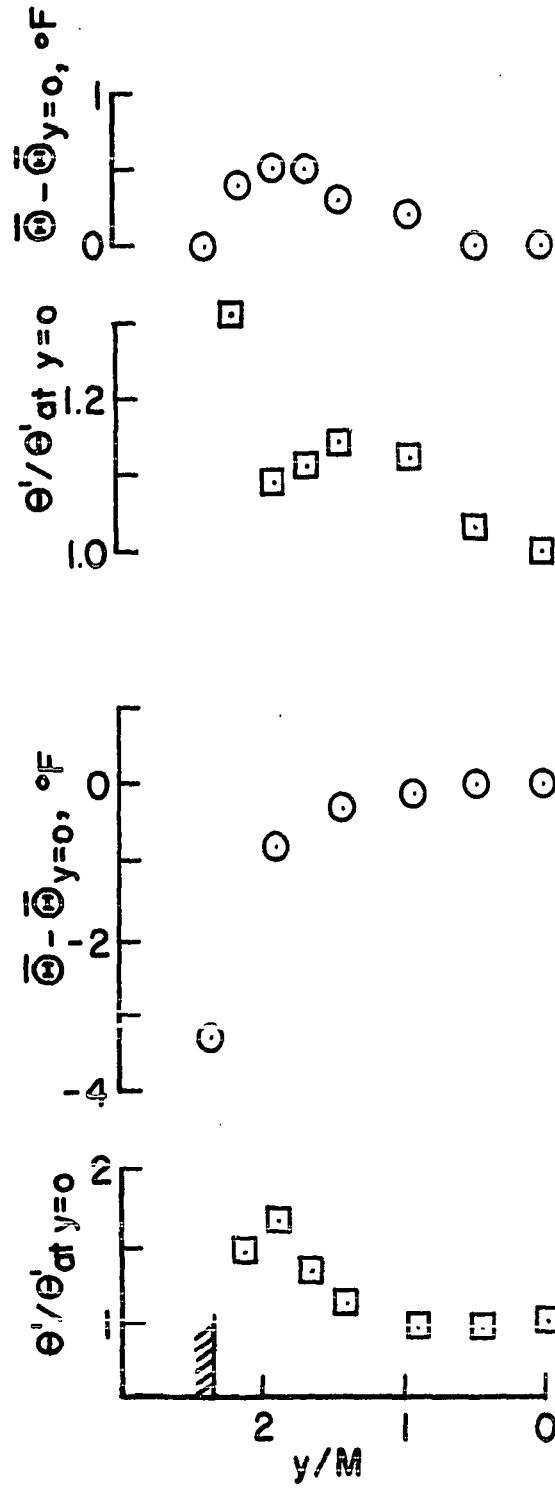


Figure 26. Lateral traverses of  $\bar{\theta}$  and  $\theta'$ ;  $x/M = 12.7$ ,  $\bar{U} = 8.3$  fps, and  $\Delta = 19^\circ F$

produced a non-constant speed test section due to boundary layer growth. Longitudinal mean velocity data were taken with the HWA at three flow control tube settings to evaluate this effect and are tabulated in Table 7. It may be seen that for settings corresponding to  $\bar{U}(x/M = 45.6) = 9.5, 12.9, \text{ and } 20.7 \text{ ft/sec}$ , the increases in speed due to area reduction were 19%, 17%, and 14%, respectively, over the range of  $x/M$  shown. Hereafter, longitudinal traverses of other quantities at a given  $\bar{U}$  will have  $\bar{U}$  specified at some  $x/M$  from Table 7. For example, most of the data to be presented were taken with the velocity setting which resulted in  $\bar{U}(x/M = 45.6) = 9.5 \text{ ft/sec}$ .

Table 7. Longitudinal variation of  $\bar{U}$ , fps with grid installed and cold for three settings on the flow control tube ( $\bar{\theta}_a = 75^\circ\text{F}$ )

$x/M$	Setting 1 (no cover)	Setting 2	Setting 3
6.78	8.0	11.0	18.1
10.3	8.1	11.2	18.1
12.7	8.3	11.4	18.1
15.0	8.3	11.4	18.1
17.4	8.5	11.4	18.1
24.4	8.6	11.7	18.9
31.5	9.1	12.6	19.6
38.5	9.3	12.8	20.3
45.6	9.5	12.9	20.7

### B. Longitudinal Turbulence Decay and Spectra

Figure 27 shows the centerline decay of longitudinal velocity fluctuations downstream of the cold grid at three mean velocity settings. These data are presented to further substantiate the flow model, to check the velocity decay law Equation 3-25, and to compare with previous experimental data. They are in good agreement with data replotted from Reference 39. Isotropy has probably been approximately achieved by  $x/M = 20$ . Replotting 27 as Figure 28 in the customary way reveals the expected linear relationship  $1/\overline{u'^2} \sim x$ . The virtual origin for our data appears to be at about  $x_0/M = 7.5$ , so the decay law corresponding to (3-25) is, approximately

$$\frac{\overline{u'^2}}{u'^2} = 100 \left[ \frac{x}{M} - 7.5 \right] \quad (6-1)$$

Thus, our data reflect a linear decay law and exhibit a virtual origin at a location consistent with previous measurements.

Spectra of  $\overline{u'^2}$  measured at three downstream locations and at two mean velocity settings are shown in Figures 29 and 30. The shapes of these spectra are typical of 1-D HWA spectra with approach to a horizontal asymptote at low frequencies due to aliasing and a monotonously decreasing slope with increasing frequency. As has been observed before (e.g., Hinze 29, or Tennekes and Lumley 48), 1-D spectra fail to reveal an appreciable  $-5/3$  power law region corresponding to an inertial subrange until much higher mesh Reynolds numbers (see, for example, Reference 32). Notice that little difference in the shape of

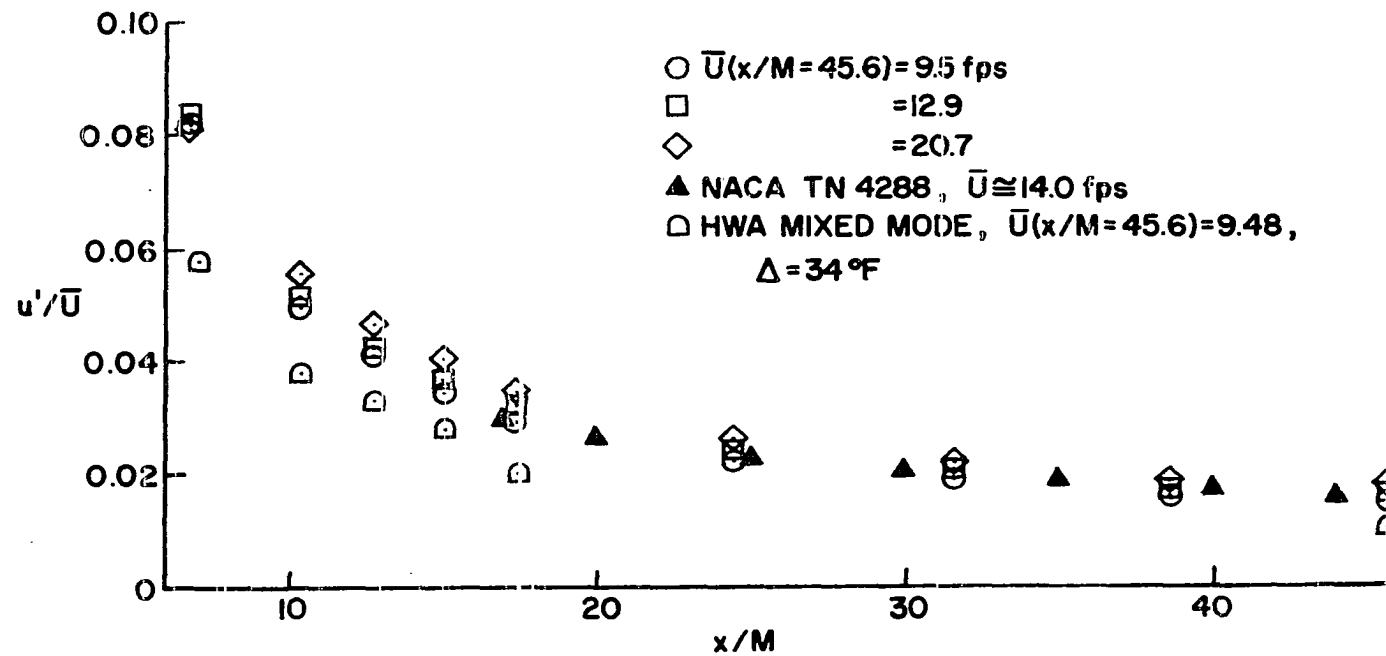


Figure 27. Decay of longitudinal turbulence

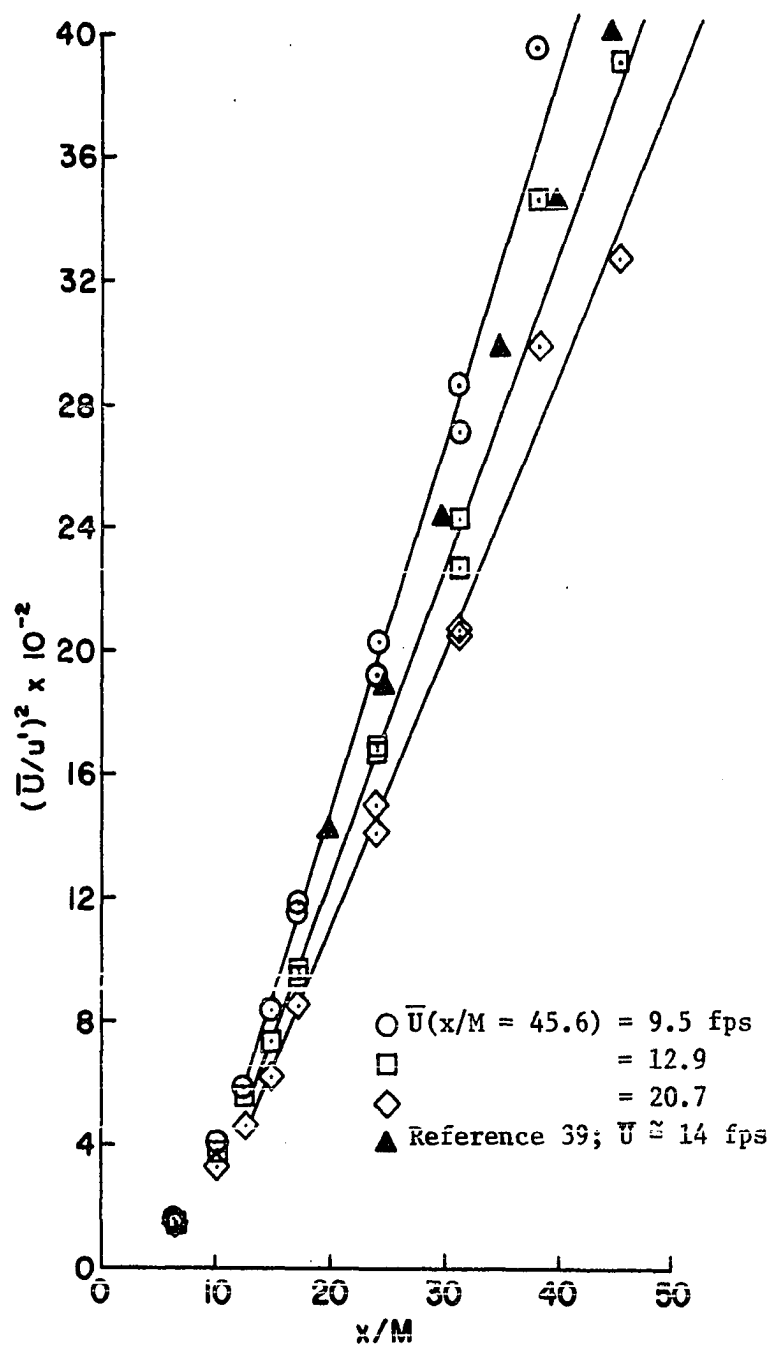
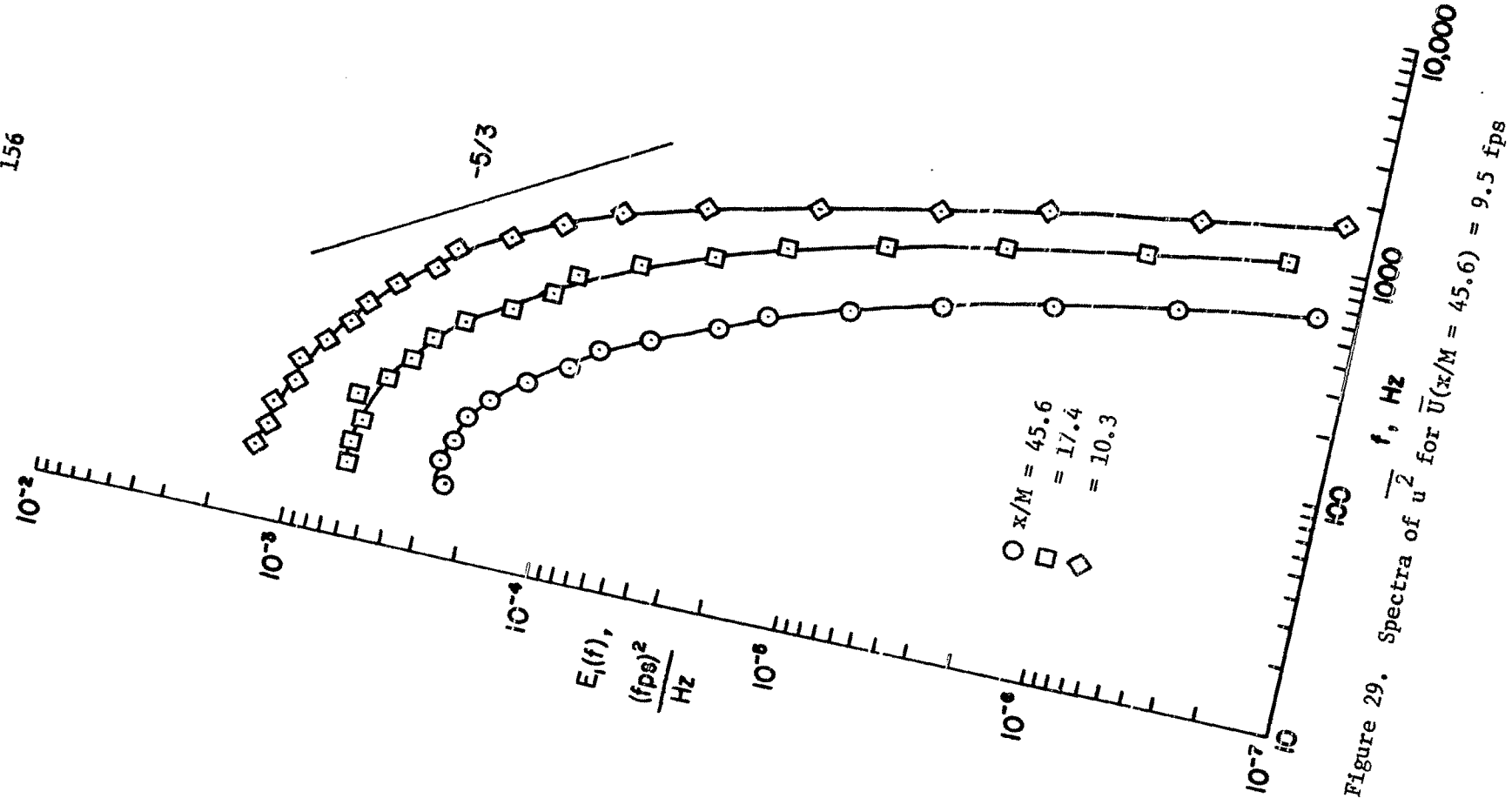


Figure 28. Inverse squares of longitudinal turbulence decay



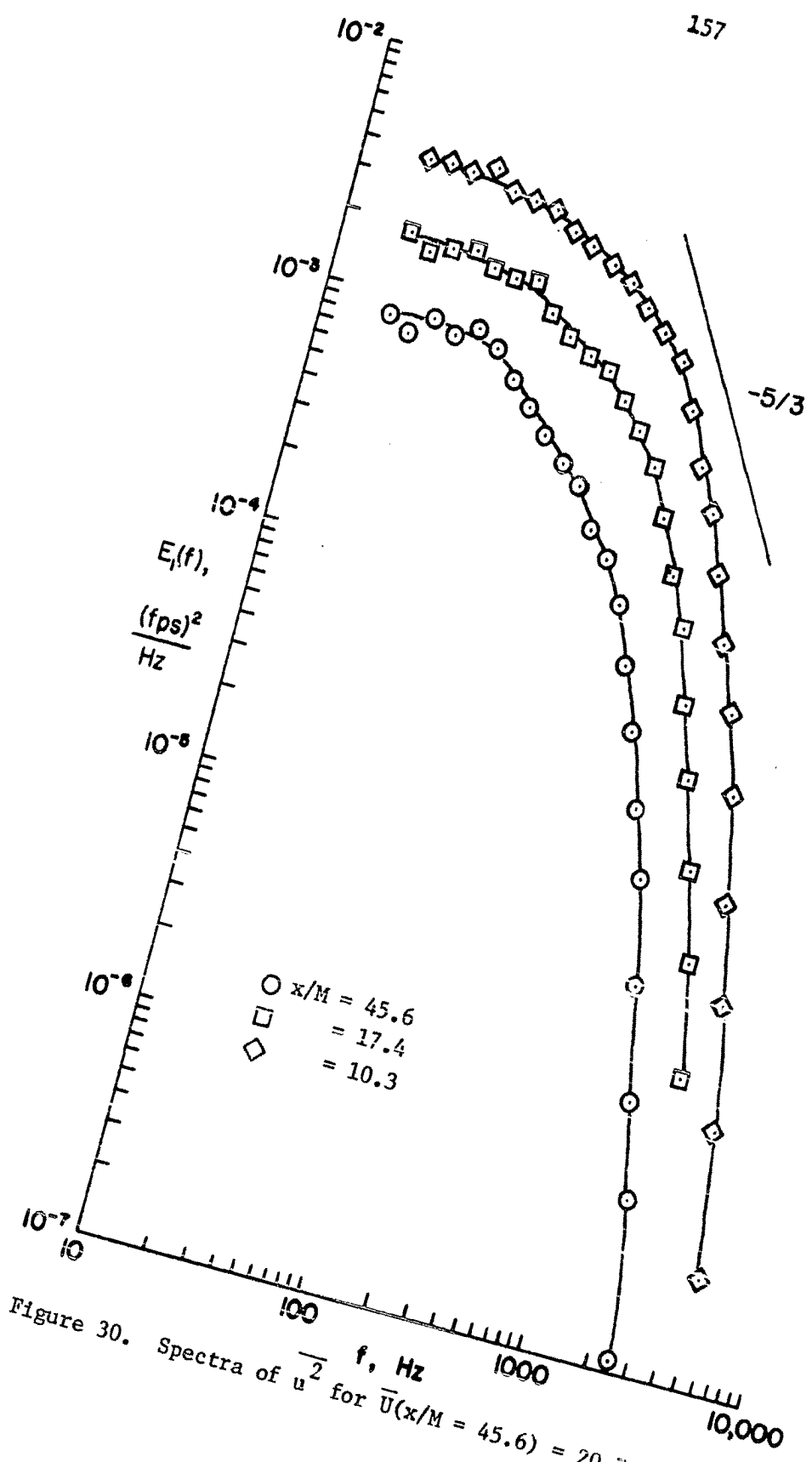


Figure 30. Spectra of  $\overline{u^2}$  for  $\overline{U}(x/M = 45.6) = 20.7$  fps



these spectra differentiates the isotropic and nonisotropic regions. The spectra at  $x/M = 45.6$  from Figures 29 and 30 are replotted in Figure 31 to show the effect of normalizing both axes to collapse these curves for comparison. For the abscissa a Strouhal effect is present due to convection at different mean speeds. This effect could be removed by plotting such curves vs a Strouhal number like  $St = fM/\bar{U}$  or wavenumber  $k = 2\pi f/\bar{U}$ . Denoting the  $\bar{U} = 9.5$  fps and  $\bar{U} = 20.7$  fps curves by a and b, respectively, we obtain  $f_b/f_a = \bar{U}_b/\bar{U}_a = 2.18$ . For the ordinate a  $\bar{u}^2$  or  $\bar{U}^2$  normalization is required since we expect

$$u' = \text{constant } \bar{U}$$

at a given  $x/M$ ; we get  $E_{1b}/E_{1a} = (\bar{U}_b/\bar{U}_a)^2 = 4.74$ . The shifted  $\bar{U} = 20.7$  fps curve is shown.

For comparison with the single  $\bar{u}^2$  spectrum presented in Reference 39 we have area-normalized and non-dimensionalized our  $x/M = 17.4$  spectrum from Figure 29 for plotting against dimensionless wavenumber (or Strouhal number) in Figure 32. Scale conversions were obtained as follows: for the ordinate

$$\frac{E_1(k_1)}{\bar{u}_M^2} = \frac{\bar{u}^2(k_1, B)}{Bu_M^2} = \frac{\bar{U}}{2\pi} \frac{E_1(f)}{\bar{u}_M^2} = \frac{\bar{U}}{2\pi} \frac{\bar{u}^2(f, B)}{Bu_M^2} \quad (6-2)$$

where  $E_1(f)$  is defined in (3-1) and we have used (3-10) and (3-30).

For the abscissa

$$kM = \frac{2\pi fM}{\bar{U}} \quad (6-3)$$

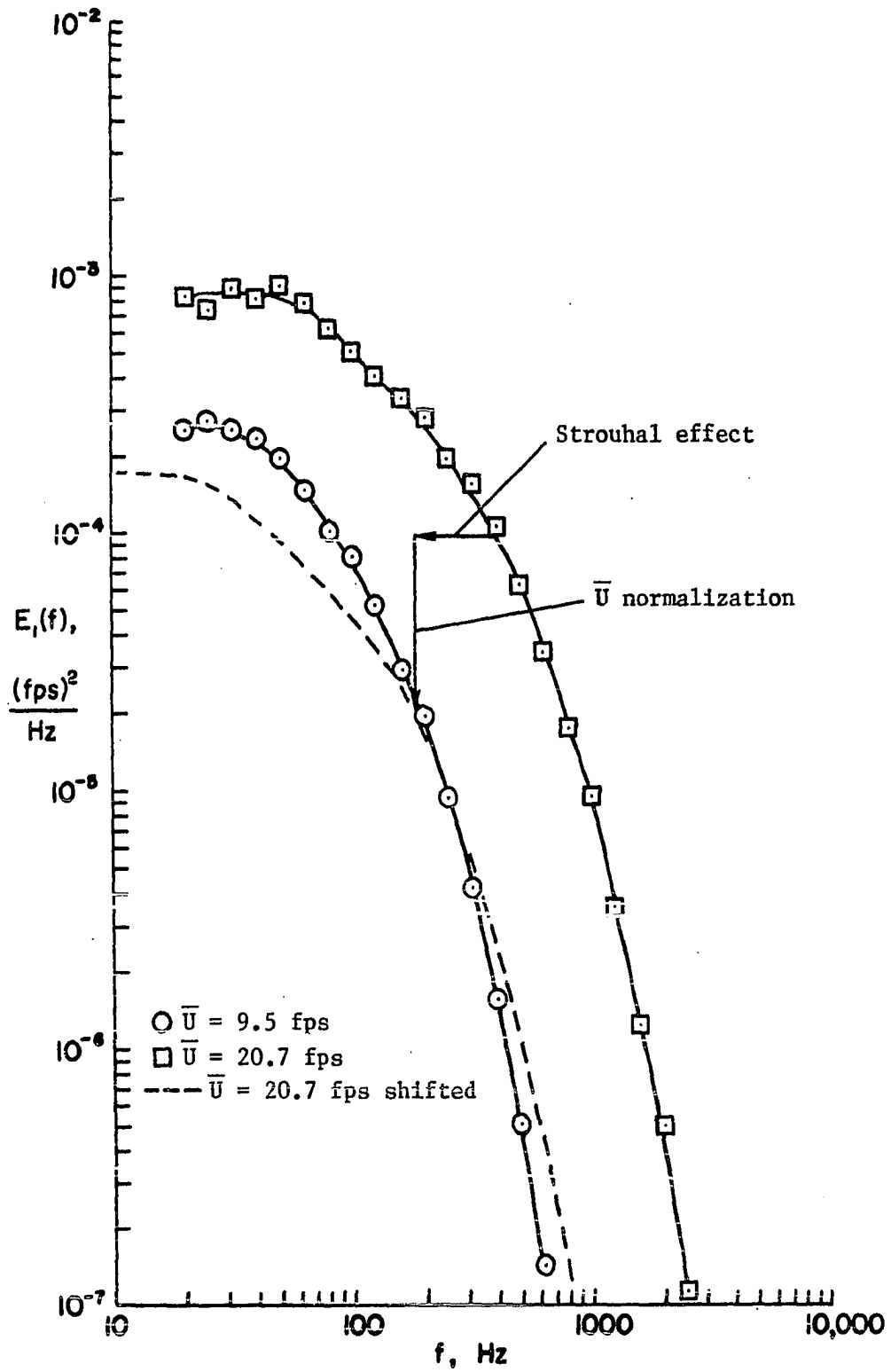
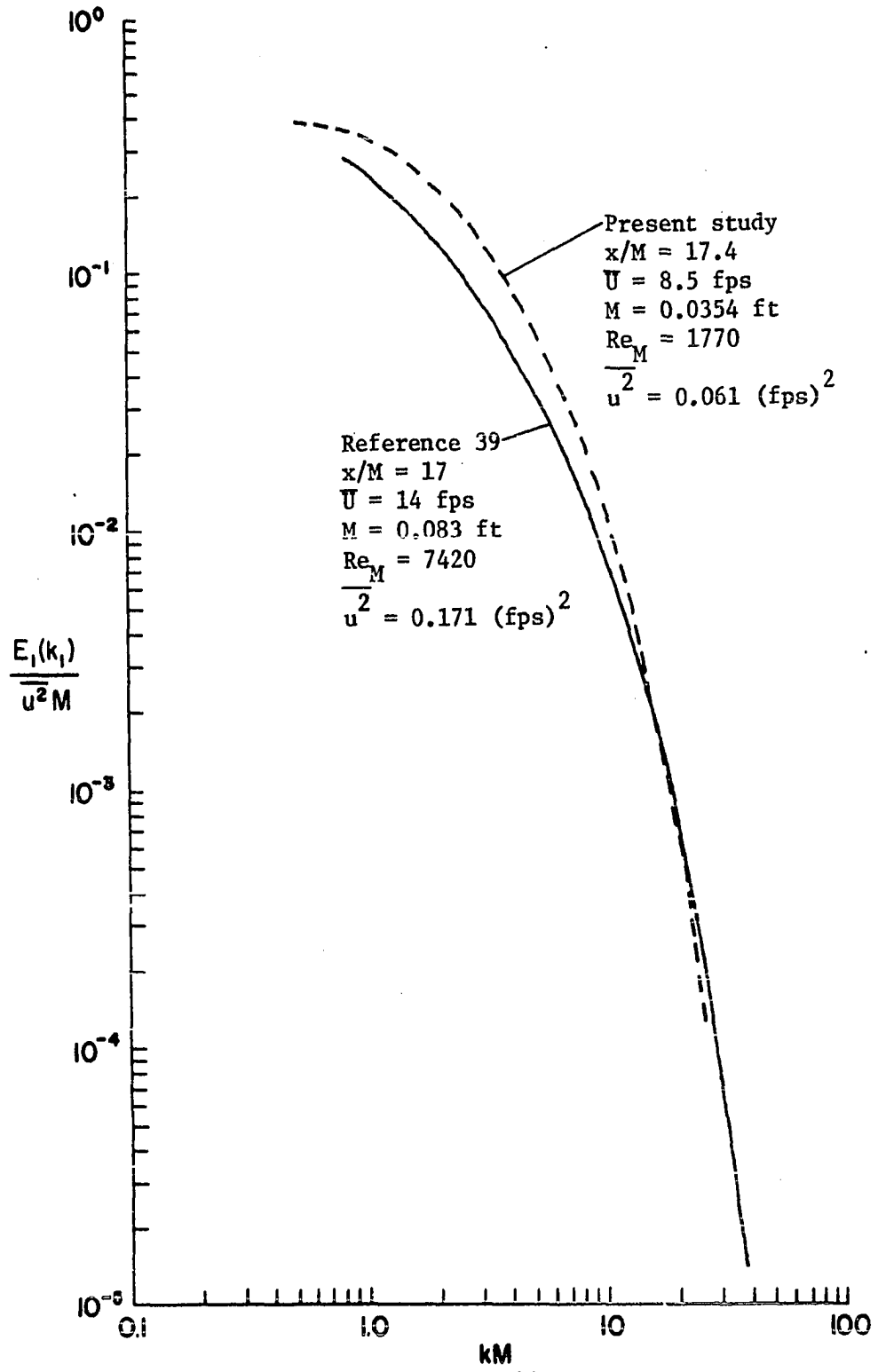


Figure 31. Spectra of  $u^2$  at  $x/M = 45.6$

Figure 32. Comparison of  $\overline{u^2}$  spectra

where we have used (3-10). From this figure we see that our velocity spectrum has essentially the same shape as that of Reference 39.

A typical Eulerian time autocorrelation coefficient of  $u$  has been plotted in Figure 33 first at small  $\tau$  to show symmetry about  $\tau = 0$  and then extended for  $\tau$  for later use. For the same conditions, a plot of the probability density function (see Reference 7) of  $u$ -fluctuations is given in Figure 34. In this figure the argument of the probability density function (pdf) is the standardized random variable  $u/u'$ , since  $\overline{u} = 0$  by definition. Coordinates of the standardized normal density function

$$p(z) = \frac{1}{(2\pi)^{1/2}} e^{-z^2/2} \quad (6-4)$$

for example,

<u>z</u>	<u>p(z)</u>
0	0.399
0.5	0.352
1.0	0.242
1.5	0.130
2.0	0.054
3.0	0.004

are indistinguishable from our pdf showing that our  $u$  data is, indeed, Gaussian.

### C. Scalar Turbulence

#### 1. CBS noise identification with probability density and correlation function samples

A discussion of crossed-beam schlieren signal composition including noise has been deferred to now because of its importance in interpreting

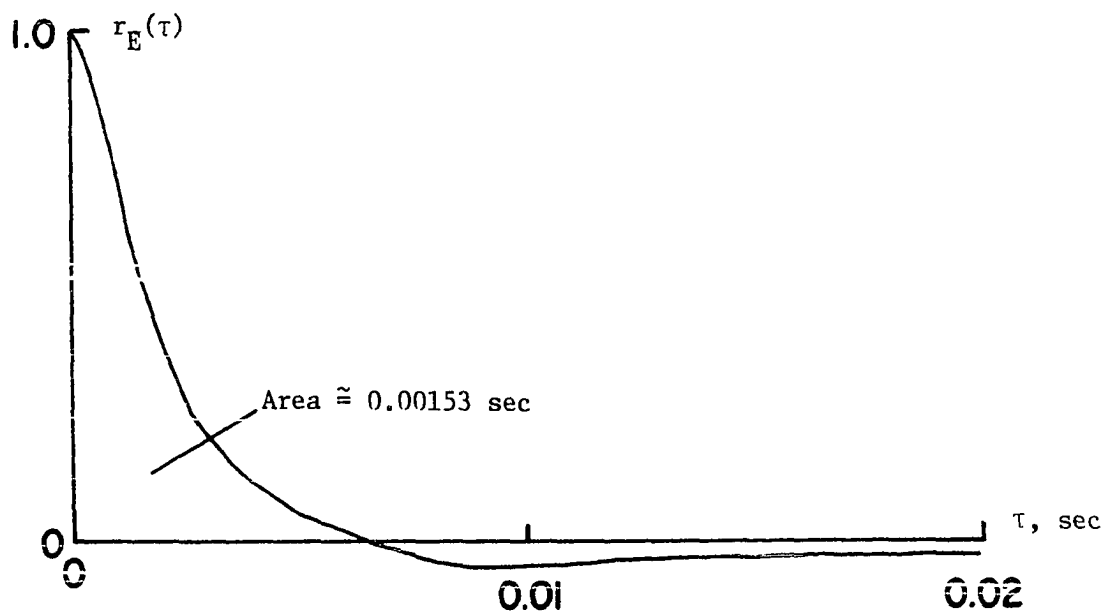
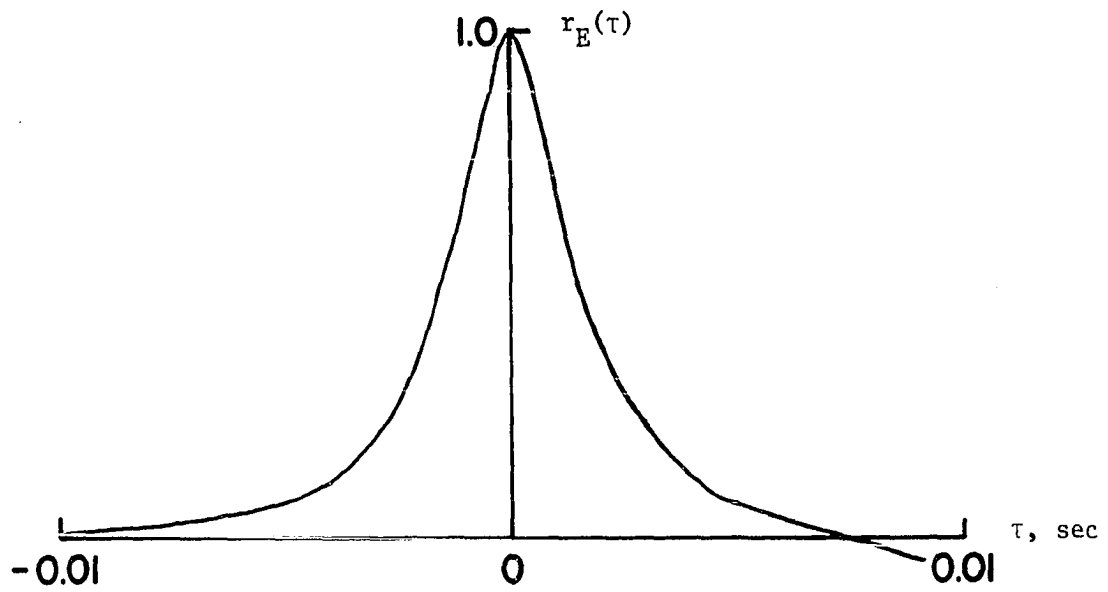


Figure 33. Eulerian time autocorrelation coefficient of longitudinal velocity fluctuations;  $x/M = 17.4$  and  $U = 8.5 \text{ fps}$

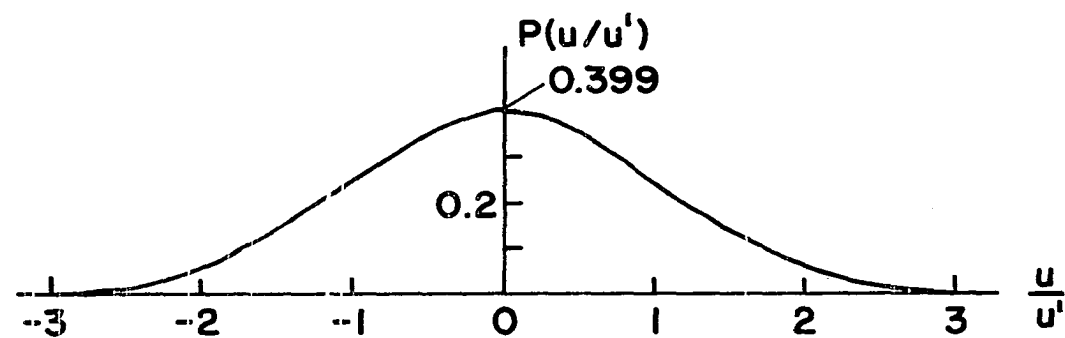


Figure 34. Probability density function of longitudinal velocity fluctuations

our CBS  $\theta'$  and  $\overline{\theta^2}$  spectral data. Whenever the effect of a physical variation is converted to variations in an electrical signal, there is likely to be some noise on the electrical signal. In our case, the electrical signal out of each photodiode was a composite of signal (due to scalar turbulence in the test section), noise due to laser ripple (see Chapter V), noise due to other electrical sources, noise due to vibration, and possibly, noise due to scattering/absorption. Fortunately, the sum of all these possible sources of noise can be isolated by running the tunnel with a cold grid and making CBS measurements.

Thus, in this section we will:

1. Identify the 120 Hz laser power ripple in the basic photodiode signal and in the CBS covariance.
2. Confirm a flow-related signal due to temperature fluctuations.
3. Illustrate 1. and 2. with auto- and cross-correlograms.
4. Eliminate scattering/absorption as a possible noise contributor.
5. Show the CBS signal due to scalar turbulence is approximately Gaussian.
6. Present single beam spectra of noise and signal-plus-noise (integrated effects across test section).
7. Identify and isolate the total noise contribution in the CBS co-spectrum (of density or temperature fluctuations) including laser ripple, electronic, and vibration effects.
8. Identify and isolate the total noise contribution in the CBS covariance, and show how signal plus noise in certain frequency bands

vary with grid overheat.

9. Show that, theoretically, we should be able to correct for noise by subtracting a noise measurement from the composite signal.

In VI.A. above we observed an increase in  $\theta$ -fluctuations in the thermal boundary layer. Here we note that while these fluctuations will contribute appreciably to the single beam signals, they are uncorrelated between beams and, consequently, will not contribute to the CBS covariance. However, the laser power supplies were connected to a common line source, so the power ripple on the two beams was correlated and, therefore, contributed to the measured covariance.

A look at the basic unfiltered, unamplified signal directly out of each photodiode on the scope and on the true rms voltmeter with knife edges set at  $\bar{E} = -0.660/2 = -0.330$  volt for maximum (linear) sensitivity produced the following results:

Blower off (laser ripple and table motion)

System A (horizontal)

$e \approx 3$  mV peak to peak (read on scope)

$e' = 1.5 \text{ mV} \pm 0.5 \text{ mV}$

This signal had a very low frequency ( $< 20\text{Hz}$ ) oscillation of about 5 mV peak to peak observed on the scope.

System B (vertical)

$e \approx 4$  mV peak to peak (scope)

$e' = 3 \text{ mV} \pm 1 \text{ mV}$

This signal had a very low frequency ( $< 20\text{Hz}$ ) oscillation of about 15 mV peak to peak

Blower on ( $\bar{U}(x/M = 45.6) = 9.5$  fps; laser ripple, table motion, and vibration)

System A

$e \approx 4$  mV peak to peak

$e' = 1.4 \text{ mV} \pm 0.4 \text{ mV}$

Low frequency oscillation: 6 mV peak to peak



## System B

$$e \approx 10 \text{ mV peak to peak}$$

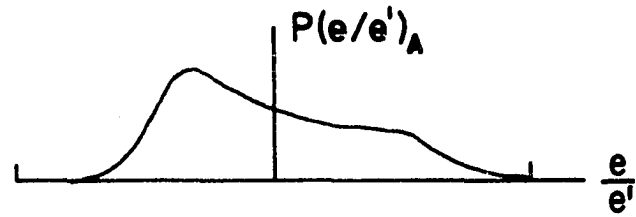
$$e' = 3.5 \text{ mV} \pm 1 \text{ mV}$$

Low frequency oscillation: 15 mV peak to peak

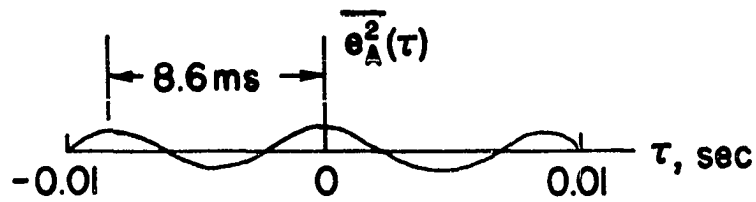
The appearance of the basic signal with blower on or off for both systems was a clean sawtooth shape with rounded peaks and a period of about 8 msec, indicative of the laser power ripple. Only a minor effect due to system vibration is evident. The low frequency oscillation was due to slight frame movement and was filtered-off with the 20 Hz high-pass.

To further investigate the CBS signal and verify a flow-related signal due to temperature fluctuations, a test was performed in which CBS covariance, pdf's, and auto- and cross-correlograms were recorded for beams crossed outside with blower off, and inside the test section at  $x/M = 6.78$  for unheated and heated flow with  $\bar{U} = 8.0 \text{ ft/sec}$  and  $\Delta = 20^\circ\text{F}$ . Some difference was observed between the pdf's and correlograms due to system vibration, but the noise signals were dominated by laser ripple. Figure 35 shows a pdf and auto- and cross-correlograms for beams crossed outside with a 20-2000 Hz bandpass. The period of characteristic ringing of the correlograms may be measured as about 8.6 msec. Notice the distorting effect of the dominant 120 Hz on the pdf which is clearly non-Gaussian. Similar measurements without high-pass filtering at 20 Hz produced dc shifts of the autocorrelograms corresponding to the presence of low frequency components. Figure 35 may be contrasted with Figure 36 which shows typical pdf's and auto- and cross-correlograms recorded in heated flow. Notice the near Gaussian shape of the pdf's and the marked difference in shape of the

Probability density function of signal A



Autocorrelogram of signal A



Cross-correlogram

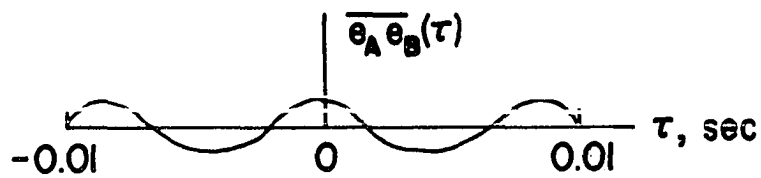


Figure 35. Samples of probability density function and correlograms for CBS beams crossed outside the test section

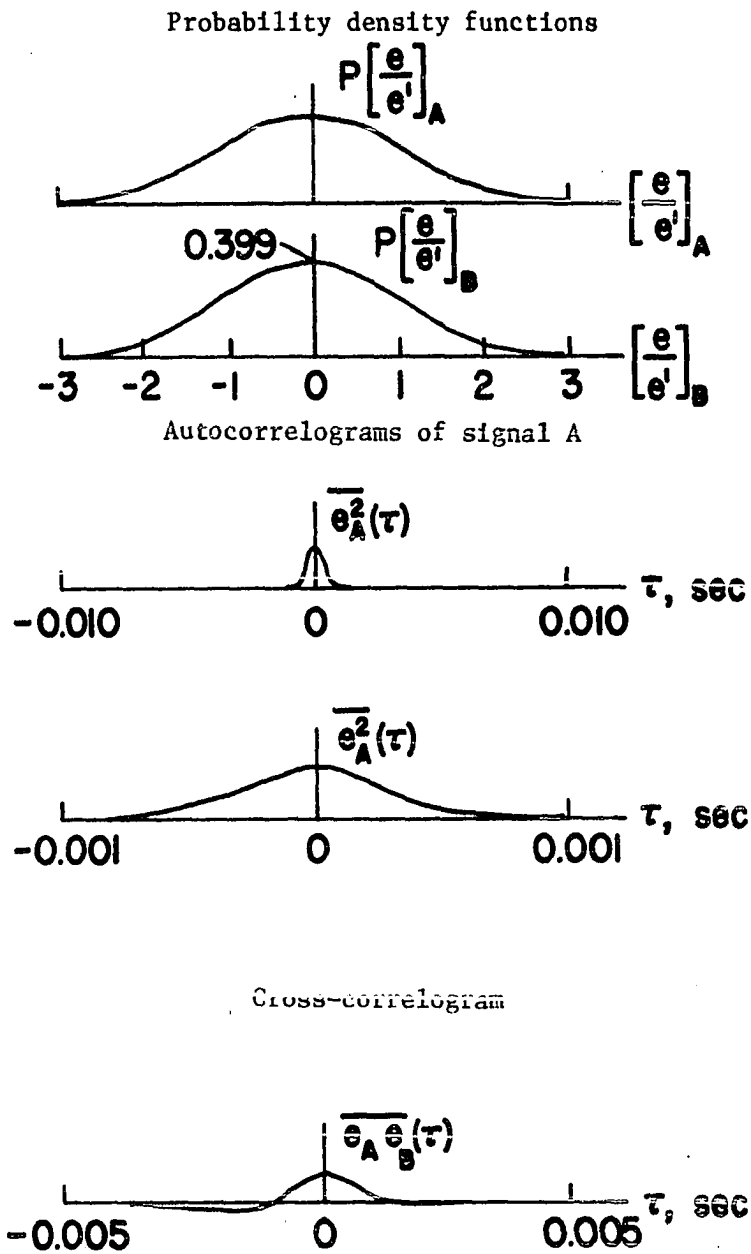


Figure 36. CBS pdf's and correlograms in heated flow at  $x/M = 6.78$ ,  
 $U = 8.0$  fps,  $\Delta \approx 20^\circ\text{F}$

correlograms from the unheated case. To prove flow association, the tunnel speed setting was changed to vary the correlogram shapes (the peaks get thinner with increasing high frequency content) and the beams were separated to shift the cross-correlogram peak in  $\tau$ , as will be seen in space-time correlograms below under Convection Speed. While substantial signals were being obtained due to scalar turbulence, these early "first-look" measurements indicated that the noise, due primarily to 120 Hz ripple, might be a significant part of the overall signal; for example, during these tests we measured  $(\overline{e_A e_B})_N = 1.58 \times 10^{-7}$  (volt)<sup>2</sup> for the noise and  $(\overline{e_A e_B})_{S+N} = 21.7 \times 10^{-7}$  (volt)<sup>2</sup> for the composite signal. At this particular overheat, the noise content is a small enough part of the composite signal to not distort the pdf's or correlograms, but it is contributing linearly to the covariance level.

To assure that none of the noise signal resulted from particulate scattering, one beam was fully exposed on its photodiode and the basic signal rms value monitored with the blower on and off; no decrease in signal level was detected.

Single beam voltage spectra measured at  $x/M = 9.13$  using the correlator and then the true rms voltmeter to measure  $\overline{e_A^2}(f, B)$  are shown in Figures 37 and 38, respectively, and are nearly identical. These power spectrums were obtained for three cases:

1.  $\overline{U} = 0$
2.  $\overline{U} = 8.5$  fps,  $\Delta = 0$
3.  $\overline{U} = 8.5$  fps,  $\Delta = 20^\circ\text{F}$

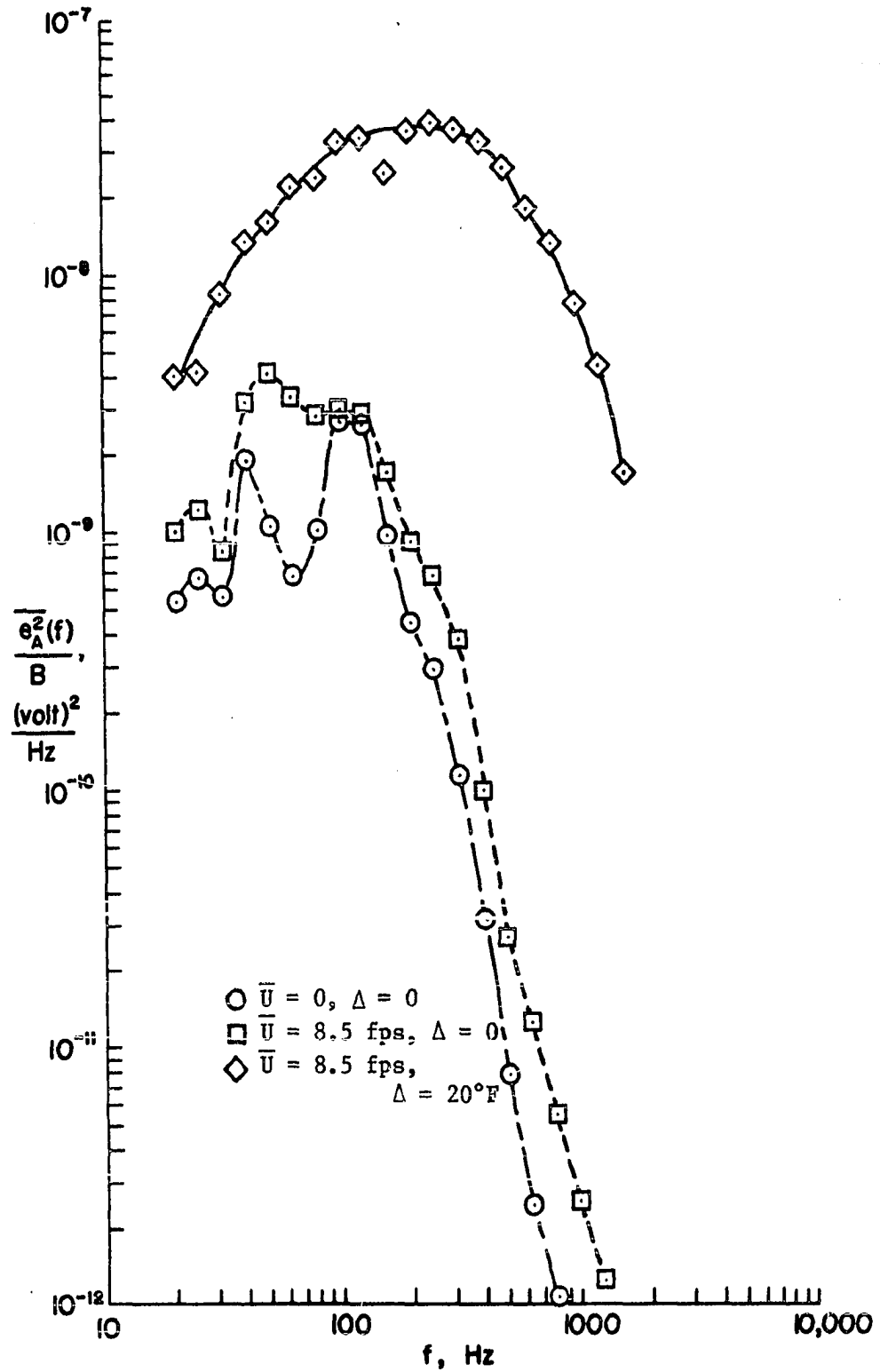


Figure 37. Single-beam voltage spectra for signal A processed on correlator

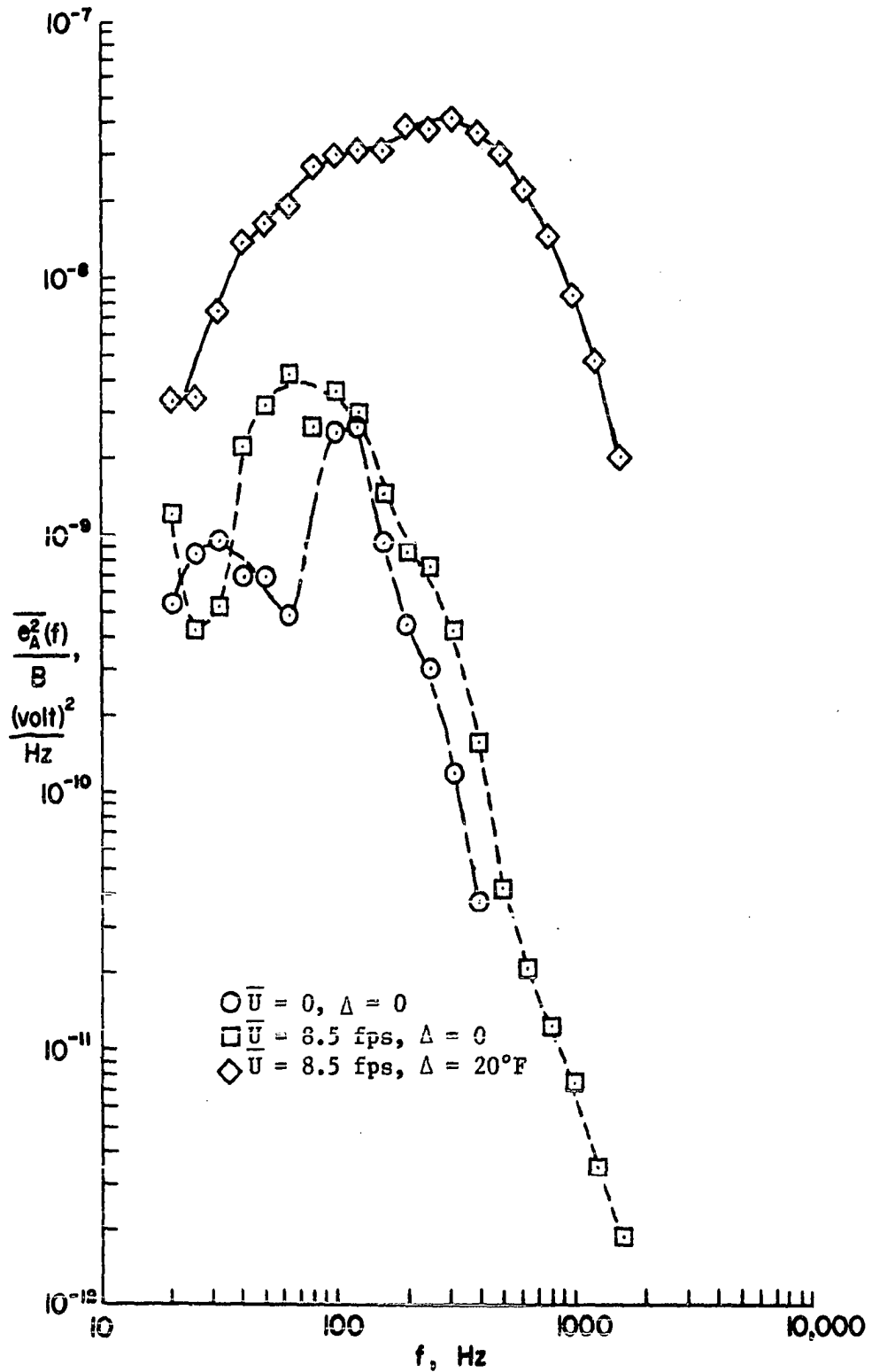


Figure 38. Single-beam voltage spectra for signal A processed on true rms voltmeter

Case 1 represents the spectrum of laser ripple plus electronic noise; Case 2 shows some energy increase at frequencies below about 100 Hz due to system vibrations, and represents the total single beam noise; and, Case 3 is the total signal-plus-noise spectrum.

To isolate and define the total contribution of laser ripple, electronic, and system vibration noise to the CBS 3-D co-spectra, a noise voltage spectrum was obtained for  $x/M = 9.13$  and  $\bar{U} = 8.1$  ft/sec with beams crossed in the test section and a cold grid. This total noise spectrum is compared in Figure 39 with the pure tone spectrum replotted from Figure 16 after area-normalizing to match up the peaks. It can be seen that the CBS noise is largely due to the pure tone at 120 Hz. The faired curve in this figure was taken as a standard noise reference, and is shown on co-spectra presented below as a convenience (the noise reference spectrum was checked two weeks later and found not to have changed appreciably in shape); no corrections have been applied to the CBS spectra. As an example, the noise reference from Figure 39 is compared in Figure 40 with a 3-D CBS co-spectrum or  $\overline{\theta^2}$  spectrum at the same location and speed, but with  $\Delta = 21^\circ\text{F}$ . Both spectra were converted from voltage to temperature spectra using Equation 5-7, so that the noise spectrum is here only in "effective" temperature units. The difference in power levels between these two spectra at any frequency is the contribution to the composite signal due to scalar turbulence. If we assume the total noise is statistically independent and, therefore, uncorrelated with the signal due to scalar turbulence, then the variance

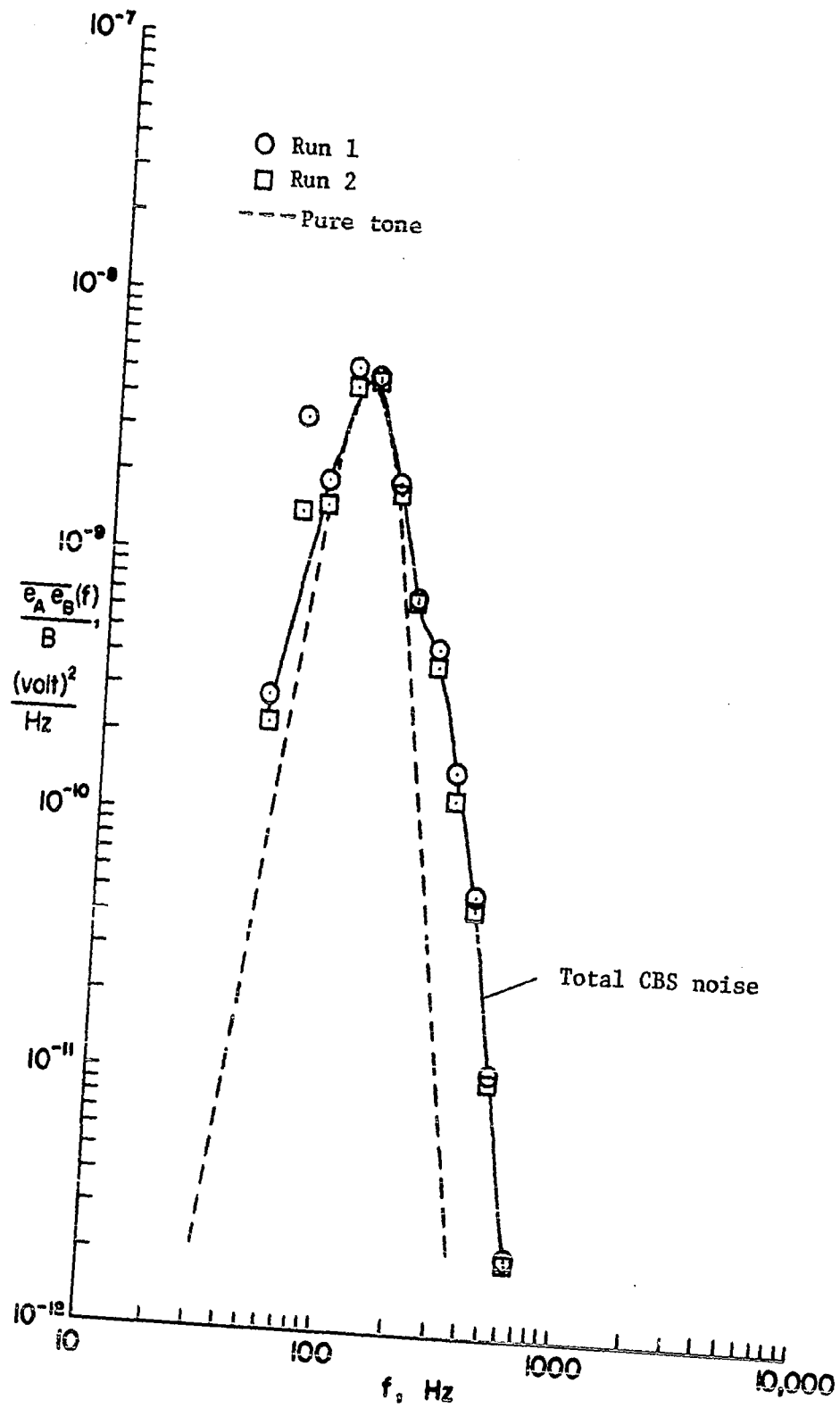


Figure 39. CBS total noise spectrum compared with pure tone spectrum



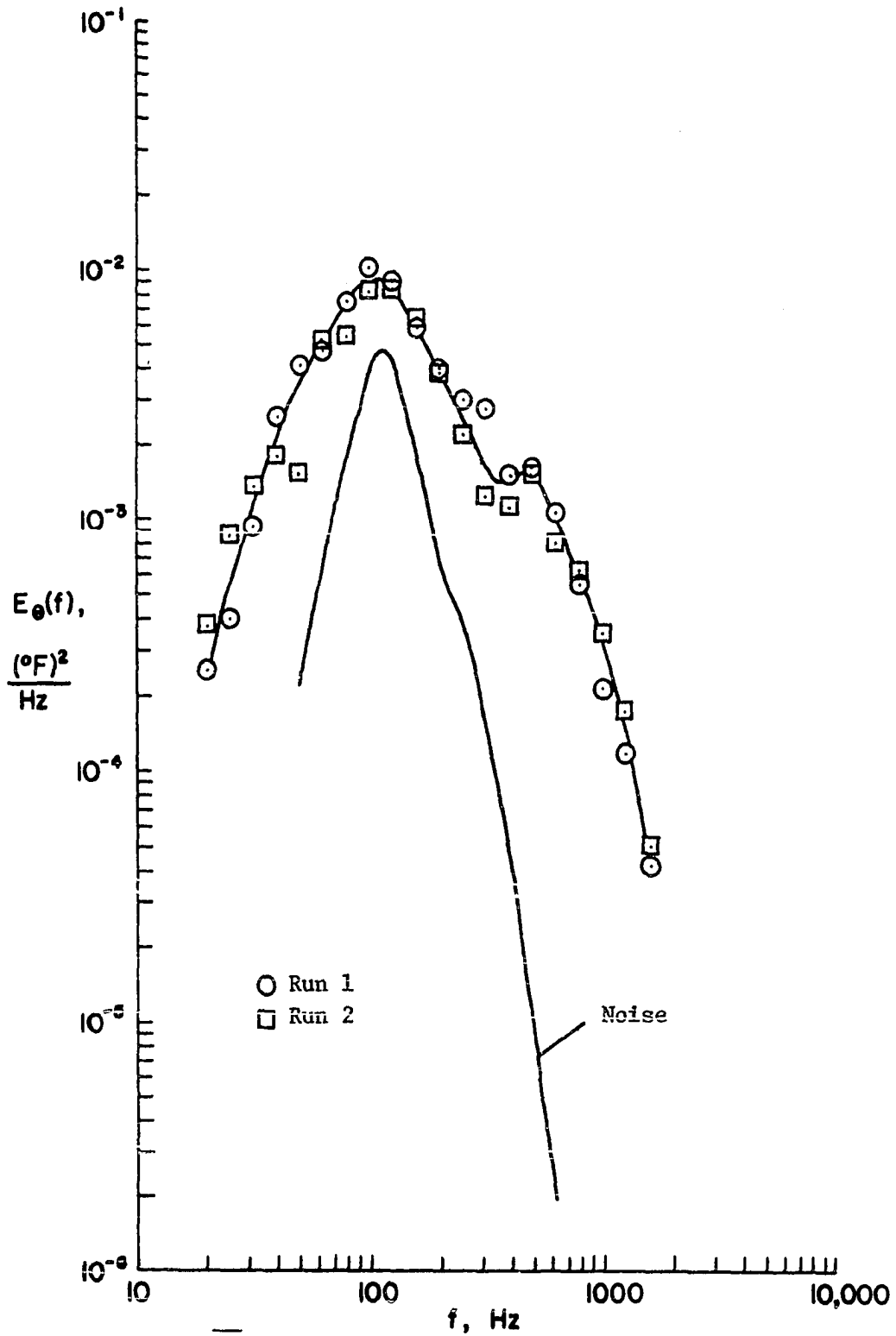


Figure 40. CBS  $\theta^2$  spectra at  $x/M = 9.13$ ,  $\bar{U} = 8.1$  fps, and  $\Delta = 21^{\circ}\text{F}$  compared with CBS total noise spectrum (in equivalent units)

of total noise subtracts directly from the variance of signal-plus-noise as we will see. So, to correct our spectra for noise we should subtract the noise energy from the signal-plus-noise energy at each frequency. Now, since we are plotting power, each decade in energy represents an order of magnitude or 10 dB change. Therefore, in this figure the upward distortion of the true  $\overline{\theta^2}$  spectrum is most significant near the peak at 120 Hz where the noise is a little over half the total signal but drops off rapidly on either side at nearly 24 dB/octave, the filter shape. As we will see, the severity of spectral distortion due to the noise spike, depends on the signal level due to scalar turbulence, which is proportional to grid overheat. Data to be presented will show that raising  $\Delta$  tends to shift the composite spectrum upward and outward on both sides making the noise less of a factor. The location of our noise peak is most unfortunate; it protrudes right up into the region of maximum energy containing eddies in the region of  $k_g$  where no theory is yet available to predict the spectral shape! Thus, we have operated the grid at some relatively high overheats to get a better look at this important region.

Before leaving Figure 40 we note for future reference that  $x/M = 9.13$  is probably well-within the nonisotropic flow region. The jog in this spectrum at about 500 Hz was not generally observed at positions further downstream, and is probably due to a Karman vortex-like periodicity in the grid wake, although 500 Hz seems a bit high based on the following estimate. Assuming  $v = 17 \times 10^{-5} \text{ ft}^2/\text{sec}$ , the Reynolds

number based on rod diameter ( $d = 0.125$  in) at  $\bar{U} = 8.1$  ft/sec is  $Re_d = 496$  which is the right range for vortex shedding with a Strouhal number  $St = fd/\bar{U} = 0.21$  (see Schlichting 45). We can then estimate the vortex shedding frequency as

$$f = \frac{0.21 (8.1 \text{ ft/sec})(12 \text{ in/ft})}{0.125 \text{ in}} = 163 \text{ Hz}$$

A frequency of  $f = 500$  Hz implies a scale of about  $d/3$ , or a higher  $\bar{U}$ , or combination of both.

To obtain a noise correction for our CBS temperature decay data, theoretically, we should be able to measure the variance of total noise with filter pass-bands of 20-2000 Hz. Assuming the composite signals from the detectors are  $e_A = e_{AS} + e_{AN}$  and  $e_B = e_{BS} + e_{BN}$  where, for example,  $e_{AS}$  is the true signal due to scalar turbulence, and  $e_{AN}$  the independent total noise including laser ripple, then the auto- and cross-correlations are

$$\overline{e_A^2} = \overline{(e_{AS} + e_{AN})^2} = \overline{e_{AS}^2} + 2 \overline{e_{AS}e_{AN}} + \overline{e_{AN}^2} \quad (6-5)$$

$$\overline{e_B^2} = \overline{(e_{BS} + e_{BN})^2} = \overline{e_{BS}^2} + 2 \overline{e_{BS}e_{BN}} + \overline{e_{BN}^2}$$

$$\overline{e_A e_B} = \overline{(e_{AS} + e_{AN})(e_{BS} + e_{BN})} = \overline{e_{AS}e_{BS}} + \overline{e_{BS}e_{AN}} + \overline{e_{AS}e_{BN}} + \overline{e_{AN}e_{BN}} \quad (6-6)$$

But,  $\overline{e_{AS}e_{AN}} = \overline{e_{BS}e_{BN}} = \overline{e_{BS}e_{AN}} = \overline{e_{AS}e_{BN}} = 0$  if we assume signal and noise were uncorrelated. However,  $\overline{e_{AN}e_{BN}} \neq 0$  due to the laser ripple. Thus, in theory

$$\overline{e_{AS}^2} = \overline{(e_{AS} + e_{AN})^2} - \overline{e_{AN}^2} \quad (6-7)$$

$$\overline{e_{BS}^2} = \overline{(e_{BS} - e_{BN})^2} - \overline{e_{BN}^2}$$

$$\overline{e_{AS}e_{BS}} = \overline{(e_{AS} + e_{AN})(e_{BS} + e_{BN})} - \overline{e_{AN}e_{BN}} \quad (6-8)$$

Attempts at measuring  $\overline{e_{AN}e_{BN}}$  were only partially successful in practice due to slight day to day changes and normal data scatter. Therefore, a fixed number could not be assigned to this covariance, say, by averaging several readings, or by measuring it prior to each run, with complete reliability. As an example, we present measurements of  $\overline{e_{AN}e_{BN}}$  under various conditions during the same run in Table 8.

Table 8. Noise measurements at  $x/M = 38.5$  and  $\bar{U} = 9.3$  fps

$\overline{e_{AN}e_{BN}}$ , (volt) <sup>2</sup>	Condition
$3.38 \times 10^{-7}$	$\Delta = 0$ ; full exposure
$3.67 \times 10^{-7}$	$\Delta = 0$ ; $\bar{E} = -0.330$ volt
$3.15 \times 10^{-7}$	$\Delta = 22^\circ\text{F}$ ; full exposure
$3.58 \times 10^{-7}$	$\Delta = 24^\circ\text{F}$ ; full exposure

The data obtained with knife edge removed (full exposure and  $\bar{E} = -0.660$  volt) were divided by four. The average of these values is  $\overline{e_A e_B} \cong 3.45 \times 10^{-7}$  (volt)<sup>2</sup>; however, the uncertainty in this number was unacceptable for obtaining consistent results at low  $\Delta$  where the composite spectrum was tending to merge with the noise spectrum.

Figure 41 presents a dissection of the CBS covariance into specific frequency bands and shows the variation of  $\overline{e_A e_B}$ , the CBS covariance of signal-plus-noise with grid overheat. This composite signal is shown in the following bandwidths (BPF): 20 to 2000 Hz, 20 to 240 Hz, centered at 120 Hz (corrected for insertion loss) and 240 to 2000 Hz. These measurements were not all made during the same run nor on the same day. However, an additional run at  $\Delta \approx 11^\circ\text{F}$  is shown with bandwidths 20 to 75 Hz, 75 to 240 Hz, and 240 to 2000 Hz. Also, several noise measurements are indicated on the  $\Delta = 0$  axis including the average from Table 8. Notice that a relatively small (but certainly non-negligible) portion of the overall signal lies in the frequency range 240 to 2000 Hz at low  $\Delta$ , in spite of the fact that this interval includes a preponderance of our bandwidth of interest (on a linear scale). The bandwidth 20 to 75 Hz is also a small contributor at  $\Delta \approx 11^\circ\text{F}$ . Most of the energy appears in the pass-band 20 to 240 Hz. Notice that energy in the pass-bands 20 to 240 Hz and 240 to 2000 Hz approximately sum up to 20 to 2000 Hz as they should. The full 20 to 2000 Hz signal approaches some initial level at  $\Delta = 0$  which is clearly inflated by a signal in the 20 to 240 Hz pass-band, and more specifically at 120 Hz. Since the noise in 20 to 240 Hz is equal to the noise due to laser ripple at 120 Hz (at  $\Delta = 0$ ), the contributions due to electronic noise and vibration must be relatively small.

Due to the uncertainty in measuring  $\overline{e_{AN} e_{BN}}$ , it was decided to least squares fit each data curve of  $\overline{e_A e_B}$  vs  $\Delta^2$  (found to be approximately

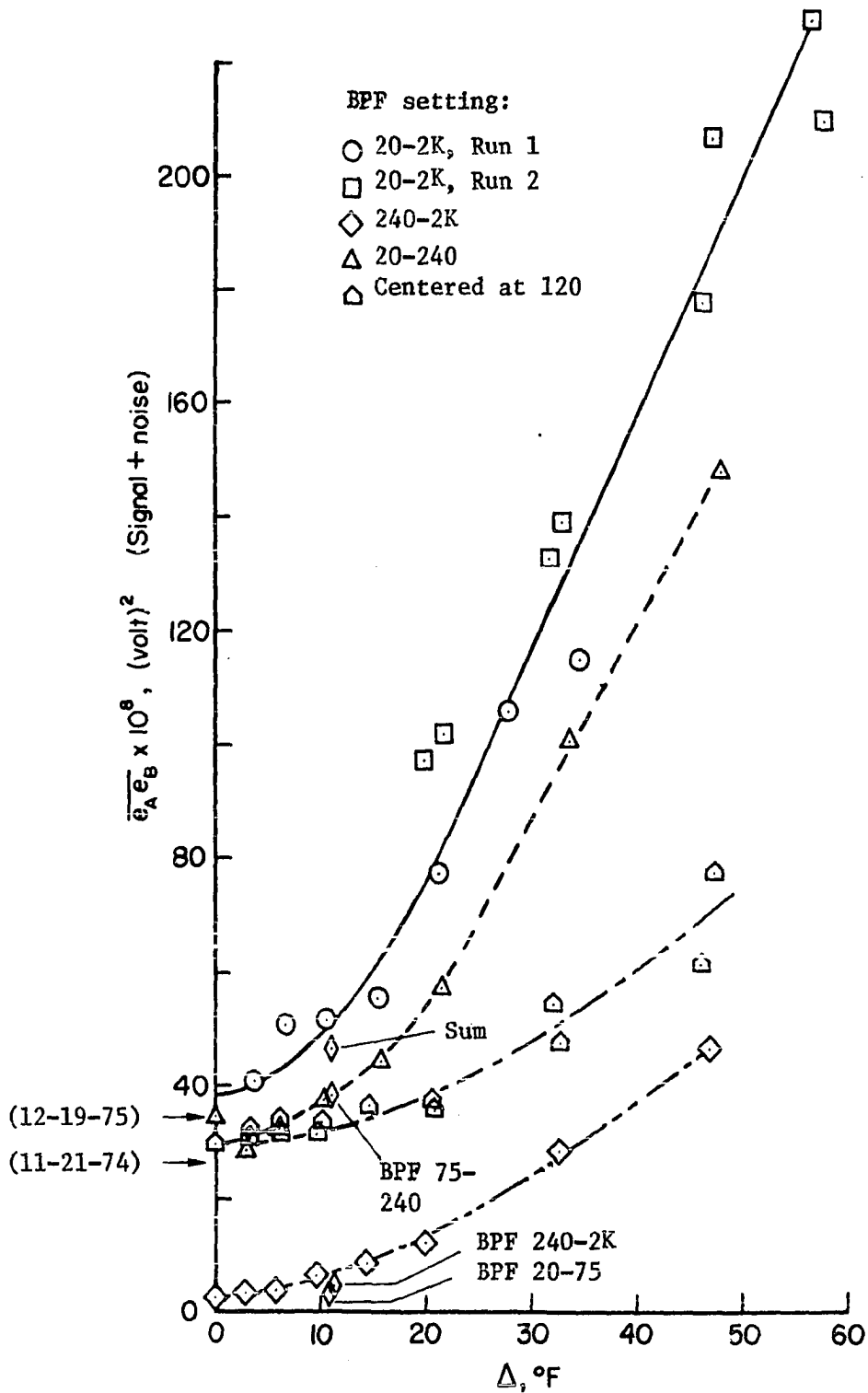


Figure 41. Separation of signal and noise in CBS covariance at  $x/M = 31.5$  and  $\bar{U} = 9.1$  fps

linear as hoped) with an expression like (6-8)

$$\overline{e_A e_B} = \overline{e_{AN} e_{BN}} + K \Delta^2 \quad (6-9)$$

so that

$$\overline{e_{AS} e_{BS}} = K \Delta^2 \quad (6-10)$$

and we can use (5-4) to get

$$\theta' = 1021 (\overline{e_{AS} e_{BS}})^{1/2} = 1021 (K)^{1/2} \Delta \quad (6-11)$$

The form of (6-9) is

$$y_k = a + b x_k$$

where

$$y_k = \overline{(e_A e_B)_k}, \quad x_k = (\Delta_k)^2$$

$$a = \overline{e_{AN} e_{BN}} = \text{noise correction}$$

$$b = K$$

The parameters  $a$  and  $b$  were solved using the normal equations for  $N$

points:

$$\sum_{k=1}^N y_k = a N + b \sum_{k=1}^N x_k$$

(6-12)

$$\sum_{k=1}^N x_k y_k = a \sum_{k=1}^N x_k + b \sum_{k=1}^N x_k^2$$

We will see that the resulting variation in  $\overline{e_{AN} e_{BN}}$  solved in this way appears to be random.

We may conclude from the above discussions that in this application of the crossed-beam schlieren, 0.5% ripple was really more than we would have desired (particularly at 120 Hz) and that additional filtering in

the laser power supplies would have been desirable. However, while laser noise was a significant problem, the author believes that it has been clearly identified and satisfactorily handled in the data reduction.

## 2. Temperature fluctuation decay

In this section  $\theta'$  decay data measured using the resistance thermometer and CBS will be presented and compared; the scalar decay rate will be examined; and, the results will be compared with data from Reference 39. Probability density functions of resistance thermometer measurements of  $\theta$  were approximately Gaussian.

Figure 42 shows a summary of our resistance thermometer decay measurements for  $\bar{U}(x/M = 45.6) = 9.5$  ft/sec. At a given  $x/M$ ,  $\theta'$  was found to vary linearly with  $\Delta$ , showing  $\Delta$  to be the proper normalizing parameter as expected. The only deviation from linearity observed was for  $x/M = 6.78$  starting at about  $\Delta = 22^\circ\text{F}$ . For all practical purposes the resolution of this instrument was not fine enough to extract the slow  $\theta'$  decay downstream of  $x/M = 17.4$ . Least square fitting the data points assuming  $\theta' = 0$  at  $\Delta = 0$  barely resolved a downward trend; thus, it was felt that the resistance thermometer  $\theta'$  decay in the isotropic region was lost in data scatter. We now shift attention to CBS data.

Least squares curve fits to the CBS single beam voltage response to grid overheat are shown in Figure 43. Assuming Equations 6-7 are



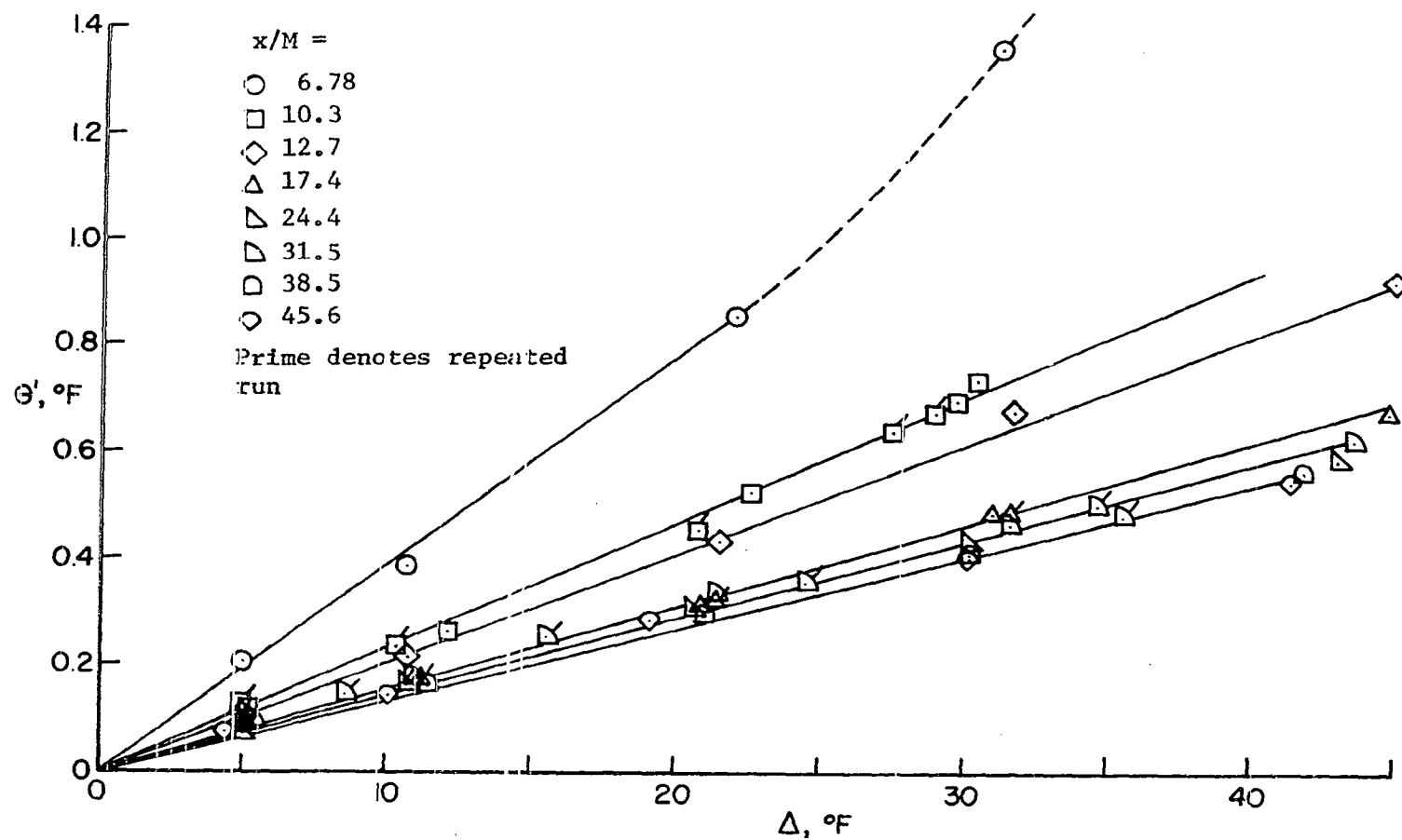


Figure 42. Resistance thermometer temperature fluctuation response to grid overhear for  $\bar{U}(x/M = 45.6) = 9.5$  fps

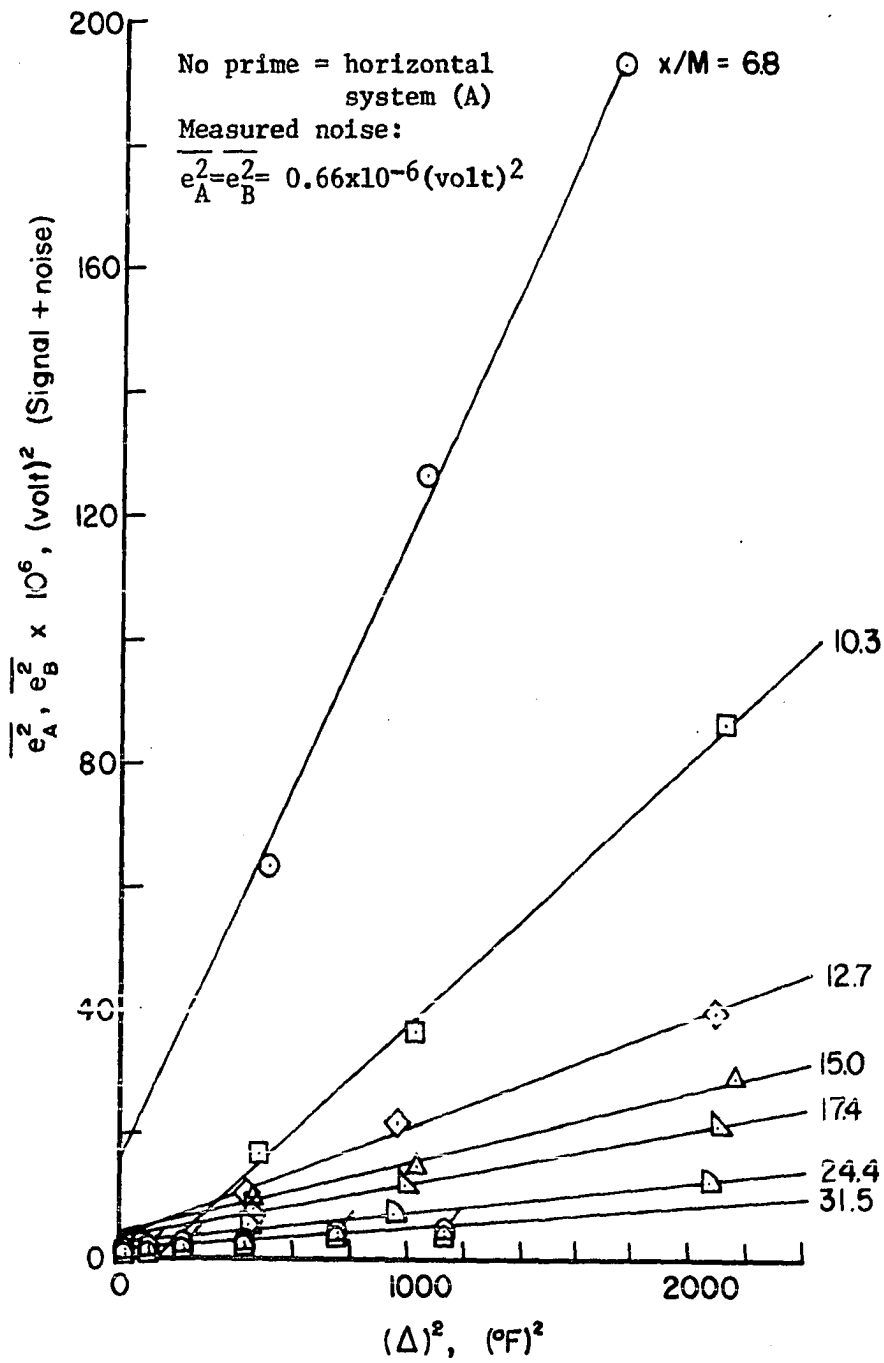


Figure 43. CBS single beam response to grid overheating with  
 $\bar{U}(x/M = 45.6) = 9.5 \text{ fps}$

applicable here, it appears that the integrated effects of scalar turbulence across the test section in  $\overline{e_{AS}^2}$  and  $\overline{e_{BS}^2}$  are linear in  $\Delta^2$ , even in the non-isotropic region, so that if a noise correction were applied, we would have

$$e'_{AS} \sim \Delta \quad (6-13)$$

The corresponding CBS covariance of signal-plus-noise is plotted in Figure 44 for  $\bar{U}(x/M = 45.6) = 9.5$  ft/sec. Notice that the variations in  $\overline{e_{AN}e_{BN}}$  (at  $\Delta = 0$ ) appear to be random. The data in this figure have been corrected for total noise  $\overline{e_{AN}e_{BN}}$  determined using the least squares technique described in the previous section (see Equations 6-9 through 6-11) and replotted in Figure 45. Before discussing the  $\theta'$  vs  $\Delta$  data we present a summary of the CBS correlation coefficient (see Equation 4-2) levels computed for the data represented in Figures 43 and 44 in Table 9. As discussed in Chapter IV,  $r_{CBS}(0)$  is a measure of the CBS instrument signal to noise ratio. The tabulated data show a low of 0.076 and a high of 0.187 for  $r_{CBS}(0)$ . The levels appear to be several percent lower for the first two  $x/M$  locations in non-isotropic flow, particularly nearest the grid; but, other than this, no noteworthy trends are evident. For the CBS instrument these numbers are about average; for conventional measuring systems they are very low signal to noise ratios, illustrating the power of cross-correlation to recover signals.

Returning to Figure 45 it is evident from the linearity of the  $\theta'$  vs  $\Delta$  lines that  $\Delta$  is again the proper normalizing parameter; that is,

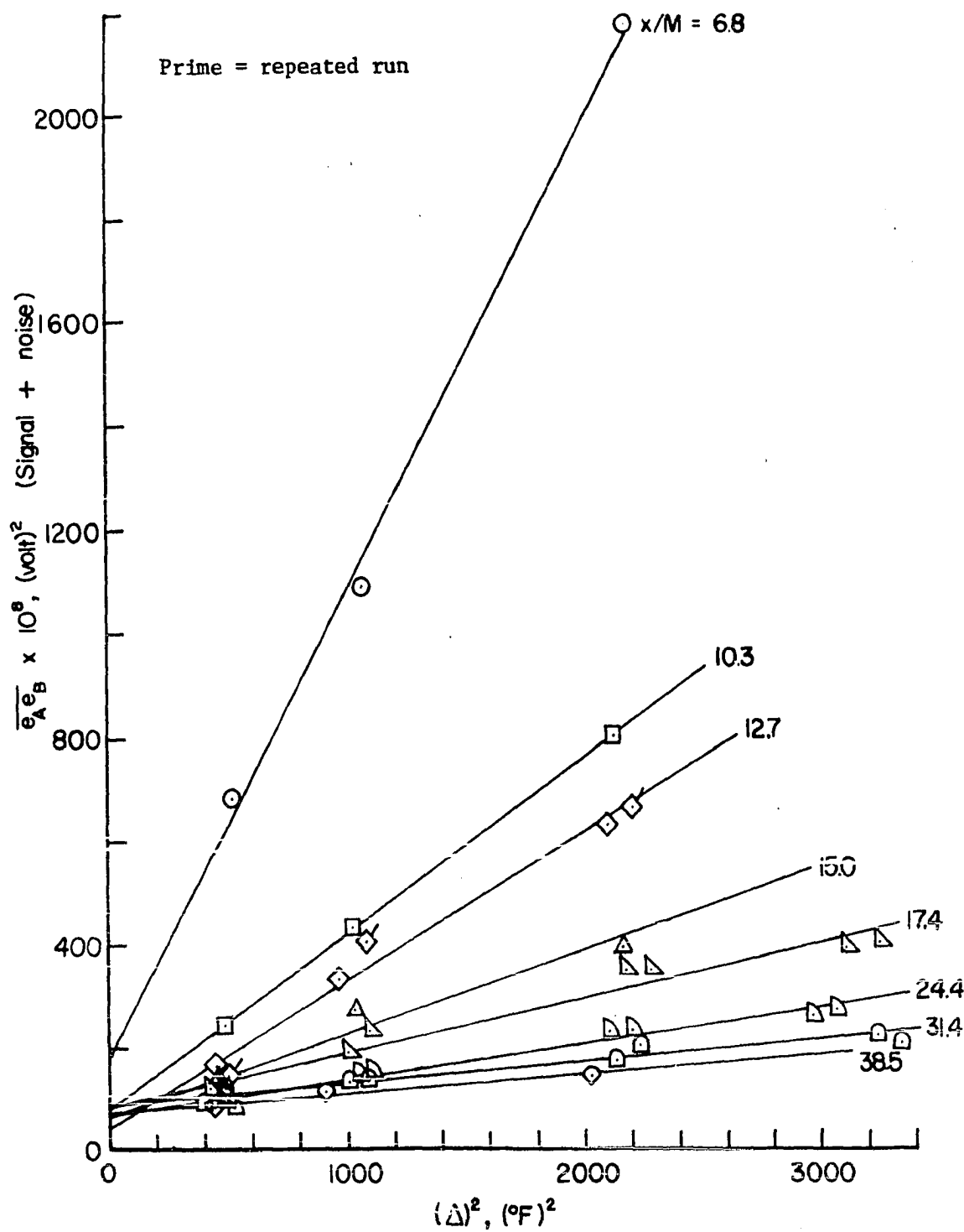


Figure 44. CBS covariance (signal plus noise) response to grid overheating with  $\bar{U}(x/M = 45.6) = 9.5$  fps

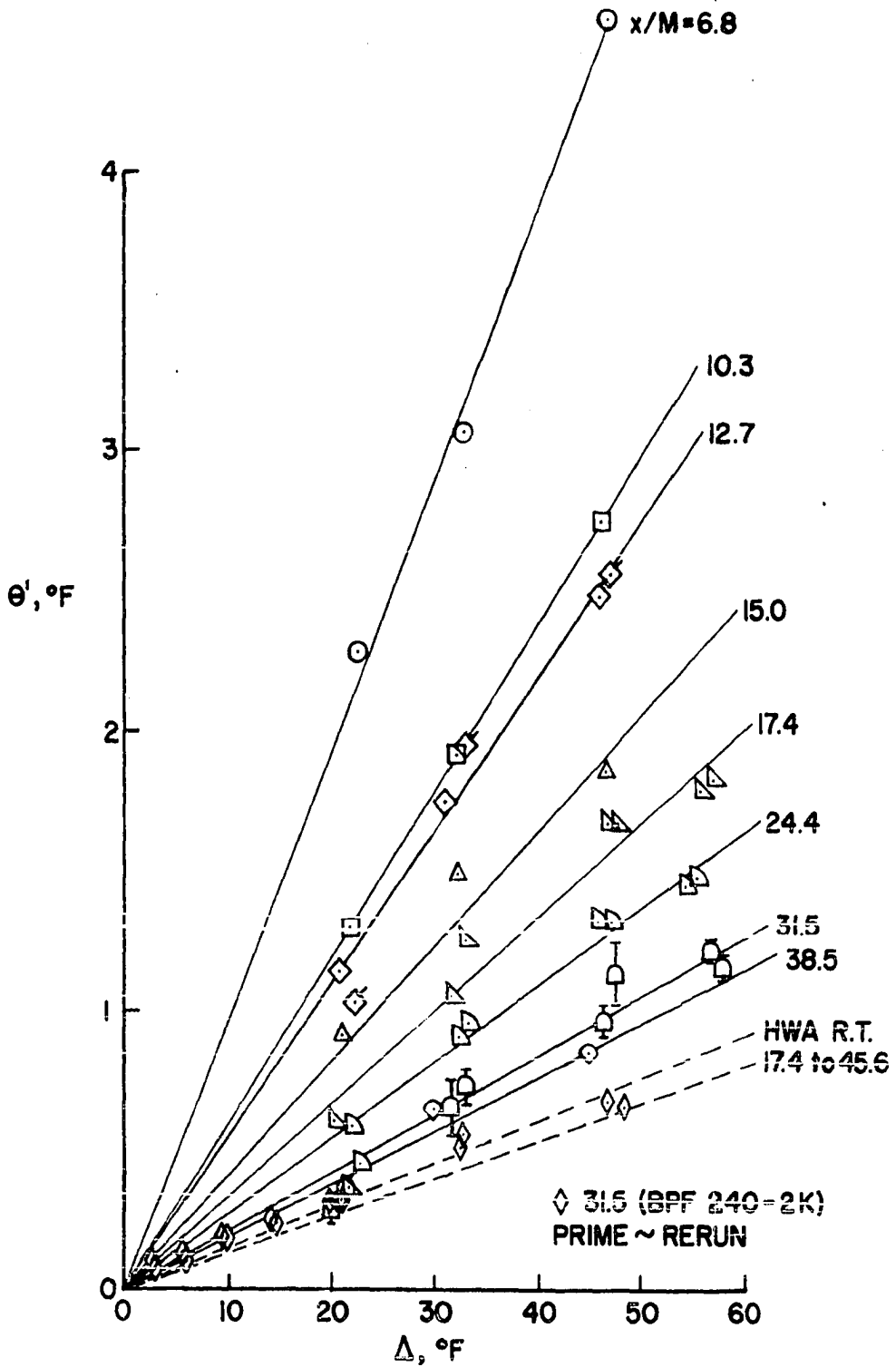


Figure 45. Crossed-beam schlieren temperature fluctuation response to grid overheating with  $U(x/M = 45.6) = 9.5$  fps

$\Delta$  is evidently proportional to the driving potential which generated the scalar turbulence. Notice that our resistance thermometer measurements, indicated as a band for the isotropic region  $17.4 \leq x/M \leq 45.6$ , are significantly lower than the corresponding region in CBS data, although it appears that the CBS data may be decaying into the HWA band at large distances. Uncertainty bands representing the extremes of the three repeated samples averaged for each point on this graph are shown for  $x/M = 31.5$ . Also shown are equivalent  $\theta'$  data for the pass-band 240 to 2000 Hz at  $x/M = 31.5$ .

Table 9. Summary of CBS correlation coefficient  $r_{\text{CBS}}(0) = [\overline{e'_A e'_B} / e'_A e'_B] = 0$  for  $\bar{U}(x/M = 45.6) = 9.5$  ft/sec

$x/M$	$\Delta, ^\circ\text{F}$	$r_{\text{CBS}}(0)$
6.78	22.5	0.103
6.78	32.6	0.076
6.78	46.7	0.077
10.3	21.9	0.128
10.3	32.0	0.117
10.3	46.0	0.100
12.7	20.9	0.137
12.7	31.0	0.148
12.7	45.7	0.146
15.0	21.1	0.131

Table 9. (cont.)

$x/M$	$\Delta, ^\circ\text{F}$	$r_{\text{CBS}}^{(0)}$
15.0	32.1	0.165
15.0	46.5	0.129
17.4	21.4	0.104
17.4	31.4	0.139
17.4	45.8	0.166
24.4	21.0	0.178
24.4	30.0	0.186
24.4	45.5	0.156
31.5	21.5	0.166
31.5	30.8	0.187
31.5	47.3	0.132
38.5	20.7	0.166
38.5	30.0	0.144
38.5	44.9	0.154

While self-similarity of the  $\theta$ -fluctuations is well-portrayed by Figure 45, decay in  $x/M$  is only implicit. Figure 46 therefore shows a replot of several curves of constant  $\Delta$  from Figure 45. The  $\Delta = 9^\circ\text{F}$  curve was included for comparison with data shown from Reference 39. Agreement between the CBS and Reference 39 data is good as early as

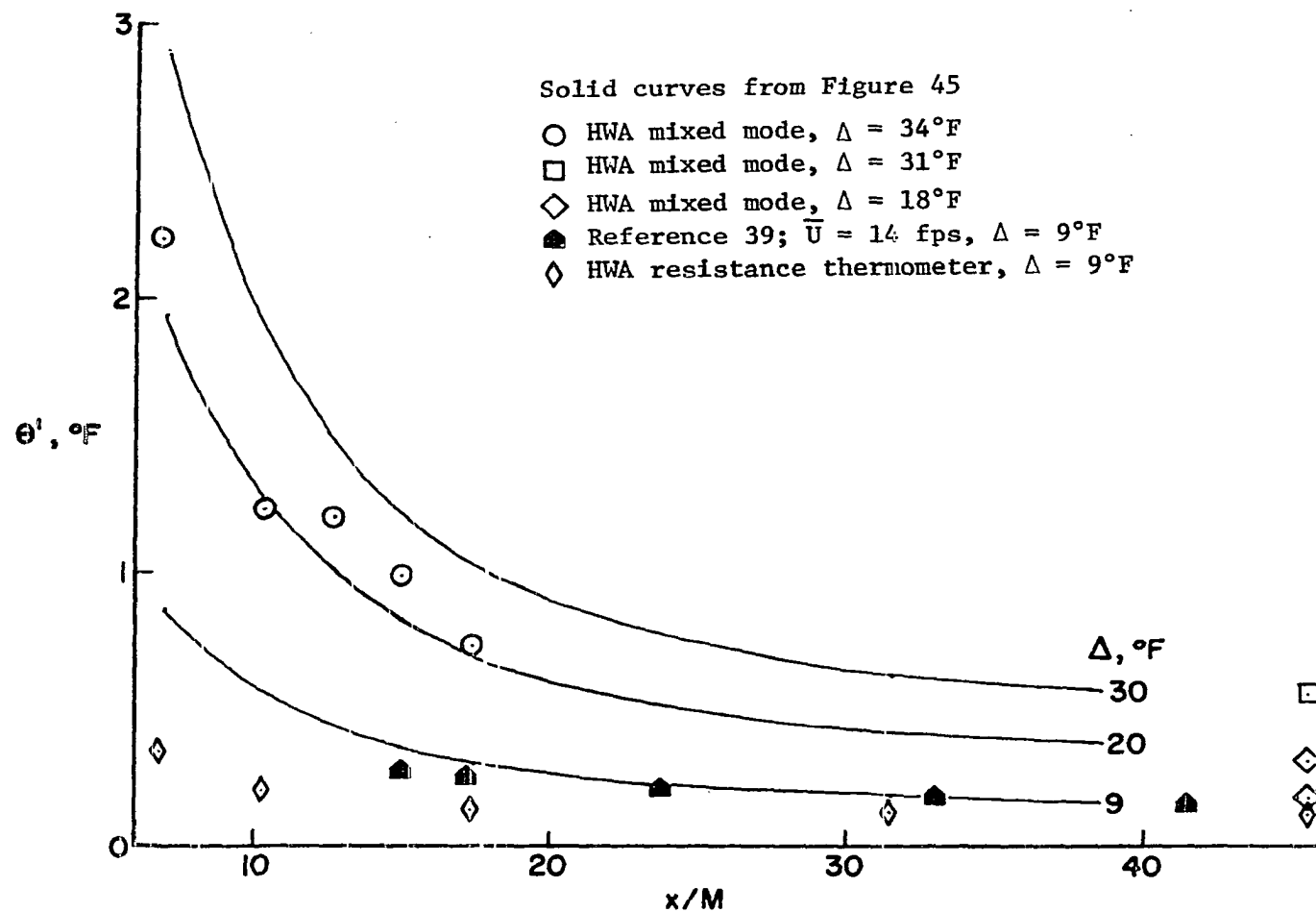


Figure 46. Decay of temperature fluctuations



$x/M = 16$ ; however, our resistance thermometer data appear significantly low until about  $x/M = 32$ . We point out that both in this figure and in Figure 45 the level  $\theta' = 1^\circ\text{F}$  corresponds to peak to peak fluctuations in  $\theta$  of about  $6^\circ\text{F}$  which just exceeds Sandborn's guideline of  $5^\circ\text{F}$  as a limit of small fluctuations.

As done in Reference 39 we plot in Figure 47 the inverse squares of our CBS  $\theta'$  decay data from Figure 45 to compare with a linear decay law. (To evaluate the actual theoretical prediction of  $\theta'^2 \sim x^{-3/2}$  for the initial period, we could plot  $(\overline{\theta^2})^{-2/3}$  vs  $x/M$  as was done in Reference 26). Also shown are data replotted from Reference 39, the  $\bar{U} = 12.9$  ft/sec line from Figure 28, and our resistance thermometer data. In all cases the  $\theta$  variance decay is approximately linear in  $x$  as was the  $u$  variance decay. The lines appear to approach the same virtual origin of about  $x/M = 7.5$ . However, the resistance thermometer has predicted a more rapid decay in the nonisotropic region which is inconsistent with the other data. We are suggesting that while the resistance thermometer data scale properly in  $\Delta$ , they may not be reflecting the true rate of decay of  $\theta$ -fluctuations and, perhaps, absolute levels of  $\overline{\theta^2}$ , at least in the nonisotropic region. This problem should be evaluated, possibly with a compensated resistance thermometer or with a subminiature filament. Our decay law for  $\overline{\theta^2}$  corresponding to (6-1) is, approximately

$$\frac{\Delta^2}{\overline{\theta'^2}} = 100 \left[ \frac{x}{M} - 7.5 \right] \quad (6-14)$$

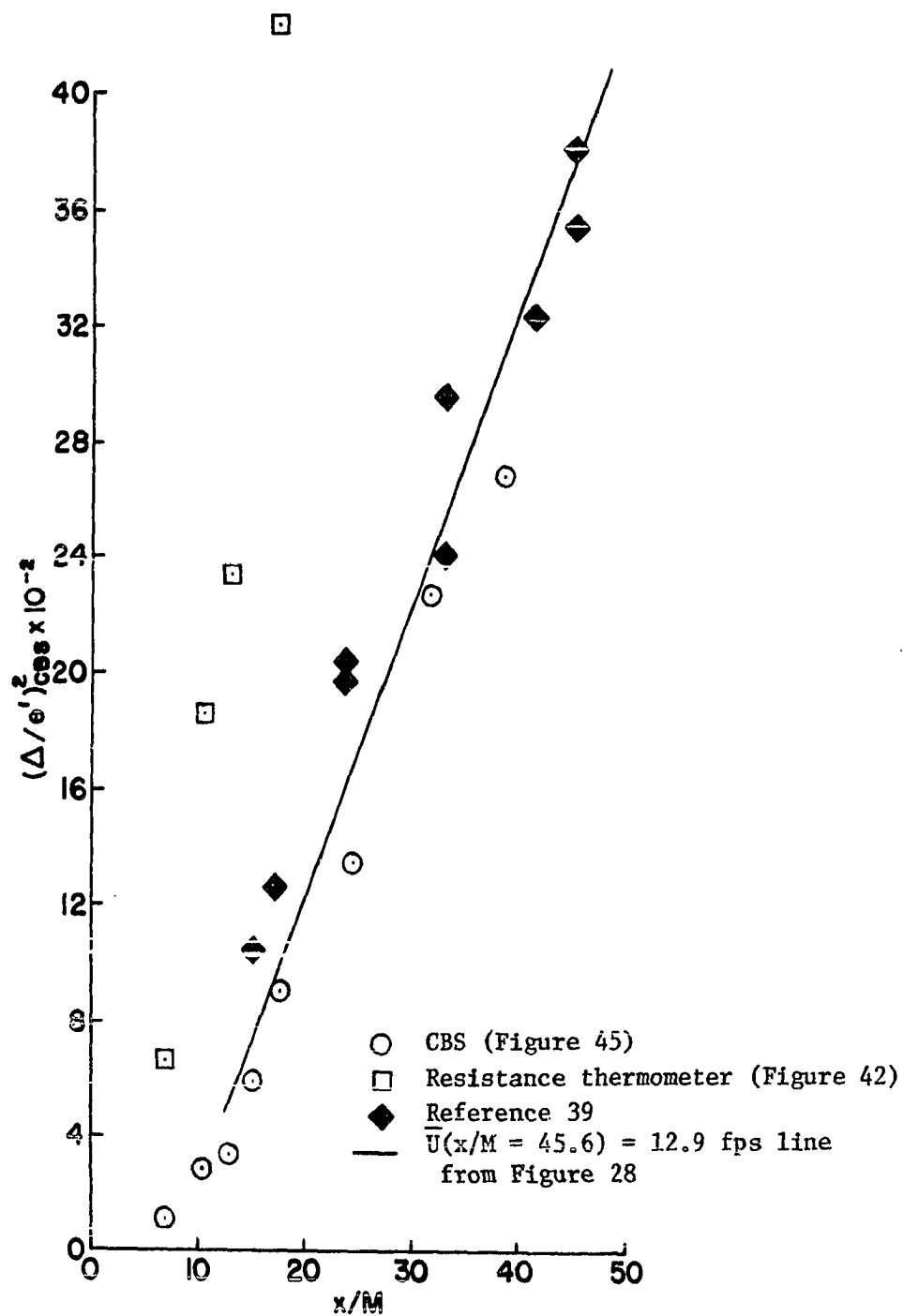


Figure 47. Inverse squares of temperature decay

### 3. Scalar spectra

The bill of fare for this central division is as follows: we will

1. Present HWA resistance thermometer (R.T.) 1-D  $\overline{\theta^2}$  spectra for various  $x/M$ ,  $\overline{U}$ , and  $\Delta$  conditions.
2. Present a number of CBS 3-D  $\overline{\theta^2}$  spectra which will exhibit the characteristic peaked shape of 3-D spectra, as opposed to 1-D spectra which approach a horizontal asymptote as  $f \rightarrow 0$  due to aliasing.
3. Discuss the shape of our CBS spectra in light of the theoretical predictions from Chapter III, in particular, the  $k^2$  rise at low frequencies and the Corrsin  $-5/3$  power law for the inertial subrange.
4. Compare the shape of our CBS 3-D spectra with Hinze's interpolation formula for 3-D spectra, Equation 3-24.
5. Derive the 1-D spectral shape by computation using Equation 3-21 and one of our CBS 3-D spectra.
6. Compare the shape of our R.T. 1-D  $\overline{\theta^2}$  spectra with the spectrum of Reference 39.
7. Compare the shape of our derived CBS 1-D spectrum from 5. with the shapes of our R.T. 1-D  $\overline{\theta^2}$  spectra and our HWA  $\overline{u^2}$  spectra to verify Equation 3-21 experimentally.
8. Compare CBS 3-D  $\overline{\theta^2}$  spectral data processed using our filtering and cross-correlation technique with results from reducing the same data on a special purpose fast-Fourier-transform digital spectrum analyzer.

Figures 48 and 49 provide samples of 1-D  $\overline{\theta^2}$  spectra recorded with the R.T. at  $x/M = 17.4$  which show the effects of varying  $\Delta$  and  $\bar{U}$ . Not surprisingly, the shapes appear similar to the HWA 1-D  $\overline{u^2}$  spectra of Figure 29 and are, in fact, almost identical. Again, no appreciable  $-5/3$  power law region is evident. Normalization using  $\overline{\theta^2}$  or  $\Delta^2$  is required to collapse the spectra in Figure 48, because from Figure 45

$$\theta' \sim \Delta \quad (6-15)$$

at a given  $x/M$  (just as  $u' \sim \bar{U}$ , before); therefore, for any two curves a and b

$$\frac{(E_{\theta 1})_a}{(E_{\theta 1})_b} = \frac{\Delta_a^2}{\Delta_b^2} \quad (6-16)$$

The spectral shape does not change appreciably with  $x/M$ , as may be seen from Figure 50 which shows similar spectra at  $\bar{U}(x/M = 45.6) = 9.5$  ft/sec and  $\Delta \cong 47^\circ\text{F}$ .

We now turn to CBS 3-D  $\overline{\theta^2}$  spectra. First, single beam voltage spectra for both systems at  $x/M = 17.4$  and  $\bar{U} = 8.5$  fps are given in Figure 51. Notice that both beams give very close results and that the observed shape at  $x/M = 17.4$  is nearly identical to the results in Figures 37 and 38 at  $x/M = 9.13$ . We will soon see that the single beam spectra are "fuller" than two beam co-spectra at the same conditions, as expected, since their autocorrelogram peaks were narrower.

The last point is illustrated in Figure 52 which includes plots of pdf's and autocorrelations of both CBS systems, along with the cross-correlation (on the same time base as the auto's) for conditions

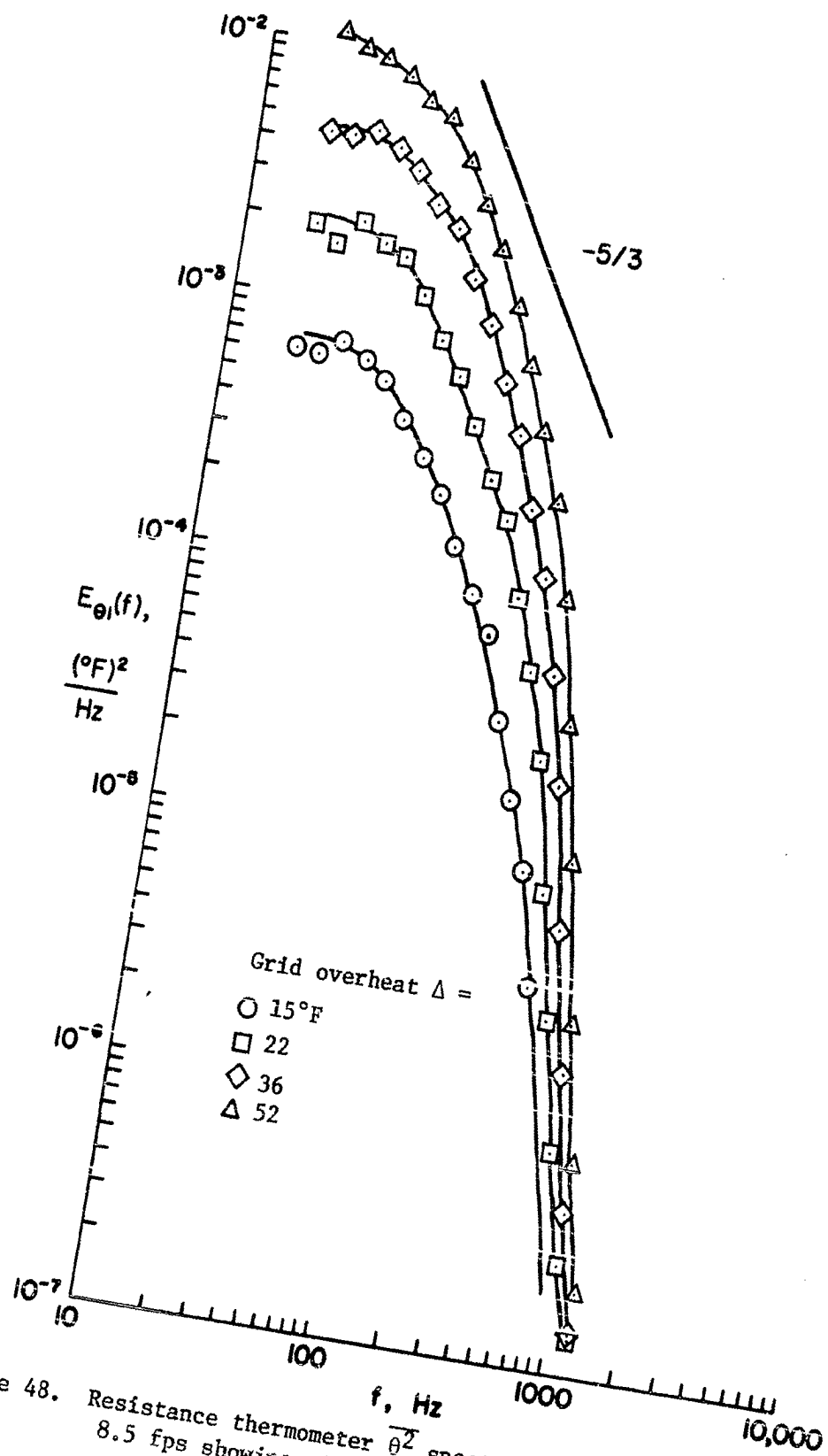


Figure 48. Resistance thermometer  $\overline{\theta^2}$  spectra at  $x/M = 17.4$  and  $\bar{U} = 8.5$  fps showing effect of grid overhear  $\Delta$

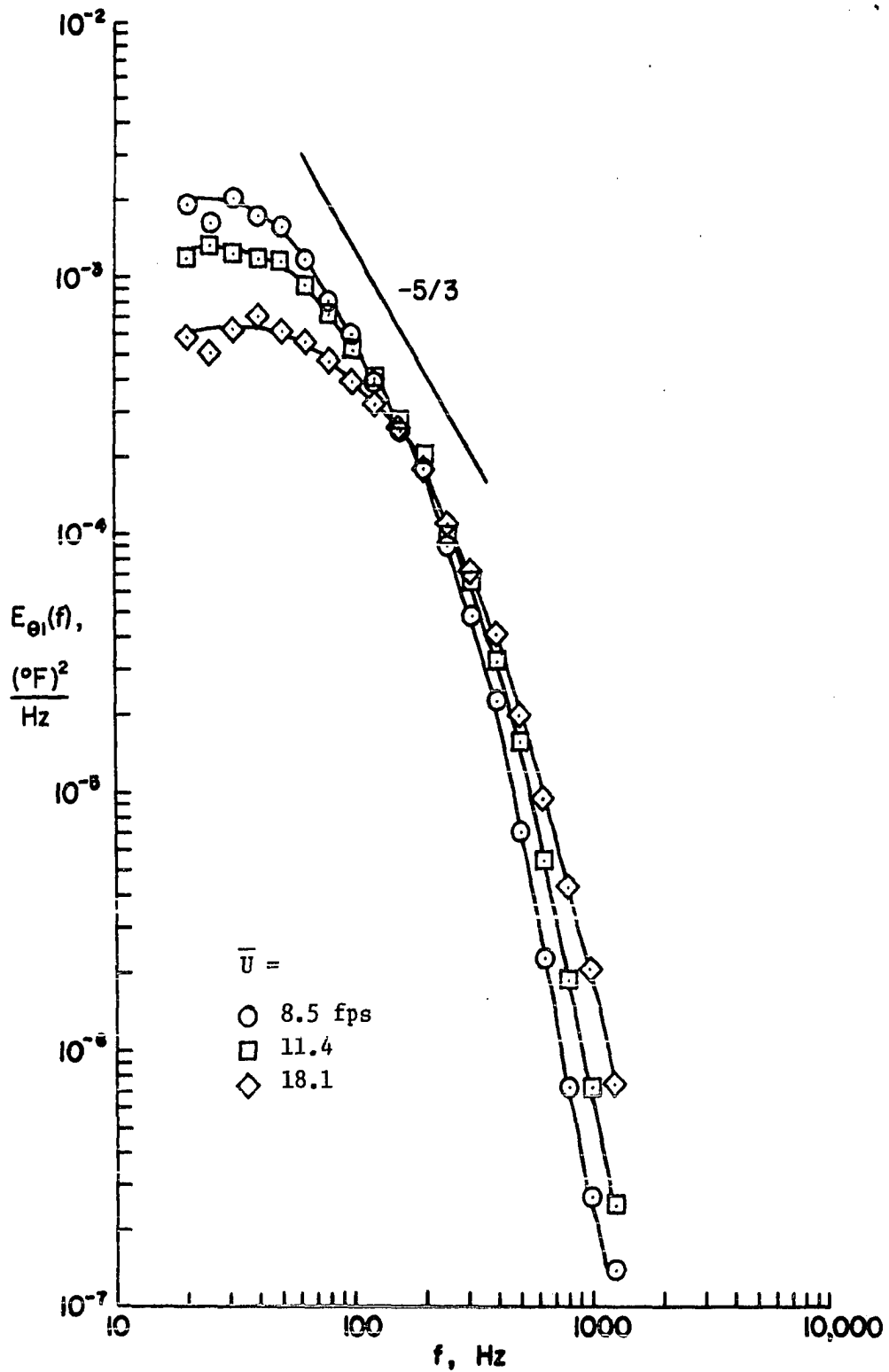


Figure 49. Resistance thermometer  $\overline{\theta^2}$  spectra at  $x/M = 17.4$  and  $\Delta = 22^\circ\text{F}$  showing effect of  $\bar{U}$

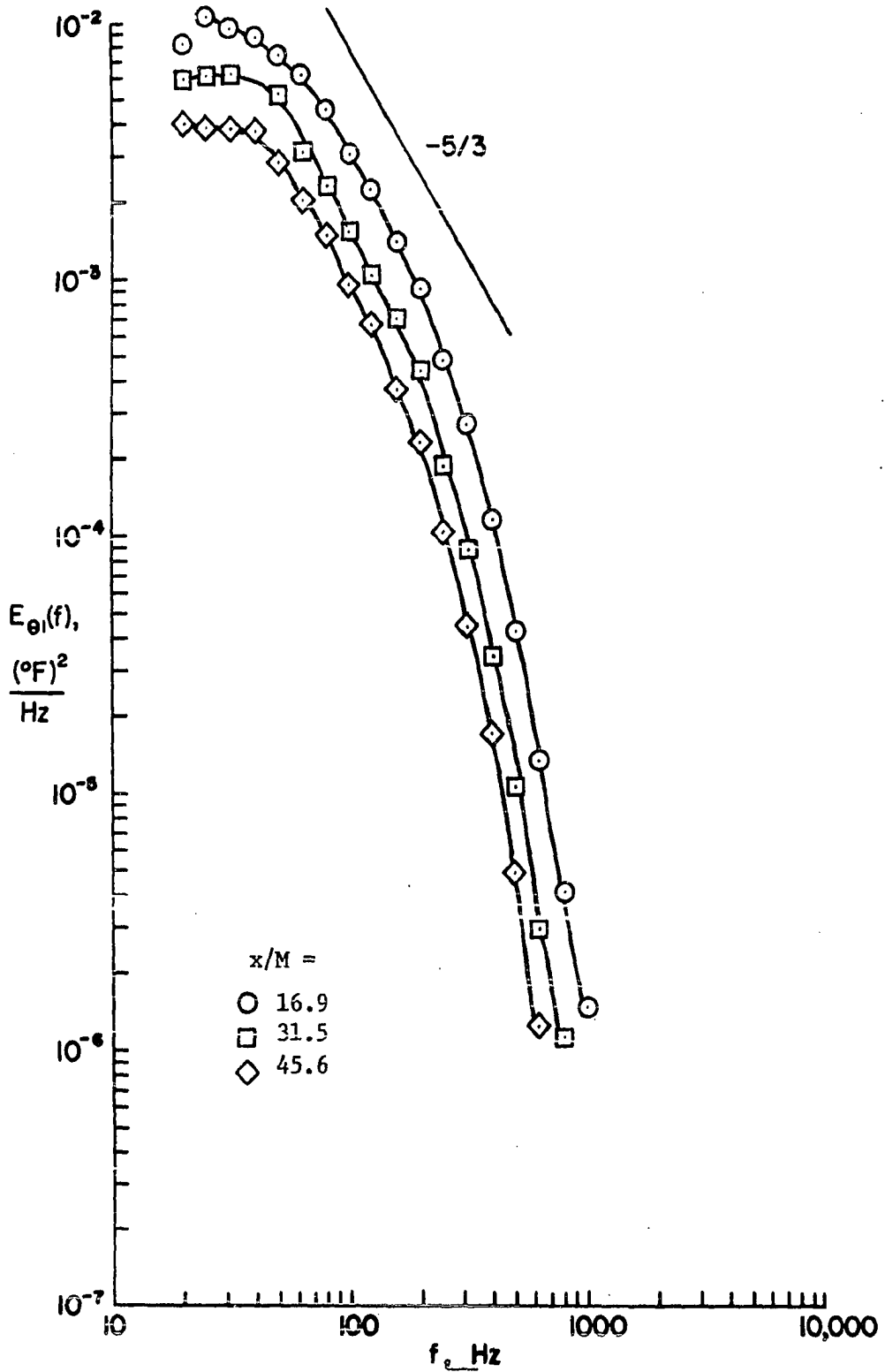


Figure 50. Resistance thermometer  $\theta^2$  spectra with  $\bar{U}$  ( $x/M = 45.6$ ) = 9.5 fps and  $\Delta \approx 47^{\circ}\text{F}$  showing effect of  $x/M$

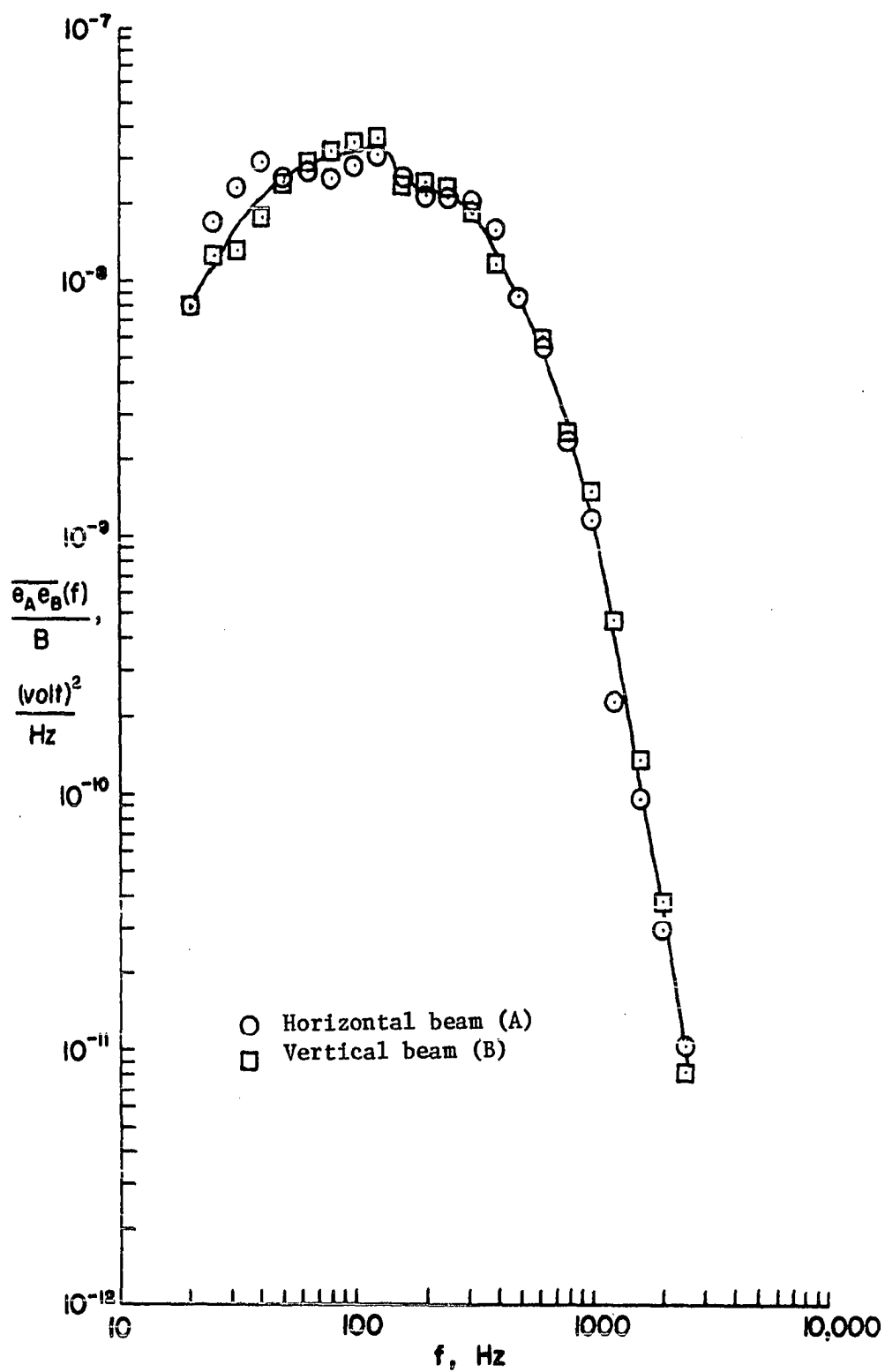
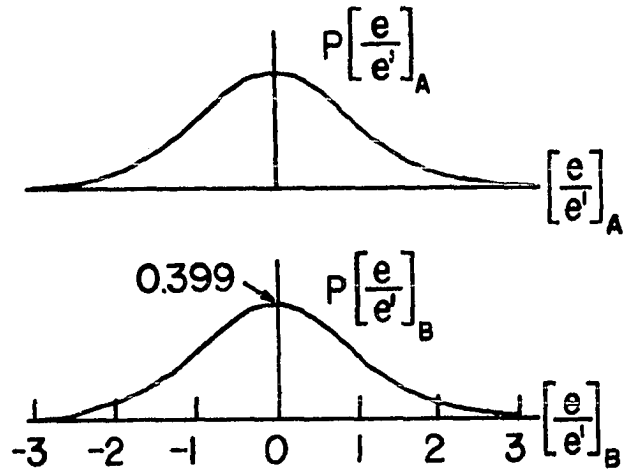


Figure 51. CBS single beam spectra

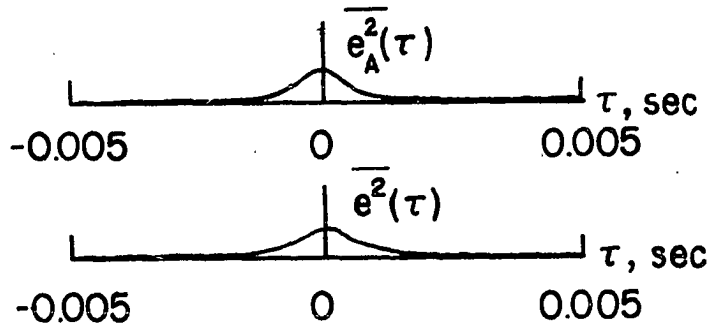


## Probability density functions



## Autocorrelograms

$$\overline{e_A^2}(0) = 11.1 \times 10^{-6} \text{ (volt)}^2, \quad \overline{e_B^2}(0) = 9.74 \times 10^{-6} \text{ (volt)}^2$$



## Cross-correlogram

$$\overline{e_A e_B}(0) = 1.90 \times 10^{-6} \text{ (volt)}^2$$

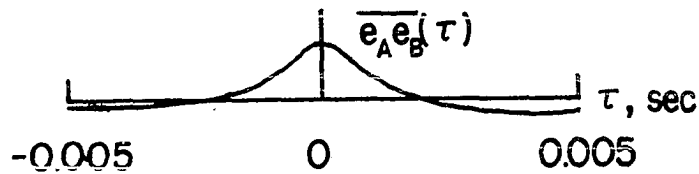


Figure 52. CBS pdf's and correlograms at  $x/M = 17.4$ ,  $\bar{U} = 8.5$  fps and  $\Delta = 32^\circ\text{F}$  with  $r_{\text{CBS}}(0) = 0.183$

$x/M = 17.4$ ,  $\bar{U} = 8.5$  ft/sec, and  $\Delta = 32^\circ\text{F}$ . First, notice that the pdf's are approximately Gaussian in shape. Next, the voltage levels for  $\overline{e_A^2}$ ,  $\overline{e_B^2}$ , and  $\overline{e_A e_B}$  at  $\tau = 0$  are indicated for the auto- and cross-correlograms and account for  $r_{\text{CBS}}(0) = 0.183$ . In the latter case, the "resume" control on the correlator was depressed nine times for  $N + 1 = 10$ ; this accounts for the cross-correlation peak being higher than the auto's. It might be added that the autocorrelograms shown here were produced without using "resume," but could have been brought up to a higher level for more graphical resolution. It will become apparent that the small differences in shape between the auto- and cross-correlograms seen here can account for significant differences in the shape of their spectra, as already mentioned.

A number of CBS 3-D  $\theta^2$  spectra are presented in Figures 53 through 60 for varying conditions in the isotropic flow region. These spectra were all obtained from their corresponding voltage spectra via a shift of the ordinate scale by applying Equation 5-7 to convert units of  $(\text{volt})^2/\text{Hz}$  to  $(^\circ\text{F})^2/\text{Hz}$ . Notice that each spectrum has been measured at least twice to reduce random errors and to guarantee repeatability. Reference lines at slopes of  $f^2$ ,  $f^{-5/3}$ , and  $f^{-5}$  together with the total noise reference spectrum of Figure 39 have been included on each curve for the reader's convenience. Several points are worthy of attention. In all cases these spectra differ basically from the familiar 1-D shape shown, for example, in Figure 48. They appear to peak at around  $f_e = 100$  Hz for  $\bar{U} = 8.5$  ft/sec; this can best be seen in Figures 54, 55,

Figure 53. CBS 3-D  $\theta^2$  spectra at  $x/M = 17.4$ ,  $\bar{u} = 8.5$  fps,  $\Delta = 21^\circ F$ , and  $Re_M = 1770$

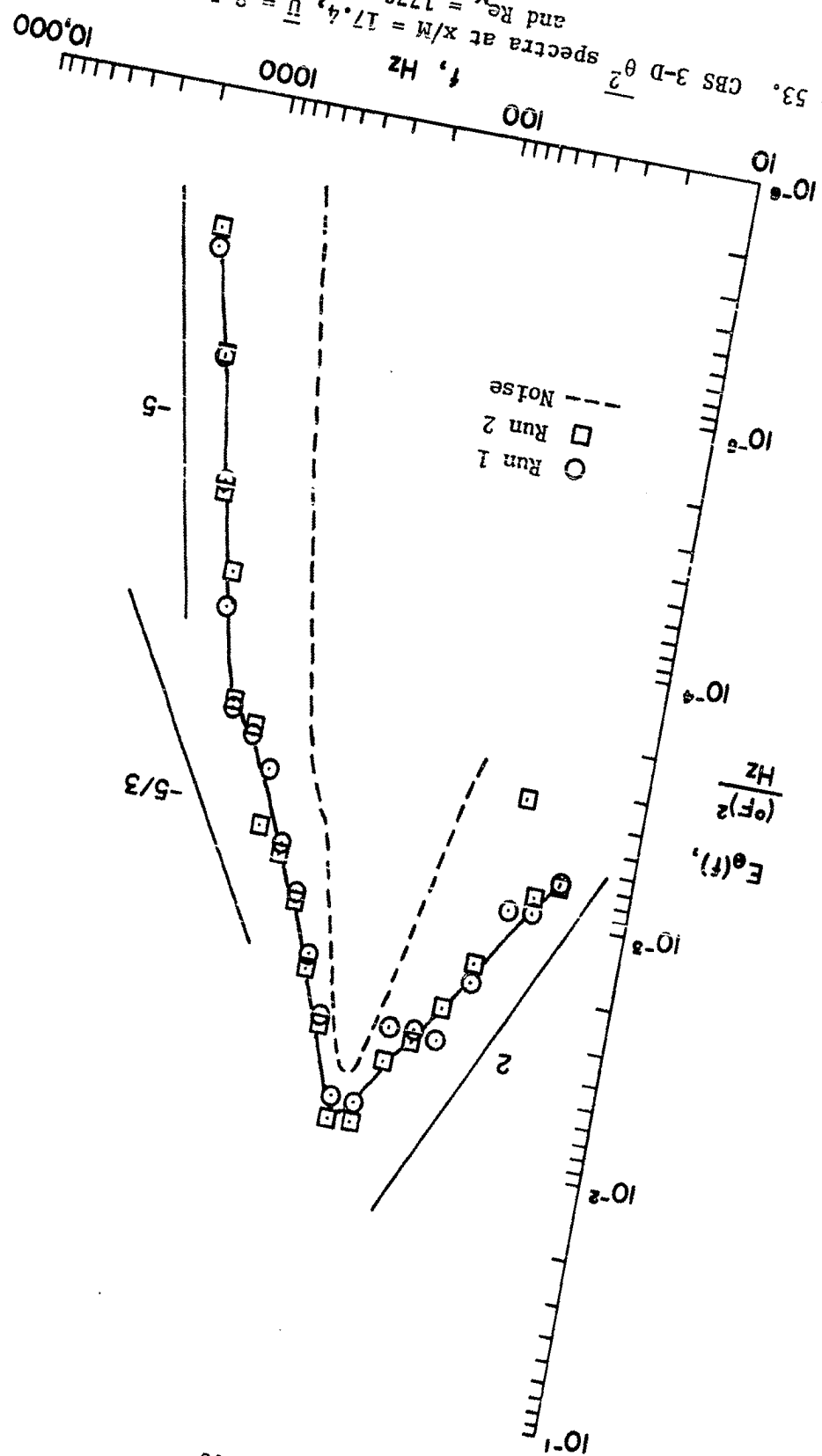
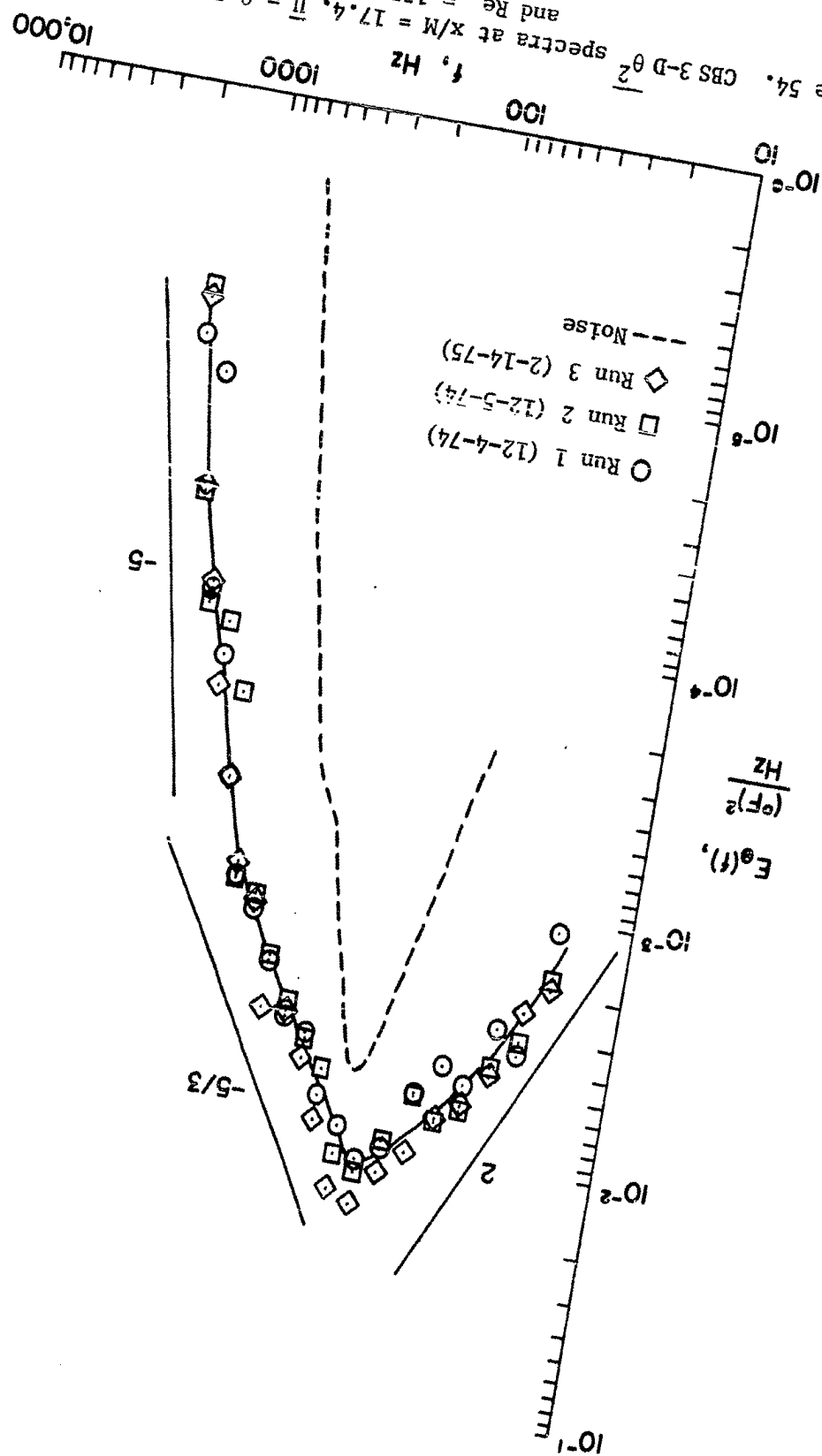


Figure 54. CBS 3-D  $\theta^2$  spectra at  $x/M = 17.4$ ,  $\bar{u} = 8.5$  fps,  $\Delta = 34^\circ$  F, and  $Re_M = 1770$



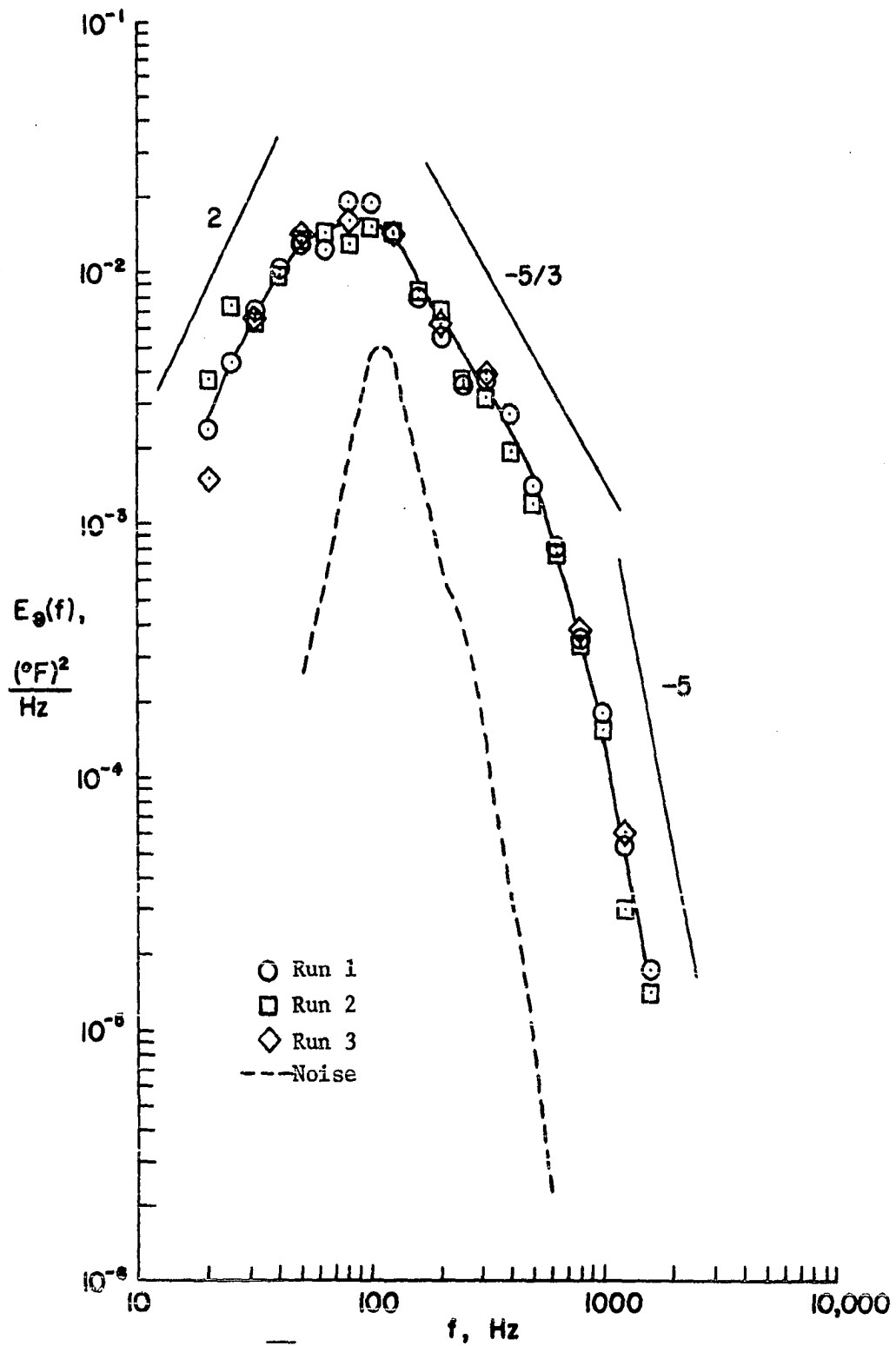


Figure 55. CBS 3-D  $\theta^2$  spectra at  $x/M = 17.4$ ,  $\bar{U} = 8.5$  fps,  $\Delta = 45^\circ\text{F}$ , and  $Re_M = 1770$

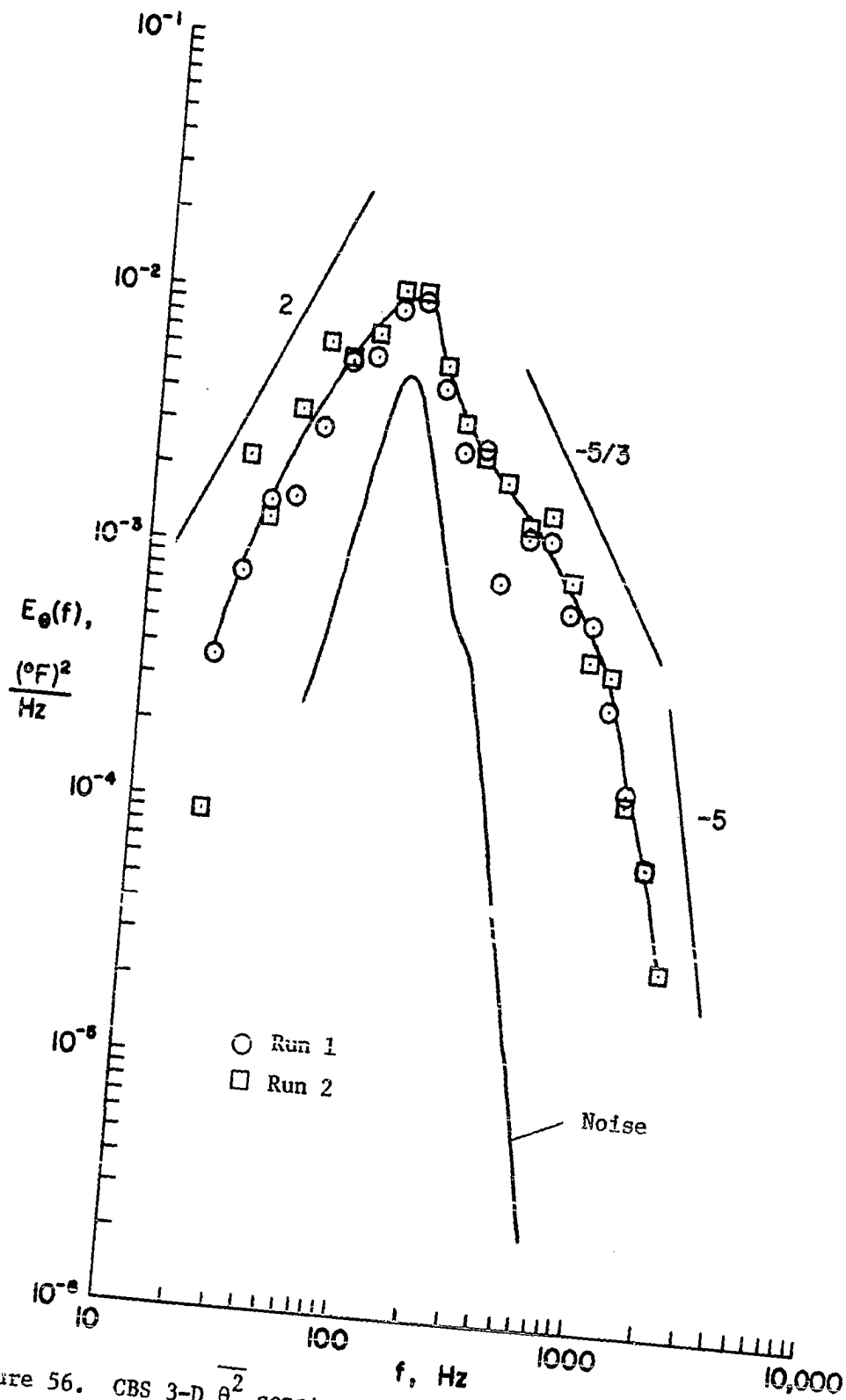


Figure 56. CBS 3-D  $\overline{\theta^2}$  spectra at  $x/M = 17.4$ ,  $\overline{U} = 11.4$  fps,  $\Delta = 38^\circ\text{F}$ , and  $Re_M = 2370$

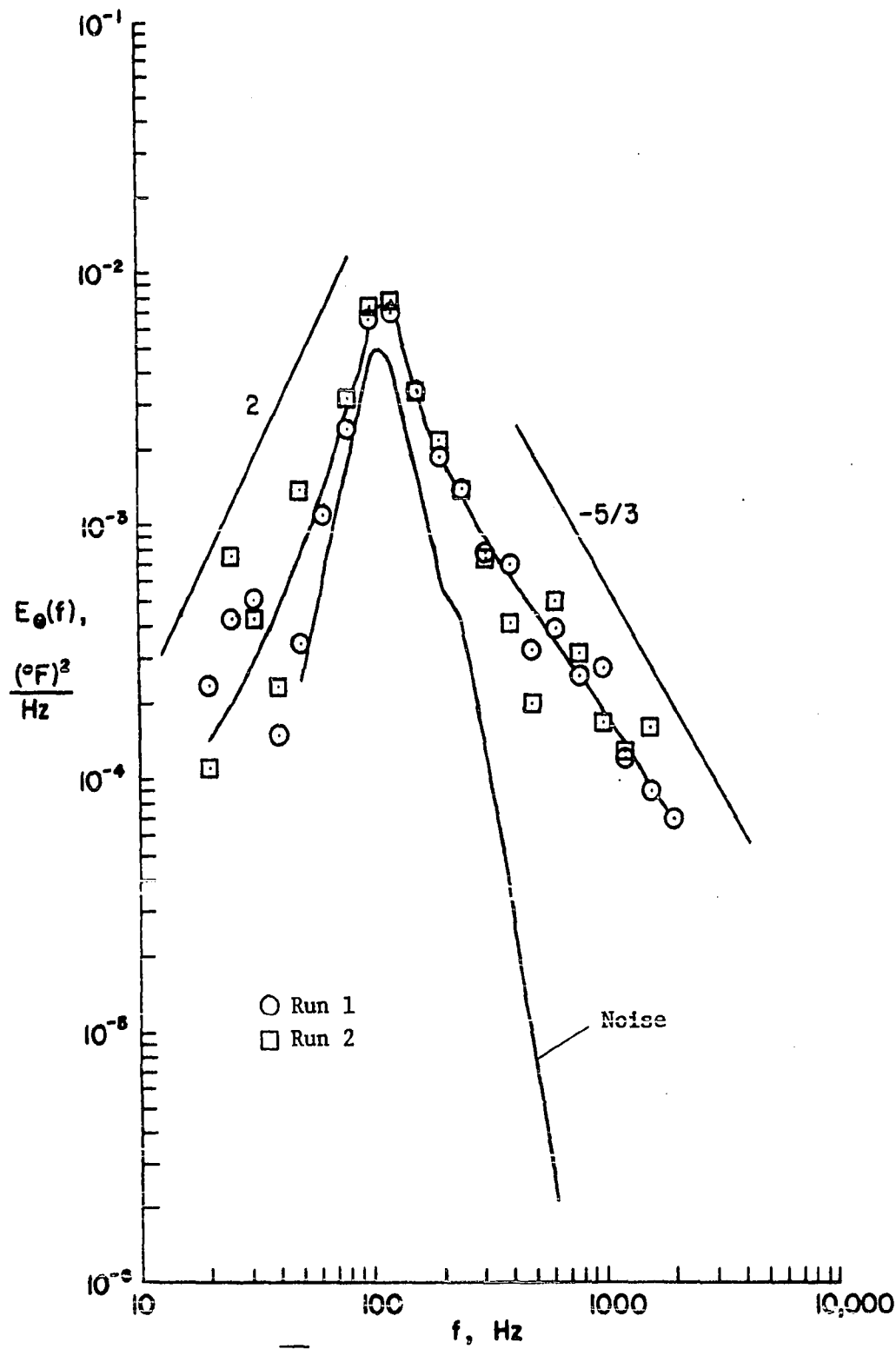


Figure 57. CBS 3-D  $\theta^2$  spectra at  $x/M = 17.4$ ,  $\bar{U} = 18.1$  fps,  $\Delta = 26^\circ\text{F}$ , and  $Re_M = 3770$

Figure 58. CBS 3-D  $\theta^2$  spectra at  $x/M = 24.4$ ,  $\bar{u} = 8.6$  fps,  $\Delta = 34^\circ F$ , and  $Re_M = 1790$

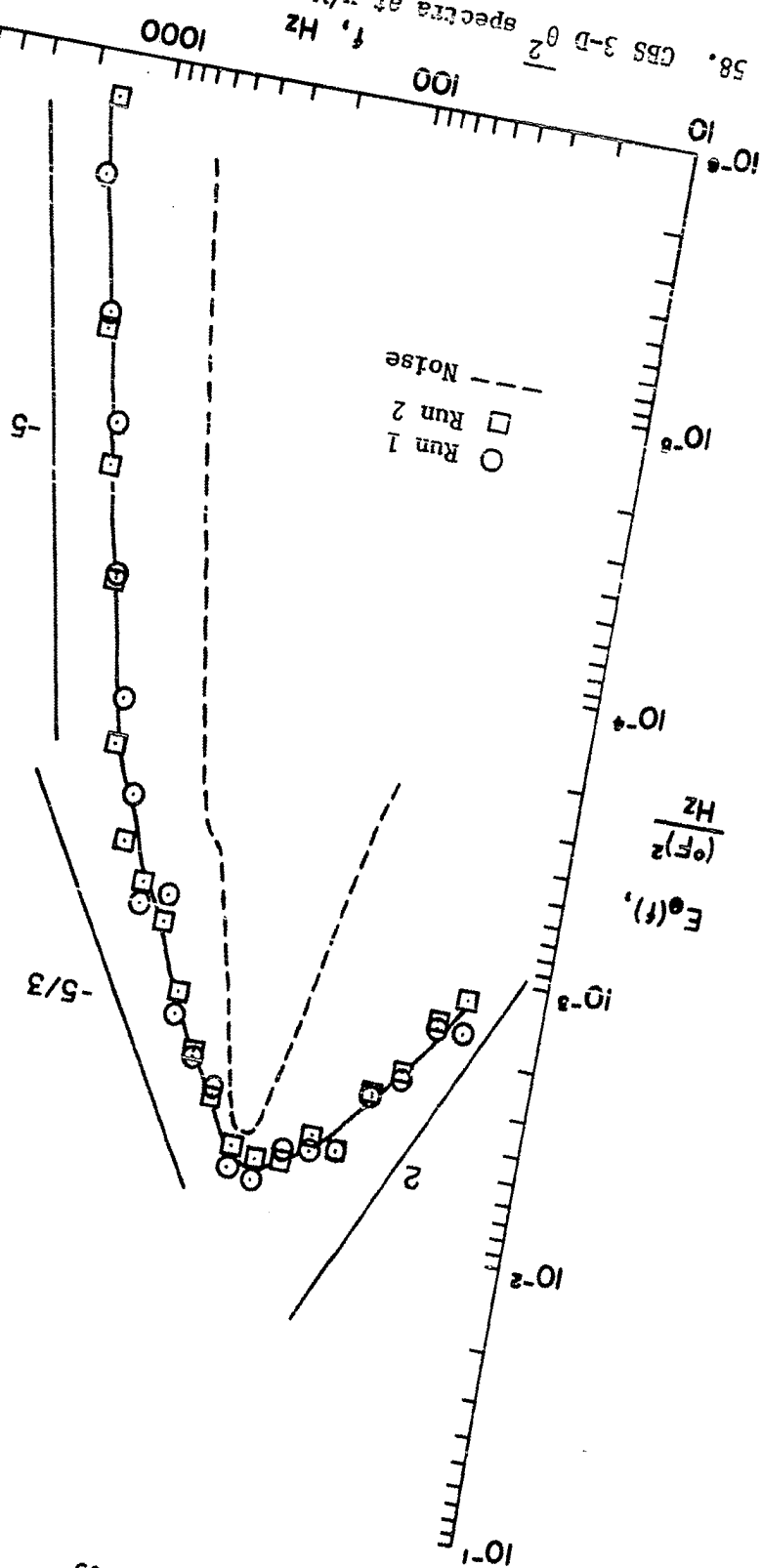
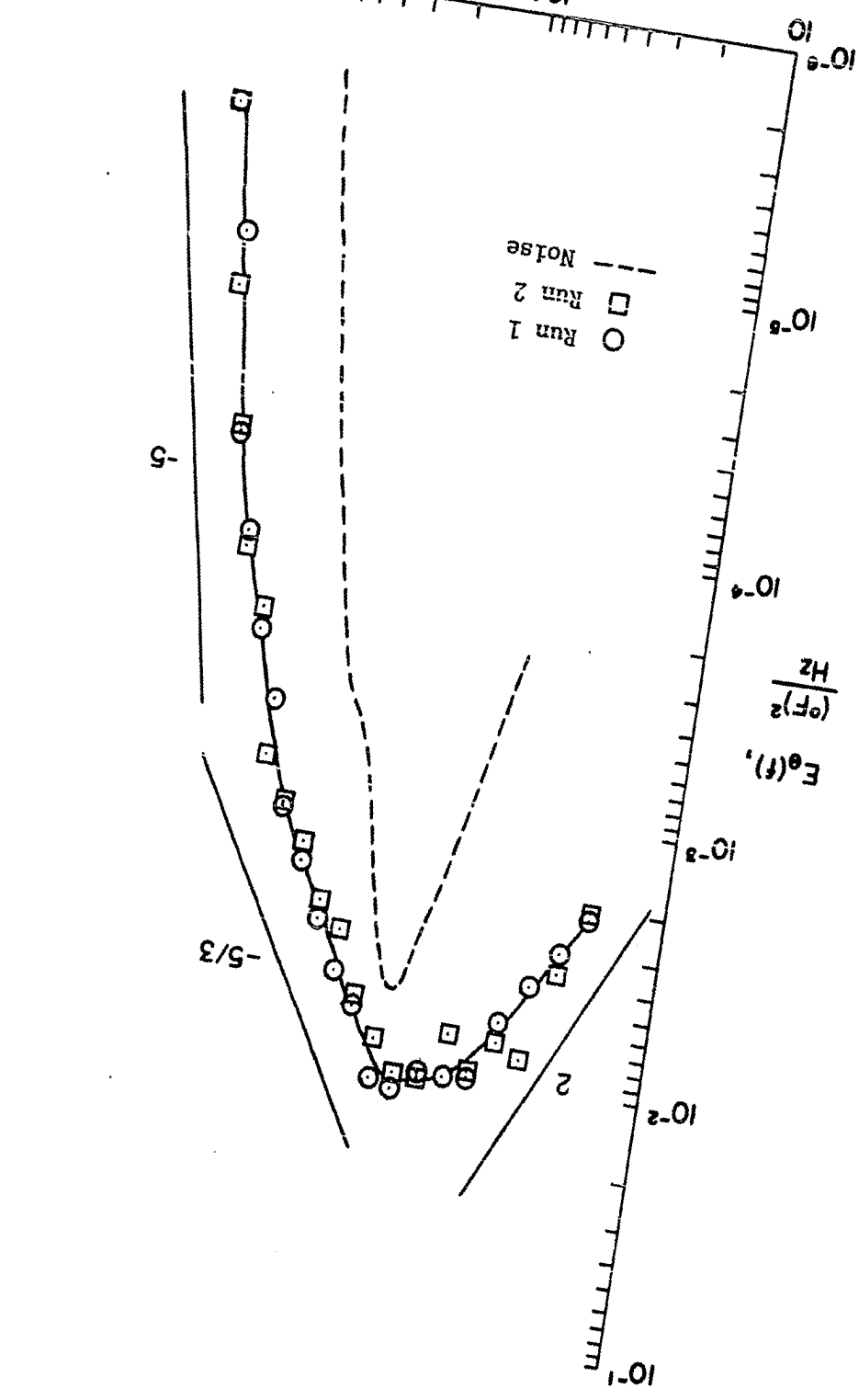




Figure 59. CBS 3-D  $\theta^2$  spectra at  $x/M = 24.4$ ,  $\bar{u} = 8.6$  fps,  $\Delta = 45^\circ$ , and  $Re_M = 1790$



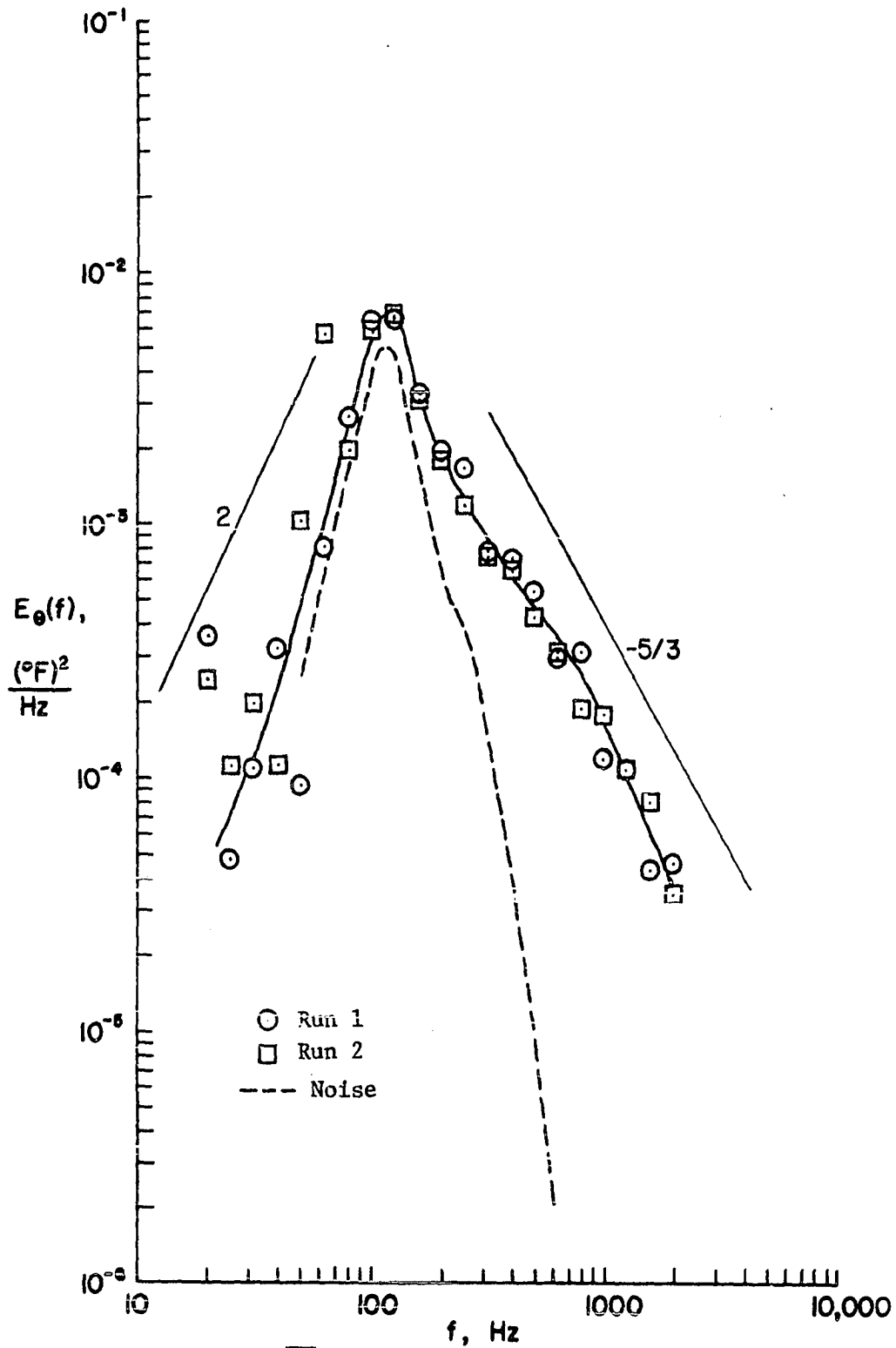


Figure 60. CBS 3-D  $\overline{\theta^2}$  spectra at  $x/M = 24.4$ ,  $\bar{U} = 18.9$  fps,  $\Delta = 27^\circ\text{F}$ , and  $Re_M = 3940$

and 59 where  $\Delta$  was high enough to raise the spectral peak further away from the influence of the noise. Also, in all cases an inertial subrange obeying the theoretically predicted Corrsin  $E_\theta \sim f^{-5/3}$  power law is present. This is in stark contrast to the usual assumption that at the low Reynolds numbers usually found in laboratories (for these figures at  $\bar{U} = 8.5$  fps,  $Re_M \approx 1770$ ; and, in Reference 39,  $Re_M \approx 7420$ ), a substantial inertial subrange is absent due to predominant viscous effects (see References 29 and 48). We note that the extent of the inertial subrange evident in these spectra is appreciable, including about 100 to 500 Hz in Figures 54, 55, and 59; in these same figures, the inertial subrange appears to begin almost immediately after the spectrum rolls out of its peak. The effect of aliasing, that is, the biasing of lower frequency energy levels with higher frequency energy, has heretofore disguised the presence of an inertial subrange in 1-D spectra by deteriorating their sensitivity to changes in slope until high enough Reynolds numbers are achieved to produce a wide enough  $-5/3$  law region to survive the smearing effect of Equation 3-21. This points out the advantage of direct measurement of 3-D spectra.

Another feature characterizing many of these spectra is a "knee" separating the apparent inertial subrange from the range of higher frequencies, the diffusive subrange. If this knee represents a demarcation between inertial and diffusive subranges, its location should be Reynolds number dependent. To check this, spectra obtained at Reynolds numbers of  $Re_M = 1770, 2370$ , and  $3770$  (assuming  $\nu = 17 \times 10^{-5}$  ft<sup>2</sup>/sec) are shown

in Figures 54, 56, and 57. Notice that one effect present in this sequence is the shift of energy out of low frequencies and into higher frequencies. As a result, the knee moves from about 500 Hz to 1000 Hz, and is apparently above the range of our data in Figure 57. The predominant effect here is a convective or Strouhal-type effect which we will remove later by plotting against wavenumber to see the actual Reynolds number effect on the knee. However, note that as the energy shifts upward in frequency, the  $-5/3$  power law is maintained and extended.

The abrupt transition in a number of these spectra at the knee between regions of slope  $-5/3$  and approximately  $-5$  may be attributable to a conductive or molecular diffusion cutoff as proposed by Corrsin. While in all cases with a conductive cutoff, our spectra appear to decay at about  $E_\theta(f) \sim f^{-5}$  we hesitate to make a firm stand on the  $-5$  number due to uncertainties in the effective filter bandwidth in regions where spectral slopes are quite steep. In terms of convective frequency response, the CBS is more than adequate; for example, using  $f_{\max} = \bar{U}/d$  and assuming  $d = 1\text{mm}$ , it will resolve

$$f_{\max} \approx 2400 \text{ Hz at } \bar{U} = 8.0 \text{ ft/sec}$$

and

$$f_{\max} \approx 6300 \text{ Hz at } \bar{U} = 20.7 \text{ ft/sec}$$

for the lowest and highest speeds encountered here, respectively.

Regarding the effective filter bandwidth, Sandborn (44) states that the actual effective bandwidth is decreased due to the turbulence. If this

is the case, then we have normalized our spectrum to too steep a slope by using the bandwidths  $B$  given in Table 1. However, we realize that the steepest slope we can hope to obtain using our filters is 24 dB/octave which is very close to  $f^{-5}$  and, therefore, conclude that after the knee, the energy in our spectra has dropped-off catastrophically at a steep slope as predicted theoretically.

In spite of the fact that our spectra are less accurate in terms of  $\epsilon$ , the normalized standard error, at the lowest frequencies (as evident in higher data scatter), many of the spectra appear to rise at about  $E_\theta(f) \sim f^2$  which is in agreement with the theory.

Clearly, in some cases, e.g., Figures 53, 57, and 60 the spectra are distorted to conform to the shape of the noise spike instead of assuming their natural lower level in the vicinity of  $f = 120$  Hz.

At this time several points will be made by cross-plotting some of the CBS spectra shown above. Figure 61 includes the single beam spectrum from Figure 51, and its noise spectrum from Figure 37, along with the voltage spectra corresponding to the curves in Figure 54. Of interest are the difference in shape of the power spectrum and the co-spectrum referred to above. Also, the difference in power level between these two curves is a graphical representation of the variation of  $r_{\text{CBS}}(0) = \overline{e_A e_B} / \overline{e_A'} e_B'$  with frequency. Since  $\overline{e_A^2} = \overline{e_B^2}$  here, and

$$r_{\text{CBS}}(0) = \frac{\overline{e_A e_B}}{\overline{e_A^2}} \leq 1$$

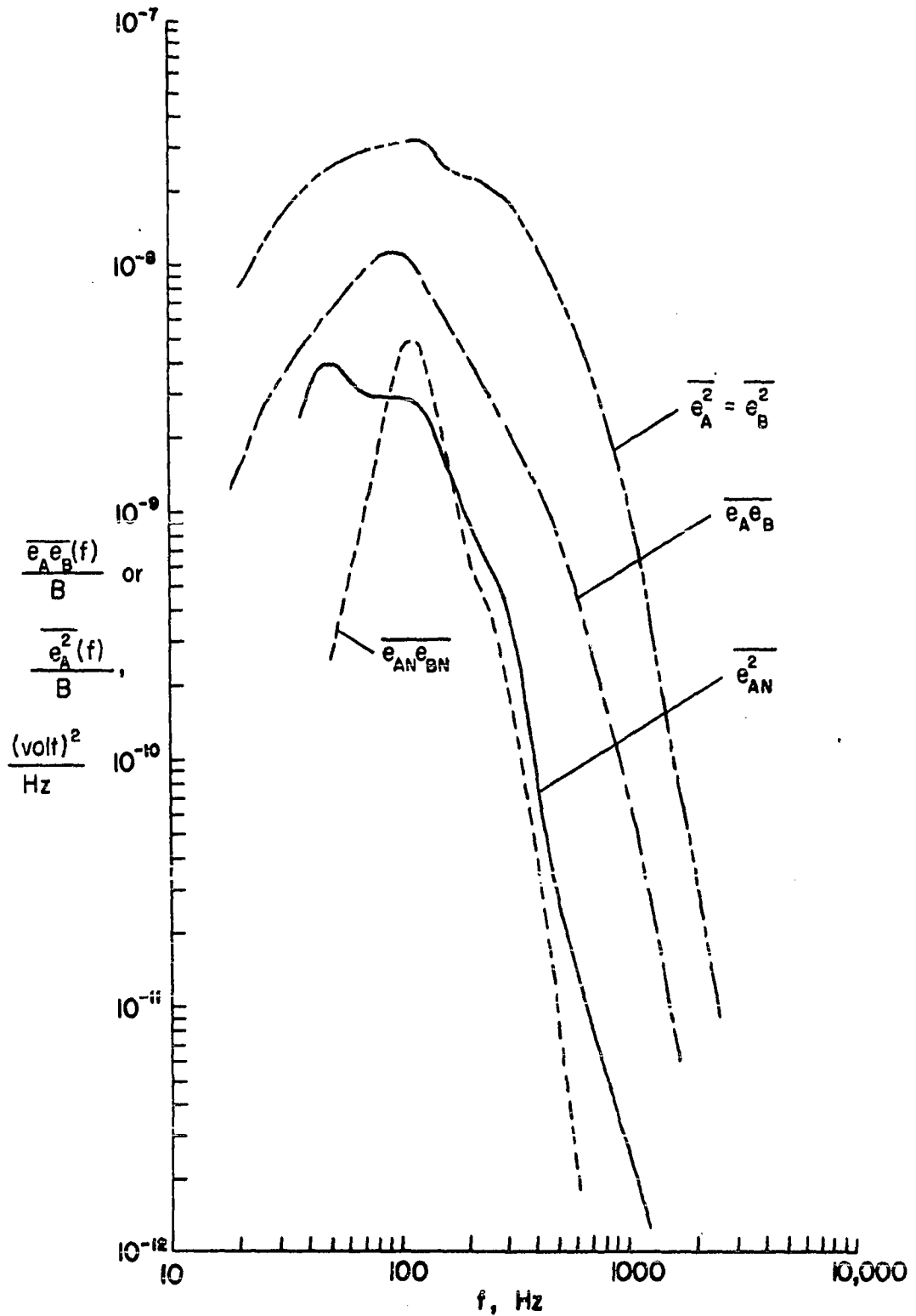


Figure 61. CBS single and crossed-beam voltage spectra at  $x/M = 17.4$ ,  $U = 8.5$  fps, and  $\Delta = 34^\circ\text{F}$  showing spectral variation of  $r_{\text{CBS}}(0)$

Taking logs to base ten,

$$\log r_{\text{CBS}}(0) = \log \overline{e_A e_B} - \log \overline{e_A^2} \leq 0$$

Therefore,

$$\frac{1}{r_{\text{CBS}}(0)} = 10^{|\log \overline{e_A e_B} - \log \overline{e_A^2}|} \quad (6-17)$$

We would expect  $r_{\text{CBS}}(0)$  to be smallest at the highest frequencies because high frequencies (or wavenumbers) imply smaller scales and, therefore, more scales across the flow region from which the CBS system is trying to resolve a single small eddy as implied by Equation 4-2. From the figure it can be seen that the difference in brackets in (6-17) is largest at high frequencies and approximately constant above about 700 Hz.

Figure 62 illustrates the effect of increasing  $\Delta$ , namely, increasing the total energy  $\overline{\theta^2}$  "inflates" the spectrum on both sides, upward and outward, away from the noise. Were it not for the distorting effect of the noise, it is possible that the spectra would be self-similar under proper scaling (see Reference 25), as the two highest level curves appear to be. Notice that  $(45/34)^2 = 1.75$  approximately accounts for the difference in level of these two curves.

Figure 63 shows the effect of decay with  $x/M$  for two locations. These curves also appear similar, and since we found approximately  $1/\overline{\theta^2} \sim x$ , we expect  $(24.4/17.4) = 1.40$  to account for the level difference, although this seems to fall short, in this particular case.

The Strouhal effect described above is summarized on Figure 64, and removed in Figure 65 along with the  $\Delta$  dependence. Now it looks

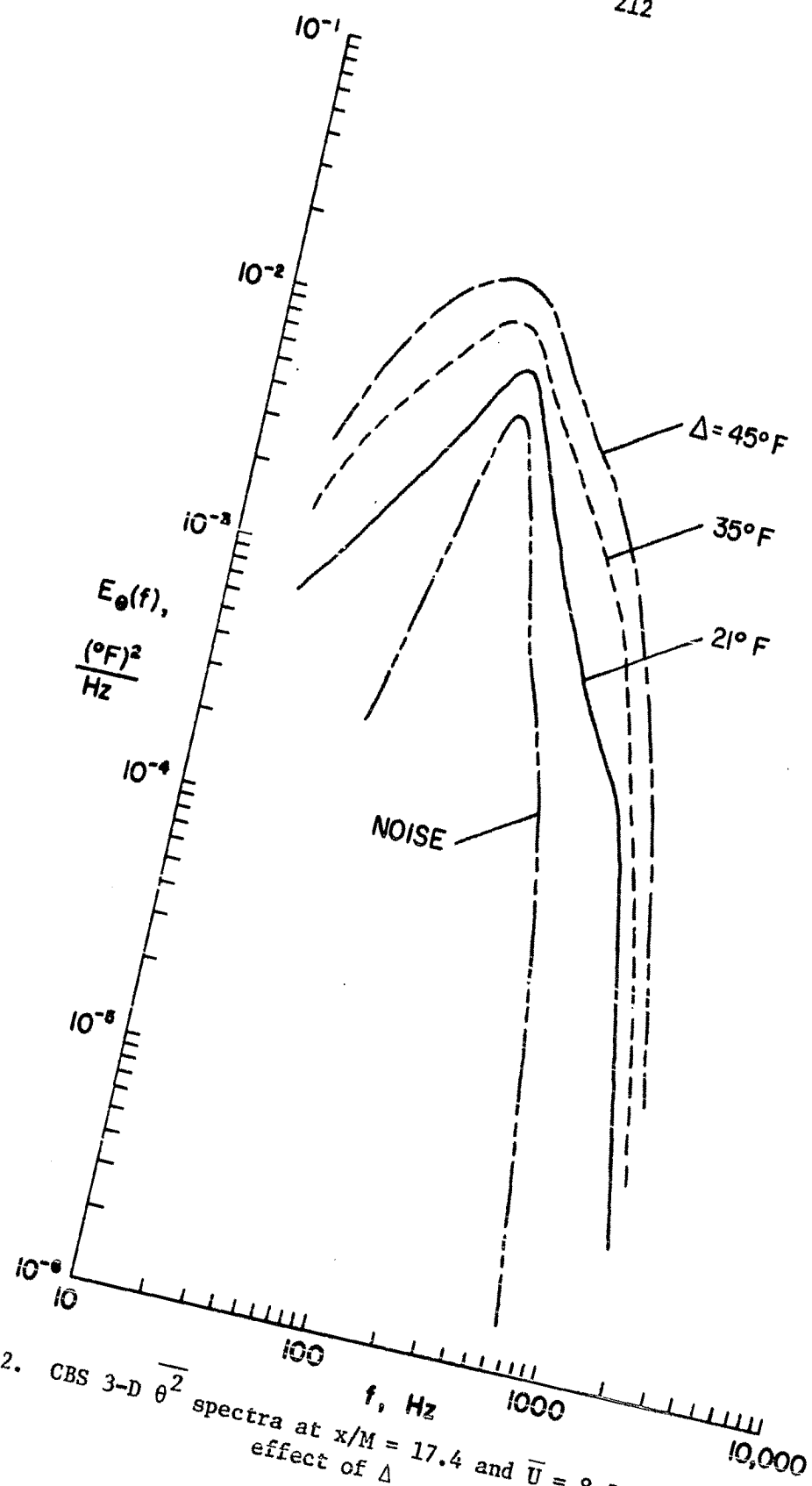


Figure 62. CBS 3-D  $\overline{\theta^2}$  spectra at  $x/M = 17.4$  and  $\bar{U} = 8.5$  fps showing effect of  $\Delta$



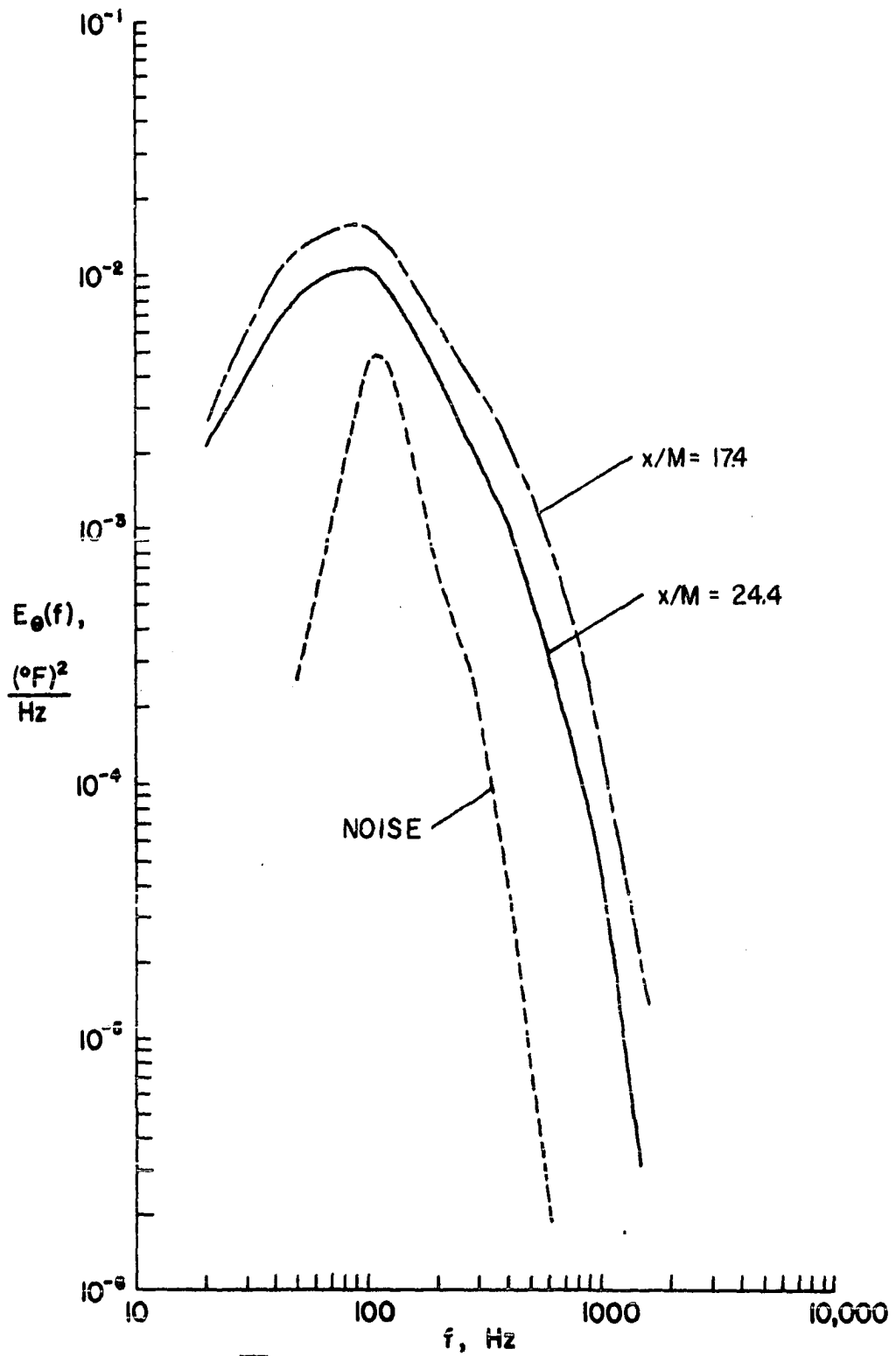


Figure 63. CBS 3-D  $\theta^2$  spectra with  $\bar{U} = 8.5$  fps and  $\Delta = 45^\circ\text{F}$  showing effect of  $x/M$

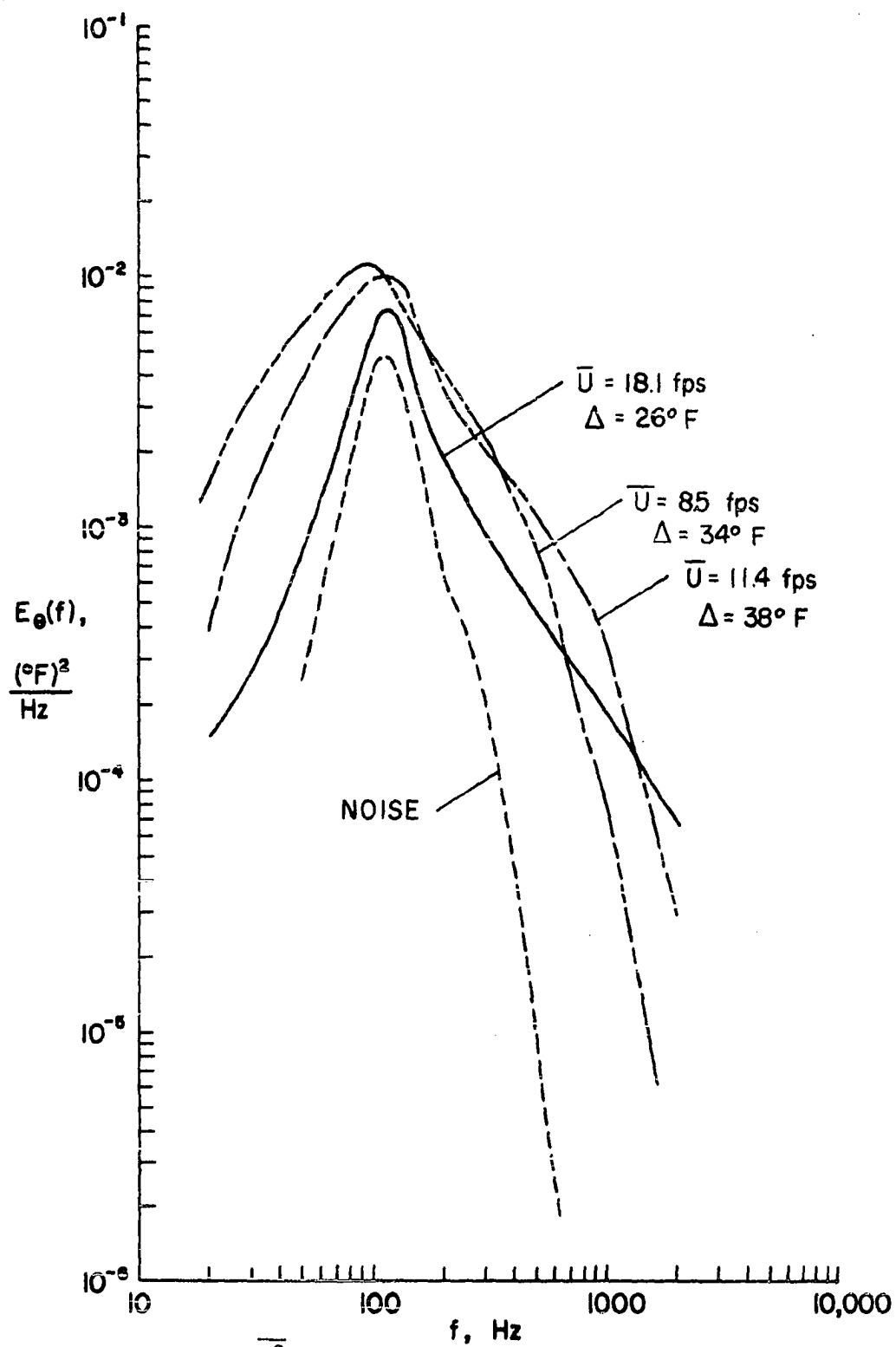


Figure 64. CBS 3-D  $\theta^2$  spectra at  $x/M = 17.4$  showing effect of  $\bar{U}$  (Strouhal effect)

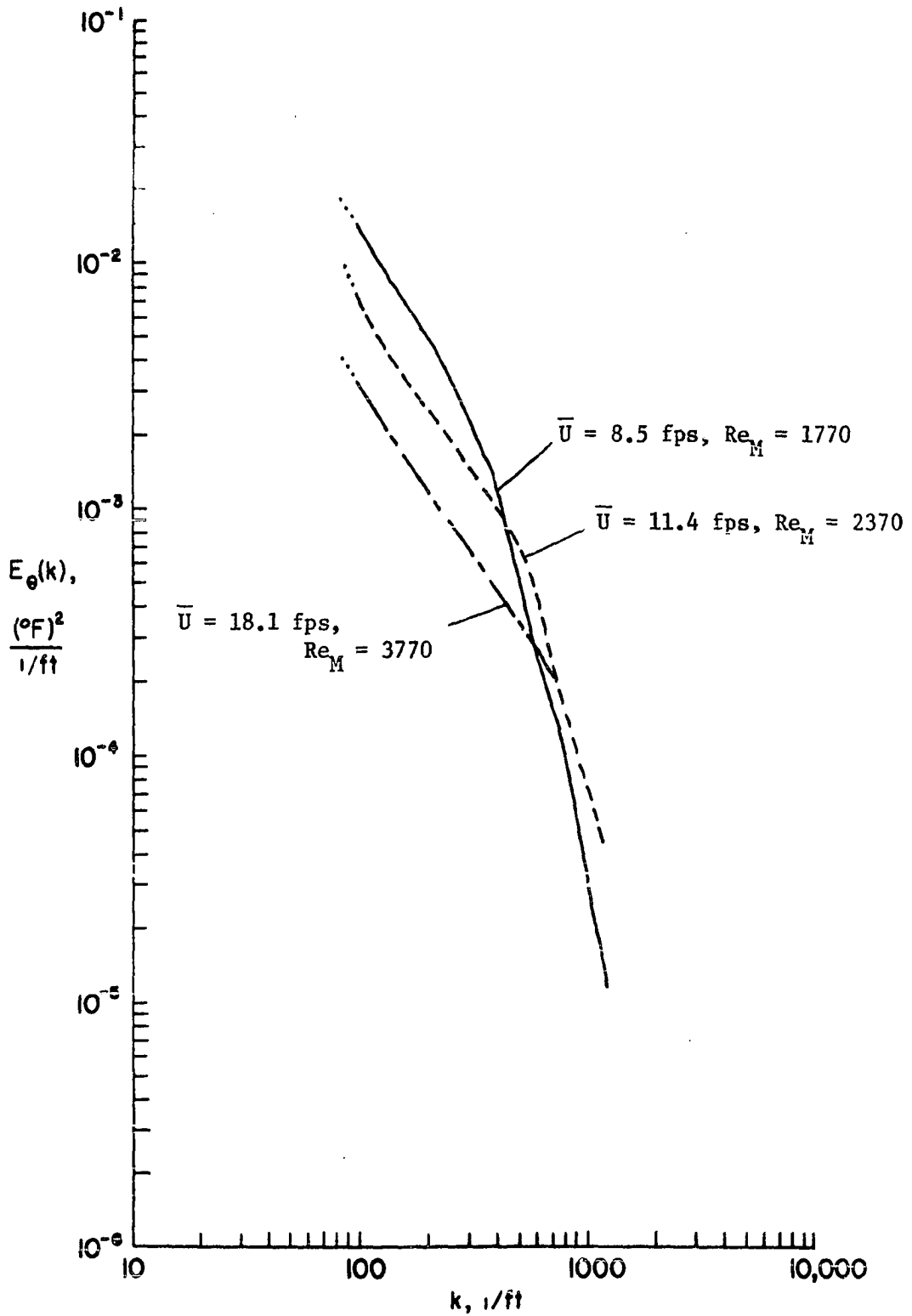


Figure 65. CBS 3-D  $\theta^2$  spectra at  $x/M = 17.4$  showing  $Re_M$  dependence of "knee" or viscous cutoff at  $k_d$

like the knee is, in fact, Reynolds number dependent, shifting upward in wavenumber with increasing  $Re_M$ . This result would be even more pronounced if the curves were properly normalized in  $E_\theta(k)$ .

Figure 66 provides a comparison of the shape of our CBS 3-D  $\overline{\theta^2}$  spectrum converted to units of wavenumber from Figure 54 using Equations 3-10 and 3-30, and the Hinze interpolation formula 3-24 which applies to the low frequency and inertial ranges. Agreement is found except in the region of maximum energy where at least part of the discrepancy is attributable to not having made a noise correction. However, Equation 3-24 is simply an algebraic equation which fits a parabolic rise to a  $-5/3$  decay without a theoretical basis for the region in between.

Equation 3-21 was used to derive the 1-D  $\overline{\theta^2}$  spectrum from one of the CBS 3-D  $\overline{\theta^2}$  spectra in Figure 54 as:

$$E_{\theta 1}(f_1) = \int_{f_1}^{\infty} \frac{E_\theta(f)}{f} df \approx \sum_{f=f_1}^{\infty} E_\theta(f) \frac{\Delta f}{f} \quad (6-18)$$

where  $\Delta f = B$ ; but,  $\Delta f/f = 0.231 = \text{constant}$ , which follows from Equations 5-9, 5-10, and 5-12. The result is shown in Figure 67 which compares the original 3-D spectrum with its derived 1-D counterpart. Notice that the physical relationship of the 3-D and 1-D spectra expressed in Equation 3-20 is approximately satisfied because they intersect at about the  $E_{\theta 1}(f) \sim f^{-1}$  point (see Equation 3-20).

Before further comparing spectra, we summarize the types of spectra

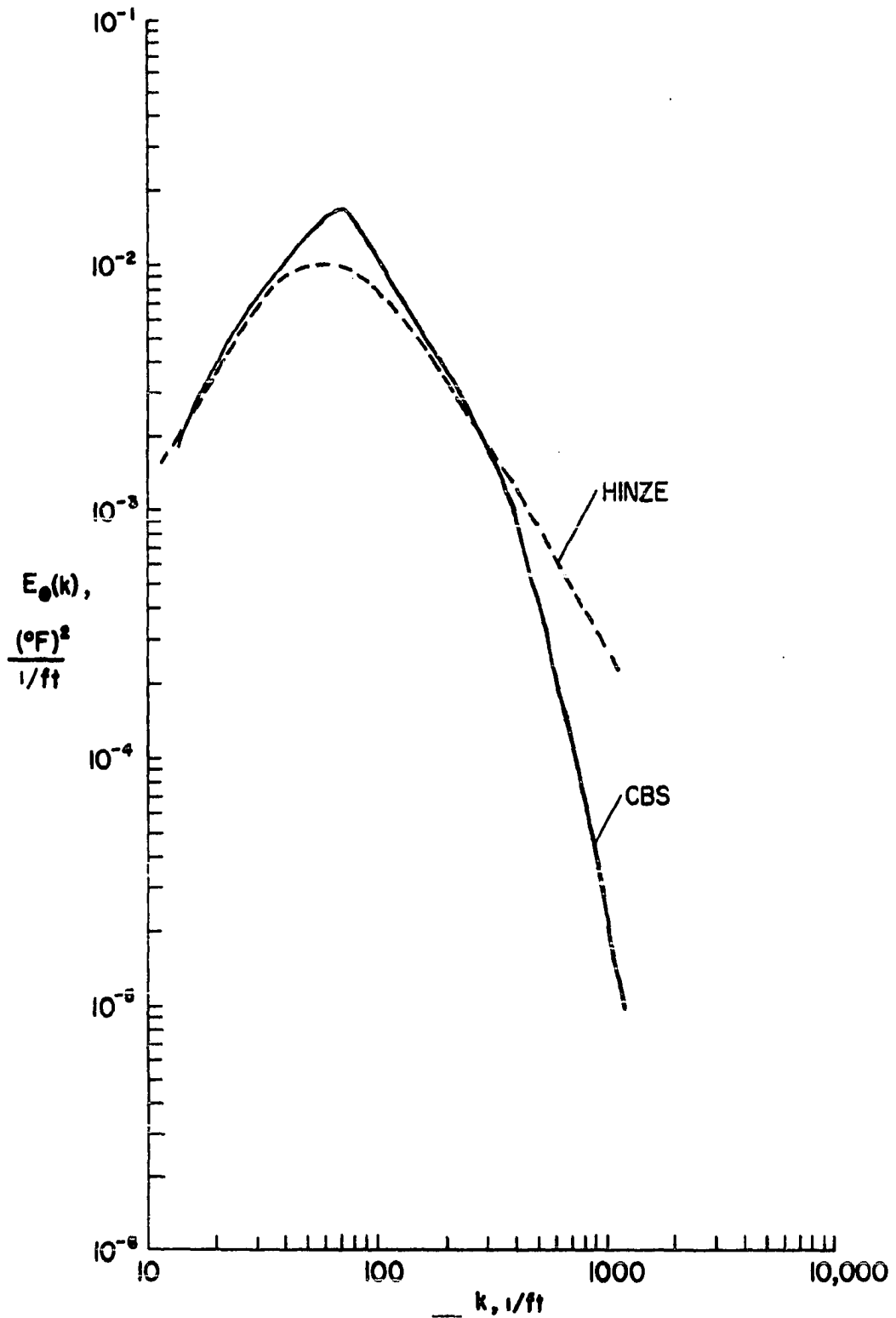


Figure 66. Comparison of CBS 3-D  $\theta^2$  spectrum at  $x/M = 17.4$ ,  $\bar{U} = 8.5$  fps, and  $\Delta = 34^\circ\text{F}$  with Equation 3-24 (from Reference 29)

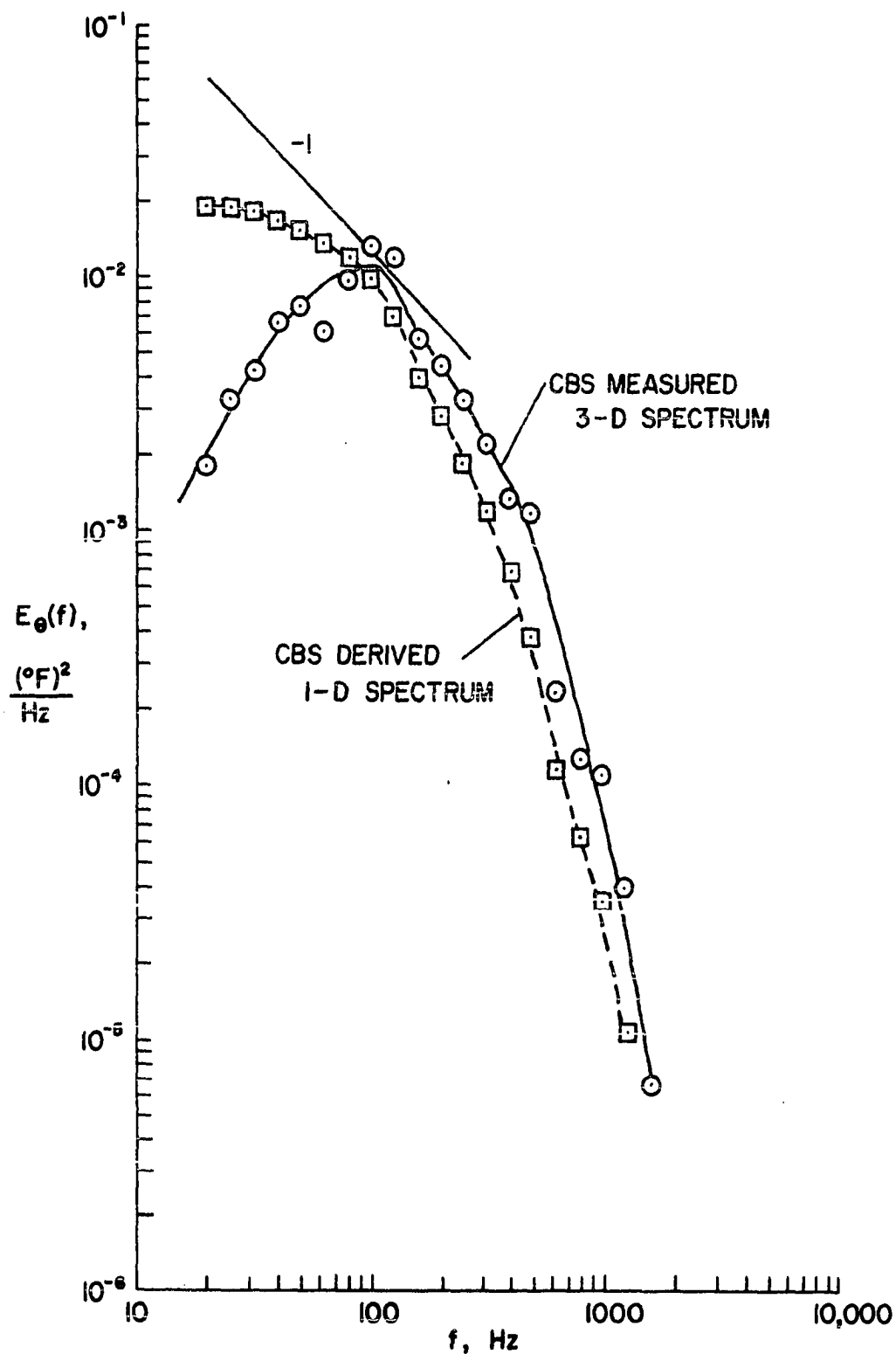


Figure 67. CBS 3-D  $\theta^2$  spectrum at  $x/M = 17.4$ ,  $\bar{U} = 8.5$  fps, and  $\Delta = 34^\circ\text{F}$  and its derived 1-D spectrum

included in this study and the dimensional forms used. We have shown essentially three types of spectra:

1. HWA 1-D  $\overline{u^2}$
2. HWA R.T. 1-D  $\overline{\theta^2}$  and CBS derived 1-D  $\overline{\theta^2}$
3. CBS 3-D  $\overline{\theta^2}$

The dimensional spectrum functions corresponding to these types and their units are, respectively:

$$\begin{aligned}
 1. \quad E_1(k_1) &= \frac{\overline{u^2}(k_1, B)}{B}, \quad \frac{(\text{ft/sec})^2}{1/\text{ft}} \\
 2. \quad E_{\theta 1}(k_1) &= \left[ \frac{\overline{\theta^2}(k_1, B)}{B} \right]_{\text{HWA}}, \quad \frac{(^{\circ}\text{F})^2}{1/\text{ft}} \\
 3. \quad E_{\theta}(k_1) &= \left[ \frac{\overline{\theta^2}(k_1, B)}{B} \right]_{\text{CBS}}, \quad \frac{(^{\circ}\text{F})^2}{1/\text{ft}}
 \end{aligned} \tag{6-19}$$

These wavenumber forms are obtained from directly measured frequency spectra using the relations (3-10) and (3-30). The corresponding area-normalized, non-dimensional forms are

$$\begin{aligned}
 1. \quad \frac{E_1(k_1)}{\overline{u^2}_M} &= \frac{\overline{u^2}(k_1, B)}{B \overline{u^2}_M} \\
 2. \quad \frac{E_{\theta 1}(k_1)}{\overline{\theta^2}_M} &= \left[ \frac{\overline{\theta^2}(k_1, B)}{B \overline{\theta^2}_M} \right]_{\text{HWA}}
 \end{aligned} \tag{6-20}$$

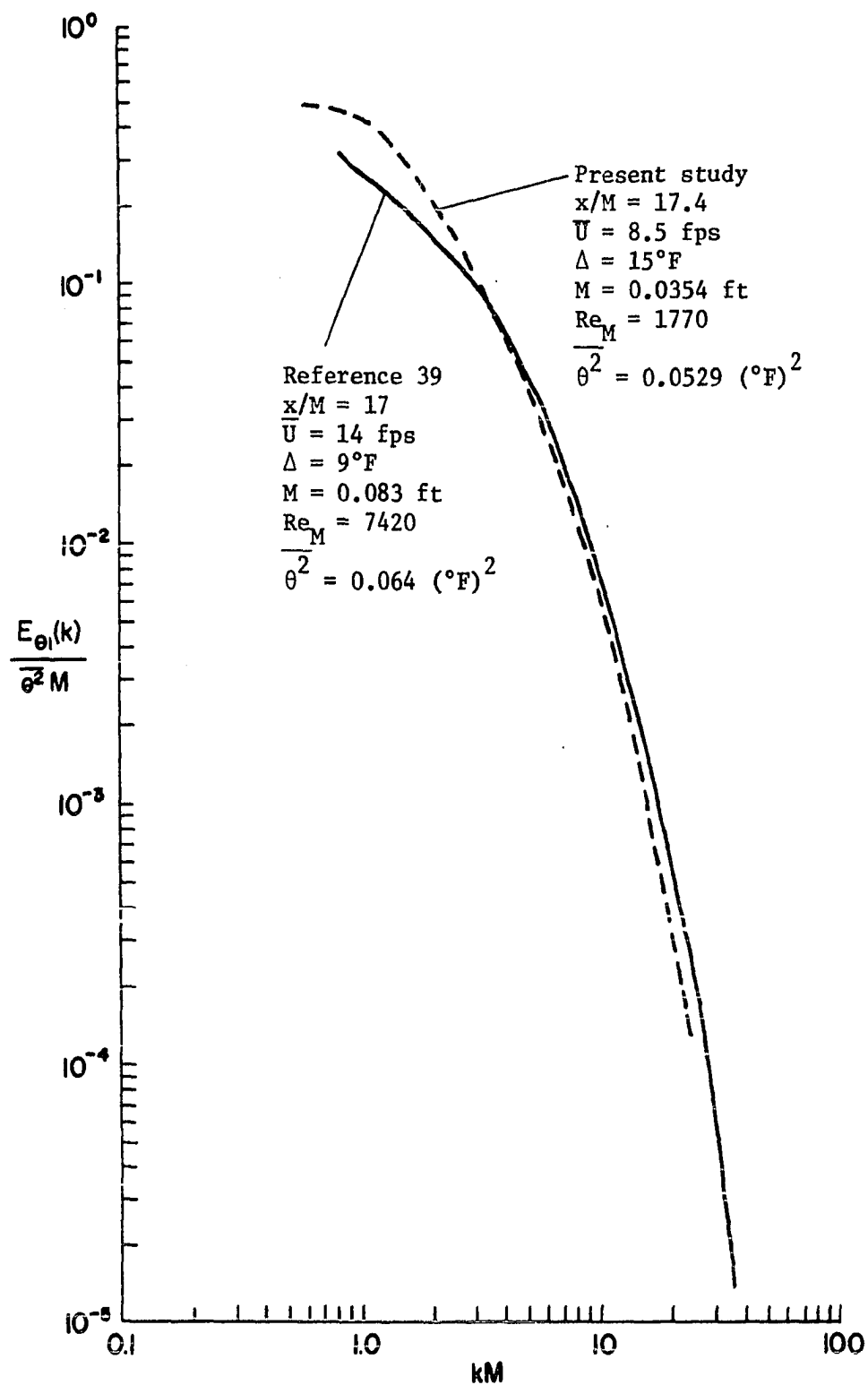
$$3. \quad \frac{E_{\theta}(k_1)}{\overline{\theta^2}_M} = \left[ \frac{\overline{\theta^2}(k_1, B)}{B \overline{\theta^2}_M} \right]_{\text{CBS}}$$

Figure 68 compares one of our HWA R.T. 1-D  $\overline{\theta^2}$  spectra from Figure 48 with one available in Reference 39, and shows that the two curves have essentially the same shape except at low frequencies.

Figure 69 includes copies of our HWA 1-D  $\overline{u^2}$  spectrum from Figure 32 and our HWA R.T. 1-D  $\overline{\theta^2}$  spectrum from Figure 68, which may be compared with our CBS 3-D  $\overline{\theta^2}$  spectrum and its derived 1-D spectrum from Figure 67. Notice that our three 1-D spectra are consistent in that their shapes are nearly the same, indicating the same frequency distribution of energy. The fact that 1-D  $\overline{u^2}$  and  $\overline{\theta^2}$  spectra have the same shapes in isotropic turbulence was noted by Mills et al. (39). The significance of Figure 69 is that we have shown the CBS derived 1-D and 3-D spectra to be consistent with HWA 1-D  $\overline{u^2}$  and  $\overline{\theta^2}$  spectra obtained independently in the same flow model. Furthermore, the latter results have been shown to be consistent with previously obtained 1-D  $\overline{u^2}$  and  $\overline{\theta^2}$  from Reference 39 using grid-generated turbulence in a much larger facility. This agreement in spectral content lends strong support of the validity of our CBS spectral measurements of isotropic scalar turbulence.

A Nicolet Scientific (formerly Federal Scientific) Corp. Omnicious F.F.T. Analyzer became available for a brief period, and was



Figure 68. Comparison of 1-D  $\overline{\theta^2}$  spectra

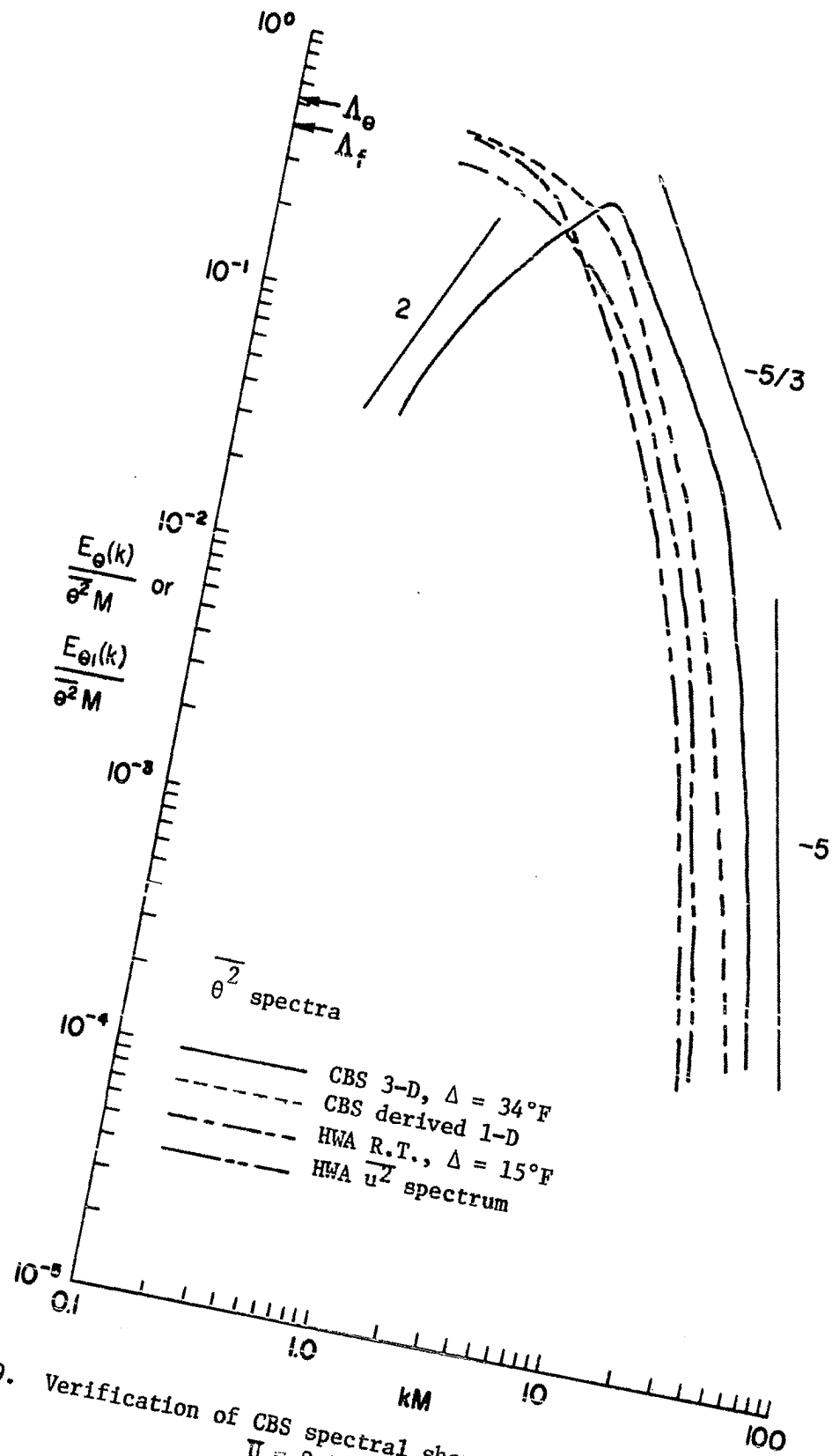


Figure 69. Verification of CBS spectral shape at  $x/M = 17.4$  and  $U = 8.5$  fps

used to compute a co-spectrum from two channels of CBS data for comparison with results processed using our techniques described above. Data were recorded at  $x/M = 17.4$ ,  $\bar{U} = 8.5$  ft/sec, and  $\Delta = 32^\circ\text{F}$  on a Sony Model TC-252 Stereo Taperecorder at 7 1/2 inches per second. While this taperecorder was not intended for research applications, its response was checked using an oscillator and found essentially flat between 20 and 10,000 Hz. Results of analyzing the data with our correlator are compared to calculations performed by the F.F.T. analyzer in Figure 70. A nominal bandwidth of 2.5 Hz was applied by the F.F.T. for the 2000 Hz analysis range. The voltage spectra shown were normalized to the product of the rms values of each channel for convenience. The peak at 60 Hz is recorder noise pickup at the main frequency. While the F.F.T. data show considerable scatter, they do tend to confirm our co-spectral results at least qualitatively over the entire frequency range.

#### 4. Convection speed

Space-time correlograms may be obtained by separating the CBS beams and using the procedures discussed above. Here we are interested in illustrating the technique, checking  $\bar{U}$  in heated flow by measuring thermal eddy convection speeds, and illustrating eddy decay in the spatial coordinate.

Figure 71 illustrates the familiar shift of cross-correlogram peaks in  $\tau$  with increasing beam separation  $\xi$ . Note that the vertical

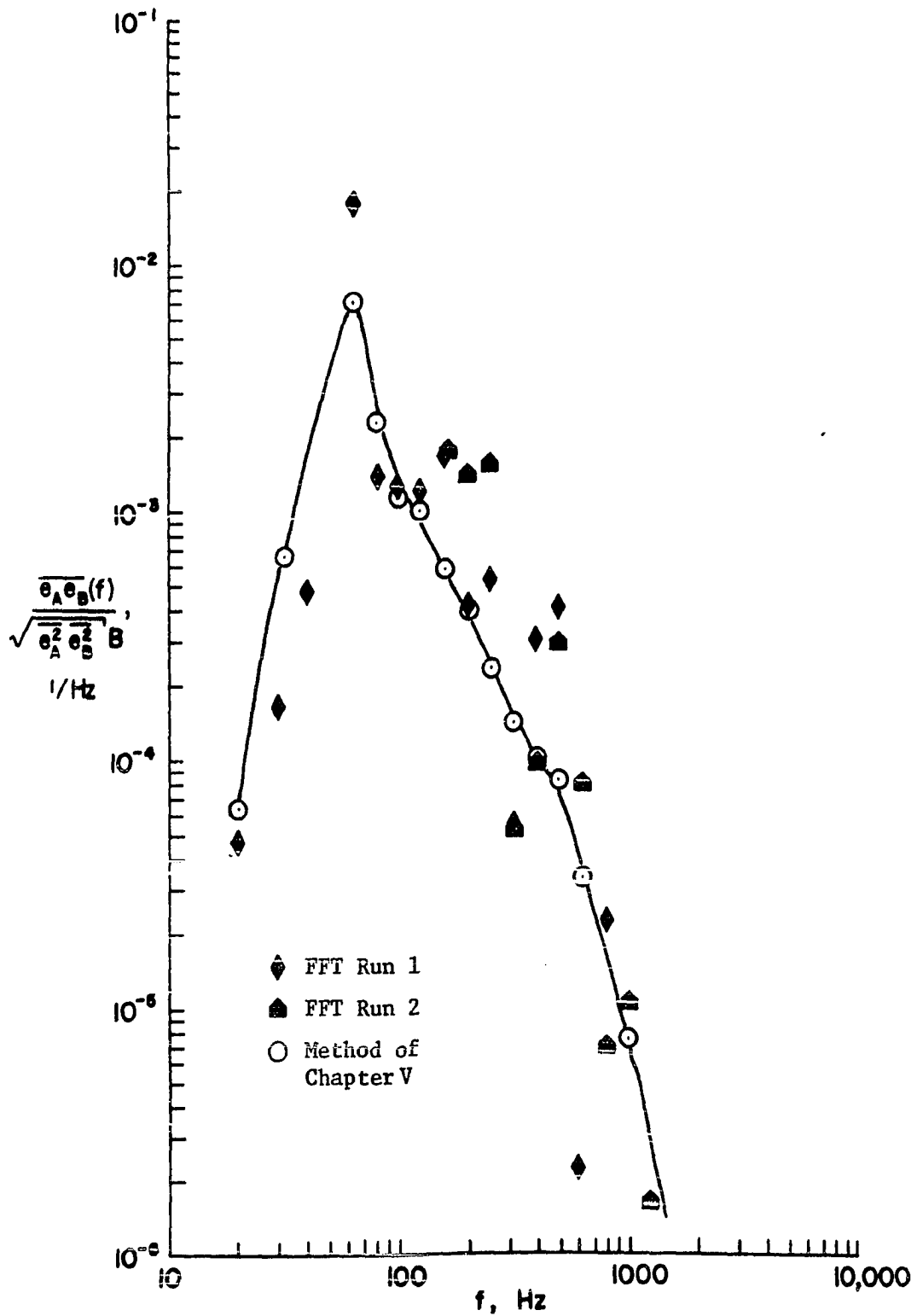


Figure 70. Comparison of CBS 3-D  $\overline{\theta^2}$  spectra at  $x/M = 17.4$ ,  $\bar{U} = 8.5$  fps, and  $\Delta = 34^\circ\text{F}$  processed using correlator and using F.F.T. analyzer

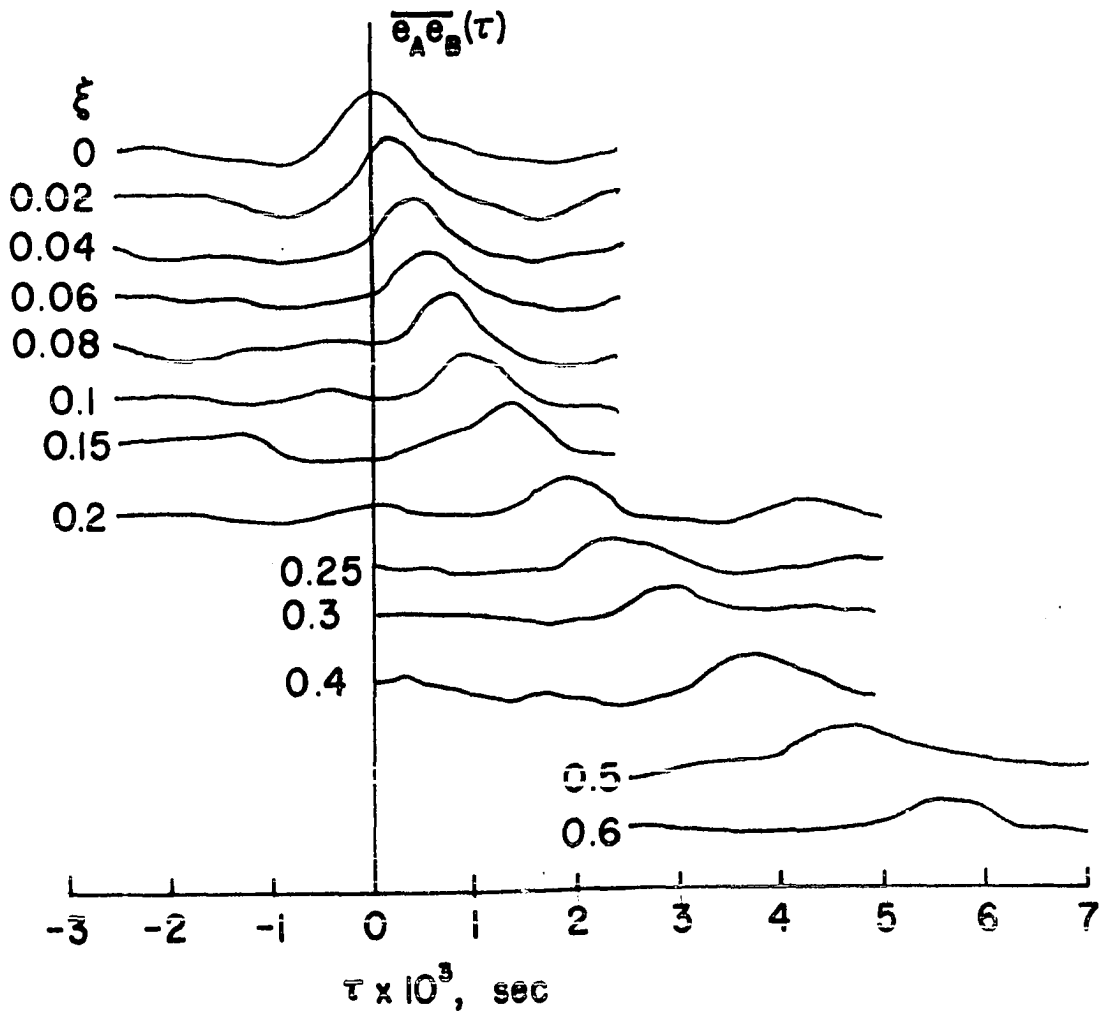


Figure 71. CBS space-time correlograms at  $x/M = 6.78$ ,  $\bar{U} = 3.0$  fps,  $\Delta = 23^\circ\text{F}$ , and BPF 150-1500 Hz (arbitrary vertical spacing)

spacing of these curves is arbitrary. As discussed in Reference 52, while each of these curves is an Eulerian cross-correlogram, the envelope tangent to the peaks represents a moving-axis cross-correlation which is indicative of the decay of a scalar eddy moving at the mean convection speed. In Reference 22 a kinematic parameter called the moving axis time scale or eddy lifetime is defined as the time delay for which the moving-axis cross-correlation falls to 1/3 of its value at  $\tau = 0$ . If we let  $\tau_\ell$  be the eddy lifetime and  $\xi_\ell$  the distance travelled by the eddy in its lifetime then

$$\xi_\ell = \bar{U}_c \tau_\ell \quad (6-21)$$

where  $\bar{U}_c$  is the eddy convection speed. While we have not bothered to measure  $\xi_\ell$  and  $\tau_\ell$ , it can be seen that a definite peak is still detectable at  $\xi = 0.6''$  and  $\tau_p = 5.6$  ms.

Figure 72 is a graph of beam separation versus corresponding correlogram-peak delay time for Figure 71. The slope of this line is approximately  $\bar{U}_c = \Delta\xi/\Delta\tau$ . We find  $\bar{U}_c = 8.87$  ft/sec, about 11% higher than the value of  $\bar{U} = 8.0$  ft/sec measured with the HWA behind a cold grid; we will return to this deviation momentarily. Figure 73 summarizes four more convection speed runs at two locations further downstream in the isotropic region. The results for  $\bar{U}_c$  are tabulated on the figure, and again show values higher than  $\bar{U}$  obtained from Table 7, in this case about 15%.

Actually, for these measurements the use of peak time delays may have introduced enough error in  $\bar{U}_c$  on the high side to account for the

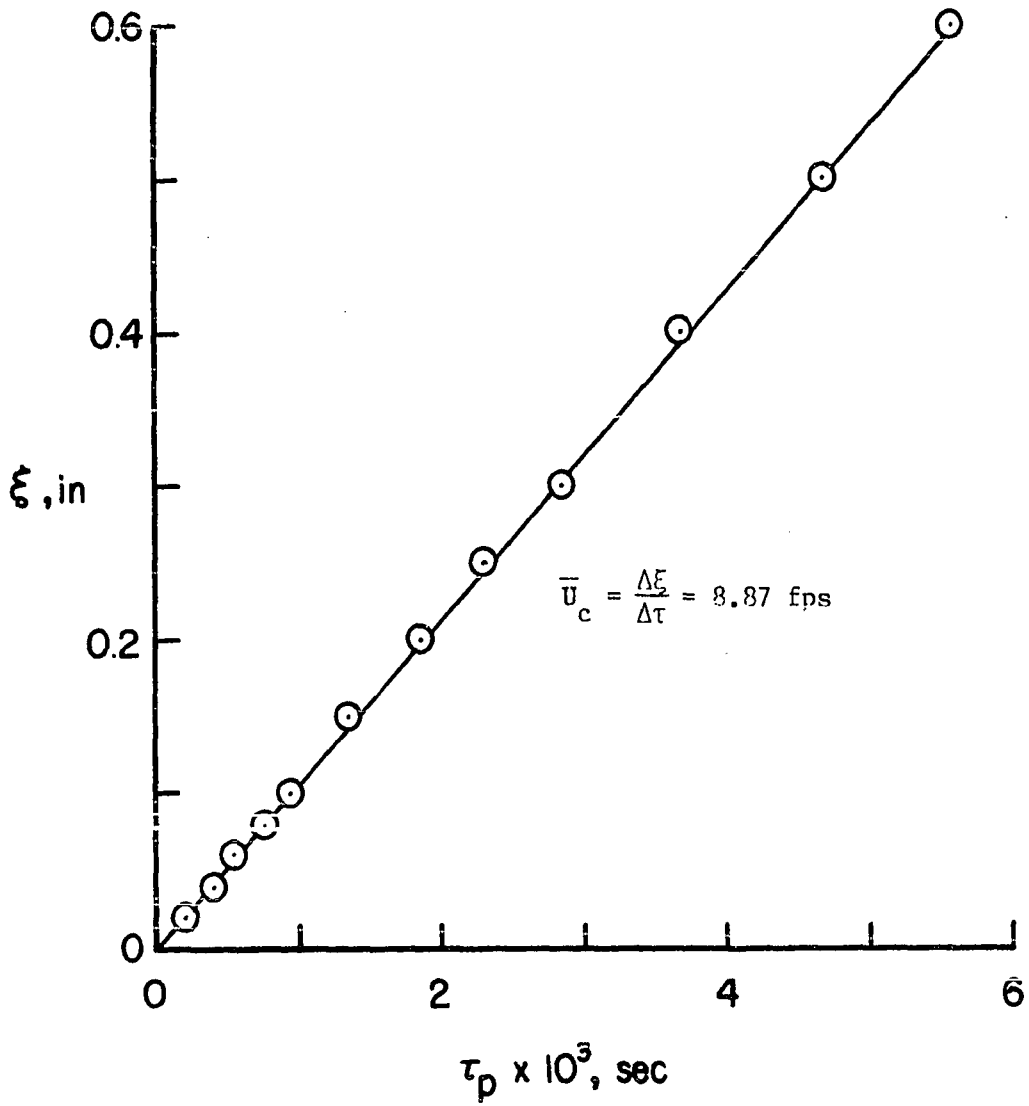


Figure 72. Approximate convection speed of scalar eddies at  $x/M = 6.78$ ,  $\bar{U} = 8.0 \text{ fps}$ , and  $\Delta = 23^\circ\text{F}$

	$x/M$	$\Delta$	$\bar{U}$	$\bar{U}_c$
○	17.4	22°F	8.5 fps	9.7 fps
□	17.4	34	8.5	9.7
◇	24.4	49	8.55	9.7
△	17.4	27	18.0	20.7

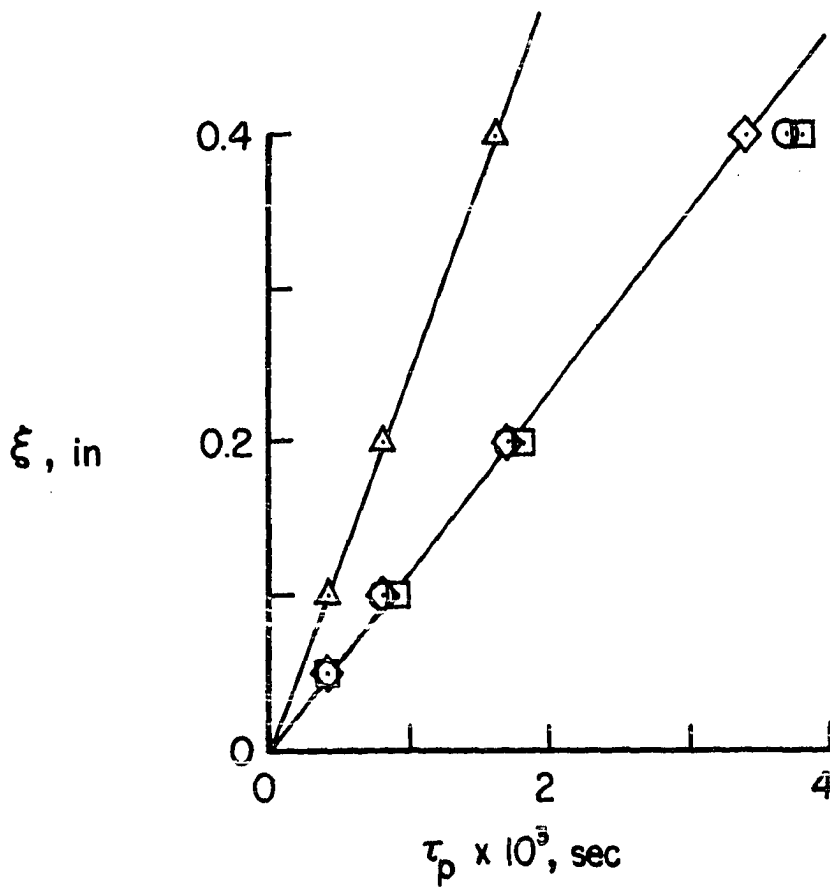


Figure 73. Approximate convection speed of scalar eddies



above deviation, since we should plot time delays and spacings representing the points of tangency. Also, the data of Table 7 were obtained in cold flow with the HWA, and were reliable only to about  $\pm 18\%$  in absolute level because of uncertainty in the reference pitot-static tube manometer reading. In heated flow, however, one might expect an increase in mean velocity in this test set-up for the following reasons. We may assume a constant mass flow rate demand by the blower at a given flow control setting irrespective of grid heating, because for all settings used, the preponderance of air going into the blower came through the flow control tube surface perforations at about ambient temperature. Thus,

$$\dot{m} = \bar{\Gamma} \bar{U} A = \text{constant} \quad (6-22)$$

Therefore, at a given station  $x/M$

$$\bar{\Gamma} \bar{U} = \text{constant}$$

and

$$\frac{d\bar{\Gamma}}{\bar{\Gamma}} = - \frac{d\bar{U}}{\bar{U}} \quad (6-23)$$

However, at the same station

$$\bar{\Gamma} \bar{\Theta} = \frac{\bar{P}}{\bar{R}} = \text{constant}$$

so,

$$\frac{d\bar{\Gamma}}{\bar{\Gamma}} = - \frac{d\bar{\Theta}}{\bar{\Theta}} \quad (6-24)$$

But  $\bar{\Theta}$  may increase, say, from  $535^\circ\text{R}$  ( $75^\circ\text{F}$ ) to  $585^\circ\text{R}$  ( $125^\circ\text{F}$ ) at a high grid overheat of  $\Delta = 50^\circ\text{F} \approx d\bar{\Theta}$ . Therefore, we expect from (6-24)

$$\frac{d\bar{\Gamma}}{\bar{\Gamma}} = - \frac{50}{585} = - 0.085$$

or about a 9% decrease in  $\bar{\Gamma}$ , which with (6-23) means about 9% increase in  $\bar{U}$ . Because of the uncertainty in  $\bar{U}$  measurements of  $\pm 18\%$ , we have not bothered to correct our specifications of  $\bar{U}$  on our heated flow data presented above, but, rather, have used Table 7. But, the difference between  $\bar{U}$  and  $\bar{U}_c$  seen in Figures 72 and 73, may be partially due to this explanation.

#### 5. Isotropy test

The measured signal for one arm of the CBS is an integrated effect across the entire flow region due to scalar fluctuations normal to the knife edge, as we have seen. It seems reasonable that for the scalar fluctuations to be isotropic and, therefore, independent of coordinate system rotations at a point, then the integrated signal should be independent of knife edge rotation. As a necessary, but not sufficient test of isotropy, the knife edge of the horizontal system was rotated from  $\beta = 0^\circ$  through  $\beta = 90^\circ$  at  $x/M = 17.4$  and  $31.5$  where  $\beta = 0^\circ$  corresponds to the normal, vertical position of the knife edge. Note that while the knife edge is being rotated  $0^\circ$  to  $90^\circ$ , the component of  $\bar{U}_c$  in the direction normal to the knife edge is going  $\bar{U}$  to 0 as

$$U_c = \bar{U} \cos \beta \quad (6-25)$$

Thus, the energy spectrum of fluctuations measured by the CBS single beam shifts on the frequency axis according to the Strouhal effect

$$St = \frac{fM}{\bar{U} \cos \beta} \quad (6-26)$$

That is, if the fluctuations are isotropic, their spectral shape (and its integral  $\overline{\theta^2}$ ) will be the same in all directions, but will be shifted successively lower in frequency as  $\beta$  goes  $0^\circ$  to  $90^\circ$ . This downward shift in frequency was observed as a broadening of the cross-correlograms about  $\tau = 0$ . The ability of the CBS to make scalar fluctuation measurements in any direction simply by rotating the supporting frame about an axis through one beam is very convenient, and was taken advantage of by Parks (42) in his study.

The results of the isotropy (knife edge rotation test) are given in Table 10.

Table 10. Isotropy test at  $\bar{U}(x/M = 45.6) = 9.5$  fps and  $\Delta \approx 25^\circ F$

$\alpha$ , degrees	$\overline{e_A e_B}$ at $x/M = 17.5$ , (volts) <sup>2</sup>	$\overline{e_A e_B}$ at $x/M = 31.5$ , (volts) <sup>2</sup>
0	$6.17 \times 10^{-6}$	$4.07 \times 10^{-6}$
15	6.05	4.07
30	5.58	4.07
45	5.82	4.07
60	6.39	4.49
90	6.55	4.07

In both cases the data scatter falls within that expected for repeated runs with the same knife edge orientation, as may be verified from Figure 43. We conclude that since the signal level was independent of knife edge orientation, the scalar turbulence was probably isotropic at these locations.

#### D. Estimates of Dissipation Rates and Scales

Estimates of velocity turbulence dissipation rate and scales based on the data presented above are included in Table 11 along with the technique used and pertinent equations. For certain entries in Table 11 the technique used will now be discussed in more detail. To obtain Entry 1, we assumed Equation 3-5 holds and used it together with (3-27) and (6-1) to obtain

$$\epsilon = -\frac{3}{2} \frac{d}{dt} \left[ \frac{\bar{U}^2}{100} \left( \frac{\bar{U}t}{M} - 7.5 \right)^{-1} \right]$$

or

$$\epsilon(x) = \frac{\bar{U}^3}{66.7M} \left( \frac{x}{M} - 7.5 \right)^{-2}, \frac{\bar{U}^2}{\text{sec}^3} \quad (6-27)$$

The Kolmogoroff or dissipation length scale is, therefore

$$\eta(x) = \left( \frac{\nu^3}{\epsilon} \right)^{1/4} = 2.86 M \left( \frac{\bar{U}M}{\nu} \right)^{-3/4} \left[ \frac{x}{M} - 7.5 \right]^{1/2} \quad (6-28)$$

Entry 2 was obtained by transforming the 1-D  $\overline{u^2}$  spectrum for  $x/M = 17.4$ ,  $\bar{U} = 8.5$  ft/sec from Figure 29, to the dissipation spectrum shown in Figure 74. The area under this curve was obtained by averaging three planimeter readings. Equations 3-28 and 3-29 then gave  $\epsilon$  and  $\lambda_f$ . The

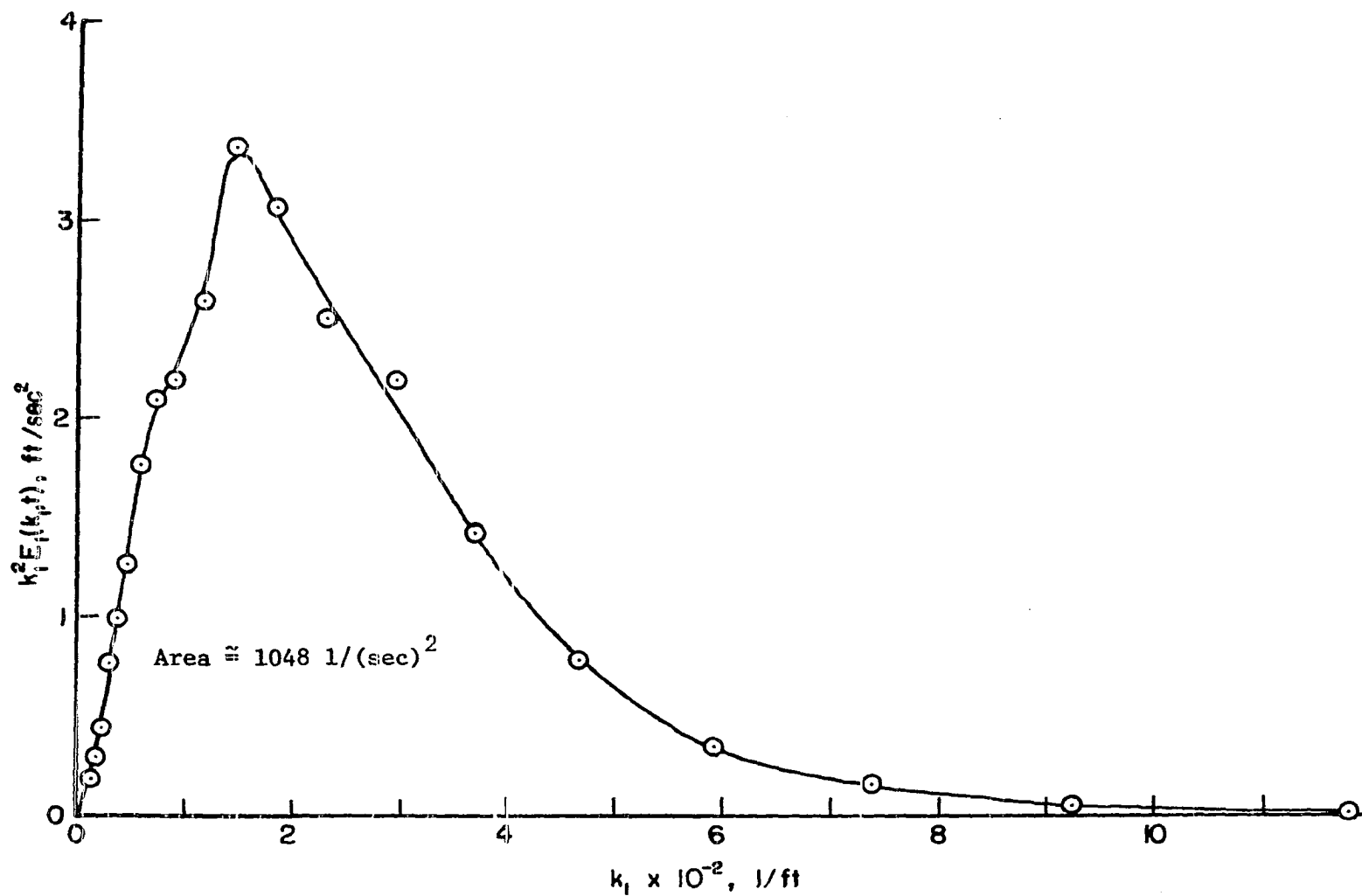


Figure 74. Dissipation spectrum of longitudinal velocity fluctuations at  $x/M = 17.4$ ,  $\bar{U} = 8.5$  fps

agreement between Entries 1 and 2 (and, therefore, 3 and 4, and 6 and 7) is extraordinary, since entirely independent techniques were used (but evaluated at the same  $x/M$ ).

Table 11. Dissipation rate and turbulence scales with evaluations at  $x/M \approx 17.4$ ,  $\bar{U} = 8.5$  fps, and assuming  $\nu = 17 \times 10^{-5}$  ft<sup>2</sup>/sec

Entry	Parameter	Value	$k_{(scale)}^M$	Technique	Equations
1.	$\epsilon$	2.65 ft <sup>2</sup> /sec <sup>3</sup>		Differentiate the semi-empirical decay law	(3-27), (6-1)
2.	$\epsilon$	2.67 ft <sup>2</sup> /sec <sup>3</sup>		Integrate dissipation spectrum at $x/M = 17.4$	(3-28), (3-29)
3.	$\eta$	0.014 inch	30.3	Used $\epsilon$ from Entry 1	$\eta = (\nu^3/\epsilon)^{1/4}$
4.	$\eta$	0.014 inch	30.3	Used $\epsilon$ from Entry 2	$\eta = (\nu^3/\epsilon)^{1/4}$
5.	$k_d$	855 1/ft	30.3	Used $\eta$ from Entry 3	$k_d = 1/\eta$
6.	$\lambda_f$	0.130 inch	3.28	Used $\epsilon$ from Entry 1	(3-28)
7.	$\lambda_f$	0.130 inch	3.28	Integrate dissipation spectrum at $x/M = 17.4$	(3-29)
8.	$\Lambda_f$	0.156 inch	2.72	Integrate Eulerian time autocorrelation coefficient	(3-7)
9.	$\Lambda_f$	0.280 inch	1.51	Locate $E_1(0)$ intercept	(3-31)

The Eulerian time autocorrelation coefficient shown previously in Figure 33 was graphically integrated using a planimeter, and Equation 3-7 was applied to obtain Entry 8. To aid in obtaining Entry 9, the Von Karman semiempirical interpolation formula for 1-D power spectra

$$E_1(k_1) = \text{constant} \left[ 1 + \left( \frac{k_1}{k_e} \right)^2 \right]^{-5/6} \quad (6-29)$$

shown in Figure 75 was used to extrapolate to  $E_1(0)$  in Figure 32 so as to use (3-31). Of the two estimates of  $\lambda_f$ , Entry 8 may be more accurate because of increased uncertainty of  $E_1(k_1)$  at low  $k_1$ .

Using the value of  $\lambda_f = 0.130$  inch from Table 11 we get  $\lambda_g = \lambda_f/(2)^{1/2} = 7.66 \times 10^{-3}$  ft, at  $x/M = 17.4$ ,  $\bar{U} = 8.5$  fps where  $u' = 0.247$  ft/sec. We can then calculate

$$Re_\lambda = \frac{u' \lambda_g}{\nu} = \frac{(0.247 \text{ ft/sec})(7.66 \times 10^{-3} \text{ ft})}{17 \times 10^{-5} \text{ ft}^2/\text{sec}} = 11.1$$

for these conditions. But, from Hinze (29) we expect

$$\frac{\lambda_g}{\eta} = (15)^{1/4} (Re_\lambda)^{1/2} \quad (6-30)$$

For the above conditions  $\lambda_g/\eta = 6.56$  or  $\lambda_f/\eta = 9.28$ ; the latter value holds in Table 11 as it must.

Table 12 includes estimates of the rate of decay of temperature variance, and estimates of temperature scales using our CBS decay and spectral data.

A good estimate of the average size of the scalar power containing eddies  $\ell_e$  (Entry 1) was obtained, as indicated, directly from the CBS 3-D spectrum peak. The unbiased view of energy distribution available from 3-D spectra is clearly advantageous.

Entry 2 was calculated using (3-5), (3-33), and (6-14) in a manner

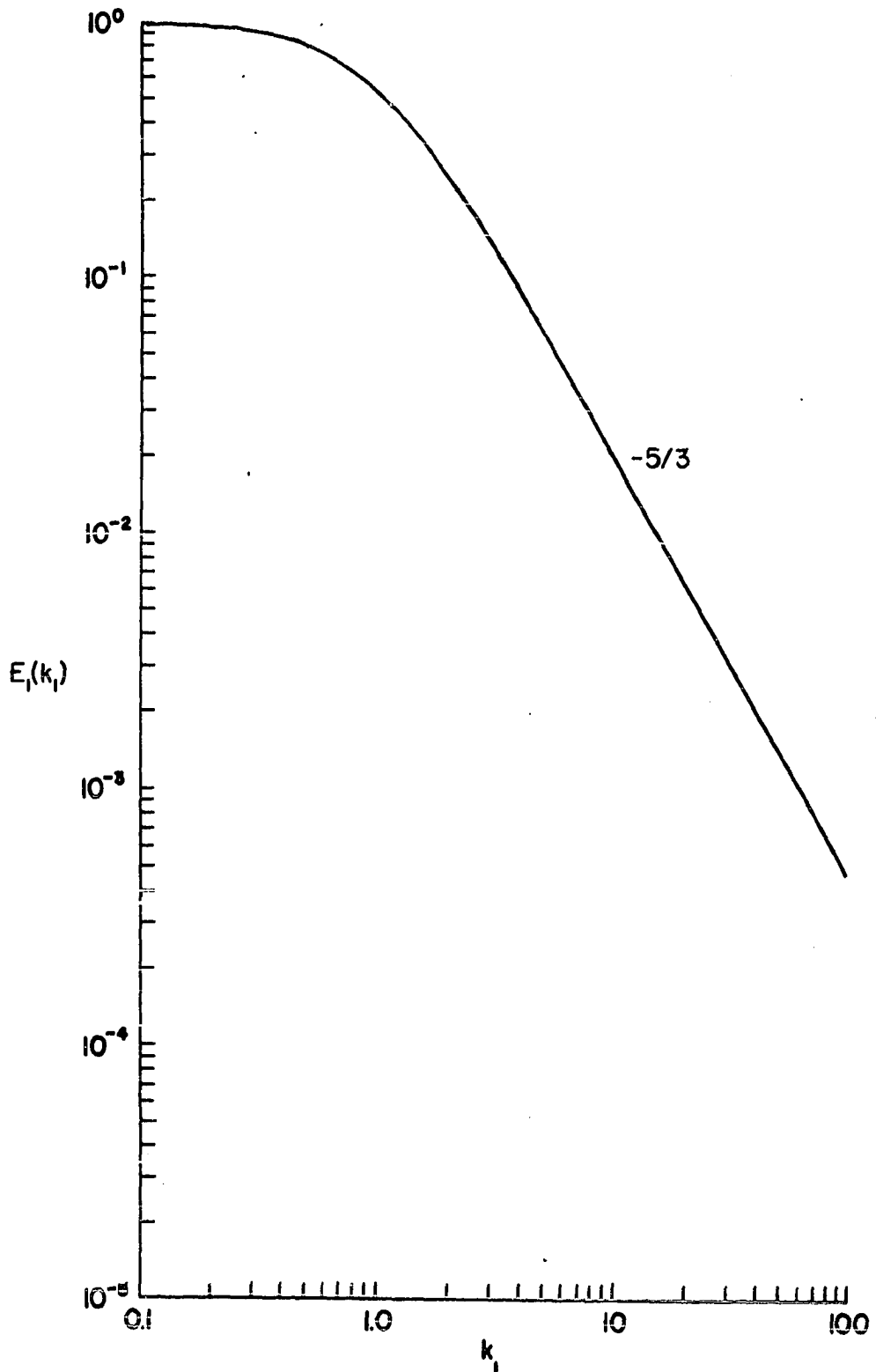


Figure 75. Von Karman semiempirical interpolation spectrum for 1-D power spectra (see Equation 6-29)



similar to that used for Equation (6-27) to get

$$\chi = \frac{\overline{U}\Delta^2}{100 M} \left( \frac{x}{M} - 7.5 \right)^{-2}, \frac{(\text{°F})^2}{\text{sec}} \quad (6-31)$$

We transformed the CBS 3-D  $\theta^2$  spectrum of Figure 66 to the dissipation spectrum shown in Figure 76. A graphical integration and Equations 3-23 and 3-34 gave Entries 5 and 3. Possible errors in (6-14) and the wide scatter of the transformed data points in Figure 76 may be partially responsible for the over 2 factor between entries 2 and 3.

Table 12. Temperature scales and rate of decay of temperature variance with evaluations at  $x/M = 17.4$ ,  $\overline{U} = 8.5$  fps,  $\Delta = 34^\circ\text{F}$ , and assuming  $\alpha = k/\overline{T}C_p = 26.6 \times 10^{-5}$  ft<sup>2</sup>/sec

Entry	Parameter	Value	$k(\text{scale})^M$	Technique	Equations
1.	$\ell_e$	0.171 inch	2.48	Estimate from peak of CBS 3-D $\theta^2$ spectrum in Figure	$\ell_e = 1/k_e$
2.	$\chi$	$28.3(\text{°F})^2/\text{sec}$		Differentiate the semi-empirical decay law	(3-33), (6-14)
3.	$\chi$	$61.4(\text{°F})^2/\text{sec}$		Integrate dissipation spectrum at $x/M = 17.4$	(3-34), (3-23)
4.	$\lambda_\theta$	0.145 inch	2.93	Used $\chi$ from Entry 2	(3-34)
5.	$\lambda_\theta$	0.0987 inch	4.31	Integrate dissipation spectrum at $x/M = 17.4$	(3-23)
6.	$\Lambda_\theta$	0.360 inch	1.18	Locate $E_{\theta 1}(0)$ intercept on CBS derived 1-D $\theta^2$ spectrum	(3-22)

Finally, Entry 6 was estimated from the CBS derived 1-D spectrum given in Figure 69 at  $E_{\theta 1}(0)$  and with (3-22).

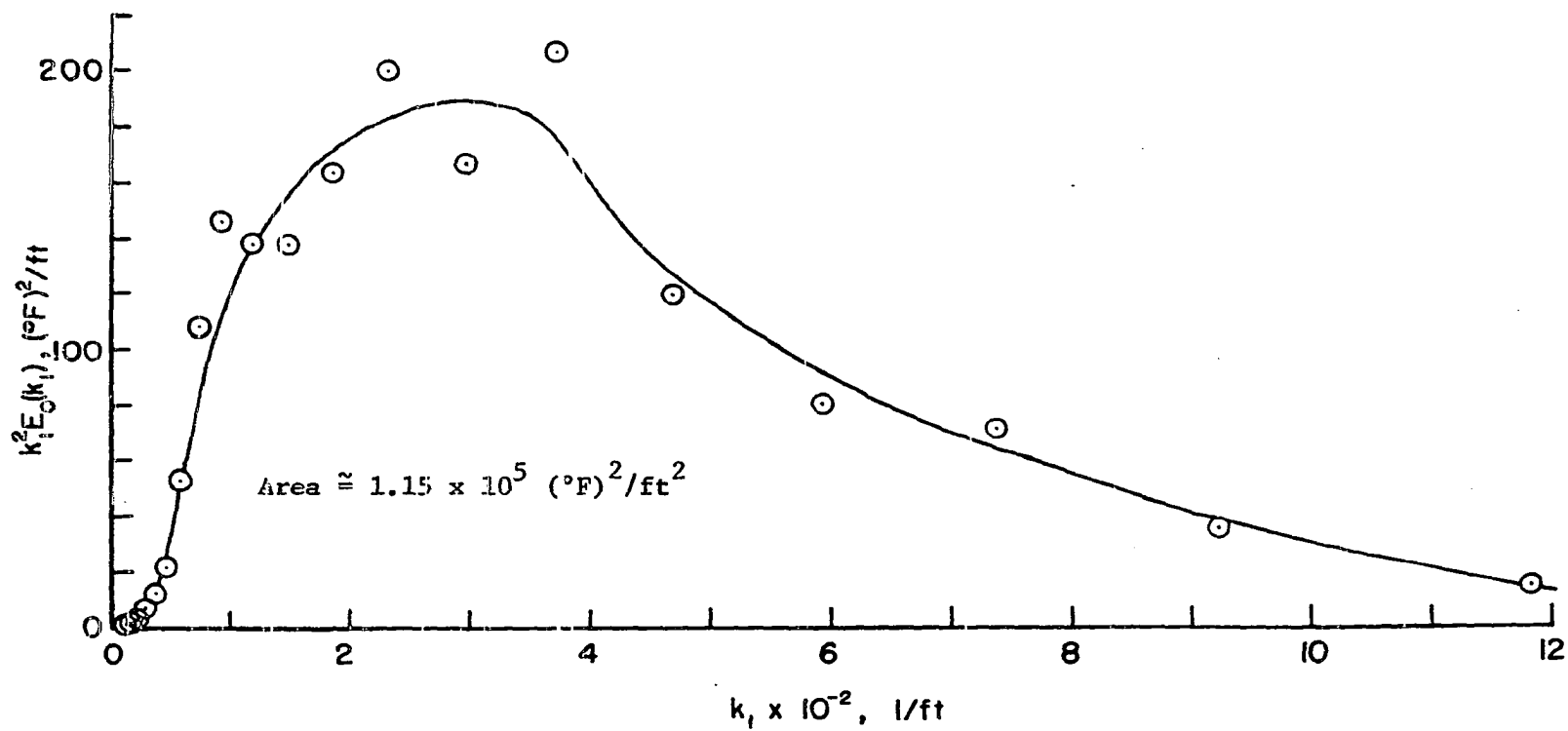


Figure 76. Dissipation spectrum of temperature fluctuations at  $x/M = 17.4$ ,  $\bar{U} = 8.5$  fps, and  $\Delta = 34^\circ\text{F}$

### E. Hot-Wire Mixed Mode

Results of the HWA mixed mode data analysis were presented in Table 4. It may be noted that these calculations did not account for mean speed increases due to increased  $\bar{\theta}_a$  as discussed in Section C.4 above. Values of  $\bar{U}$  in cold flow were used for all calculations here. We surmised in Chapter V that these results might be useful for indicating trends at best. However, even an indication of the trend of  $\overline{u\theta}$  in this particular flow is of interest to us, for  $\overline{u\theta}$  is a measure of the heat transported by turbulence, and we anticipate  $\overline{u\theta} \rightarrow 0$  as the combined fluctuations approach isotropy (see Hinze 29 or Tennekes and Lumley 48). In addition, the HWA and CBS  $u$  and  $\theta$  decay and spectral results shown above have shown nothing unusual in what, from previous measurements in grid-generated turbulence, we believed to be the nonisotropic region. This is, of course, important because of our interest in investigating the applicability of the CBS instrument in nonisotropic flows (recall isotropy was used to get to scalar variance from the CBS covariance).

The trend in  $\overline{u\theta}$  with  $x/M$  for the first six entries in Table 4 is basically downward as expected. In fact, the initial drop-off is precipitous between  $x/M = 6.78$  and  $10.3$ , after which the decay appears gradual into the isotropic region, with additional reduction by  $x/M = 45.6$  which should be well into the isotropic zone. However, except for the trend, these results are inconclusive even on a relative basis, since the final two entries at a lower overheat show that at least a

factor of about 2 reduction in  $\overline{u\theta}$  is still measured. In other words, we are not sure what small  $\overline{u\theta}$  means.

Turning to the  $u'/\bar{U}$  data in Table 4, Sandborn (44) has suggested that, since at low velocities and high wire overheats  $S_\theta$  may be reduced to as little as 5% of  $S_u$ , it is possible to measure  $\overline{u^2}$  in the presence of temperature fluctuations. For example, from Equation 3-60 if  $S_\theta = 0.1 S_u$  and  $\overline{u\theta} = 0$ , then  $\overline{e^2}$  is proportional to  $\overline{u^2}$  with only  $0.01 \overline{\theta^2}$  error. Sandborn cites a study in which this approximation was investigated. To check such an approximation with our data, consider Run 1 of Table 3 where for  $\bar{U} = 9.48$ ,  $\Delta = 18^\circ\text{F}$ , and  $\bar{\theta}_w - \bar{\theta}_a = 402^\circ\text{F}$ , we calculate  $S_\theta/S_u = 0.072$ . Assuming  $\overline{u\theta} = 0$  at  $x/M = 45.6$  and neglecting  $S_\theta^2 \overline{\theta^2}$  in (3-60), then with  $e'$  and  $S_u$  from the table we get  $u' = e'/S_u = 0.0047/0.0324 = 0.145 \text{ ft/sec}$  or  $u'/\bar{U} = 0.145/9.48 = 0.0153$ . This compares with  $u'/\bar{U} = 0.0142$  for isothermal flow from Figure 27 for a difference of about 8%.

The  $u'/\bar{U}$  data from Table 4 are shown plotted in Figure 27. This data indicates the proper trend, but appears significantly low at all locations. The  $\theta'$  data from Table 4 plotted on Figure 46 also appear low for  $\Delta = 34^\circ$  compared with the CBS decay data, but the agreement is fairly good at  $x/M = 45.6$  if we extrapolate the CBS data. As before, the CBS and HWA  $\theta$  data show better agreement far enough downstream.

## VII. SUMMARY OF RESULTS AND CONCLUSIONS

An experimental study of scalar turbulence in air has been conducted in the low-speed wake of a heated, biplane grid of round rods which was installed in a specially designed, miniature, low-turbulence ( $u'/\bar{U} = 0.007$  at  $\bar{U} = 11.5$  ft/sec) wind tunnel. Crossed-beam schlieren and hot-wire anemometer systems were applied to obtain data in both isotropic and nonisotropic regions. Test conditions encompassed various downstream locations ( $6.78 \leq x/M \leq 45.6$ ), mean velocities ( $8 \leq \bar{U} \leq 21$  ft/sec), and grid overheats ( $0 \leq \Delta \leq 60^\circ\text{F}$ ); the data were compared with previous experimental results. This study was unique in that it was the first known application of a CBS to a confined flow field of air within glass walls. (The test section plexiglass sidewalls imposed no particular operational problems.) In addition, it was the first CBS application to grid-generated scalar turbulence, and the only one to date which has successfully produced three-dimensional scalar spectra.

We have demonstrated in this study the usefulness of the CBS instrument in directly portraying the actual 3-D scalar spectral shape, in that these spectra reveal a peak corresponding to the range of maximum energy containing eddies. These spectra also tend to confirm, for the first time, the theoretically predicted spectral slopes on either side of the peak even at our very low mesh Reynolds numbers of order 2000. Such detail has not heretofore been observable in 1-D hot-wire or hot-film spectra due to the aliasing problem. In fact, support for the

-5/3 power law region has come almost exclusively from HWA data obtained in geophysical flows which provide high Reynolds numbers and, therefore, wide enough inertial subranges to survive the smearing effect of aliasing.

Regarding CBS measurements, we remind the reader that a CBS responds to gradients in index of refraction which are proportional to gradients in density for constant specific refractivity (52). Wilson found that, under certain conditions (including isotropy), a CBS has the theoretical capability of measuring the density fluctuation variance, as well as one component of the true 3-D scalar spectrum function. In incompressible flow and when density and temperature fluctuations are relatable, then the direct CBS scalar fluctuation measurements may be interpreted as temperature fluctuations. We are emphasizing the fact that the CBS measures temperature fluctuations only in the sense that these give rise to concomitant density and, therefore, index of refraction fluctuations.

The basic flow field core of temperature fluctuations superimposed on velocity fluctuations was investigated and found to be approximately uniform and homogeneous in velocity and temperature as desired. Turbulence levels, decay rate, and spectral shapes were found to be in good agreement with data of Mills et al. (39) in spite of a non-constant test-section speed.

An unfortunate, but not insurmountable problem with the CBS system was encountered in the form of noise due to laser power ripple. The

noise was carefully identified in probability density functions, spectra, and correlograms and, ultimately, corrected for only in the CBS covariance level measurements. We note that this laser noise problem is not inherent to the CBS technique and would not have occurred had additional filtering been present in the laser power supplies. While other forms of noise were measurable, they were found not to contribute appreciably to the CBS covariance. CBS single beam pdf's were Gaussian in shape as were pdf's of the HWA velocity and temperature signals.

Except for 1-D  $\overline{\theta^2}$  spectra, the HWA resistance thermometer measurements were rather disappointing. A  $\overline{\theta^2}$  decay was barely discernable in the data scatter through the isotropic region, although  $\theta'$  showed-up linear with  $\Delta$ . The R.T. measured a more rapid decay rate of  $\overline{\theta^2}$  in the nonisotropic region than the CBS; also, it produced lower absolute  $\theta$ -fluctuation levels over the entire flow field than the CBS and the Johns Hopkins group (39).

The CBS  $\theta'$  data also varied linearly with  $\Delta$  (and so did the single beam data). These results were found to agree reasonably with the data of Reference 39 for  $\Delta = 9^\circ\text{F}$ , and to similarly show a "linear"  $\overline{\theta^2}$  decay over the region surveyed (early initial period) in contrast to the  $-3/2$  prediction.

One-dimensional  $\overline{\theta^2}$  power spectra recorded by the R.T. had essentially the same shape as the  $\overline{u^2}$  spectra. However, numerous measurements of CBS 3-D scalar spectra revealed a peak at about  $f_e = 100 \text{ Hz}$  for  $\overline{U} = 8.5 \text{ ft/sec}$ , with a shape on either side which consistently

tended to support the  $k^2$  and  $k^{-5/3}$  theoretical power laws for the lowest wavenumbers and inertial subrange, respectively, despite presence of the laser ripple noise. Furthermore, these CBS spectra exhibited a "knee" which appeared to be Reynolds number dependent and, therefore, indicative of a diffusive cutoff. No conclusions could be drawn about the spectral rolloff slope beyond the knee, except that it appeared to be significantly steeper than in the inertial range.

A CBS 1-D  $\overline{\theta^2}$  spectrum was derived from its 3-D counterpart using the theoretical transformation between isotropic scalar spectra (Equation 3-21) given by Kovaszny et al. (36). The shape of this derived spectrum was found to compare favorably with that of our HWA  $\overline{u^2}$  and  $\overline{\theta^2}$  spectra, which were in turn consistent with previously measured experimental data of Reference 39. Thus, in addition to providing experimental verification of Equation 3-21, we have shown that the CBS measures the correct scalar spectral content.

We mention in passing that while the 1-D  $\overline{u^2}$  and  $\overline{\theta^2}$  spectra have the same shape, the 3-D spectra will not necessarily be the same. Recall that the theoretical expression relating 1-D and 3-D  $\overline{u^2}$  spectra is not identical in form to (3-21); see, for example, Hinze (29) or Panchev (41).

Convection speed data yielded eddy mean speeds higher than measured with the HWA in turbulent flow at ambient temperature, as might be expected in a constant mass flow situation. The scalar fluctuations in a highly probable isotropic flow region approximately passed a necessary



CBS test for isotropy. Several estimates of turbulence and scalar turbulence length scales were presented and, in general, appeared realistic in view of the geometry of the grid and observed spectral content of the fluctuations.

We note our mesh Reynolds numbers  $Re_M$  and turbulence Reynolds numbers  $Re_\lambda$  of order 2000 and 10, respectively, are far below those which we would expect to justify an assumption like Kolmogoroff's second hypothesis and the subsequent dimensional derivation of the  $-5/3$  power law for an inertial subrange in which the turbulence is dependent on  $\epsilon$  but not  $\nu$ . Nor would we expect such low values to justify neglect of the viscous term in the dynamic equation for turbulence or scalars. This is to say, the Reynolds numbers, Peclet numbers, and Prandtl numbers assumed in the theories reviewed above simply are not directly applicable to the present study where  $Re_M \sim 2000$ ,  $Pe \sim 10$  (assuming  $\lambda_0 = 0.13''$ ), and  $Pr \sim 0.70$ .

To more fully substantiate or calibrate the CBS  $\overline{\theta^2}$  absolute levels, a better standard than the particular HWA sensor used here as a resistance thermometer is needed along with more refined measurements. The best standard seems to be a microminiature resistance thermometer. Solving mixed mode equations for  $\overline{\theta^2}$  does not appear to be accurate enough for this purpose, although this technique can produce valuable  $\overline{u\theta}$  estimates in non-isothermal flow. Measurements of  $\overline{\theta^2}$  using both CBS and resistance thermometer should then be made simultaneously (for identical flow conditions) and, perhaps, recorded on magnetic tape.

A lingering question is the validity of CBS  $\overline{\rho^2}$  or  $\overline{\theta^2}$  results obtained in non-isotropic shear flows. Recall that, in theory, CBS covariance and spectral measurements in such flows will be valid, provided they are locally homogeneous. That is, isotropy is not an essential assumption for CBS usage. The literature review has cited several studies in which CBS covariance profiles and valuable kinematic properties were successfully obtained in boundary-free shear flows. Also, Parks (42) has measured CBS covariance levels under highly non-isotropic conditions across a two-dimensional, turbulent flame front with the intent of quantizing reaction intensity in terms of density variance levels. While we cannot completely resolve this question, we have shown CBS measurements of scalar fluctuation level, decay, and spectra for the probable non-isotropic region of our flow model; these results were at least consistent with our expectations on approach to the grid. The question of CBS  $\overline{\rho^2}$  validity in non-isotropic situations deserves, and undoubtedly will receive further attention in light of the accessibility of more complicated high-speed turbulent shear flows and turbulent flows with temperature gradients to CBS measurement of density or temperature statistics.

## VIII. REFERENCES

1. Arya, S. P. S. and E. J. Plate. "Hot-Wire Measurements in Non-Isothermal Flow." Instruments and Control Systems, 42 March (1969), 87-90.
2. Batchelor, G. K. Homogeneous Turbulence. Cambridge, Great Britain: Cambridge University Press, 1953.
3. Batchelor, G. K. "Small Scale Variations of Convected Quantities Like Temperature in a Turbulent Fluid. Part 1. General Discussion and the Case of Small Conductivity." J. Fluid Mech., 5 (1959), 113-133.
4. Batchelor, G. K. and A. A. Townsend. "Decay of Isotropic Turbulence in the Initial Period." Proc. Roy. Soc. (London), 193A (1948), 593.
5. Batchelor, G. K., I. D. Howells and A. A. Townsend. "Small Scale Variations of Convected Quantities Like Temperature in a Turbulent Fluid. Part 2. The Case of Large Conductivity." J. Fluid Mech., 5 (1959), 134-139.
6. Becker, H. A., H. C. Hottel and G. C. Williams. "On the Light Scattering Technique for the Study of Turbulence and Mixing." J. Fluid Mech., 30 (1967), 259-284.
7. Bendat, J. S. and A. G. Piersol. Measurement and Analysis of Random Data. New York: John Wiley and Sons, 1966.
8. Burchill, W. E. and B. G. Jones. "Interpretation of Hot-Film Anemometer Response in a Non-Isothermal Field." Symposium on Turbulence in Liquids, University of Missouri-Rolla, Rolla, Missouri, October 4-6, 1971.
9. Carr, A. D., M. A. Connor and H. D. Buhr. "Velocity, Temperature and Turbulence Measurements in Air for Pipe Flow with Combined Free and Forced Convection." ASME J. Heat Transfer, 95 (November 1973), 445.
10. Chandrasekhar, S. "The Fluctuations in Density in Isotropic Turbulence." Proc. Roy. Soc. (London), 210A (1951), 18.
11. Chevray, R., and N. K. Tutu. "On Velocity Measurements in Non-Isothermal Turbulent Flows." Symposium on Turbulence in Liquids, University of Missouri-Rolla, Rolla, Missouri, October 4-6, 1971.

12. Collis, D. C. and M. J. Williams. "Two-Dimensional Convection from Heated Wires at Low Reynolds Numbers." J. Fluid Mech., 6 (1959), 357-384.
13. Corrsin, S. "The Decay of Isotropic Temperature Fluctuations in an Isotropic Turbulence." J. Aero. Sci., 18, No. 6 (June 1951), 417-423.
14. Corrsin, S. "Extended Applications of the Hot Wire Anemometer." NASA TN 1864, 1949.
15. Corrsin, S. "Heat Transfer in Isotropic Turbulence." J. Appl. Phys., 23, No. 1 (January 1952), 113-118.
16. Corrsin, S. "On the Spectrum of Isotropic Temperature Fluctuations in an Isotropic Turbulence." J. Appl. Physics, 22, No. 4 (April 1951), 469-473.
17. Corrsin, S. and M. S. Uberoi. "Spectra and Diffusion in a Round Turbulent Jet." NACA Rep. 1040, 1951 (Supersedes NASA TN 2124).
18. Demetriades, A. "Theory of Hot-Wire Correlation Measurements in Compressible Flow with Application to Wakes." AIAA Paper No. 72-117, January, 1972.
19. Dryden, H. L. and I. H. Abbott. "The Design of Low Turbulence Wind Tunnels." NACA Rep. 940, 1949.
20. Fisher, M. J. and R. J. Damkevala. "Fundamental Considerations of the Crossed-Beam Correlation Technique." NASA CR 61252, 1969.
21. Fisher, M. J. and F. R. Krause. "The Crossed Beam Correlation Technique." J. Fluid Mech., 28 (1967), 705-717.
22. Fisher, M. J., W. T. Mayo, D. M. Meadows, R. H. Burrin and G. E. Beisel. "The Generation and Radiation of Supersonic Jet Noise; Jet Flow Measurement and Analysis with Special Emphasis on Remote Sensing Devices." Air Force Aero Propulsion Laboratory, Wright-Patterson AFB, Ohio, AFAPL-TR-75-53-Vol. VI, July, 1972.
23. Freymuth, P. "Hot-Wire Anemometer Thermal Calibration Errors." Instruments and Control Systems, 43 (October 1970), 82-83.
24. Gibson, Carl H. "Fine Structure of Scalar Fields Mixed by Turbulence I. Zero Gradient Points and Points of Minimal Gradients." Phys. of Fluids, 11. No. 11 (November 1968), 2305-2315.

25. Gibson, Carl H. "Fine Structure of Scalar Fields Mixed by Turbulence II. Spectral Theory." Phys. of Fluids, 11, No. 11 (November 1968), 2316-2327.
26. Gibson, C. H. and W. H. Schwartz. "The Universal Equilibrium Spectra of Turbulent Velocity and Scalar Fields." J. Fluid Mech., 16 (1963), 365-384.
27. Grant, H. L., B. A. Hughes, W. M. Vogel and A. Moilliet. "The Spectrum of Temperature Fluctuations in Turbulent Flow." J. Fluid Mech., 34 (1968), 423-442.
28. Hanson, Carl E. "The Design and Construction of a Low Noise, Low Turbulence Wind Tunnel." Engineering Projects Lab., Dept. of Mech. Engr., M.I.T., Cambridge, Mass., Tech. Rept. DSR 79611-1, January, 1969.
29. Hinze, J. O. Turbulence. New York: McGraw-Hill, 1959.
30. "Hot-Wire Measurements of Air Velocity, Direction, and Temperature." Datametrics (formerly Flow Corp.), Wilmington, Mass., Technical Memorandum Bulletin 94B, 1968.
31. Kaimal, J. C., J. C. Wyngaard, Y. Izumi and O. R. Cote. "Spectral Characteristics of Surface-Layer Turbulence." Quart. J. R. Met. Soc., 98 (1972), 563-589.
32. Kistler, A. L. and T. Vrebalovich. "Grid Turbulence at Large Reynolds Numbers." J. Fluid Mech., 26 (1966), 37-47.
33. Kistler, A. L., V. O'Brien and S. Corrsin. "Preliminary Measurements of Turbulence and Temperature Fluctuations Behind a Heated Grid." NACA RM 54D19, June, 1954.
34. Kovasznay, L. S. G. "The Hot-Wire Anemometer in Supersonic Flow." J. Aero. Sci., 17, No. 9 (1950), 595.
35. Kovasznay, L. S. G. "Turbulence in Supersonic Flow." J. Aero. Sci., 20, No. 10 (October 1953), 657.
36. Kovasznay, L. S. G., M. S. Uberoi and S. Corrsin. "The Transformation Between One- and Three-Dimensional Power Spectra for an Isotropic Scalar Fluctuation Field." Phys. Rev., 76 (1949), 1263.
37. Liepmann, H. W. "Experimental Fluid Mechanics: The Impact of Modern Instrumentation." In Applied Mechanics, Proc. 13th International Congress of Theoretical and Applied Mechanics, Moscow, August, 1972.

38. Liepmann, H. W. and A. Roshko. Elements of Gas Dynamics. New York: John Wiley and Sons, 1967.
39. Mills, R. R., Jr., A. L. Kistler, V. O'Brien and S. Corrsin. "Turbulence and Temperature Fluctuations Behind a Heated Grid." NASA TN 4288, August, 1958.
40. Morkovin, M. V. "Fluctuations and Hot-Wire Anemometry in Compressible Flows." NATO AGARDograph No. 24, 1956.
41. Panchev, S. Random Fluctuations and Turbulence. Oxford, Great Britain: Pergamon Press, 1971.
42. Parks, F. B. "An Optical Crosscorrelation Technique for Turbulent Density Measurement in Flames." Ph.D. Dissertation, University of Missouri-Columbia, Columbia, Missouri, 1973.
43. Roe, G. E. "An Optical Study of Turbulence." J. Fluid Mech., 43 (1970), 607-635.
44. Sandborn, Virgil A. Resistance Temperature Transducers. Water Resources Publications, Colorado State University, Fort Collins, Colo., 1972.
45. Schlichting, Hermann. Boundary Layer Theory. New York: McGraw-Hill, 1968.
46. Schubauer, G. B. and W. G. Spangenberg. "Aerodynamic Characteristics of Damping Screens." NACA TN 2001, January, 1950.
47. "Temperature Compensation of Thermal Sensors." Thermo-Systems Inc., St. Paul, Minn., Anemometry News, 2, No. 1, 1973.
48. Tennekes, H. and J. L. Lumley. A First Course in Turbulence. Cambridge, Mass.: M.I.T. Press, 1972.
49. Townsend, A. A. "The Diffusion of Heat Spots in Isotropic Turbulence." Proc. Roy. Soc. (London), 209A (1951), 418.
50. Uberoi, M. S. and S. Corrsin. "Diffusion of Heat from a Line Source in Isotropic Turbulence." NACA Rep. 1142, 1953 (Supersedes NACA TN 2710).
51. Van Atta, C. W. "Sampling Techniques in Turbulence Measurements." In Annual Review of Fluid Mechanics, Vol. 6. Palo Alto, Calif.: Annual Reviews Inc., 1974.

52. Wilson, L. N. and R. J. Damkevala. "Statistical Properties of Turbulent Density Fluctuations." J. Fluid Mech., 43 (1970), 291-303.
53. Wilson, L. N., F. R. Krause and F. A. Kadrmas. "Optical Measurements of Sound Source Intensities in Jets." In Basic Aerodynamic Noise Research, I. R. Schwartz, Ed. NASA SP-207, 1969.

## IX. ACKNOWLEDGEMENTS

This dissertation is dedicated to Dr. Lennox N. Wilson and Nancy Martin. The author thanks Dr. Wilson for his guidance and support through this research endeavor.

Appreciation is extended to Dr. R. F. Brodsky, Dr. C. T. Hsu, Dr. J. D. Iversen, and Dr. G. A. Nariboli for serving as members of the author's examining committee. Financial support was provided by an Iowa State University Research Foundation (National Science Foundation) grant as well as the Engineering Research Institute. The author thanks Ms. Cecelia Byers for typing the manuscript.